

**PROCESS-BASED MODELLING OF
TURBIDITY-CURRENT
HYDRODYNAMICS AND SEDIMENTATION**

REMCO GROENENBERG

PROCESS-BASED MODELLING OF TURBIDITY-CURRENT HYDRODYNAMICS AND SEDIMENTATION

HET PROCES-GEBASEERD MODELLEREN VAN DE
HYDRODYNAMICA EN SEDIMENTATIE
VAN TROEBELSTROMEN

(met een samenvatting in het Nederlands)

Proefschrift

ter verkrijging van de graad van doctor
aan de Technische Universiteit Delft,
op gezag van de Rector Magnificus prof. dr. ir. J.T. Fokkema,
voorzitter van het College voor Promoties,
in het openbaar te verdedigen

op maandag 5 maart 2007 om 15:00 uur

door

Remco Maarten GROENENBERG

doctorandus in de Geologie
geboren te Eindhoven

Dit proefschrift is goedgekeurd door de promotoren:

Prof. dr. S. B. Kroonenberg

Prof. dr. S. M. Luthi

Toegevoegd promotor:

Dr. G. J. Weltje

Samenstelling promotiecommissie:

Rector Magnificus,	voorzitter
Prof. dr. S. B. Kroonenberg,	Technische Universiteit Delft, promotor
Prof. dr. S. M. Luthi,	Technische Universiteit Delft, promotor
Dr. G. J. Weltje,	Technische Universiteit Delft, toegevoegd promotor
Prof. dr. ir. H. J. De Vriend,	Technische Universiteit Delft
Prof. J. P. M. Syvitski,	Institute of Arctic and Alpine Research, University of Colorado
Dr. W. McCaffrey,	School of Earth and Environment, University of Leeds
Dr. ir. C. J. Sloff,	Waterloopkundig Laboratorium Delft
Prof. dr. ir. G. J. Stelling,	Technische Universiteit Delft, reservelid

ISBN 978-90-8570-155-2

NUR 933

Copyright © 2007 by R. M. Groenenberg, Section of Applied Geology, Faculty of Civil Engineering and Geotechnology, Delft University of Technology. All rights reserved, no parts of this thesis may be reproduced, stored in any retrieval system or transmitted, in any form or by any means, electronic, mechanical, photocopying, recording or otherwise, without the prior written permission of the author.

Printed with generous financial support from Hans and Elma Groenenberg and DUT.
Cover artwork by Judith Lutje Spelberg.

*A wise man once said that everything could be explained with mathematics.
He had denied his feminine side.
Now where is the wisdom in that?*

-S. Hogarth-

*Take a train to the sea
Be anyone you want to be
A little spark of light inside your mind
Safe and sound off the ground upside down*

-S. Hogarth-

Aan mijn ouders en grootouders,
voor wat mij is gegeven

CONTENTS

VOORWOORD	v
1. INTRODUCTION	1
1.1 Background	1
1.2 Relevance	2
1.3 Challenge	3
1.4 Approach	5
1.5 Thesis outline	6
2. A REVIEW OF PHYSICS, MODELS AND TECHNIQUES	9
2.1 Introduction	9
2.2 Historical perspective	9
2.3 Sediment-gravity flows	12
2.3.1 Cohesive flows	13
2.3.2 Frictional flows	15
2.3.3 Characteristic depositional features	18
2.4 Turbidity currents	19
2.4.1 Initiation mechanisms	21
2.4.2 Magnitude and duration	22
2.4.2.1 Turbid surges	23
2.4.2.2 Quasi-steady turbidity currents	23
2.4.3 Anatomy	25
2.4.3.1 Head	25
2.4.3.2 Body and tail	27
2.4.3.3 Stratification	28
2.5 Research methods	30
2.5.1 Study of modern and ancient turbidite systems	30
2.5.2 Experimental modelling	31
2.5.3 Numerical modelling	33
2.6 Modelling techniques	34
2.6.1 Assumptions and simplifications	34
2.6.2 Reduction of model dimensions	38
2.6.3 Parameterization of sediment transport	39
2.6.4 Turbulence modelling	40
2.6.5 Numerical techniques	42
2.7 Modelling fan stratigraphy: past and present	45
2.7.1 1D Process-based models	45
2.7.2 2D Process-based models	47
2.7.3 Models including turbulence	49
2.7.4 The <i>FanBuilder</i> model	50

3.	MATHEMATICAL MODEL	51
3.1	Introduction	51
3.2	Mathematical model	51
3.2.1	Configuration	51
3.2.2	Governing equations	53
3.2.3	Closure relations	54
3.2.3.1	Shear velocity	55
3.2.3.2	Ambient-water entrainment	55
3.2.3.3	Near-bed sediment concentration	56
3.2.3.4	Erosion	56
3.2.3.5	Deposition	58
3.2.3.6	Bed change	58
3.3	Head region	59
3.4	Analytical solutions	61
4.	NUMERICAL IMPLEMENTATION	63
4.1	Introduction	63
4.2	Conservative vs. non-conservative form	63
4.3	Solution method	65
4.3.1	Requirements and conditions	65
4.3.2	MacCormack scheme	66
4.3.3	Operator splitting	67
4.3.4	Empirical artificial viscosity	69
4.3.5	TVD artificial viscosity	70
4.3.6	Boundary conditions	73
4.3.7	Initial conditions	76
4.3.8	Head region	76
4.3.9	Stability	79
4.3.10	The <i>FanBuilder</i> model	79
5.	QUANTITATIVE VALIDATION EXPERIMENTS	83
5.1	Introduction	83
5.2	Experimental set-up	83
5.3	Quasi-steady flow	85
5.4	Waning flow	88
5.5	Sensitivity to spatial and temporal resolution	93
5.5.1	Sensitivity to length of computational time step	93
5.5.1.1	Quasi-steady flows	93
5.5.1.2	Waning flows	95
5.5.2	Sensitivity to grid-cell size	98
5.5.2.1	Quasi-steady flows	98
5.5.2.2	Waning flows	101
5.6	Discussion	104

6.	QUALITATIVE VALIDATION EXPERIMENTS	107
6.1	Introduction	107
6.2	Complex topography	107
6.2.1	Experimental set-up	108
6.2.2	Unobstructed flow	110
6.2.3	Perpendicular obstacle	113
6.2.4	Circular obstacle	115
6.2.5	Flow constriction	118
6.2.6	Parallel obstacle	120
6.3	Experiments in a small subsiding basin with a turbidite fan system	122
6.3.1	Experimental set-up	122
6.3.2	Hydrodynamics	125
6.3.3	Geometry of deposit	126
6.3.4	Stratigraphy	129
6.4	Discussion	135
7.	SYNTHESIS	139
7.1	Conclusions	139
7.2	Improvements	140
7.3	Future work	143
7.3.1	Field-scale application	143
7.3.2	Numerical experiments	144
	REFERENCES	145
	APPENDIX	167
A.1	List of symbols	167
A.2	Operator discretization	170
A.3	TVD artificial viscosity	174
A.3.1	Roe's linearization technique	174
A.3.2	Roe's technique applied to the 1-D system	175
A.4	Flux limiters	180
A.5	The entropy correction	182
	SUMMARY	185
	SAMENVATTING	191
	CURRICULUM VITAE	197
	LIST OF PUBLICATIONS	199

VOORWOORD

De ervaring leert dat het voorwoord/dankwoord niet alleen het meest gelezen wordt, maar ook het eerst. Om dus maar direct met de deur in huis te vallen: het is zover, het is af. Ook voor promovendi geldt dat het “de dood wordt, of de gladiolen”. Ik kan U vertellen dat het voor mij de gladiolen geworden zijn. Sportverslaggevers vragen op een dergelijk moment “Hoe voel je je nu?” Zonder meer een legitieme vraag, zo blijkt ik nu te vinden, en eentje die ik ook graag beantwoord: “moe, apetrots en heel gelukkig”. Voor U ligt het werk van vijf jaar toewijding aan een fascinerende wetenschap waaraan ik al tijdens mijn studie mijn hart heb verpand. Het gaat me te ver om het een hobby te noemen, want het is veel meer dan dat. Niettemin heb ik het vaak als hobby beleefd, en het altijd een voorrecht gevonden me te mogen verdiepen in een onderwerp waarvan ik tijdens mijn studie Geologie nooit had gedacht dat het zo boeiend kon zijn.

Dit proefschrift zou er niet zijn geweest zonder de steun van een heleboel mensen. Ik wil graag in de eerste plaats mijn beide promotoren, Salomon Kroonenberg en Stefan Luthi, bedanken voor de mij geboden mogelijkheid om deze promotie te doen, voor de steun die ik in die jaren heb gekregen en het gevoelde vertrouwen. Salle, jij hebt me, als initiator van het geheel, aan het begin een kompas gegeven dat naar Gert Jan wees, en daar heb ik dankbaar gebruik van gemaakt. Stefan, jouw bijdrage, vooral tijdens het schrijven, is van grote waarde geweest. Het is de kwaliteit van het proefschrift ten goede gekomen, en ik heb er veel van geleerd.

Gert Jan, ik wil jou als begeleider en toegevoegd promotor in het bijzonder bedanken voor het enorme vertrouwen dat ik altijd van je gevoeld heb, en de daaruit voortvloeiende vrijheid in de invulling van mijn promotie onderzoek. Stiekem is dit toch al het tweede succesvolle wetenschappelijke project dat ik onder jouw begeleiding heb afgerond, dat vind ik een applaus waard. Het staat buiten kijf dat ik van jou in al die jaren heel veel heb geleerd. En zoals je inmiddels weet ben ik uiteindelijk toch “sometjes gaan maken”.

Voor de hulp bij het maken van die sommetjes wil ik graag Kees Sloff bedanken. Kees, ik ben eindeloos bij je geweest met vragen, vragen en nog eens vragen, en nooit heb ik van jou het gevoel gehad dat het te veel was. Ook van jou heb ik veel geleerd, en over een vakgebied (waterloopkunde) waar ik niet in thuis was. Verder wil ik in dit kader nog Zheng Bin Wang en Guus Stelling bedanken voor hun hulp en advies.

Voor de dagelijkse zinnigheden, onzinnigheden en gezelligheid wil ik graag mijn collega AIOs bedanken. Marit, Jose, Irina, Wiebke, Tine, Bob, Joep, Klaas, Luc, Albert, Israel en Rory, de lunchclub, met zijn grappen en grollen, de diepzinnige discussies over allerhande onderwerpen, de knakworsten, gehaktballen, gekookte eitjes en tosti's, is uniek, en nu we borden en bestek hebben, en leren om netjes de tafel schoon te maken, mogen we vast in het nieuwe gebouw ook samen lunchen. Ik denk alleen wel dat er een nieuwe koelkast moet komen, en een nieuwe waterkoker!

Gedurende mijn promotie ben ik drie keer als begeleider meegegaan naar het VESC veldwerk. Jan Kees en Rick, bedankt voor de leuke tijd daar, en de fijne samenwerking. Jan Kees, staat mijn recordtijd op de Col d'Ey nog?

Gelukkig is er voor mij ook leven buiten de wetenschap. Ik voel me rijk met de vele goede vrienden die ik heb, waarvan ik ondervonden heb dat ze er voor me zijn als ik ze nodig heb. Fred, omdat we zo geregeld samen fietsen (op vlakke wegen), ook doordeweeks, heb jij mijn pieken en dalen van vrij dichtbij meegemaakt. Dat scheidt ook een band, of beter gezegd, heeft de onze versterkt. Jan, stiekem heb ik van jouw promotie ervaringen natuurlijk ook het een en ander geleerd, en je adviezen gretig ter harte genomen. Ik hoop dat we, jij, Fred en ik, nog heel veel kilometers samen zullen fietsen! Michiel, jij en ik gaan net zo ver terug als Fred en Jan. Ik vind het geweldig dat we elkaar nog zo regelmatig zien. En hoewel we elkaar wat minder regelmatig zien, geldt dat ook voor Jan-Berend, Esther, Peter-Paul en Leon.

Barbara, een leven kan raar lopen. Jij en ik gaan ook een hele tijd terug, en hebben lief en leed van elkaar van dichtbij meegemaakt. Van de MarBarIllies ben jij het enige blijvertje gebleken in mijn leven, is dat niet wonderlijk? Onze band is zelfs gegroeid de afgelopen jaren. Ik hoop dat je nog jaren in mijn leven blijft, en dat we nog regelmatig samen wat zullen ondernemen.

De oplettende lezer zal het opgefallen zijn dat ik steeds dichterbij huis kom. Ik heb het geluk nog twee oma's te hebben wiens liefde en steun altijd voelbaar is. Wat een weelde. Met jullie en de beide opa's, die elkaar nu ongetwijfeld ergens een high-five geven, is het allemaal begonnen.

Pap en mam, liefde, steun en vertrouwen heb ik ook altijd van jullie gevoeld. Jullie hebben me altijd de keuze gelaten om datgene te doen wat ik graag wilde. Ik wil jullie op deze plaats opnieuw bedanken voor alles wat jullie mij in al die jaren gegeven hebben.

Sasje, je bent ver weg op dit moment, aan het genieten van jezelf en de omgeving, maar straks, tijdens de verdediging, ben je er gelukkig bij. Je bent het liefste, moedigste en mooiste zusje dat ik ken.

Lieve Judith, jij hebt, sinds we elkaar leerden kennen, ongeveer anderhalf jaar geleden, het dichtst bij me gestaan. Jij kent mij niet anders dan dat ik deze zelf gegeven opdracht aan het volbrengen ben, en weet niet beter dan dat het "volgende week af is". Ik dank je met heel mijn hart voor al je liefde, warmte, steun, geduld en vertrouwen, je prachtige coverdesign en ja, gewoon, omdat je bij me wilt zijn.

Als ik je zo bel, om half zes in de ochtend, dan is het echt af.

**PROCESS-BASED MODELLING OF
TURBIDITY-CURRENT
HYDRODYNAMICS AND SEDIMENTATION**

REMCO GROENENBERG

1 INTRODUCTION

1.1 Background

Annually an estimated 15 billion tons of sediment (approximately 5.7 billion m^3) is delivered to the continental margins worldwide (Figure 1.1; Hoogendoorn, 2006). The sediment is transported from mountain ranges to the coastline, where rivers debouch into the oceans to form deltas. At and near deltas, long-shore currents, wave action and tides redistribute and rework the sediment, until it is transported to the deeper oceans by sediment-gravity flows. Over geologic time periods, sustained sediment-gravity flow activity results in large accumulations of sediment in the deep oceans, which form submarine fans that are known to form good hydrocarbon reservoirs.

Sediment-gravity flows are mixtures of sediment and fluid (air, water) which flow downslope by virtue of gravity acting on the sediment grains. Their flow behaviour depends on the density of the ambient fluid, the density of the interstitial fluid, the relative proportion of sediment in the mixture (concentration) and the amount of cohesive material (clay) in the sediment. On land, the ambient fluid is air and the interstitial fluid is air or, in the case of e.g. pyroclastic flows, a mixture of air and hot volcanic gases. In lakes, seas and oceans, the ambient as well as interstitial fluid is water.

In this thesis, the focus is on the contribution of turbidity currents to the evolution of submarine fans in sedimentary basins at the margins of continents. Turbidity currents are sediment-gravity flows that contain a relatively minor proportion of fine-grained sediment. Downslope flow occurs by virtue of the force of gravity acting on the sediment grains in the suspension which, on their way to being deposited, drag the seawater along with them, thereby effectively generating a turbid underflow. Upon reaching lower slope gradients the gravitational force diminishes and the flow may eventually decelerate. Lateral spreading occurs due to a pressure difference with the ambient fluid.

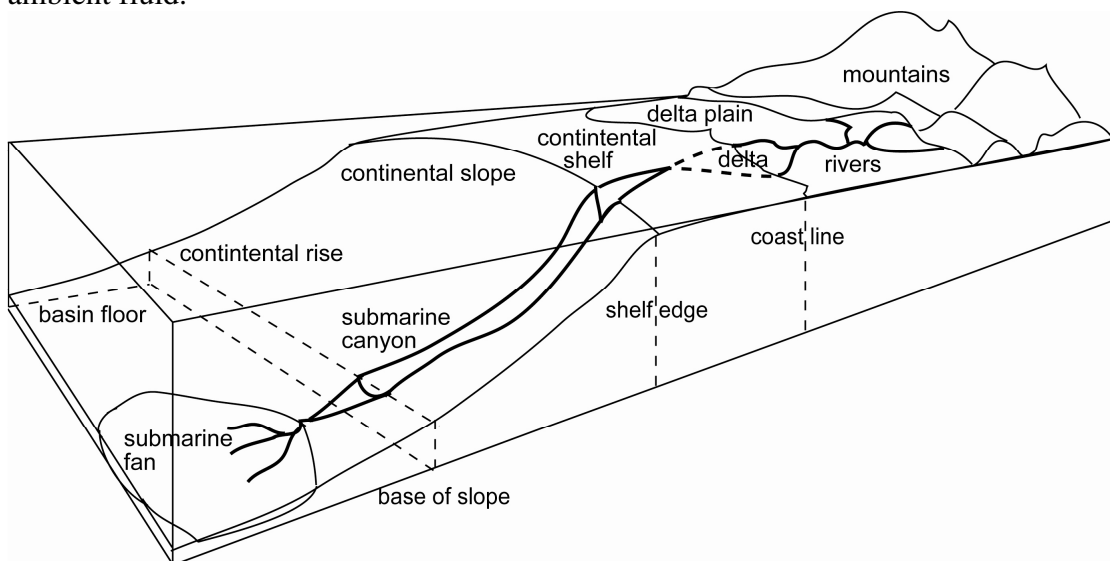


Figure 1.1: Schematic illustration of a (passive) continental margin, displaying the transport path of sediment from a mountainous hinterland to an ocean basin at the margin of a continent.

As the flow thus loses its capacity to carry sediment in suspension, grains will start settling out of suspension, first the coarser ones, then successively the finer ones. Individual beds thus deposited range in thickness from centimetres to meters, but sequential occurrence of turbidity currents over geologic time periods results in turbidite fans with thicknesses of tens to hundreds of meters.

1.2 *Relevance*

Flows along the seafloor, such as turbidity currents, have economical and societal importance. Their genesis or triggering mechanism is usually in the form of earthquakes or subaerial landslides (e.g. associated with volcanic eruptions), and they have the potential to cause industrial, environmental and human disasters such as pipeline or cable breaks, pollutant dispersal and tsunamis. The Grand Banks “turbidity current” on the Laurentian Fan in 1929 for example, was triggered by an earthquake of magnitude 7.2 that occurred off the coast of Grand Banks, Newfoundland (Heezen and Ewing, 1952; Kuenen, 1952). It transported sediment over a distance of 1000 km along the ocean floor (Kuenen, 1952), and provided evidence that large submarine slides could generate turbulent, gravity-driven sediment flows in the ocean (Mulder and Alexander, 2001a). The tsunami, which was triggered by the combined effect of a submarine landslide and the earthquake, caused a damage of \$400,000 (a considerable amount of money in those days) and killed twenty-nine people, the highest death toll attributed to an earthquake in Canada to date. It was registered as far as South Carolina and Portugal (Lander and Lockridge, 1989; Whelan, 1994). The most damaging factor in the Grand Banks event was the submarine landslide, which contributed to the effect of the tsunami and damaged many transatlantic telegraph cables. The reconstructed evolution of the Grand Banks turbidity current (Heezen and Ewing, 1952), which resulted from the submarine landslide, was largely based on location and timing of these submarine cable breaks on the ocean floor. The total volume of sediment released in the landslide was estimated to be 200 km³ (Piper et al., 1988, 1999).

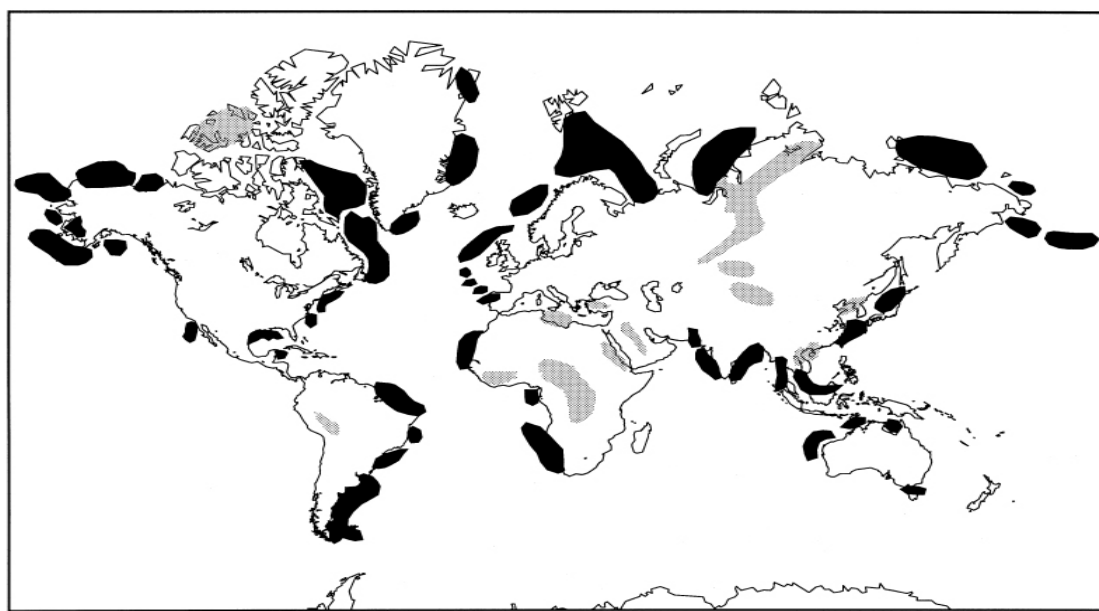


Figure 1.2: World map showing the principal frontier areas for hydrocarbon exploration, including the main deep-water provinces, indicated in black (Stow and Mayall, 2000).

Submarine fan systems, which form through sequential occurrences of sediment-gravity flows over long periods of time in the same area, are volumetrically the most significant clastic accumulations in the deep sea (Normark et al, 1993). Some of the world's largest sedimentary bodies such as the submarine fans of the Mississippi, the Indus, and the Amazon, are deposited by turbidity currents and associated sediment-gravity flows over thousands of years.

Submarine fan systems constitute major petroleum reservoirs throughout the world (Figure 1.2). An estimated 1200 to 1300 oil and gas fields are known from turbidite systems, of which forty-three are classified as giants with more than 500 billion barrels of oil equivalent (Stow and Mayall, 2000). Many of these fields are located in well-established hydrocarbon provinces on continents (onshore) and below shallow shelves (offshore), such as California, the North Sea and the Gulf of Bohai (north-eastern China). Of the twenty-five largest oil and gas fields in the United States, six occur in turbidite reservoirs (Weimer and Link, 1991). Turbidite reservoirs are responsible for 22% of petroleum production in the North Sea (Watson, 1984), 83% of the production in the Campos Basin offshore Brazil (Bacoccolli and Toffoli, 1988) and 90% of the production in the Los Angeles basin (Taylor, 1976).

The relevance of the research presented in this thesis primarily relates to challenges faced in exploration and production of oil and gas reservoirs. The world economy depends heavily on hydrocarbons, and oil and gas reservoirs are the principal source of hydrocarbons for the energy, transport and petrochemical industries. Since the 1980s, turbidite reservoirs have drawn an overwhelming interest from the oil industry. Initially, exploration and development of turbidite reservoirs focused on plays located onshore and offshore in the shallow waters of the continental shelf. From the late 1980s onwards, exploration has progressed into continuously deeper water on the continental slopes, and numerous large discoveries were made in turbiditic settings (channels, base-of-slope fans, basin-floor fans). Since then, more than fifty-seven billion barrels of oil equivalent have been discovered in offshore areas including West Africa, the southeast Gulf of Mexico, Brazil, the northwest shelf of Australia, the North Sea and Southeast Asia. However, drilling and infrastructure costs required to develop these deep-water plays are high. Although today only a part of these reserves is being developed (Slatt, 2003), it is likely that the increase in oil price in recent years will further increase exploration and production efforts in deep-water areas. The mechanisms of deposition, however, are still not fully understood.

1.3 Challenge

The potential for sedimentary rocks to constitute a good reservoir primarily depends on two properties: porosity and permeability. Porosity (commonly symbolized as ϕ) is defined as the relative volume of rock not occupied by solids, and effectively determines the proportion of space (volume) between the grains available for storage of hydrocarbons. Its value is expressed by a number between zero and unity, but commonly ranges between less than 0.01 for granite and 0.5 for peat (Bear, 1972). Freshly deposited sand has a porosity of about 0.4 (40% of the volume of the rock is filled with air or other fluids), but compaction due to burial, which transforms sediment into sedimentary rock, may lower the porosity to below 0.1. Porosity is influenced by, amongst others, the sorting of the sediment. In a well-sorted

sedimentary rock, the grains all have approximately the same size, whereas in a poorly-sorted sedimentary rock, the grains have different sizes with the smaller grains filling the gaps between the larger grains and thus reducing the pore space.

Permeability (commonly symbolized as K) is a measure of the degree to which the pores are connected with each other, and pertains to the ability of fluids to flow through rock. Permeability is an intrinsic rock property. Values of permeability range between 10^6 mD (milliDarcies, $1 \text{ mD} = 10^{-15} \text{ m}^2$) for well-sorted sandstones and 0.0001 mD for granite (Bear, 1972). Rocks with permeabilities much lower than 10^{-3} mD, such as e.g. claystones or evaporites (10^{-6} mD) are considered impermeable and form effective seals of hydrocarbon reservoirs. Porosity and permeability are generally higher in sandstones and lower in siltstones and claystones. Therefore, the distribution of sand, silt and clay in turbidite reservoirs is of primary importance in assessing their production potential. Vertical variations in grain size and bedding occur on a scale ranging from centimetres to meters, whereas horizontal variations typically are at a scale of tens of meters to several kilometres. The interbedding of contrasting lithologies such as sandstones and shales, which is characteristic for turbidite reservoirs, results in horizontally stratified reservoirs with a high degree of vertical heterogeneity. This greatly affects the fluid flow properties of the reservoir.

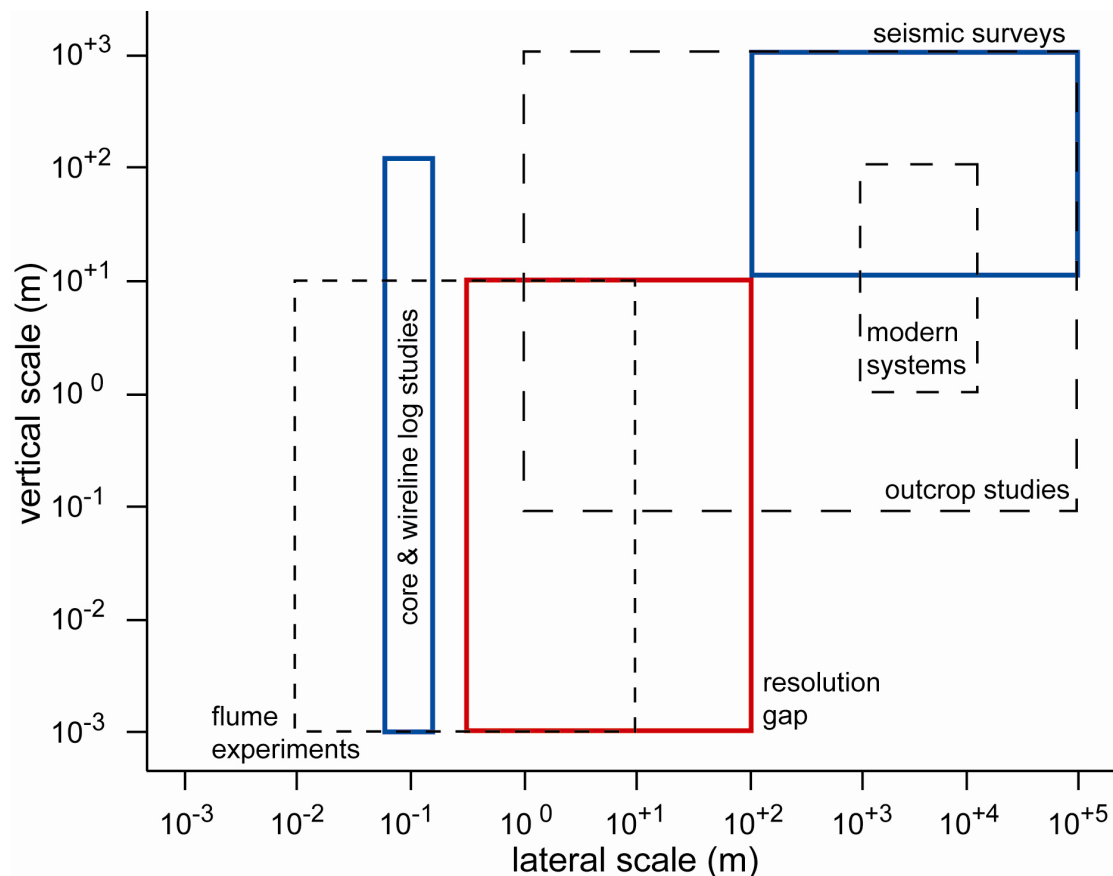


Figure 1.3: Graph illustrating the lateral and vertical scale of observations and data in studies of turbidite reservoirs. Blue boxes indicate commonly acquired data in hydrocarbon reservoirs. The red box indicates the resolution gap, i.e., scales not covered by any of the available data.

Unfortunately, the typical resolution of the main data used in reservoir characterization is either too low or too localized (Figure 1.3, blue boxes). Well data have a high resolution, but they cannot be extrapolated far beyond the immediate vicinity of the wellbore without loss of certainty. By contrast, seismic volumes are large. Data cubes may have horizontal dimensions of tens of kilometres and may be up to several kilometres in depth, but the typical vertical resolution is about thirty meters. This means that heterogeneities that are significantly smaller than thirty meters in thickness cannot be resolved.

Heterogeneities in turbidite reservoirs typically occur on a scale of meters to one-hundred meters horizontally and millimetres to meters vertically (Figure 1.3, red box). Consequently, on the scale of the reservoir architectural elements of turbidite reservoirs uncertainty exists on the anatomy and spatial variability of reservoir properties. Quantification of the geometry and distribution of these elements in a reservoir can provide crucial information to assess sand body volume, connectivity and the distribution of permeability baffles. The work presented here tries to contribute to a better understanding of the architectural elements of turbidity systems and thus to help producing reservoirs contained in such systems more efficiently.

1.4 Approach

In general, two different approaches exist to gaining insight into the distribution of heterogeneities in turbidite reservoirs at the interwell scale. The analogue, or ‘product-based’, approach is to study modern turbidite fans (e.g. Amazon Fan: Lopez, 2001; Mississippi Fan: Stow et al., 1985; Monterey Fan: Fildani and Normark, 2004) and ancient fans (e.g. Skoorsteenberg Formation, Karoo Basin, South Africa: Hodgson et al., 2006; Brushy Canyon Formation, West Texas, USA: Gardner and Borer, 2000) that are now situated in accessible locations above sea level. The aim of these studies is to infer the characteristics of the depositional process (turbidity currents) and geological setting. Notwithstanding the scientific value of such studies, the results obtained are mostly specific to the fan system and extrapolation of findings to other fans or fan systems often proves to be difficult.

The ‘process-based’ approach focuses on the turbidity currents themselves. Quantification of the distribution of heterogeneities in turbidite reservoirs requires an understanding of turbidity-current hydrodynamics and sedimentation. Because of the hazardous nature of turbidity currents, and their rare occurrence, data on their behaviour under natural conditions are extremely difficult to obtain. Consequently, studies on turbidity current hydrodynamics and sedimentation rely on scaled-down physical models and process-based numerical models.

A substantial number of experimental studies has been published on turbidity currents in laterally confined (lock-exchange) as well as unconfined (expansion table) settings. These studies have provided fundamental information on current hydrodynamics such as the velocity, concentration, head dynamics, turbulence structure and, to a lesser degree, the sedimentation process (Baas et al. 2004). However, the majority of experiments use Froude-scaling to capture the hydraulics of the flow, in which the current is fully characterized by a series of dimensionless variables. As long as the values of the dimensionless variables in laboratory currents are thought to be

comparable to those of natural currents, the experiment is assumed to be adequately scaled with respect to the parameters included in that variable, allowing modelling of large-scale phenomena in the laboratory (e.g. Middleton, 1966a).

To assess if the scaled-down experimental flow is dynamically similar to the prototype, two dimensionless numbers are used: the Froude number, and the Reynolds number. The Froude number is defined as the ratio of inertial to gravitational forces, whereas the Reynolds number is defined as the ratio of inertial to viscous forces. In Froude-scale modelling, the experimental flow is scaled such that the Froude number is similar to the prototype. However, when using Froude scaling, exact similarity in Reynolds number between the scaled-down experiment and the prototype is difficult to achieve. Consequently, laboratory experiments over-emphasize viscous effects, which results in incorrect scaling of, amongst others, the sediment phase in the flow. As such, results from laboratory experiments are only roughly applicable to natural currents (Bradford and Katapodes, 1999a).

Numerical models are more generic in applicability than scaled-down physical models. Process-based numerical models of turbidity currents, although complex and cumbersome to build, do not suffer from scaling limitations, nor are they uniquely applicable to a single example. They improve our understanding of turbidity-current flow and sedimentation by taking into account the interdependence between flow and sedimentation parameters based on elementary physics. Instead of investigating the characteristics of modern and ancient turbidite reservoir analogues, this approach focuses on the characteristics of the turbidity currents themselves, and on how their hydrodynamic evolution influences the distribution of sand and clay in turbidite fans.

This study aims to formulate, analyse, implement and validate a model which is capable of simulating turbidity-current hydrodynamics and sedimentation. The model, *FanBuilder*, will be used in field-scale research of hydrodynamic parameters governing turbidity current flow, such as relief, flow density, and grain-size distribution of the suspended sediment, and their effects on depositional patterns observed in turbidite fans.

1.5 Thesis outline

This thesis focuses on the formulation, numerical implementation and validation of the *FanBuilder* model, a generic three-dimensional process-based model, capable of simulating the construction of fan stratigraphy by sequential turbidity-current events. The model, which employs best practices from various fields of expertise (e.g. Earth Science, Civil Engineering, Aeronautics), unifies conservation of mass and momentum for fluid and sediment in the form of the depth-averaged shallow-water approximation in combination with the Boussinesq (1877) approximation in three dimensions. Transport of suspended sediment is modelled by an advection-diffusion equation. Exchange of sediment with the bed is largely based on existing models for entrainment and deposition. The model is solved numerically on a rectangular grid (representing topography) by means of a second-order finite-difference approximation. Multiple grain sizes are supported. Input for the model consists of parameters defining the initial topography and time-dependent variations therein such as, for example, through tectonic activity, as well as parameters related to the

composition of the flows (grain-size distribution, concentrations, magnitude and frequency of the flows). The model is embedded in a computer application which visualizes the evolution of the flows and the resulting stratigraphy (thickness, mean grain size) instantaneously during simulation.

Prior to describing the mathematical formulation and numerical implementation of the model, Chapter 2 provides an overview on deep-water sedimentation by sediment-gravity flows and their deposits, commonly used research methods, and approaches to modelling turbidity currents, sediment transport and stratigraphy. Chapter 3 discusses the design of the model from a physical and mathematical point of view. The numerical implementation is discussed in detail in Chapter 4.

An imperative requirement for any model is its capability to simulate reality as accurately as possible. In the case of process-based models, this is commonly assessed by means of one or more validation tests in which model results are compared to data from experiments for which initial and boundary conditions are known. Validation of the *FanBuilder* model under a wide range of experimental conditions will be discussed in Chapter 5 and Chapter 6 of this thesis.

In the first part of Chapter 5, simulated modelling results from quasi-steady and waning turbidity currents are quantitatively compared to experimental data. In the second part, the sensitivity of the *FanBuilder* model to time-step length and grid-cell size are evaluated by comparing the validated modelling results to simulations in which different spatial and temporal resolutions were used. In Chapter 6, results are presented from two series of validation experiments involving complex topographic features and multiple successive flows over the same erodible bed.

Chapter 7 summarizes the conclusions of this thesis, discusses suggested improvements to the model and contains an outlook on future work.

2 A REVIEW OF PHYSICS, MODELS AND TECHNIQUES

2.1 *Introduction*

Research on deep-water processes and deposits takes place on a wide range of temporal and spatial scales. Sediment transport by flowing water and exchange with the bed may be considered a field of expertise in Earth science that overlaps with hydraulic engineering. Hydraulic engineers are mainly concerned with short-term effects of sedimentation on the morphology of e.g. rivers and coastlines on a time scale of days to decades. Earth scientists are interested in the long-term (thousands to millions of years) accumulation of sediment at e.g. the margins of continents and on how it is influenced by changes in sea level, climate and tectonic activity. As such, the combination of best practices and techniques from long-term, large-scale stratigraphic modelling with short-term, small-scale models of sediment transport by flowing water from hydraulic engineering seems promising in advancing the field of stratigraphic modelling to a higher level of detail, i.e., smaller spatial and temporal scale. This chapter reviews some best practices and techniques in the fields of hydraulic engineering and stratigraphic modelling, and gives background information on research into deep-water deposits and processes, sediment-gravity flows and the nature of their deposits, and approaches to modelling turbidity currents, sediment transport and stratigraphy. It is intended to provide a framework in which to place the research on turbidity-current hydrodynamics and sedimentation presented in this thesis.

2.2 *Historical perspective*

Prior to the 1950s, geologists were sceptical of the role of sediment-gravity flows in eroding submarine canyons and depositing graded beds in the deep sea (Shanmugam, 2000). The general belief was that the deep sea was a tranquil realm free of current activity where only mud slowly accumulated from pelagic settling (Friedman and Sanders, 1997), even though signs of deep-water current action had already been inferred from submarine telegraph-cable breaks as early as the late nineteenth century (Milne, 1897). Shallow coring of continental margin and abyssal-plain sediments at the beginning of the nineteen forties confirmed the existence of turbidity currents and related gravity-controlled deposition of sediment in the deep sea (Shanmugam, 2000), but the real turnaround came with the paper by Kuenen and Migliorini (1950) on “turbidity currents as a cause of graded bedding”. From then on, many scientists focused on deep marine sediments and their origin.

During the 1950s and 1960s, evidence for the role of gravity-driven transport of sediment from shelf edge to base-of-slope and beyond came from observations of currents in moderns submarine canyons (e.g. cable breaks caused by the Grand Banks event; Heezen and Ewing, 1952), deep sea cores, outcrop studies (e.g. Annot Sandstone outcrops in SE France by Bouma, 1962) and laboratory experiments (Kuenen, 1950; Bagnold, 1962; Middleton, 1966a, 1966b, 1967). Kuenen (1957) introduced the term *turbidite* for a deposit from a turbidity current, but the sequence of structures that would later become the Bouma sequence was already recognized as early as 1928 (Sheldon, 1928; Signorini, 1936). Bouma (1962) first described the

vertical facies model of turbidites, which has become known as the Bouma sequence, from the Annot Sandstone outcrops in SE France.

The characteristics of many deep-water deposits however did not fit the classification as “a graded deposit originating through suspension fall-out from a turbid underflow”. Hence, other mechanisms for sediment transport in deeper water, such as sliding and slumping (Doreen, 1951), debris flow (Doreen, 1951; Crowell, 1957) and high-concentration granular flow (Bagnold, 1954; Hsu, 1959) were proposed. Later on, the importance of other gravity-driven transport processes (debris flows, grain flows, liquefied flows, slumps and slides) for the origin of the Annot Sandstones was discussed by Stanley (1963). Others concluded that not all sediment transport on the continental slope and in the deep ocean was gravity-driven, and introduced the terms “contour current” and “contourite” for parallel-to-slope thermohaline bottom currents and their deposits.

Gradually, the earth-science community came to realize that a whole suite of transport processes, not all of them gravity-driven, were accountable for the transport of large amounts of sediment into the deep sea over periods long enough to be potentially influenced by changes in sea-level, climate and tectonic activity. It initiated the development of submarine-fan models based on cores and outcrop studies, first of modern passive-margin fan systems (e.g. suprafan-lobe concept by Normark, 1970) and later of ancient fan systems. Mutti and Ricchi Lucchi (1972) introduced the channel-lobe submarine-fan model, based on outcrop studies of ancient active margin systems in Italy and Spain.

The hydrocarbon reservoir potential of turbidites was first discussed by Sullwold (1961). In the 1970s, the availability of seismic added a new dimension to the development of fan models based on cores and outcrops. It initiated the development of fan models and deep-marine facies classification schemes based on seismic in the form of seismic stratigraphic models. In the late 1970s, Walker (1978) proposed a general submarine-fan model (Figure 2.1), based on studies of both modern and ancient systems, with an emphasis on stratigraphic traps for hydrocarbon exploration. It contains the classical division of a submarine fan into an upper, mid- and lower fan region, corresponding to deposits that are interpreted to range from the base-of-slope to the basin plain.

Building on Kuenen’s work, experimental work on gravity-driven sediment transport in the 1960s focused on the hydrodynamics of turbidity flow and sediment transport. Bagnold (1962) introduced the autosuspension concept, originally proposed by Knapp (1938), which implies that, depending on the ratio of particle settling velocity to the product of mean flow velocity and bed slope, sediment suspends itself in a sense that no net expenditure of energy by the flow is needed to keep the grains suspended. Using flume experiments, Middleton (1966a, 1966b) investigated the anatomy of turbidity currents, and reported on the existence of a head, body and tail. He concluded that the velocity of the head is independent of slope. Komar (1971) first discussed the origin and significance of (internal) hydraulic jumps in turbidity currents, and, in a later publication, applied a simple, one-dimensional hydrodynamic model to investigate turbidity-current behaviour with the use of a computer (Komar, 1977).

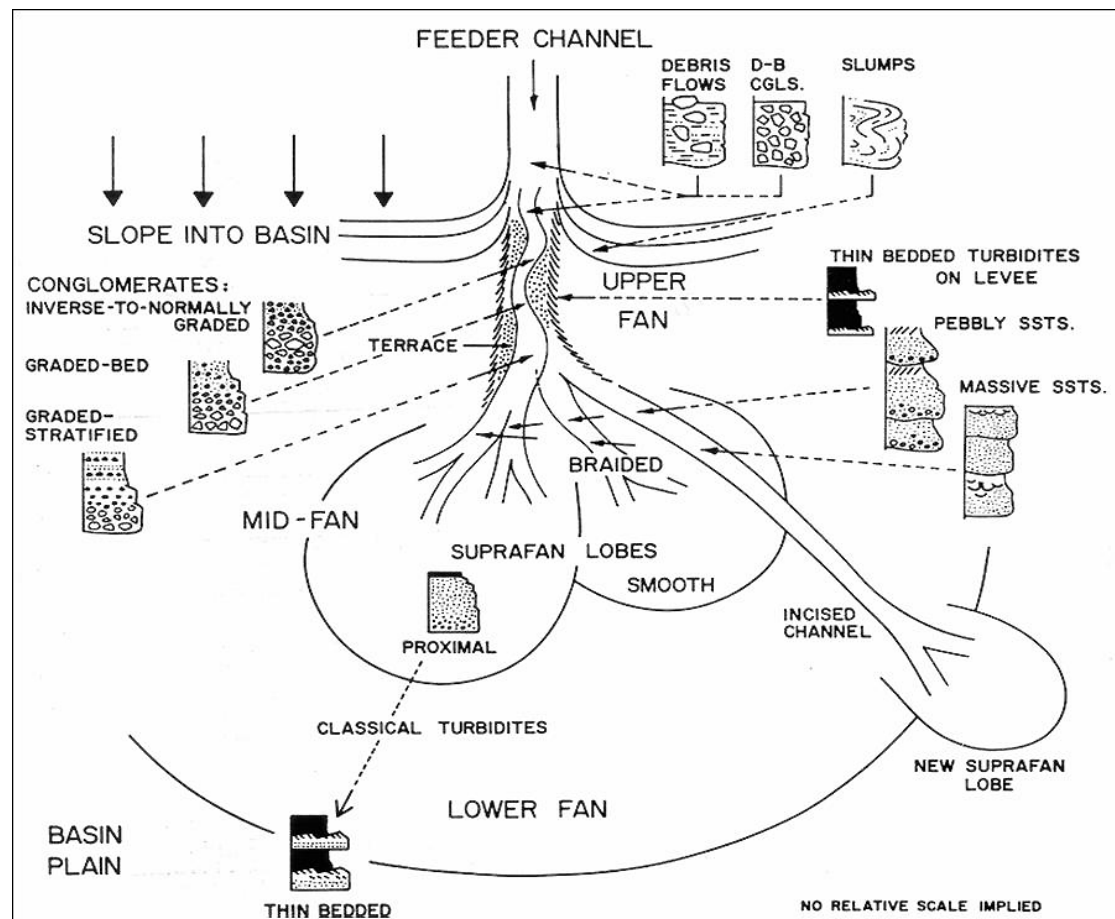


Figure 2.1: Fan model proposed by Walker (1978), based on studies of both ancient (active margin) and modern (passive margin) submarine fans.

Dott (1963) first introduced a classification based on fluid rheology, i.e., based primarily on characteristics of the process and not on the deposits. He recognized that the hydrodynamic behaviour of sediment-gravity flows is largely controlled by the volumetric concentration of transported sediment and its coherence. A related classification scheme for gravity flows, based on sediment-support mechanism, was proposed by Middleton and Hampton (1973). Hampton (1972) also was the first to conduct experiments on subaqueous debris flows. A hybrid scheme, based on fluid rheology and sediment-support mechanism was first proposed by Lowe (1979), who later proposed a theoretical model for deposits of “high-density turbidity currents” (Lowe, 1982), a term which is still subject to considerable debate.

In the 1970s and 1980s, models and classification schemes diversified. With every new study, either based on cores, outcrops, seismic or experiments, exceptions to existing models and classification schemes were found, leading to a wealth of terminology. Nonetheless, this led to new insights, and in turn to the realization that attempts to classify sedimentary systems in the deep-marine realm should be primarily based on physical characteristics of sedimentary processes for which evidence is actually preserved in the rock record (e.g. Shanmugam, 2000).

Since then, the deep-water community has been trying to bridge the gap between classifications based on process (fluid rheology, sediment-support mechanism) and product (deposit). ‘Process-based’ research focuses on the transitions between flow

types, the coupling between turbulence structure and vertical profiles of suspended sediment, and the influence of topography on hydrodynamics and sedimentation patterns. 'Product-based' research focuses on the origin of yet poorly understood observations in deposits, such as massive deep-water sands, sediment waves, sand injection, and the origin of inverse grading. On a larger scale, the origin and evolution of meandering channels by unsteady turbidity currents in deep-marine environments is an unresolved issue receiving much attention (e.g. Peakall et al., 2000).

Regardless of classification schemes and related terminology, the distinction between types of sediment-gravity flow based on rheology and sediment-support mechanism (e.g. Mulder and Alexander, 2001a) now seems to be widely accepted. Evidence for fluid rheology and sediment-support mechanism is preserved in the rock record, whereas for other criteria, such as the evolution of the velocity of flow with time (Kneller, 1995) and driving force (density), evidence is not preserved. The distinction based on rheology and sediment-support mechanism provides a framework that forms the basis to discuss the physics of sediment-gravity flows, and turbidity currents in particular.

2.3 *Sediment-gravity flows*

Sediment-gravity flows are mixtures of sediment and fluid which flow down a slope by virtue of the force of gravity. Gravity moves the sediment in the mixture, which drags the fluid along. In subaqueous sediment-gravity flows, the fluid is water. The nature of the deposits from sediment-gravity flows is largely controlled by the hydrodynamic behaviour of the flow. Four important parameters may be considered in sediment-gravity flow behaviour: sediment concentration, sediment-support mechanism, flow state and rheology. Of these four parameters, sediment concentration directly influences the other three parameters. However, flow behaviour is also influenced by the grain-size distribution of the sediment and the clay content. Consequently, threshold values for transitions between different types of sediment-gravity flow are difficult to establish (Shanmugam, 1996).

Sediment-support mechanisms include matrix-strength, dispersive grain pressure arising from grain collisions, escaping pore fluid, and fluid turbulence. As the volume of sediment and the clay-content increase, sediment-support changes gradationally from turbulence in low-density flows to matrix-support in high-density cohesive flows. More than one sediment-support mechanism may operate simultaneously in a specific type of sediment-gravity flow. Likewise, the flow state may change from laminar to turbulent and vice versa, depending on sediment concentration and bed slope.

A classification based on rheology divides sediment-gravity flows according to their behaviour under applied stress (Figure 2.2). Newtonian fluids deform instantaneously when a stress is applied, whereby the rate of strain is linearly related to the applied stress. Fluids that exhibit behaviour which deviates from this characteristic behaviour of Newtonian fluids are non-Newtonian fluids. Non-Newtonian fluids can be further subdivided into power-law fluids and plastic fluids.

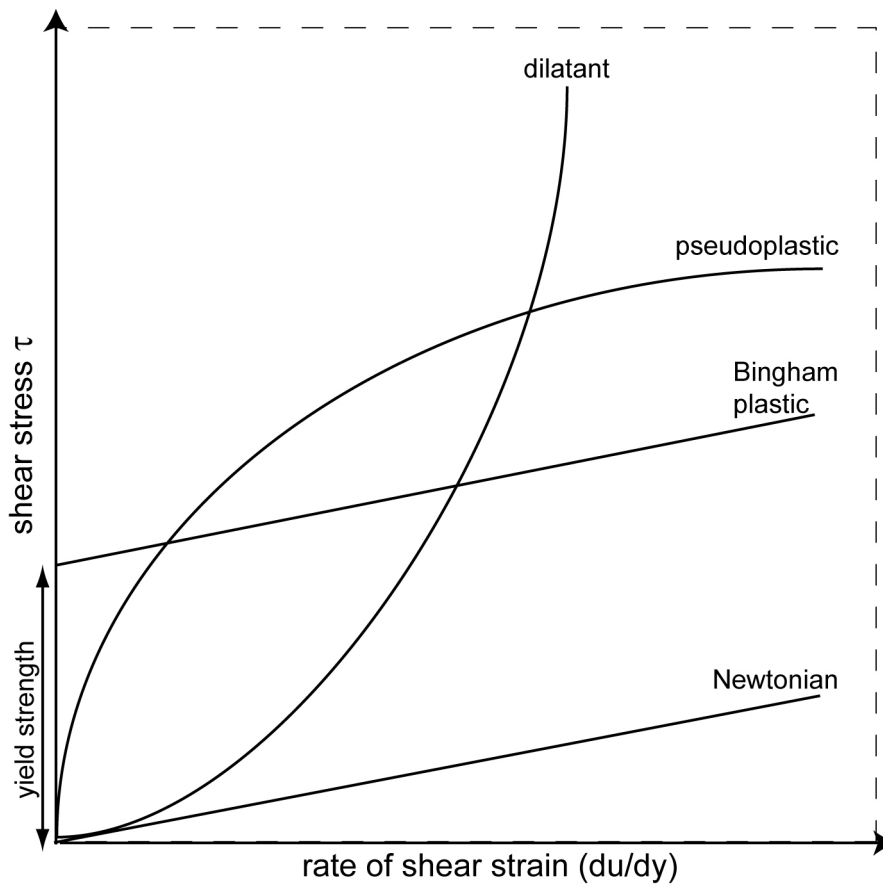


Figure 2.2: Rheology (stress-strain relationships) of Newtonian and non-Newtonian fluids.

Power-law fluids are so-called because the viscosity changes with the rate of strain according to a power-law relation. Power-law fluids may be divided into pseudo-plastic and dilatant fluids. In pseudo-plastic fluids, the viscosity decreases with the rate of strain. In contrast, in dilatant fluids, the viscosity increases with the rate of strain. Pseudo-plastic fluids are shear-thinning fluids, i.e., their strength decreases with increasing rate of deformation. Dilatant fluids are shear-thickening fluids, i.e., their strength increases with increasing rate of deformation (Larson, 1999).

Plastic fluids are different from power-law fluids in that they have a yield strength, which must be overcome for deformation to occur. Bingham-plastic fluids deform only when the applied stress is sufficient to overcome the yield strength of the material, after which the rate of deformation (strain rate) is linearly related to the applied stress. When the rate of deformation is non-linear above the yield point, the fluid is either yield-pseudo-plastic or yield-dilatant (Larson, 1999; Royhan Gani, 2004).

2.3.1 Cohesive flows

Cohesive sediment-gravity flows have a matrix strength that results from cohesion between fine-grained particles, which leads to a high kinematic viscosity and prevents entrainment of water into the flow (Shanmugam, 2000). Consequently, the flow maintains coherence. Their rheology is either Bingham-plastic or pseudo-plastic (Figure 2.2). Debris flows and mud flows are both cohesive flows. Mud flows contain mostly fine sediment, of which a large portion is mud. Debris flows are characterized by very poor sediment-size sorting, and contain a large portion of sand and gravel. They generally contain more than 5% gravel, and may transport boulder-sized clasts of soft sediment or rock and very large blocks or rafts of still coherent material (Johnson, 1970, 1984; Leigh and Hartley, 1992). Although they contain little mud (2-5%), the amount of mud in the flow is sufficient to render the flow cohesive. Debris flows probably develop as an advanced phase of slumping whereby, in the transition from slumping to debris flow the coherence of the beds is lost due to folding, low-angle thrusting, and break-up of internal bedding. Debris flows are known to be able to travel several hundreds of kilometres (Gardner and Kidd, 1983; Simm et al., 1991; Gee et al., 1999) and, although they can reach high speeds, they generally appear to be only slightly erosional (cf. Pickering et al., 1989; Gee et al., 1999).

The seemingly contradictory combination of a dense, high-speed flow with little erosive power has been attributed to hydroplaning (Mohrig et al., 1998, 1999; Marr et al., 2001; Iltstad et al., 2004). Due to the combined action of stagnation pressure at the head and dynamic underpressure above the head (Hampton, 1972), the debris-flow front is no longer capable of maintaining contact with the bed beyond a threshold velocity that is primarily determined by the flow thickness and the submerged density (Elverhøi et al., 2005). The head of the flow thus overrides the ambient water which, due to the coherent nature of the flow, cannot rise upward into the flow itself. Hence, a thin layer of ambient water develops under the flow, which reduces friction with the bed and limits erosion. The thickness of this lubricating layer beneath a hydroplaning debris flow was consistently observed to decrease with distance from the flow front in laboratory experiments (Mohrig et al., 1998, 1999). The spatial change in thickness of this lubricating layer caused a difference in propagation velocity between the part of the debris flow riding on the thin layer of water and the trailing part which was more attached to the bed, which resulted in stretching and attenuation of the flow directly behind its head. In some runs the head separated from the body (autocephalates) causing a new head to form (Parsons et al., 2007). The detached blocks (Figure 2.3) slid to the end of the channel in front of the newly formed head of the flow. These isolated blocks are commonly observed associated with the deposits of submarine debris flows (Prior et al., 1984; Lipman et al., 1988; Nissen et al., 1999) and are perhaps the best evidence for hydroplaning under natural conditions.

Deposition from a debris flow occurs when the force related to shear resistance of the flow (mainly controlled by viscosity and friction) becomes greater than the driving force due to gravity. At this point, cohesive freezing results in en-masse deposition, which explains the relatively chaotic arrangement of the deposits (Figure 2.3; Lowe, 1982; Postma, 1986). The water content in this kind of flow is low and, therefore, the thickness of the deposit is close to the thickness of the flow during motion. Ancient subaqueous debris-flow deposits are commonly found to be tens to hundreds of meters thick (Hiscott and James, 1985).

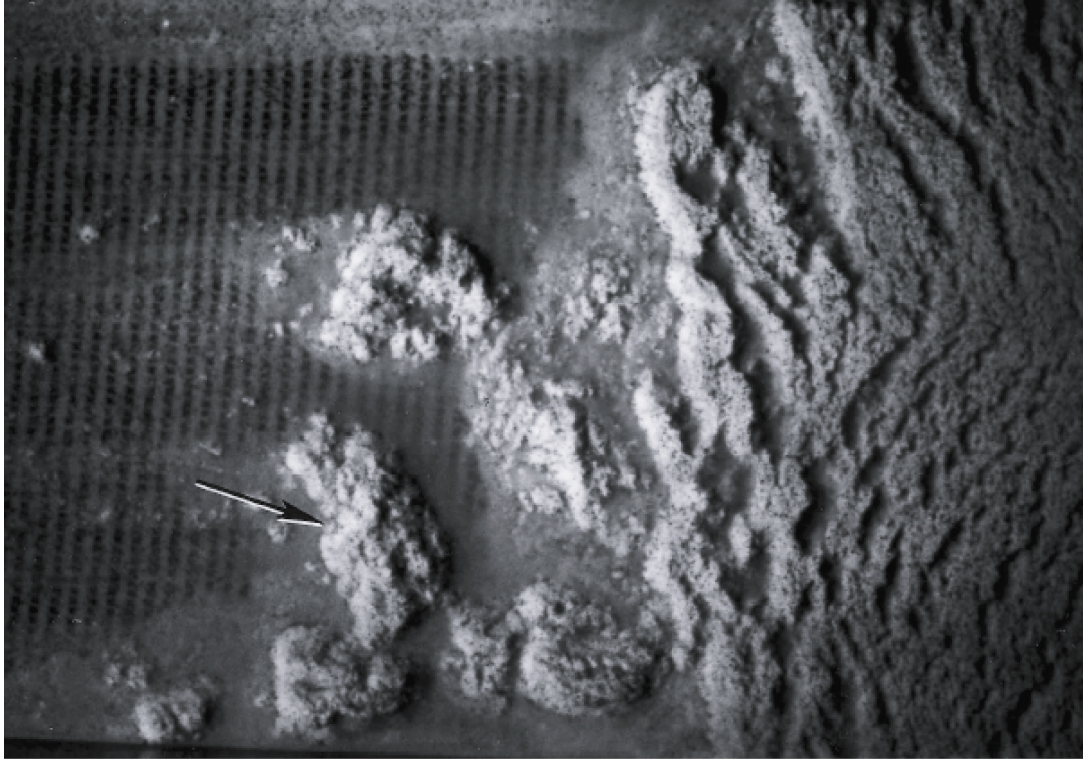


Figure 2.3: Plan view of an experimental (cohesive) sandy debris flow (after Shanmugam, 2000). Isolated blocks slowly get detached from the main body by tension and hydroplaning of sections of the flow. Flow evolves from right to left; width of the photograph is 10cm

Inclusion of water into a debris flow can lower its cohesive strength to a level where the flow is no longer cohesive but becomes frictional (Mulder and Alexander, 2001a). In frictional sediment-gravity flows, frictional forces are dominant over cohesive forces. Consequently, the grains do not stick together, and the space between them, which varies during flow, gets filled with water. The proportion of cohesive (clay) and non-cohesive (sand) particles that define the threshold between cohesive and frictional behaviour is not well known for subaqueous flow and varies according to flow conditions and concentration (cf. Fisher, 1971; Iverson, 1997). Sandy sediment can move as a cohesive flow with as little as 2% clay content by volume if the sand is fine-grained and 19% by volume if the sand is coarse-grained (Hampton, 1975).

2.3.2 Frictional flows

The subdivision of subaqueous frictional sediment-gravity flows in the literature is primarily based on sediment concentration. Mulder and Alexander (2001a) define three main classes, based on observed variations in flow behaviour at differing sediment concentrations (Hallworth and Huppert, 1998): hyperconcentrated density flows, concentrated density flows and turbidity currents. In reality, flow behaviour and deposit characteristics probably depend on concentration in a continuous manner, i.e., there is no discrete boundary between sediment-concentration ranges for these three types of flow (Figure 2.4).

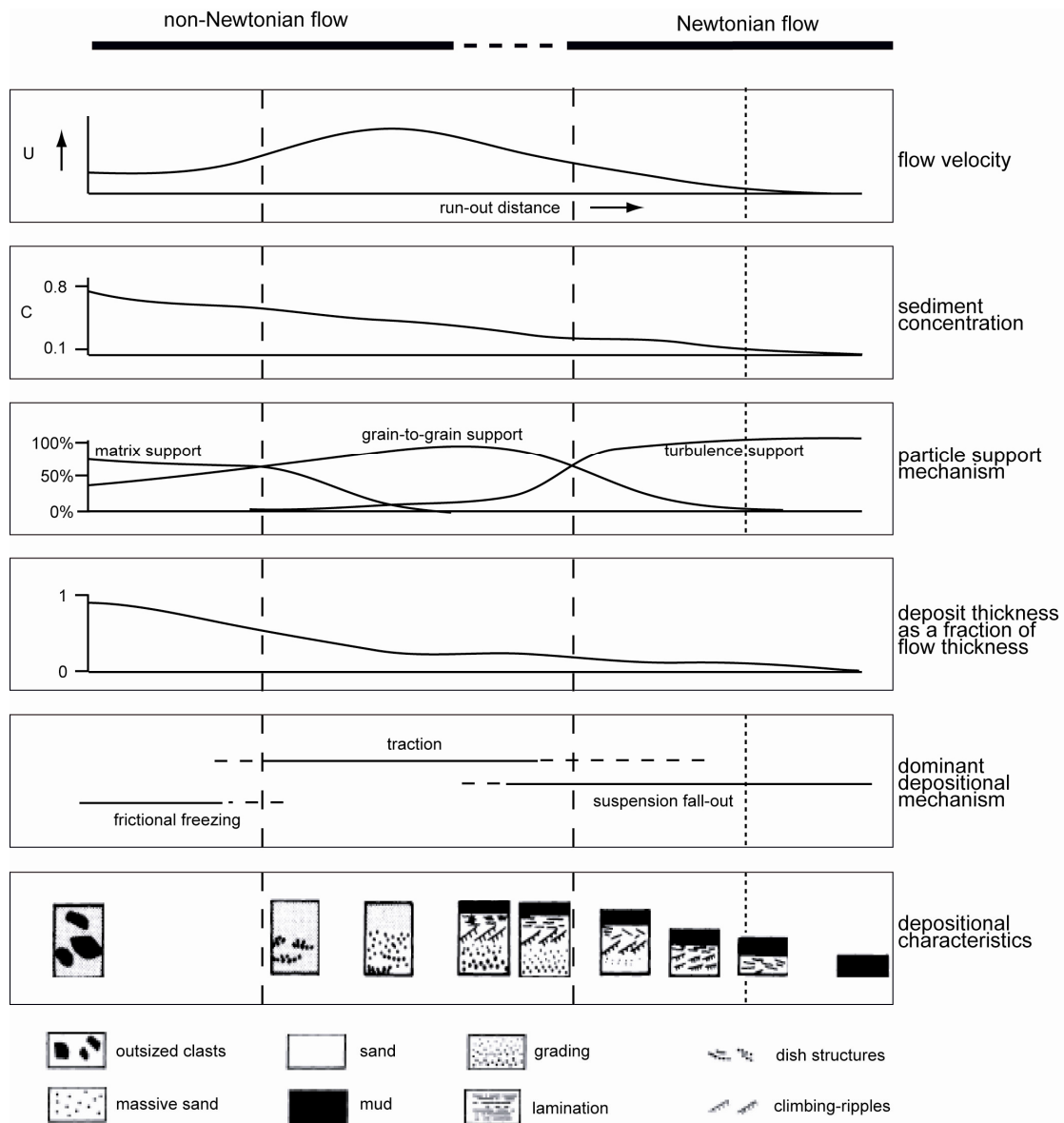


Figure 2.4: Composite diagram (modified from Mulder and Alexander, 2001a) illustrating the relationship between flow variables, flow behaviour and deposit character for frictional flows, i.e., non-cohesive sediment-laden density flows (non-cohesive sandy debris flows, grain flows).

The character of hyperconcentrated frictional sediment-gravity flows depends on the proportion of cohesive and non-cohesive particles, water content and flow velocity. Hyperconcentrated density flows may have proportions of sediment and water similar to cohesive sediment-gravity flows. They are non-Newtonian in nature but have no yield strength, i.e., they are not plastic flows (Figure 2.2). As it is difficult to imagine a natural flow completely devoid of cohesive particles, it is likely that, in hyperconcentrated density flows, the small cohesive forces instigated by the low proportion (<2% by volume) of cohesive particles are easily overcome by other forces related to e.g. grain-to-grain collisions and turbulence. Turbulence generation is relatively easy in flows with few cohesive particles (Kneller and Buckee, 2000), and transformation to a density flow with lower concentration (e.g. concentrated density flow) may be triggered by e.g. changes in topography.

Turbulence is thought to be the dominant particle-support mechanism up to concentrations of about 20% by volume, above which grain-to-grain interaction becomes the dominant particle-support mechanism. This values lies close to the concentration limit of 23% at which fluids are considered to be non-Newtonian. Mulder and Alexander (2001a) take this limit as the boundary distinction between concentrated and hyperconcentrated density flows (Figure 2.4).

A variety of particle-support mechanisms operates in concentrated density flows, the intensity of which varies in space and time. Grain-to-grain interaction causes dispersal pressure and non-elastic collisions between grains. Dispersive pressure is caused by differential movement between particles, and contributes to particle support by keeping the grains in motion. Non-elastic collisions between particles cause transfer of energy between particles, but also result in dissipation of energy due to friction, which ultimately causes the flow to decelerate (Mulder and Alexander, 2001a). Progressive entrainment of ambient water into a concentrated density flow leads to fewer grain collisions. Hence, as the flow dilutes, turbulence progressively replaces grain-to-grain interaction as the primary particle-support mechanism. Parker (1982) defined concentration and velocity optima, related to slope gradient, for which flows can move and entrain enough water to prevent freezing.

If a flow moves down a very low-angle slope, such as a prodelta slope or over a basin floor, the rate of water entrainment is low, and grain-to-grain interaction may lead to frictional freezing and deposition. If velocity is high enough, entrainment of sea water progressively decreases the sediment concentration, despite erosion, and the flow is prevented from freezing. Concentrated density flows can achieve high velocities on steep slopes by virtue of the large density contrast with the ambient water. Hence, they can be strongly erosional. Erosion and entrainment of bed sediment contributes to the driving force of the flow and causes it to accelerate and grow. High-density turbidity currents fit into the class of concentrated density flows according to Mulder and Alexander (2001a). The base of the flow may be characterized by an intense near-bed transport of coarse particles (gravel and coarse sand) forming a traction load (Figure 2.5).

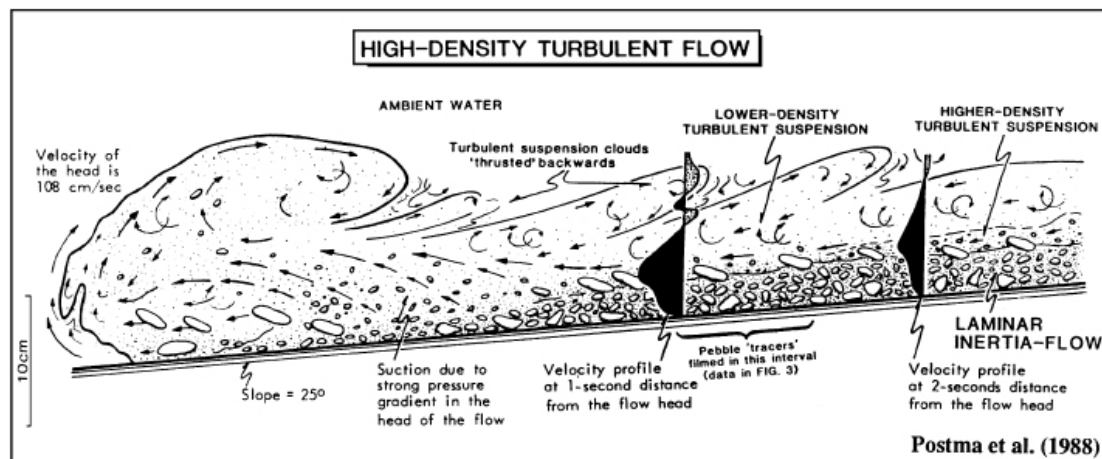


Figure 2.5: Schematic illustration of an experimental concentrated density flow (high-density turbidity flow) based on observations by Postma et al. (1988), displaying essentially a two-layer flow consisting of a high-concentration (laminar?) basal layer in which grains are supported through collision and dispersive pressure, and a low-concentration turbulent upper layer in which grains are supported through turbulence. Note also the high slope-angle of 25°.

Very close to the bed, grain-to-grain interaction may be the dominant particle-support mechanism, albeit that additional shear is supplied from the overriding concentrated density flow. In contrast, at the top of the flow, entrainment and the development of a mixing cloud leads to a region of low sediment concentration and turbulent particle support dominates. In this way, concentrated density flows may become stratified (Lowe, 1982; Postma, 1986).

The Bagnold (1962) concentration limit for turbulent suspension (9% by volume) is often used to distinguish between turbidity currents and concentrated density flows. Below this limit, turbulence is the dominant particle-support mechanism. Bagnold assumed that although grain collisions probably still occur, their frequency of occurrence is likely too low to substantially contribute to keeping the grains suspended. The Bagnold limit is subject to debate, as some believe that particle interactions (collisions, flocculation) also contribute significantly to keeping the grains suspended in flows with concentrations below the Bagnold limit. Here we consider sediment-gravity flows with sediment concentrations below 9% to be turbidity currents, in which turbulence is the dominant particle-support mechanism. Their hydrodynamics will be reviewed in more detail in Paragraph 2.4.

2.3.3 Characteristic depositional features

Changes in dominance of particle-support mechanism likely correlate with a change in characteristics of the resulting deposit. Unhindered particle settling during the passage of the flow depends on sediment concentration. Well-developed normal vertical grading (fining-upward) is typical of suspension deposits from a turbidity current. In contrast, there is little or no normal grading in hyperconcentrated density flows, except probably at the very top of the deposit where deposition occurs from the more dilute mixing cloud. The characteristics of deposits of concentrated density flows are related to the two particle-support mechanisms operating in such flows.

Processes of deposition in concentrated density flows, and the nature of the resulting deposits, are probably influenced by two simultaneously operating particle-support mechanisms: grain-to-grain interaction and turbulence. At higher concentrations, free particle sorting is hindered by the large amount of sediment in the flow. Hence, normal grading, such as in the classic Bouma sequence is not developed. However, in stratified concentrated density flows (Figure 2.5) normal grading may still develop from the upper dilute turbulent layer.

Furthermore, deposits of concentrated density flows (Figure 2.6, upper left graph) may have an erosional base, overlain by massive sands or gravel. In concentrated density flows, the thickness of this basal massive sand layer is generally much larger than in turbidity currents. Under highly concentrated basal layers (Figure 2.5), inversely-graded deposits may develop. There are several possible causes for different inverse grading styles, including moving bed conditions producing traction carpets, sediment-supply variation and the pulsing flow of turbulent sweeps. Inverse grading may also occur during the waxing phase of (quasi-steady) hyperpycnal turbidity currents.

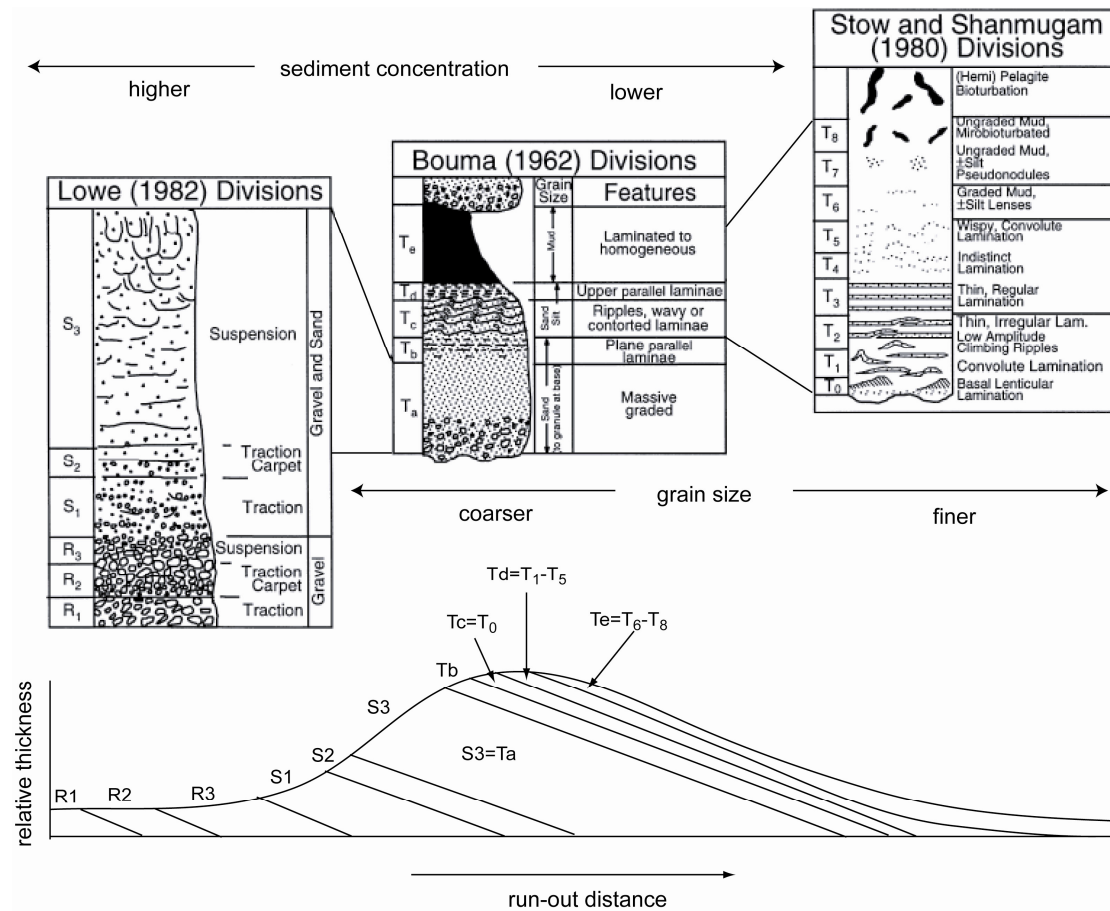


Figure 2.6: Characteristic features of deposits of density flows in which turbulence is the primary grain-support mechanism (concentration < 20% approximately). Upper three graphs illustrate typical vertical sequence of deposit from high-density turbulent flow (coarse-grained), turbidity flow and low-density turbidity flow (fine-grained). Lower graph illustrates idealistic streamwise distribution of sequence divisions expected from a hypothetical flow with an initial concentration of suspended sediment far above the Bagnold limit (9%), the composition of which ranges from coarse sand to silt. Modified from Shanmugam (2000), and based on Lowe (1982), Stow and Shanmugam (1980) and Bouma (1962).

The stability fields for sedimentary bedforms at high sedimentation rates are not well known, and the conditions for, and behaviour of, traction carpets and mobile bed layers are subject to considerable debate (Hiscott, 1994, 1995; Sohn, 1995, 1997, 1999). Bedform development is usually studied for conditions of quasi-steady flow. In flows where the basal flow layer has lower particle concentration, bedforms (ripples, dunes) can develop if flow conditions are maintained long enough to achieve hydrodynamic equilibrium (Southard, 1971; Southard and Boguchwal, 1973). Climbing ripples are known to be associated with high sedimentation rates from a quasi-steady flow, which implies that establishment of a hydrodynamic equilibrium is a requirement for the development of bedforms. In general, bedforms are thought to occur in deposits of concentrated density flows and turbidity currents, but not in hyperconcentrated flows (Mulder and Alexander, 2001a).

Erosional features (scours, flutes) are likely to develop more extensively in deposits from concentrated flows than in deposits from hyperconcentrated flows or turbidity currents. Concentrated flows are partly turbulent, more prolonged and may attain high velocities. Both the longer duration and the greater turbulence allow for more erosion.

2.4 Turbidity currents

The term turbidity current was introduced by Johnson (1938) to define a current generated due to turbid or muddy water. Etymologically, “turbidity current” means turbid flow (i.e., opaque with suspended sediment; Shanmugam, 2000), but widely accepted definitions (e.g. Middleton and Hampton, 1973) state that turbidity currents are sediment-gravity flows in which the sediment is supported mainly by the upward component of fluid turbulence. As reviewed in the previous paragraph, turbidity currents constitute the dilute (low-density) end member of a suite of subaqueous sediment-gravity flows. However, with reference to the density difference between the flow and the ambient water, sediment-gravity flows constitute the high-density end member in the classification of density flows. Density flows are classified according to the density difference between the flow (ρ_f) and the ambient water (ρ_w). This allows the definition of four types of density flow (Figure 2.7): hypopycnal flows, homopycnal flows, mesopycnal flows and hyperpycnal flows (Mulder and Alexander, 2001a).

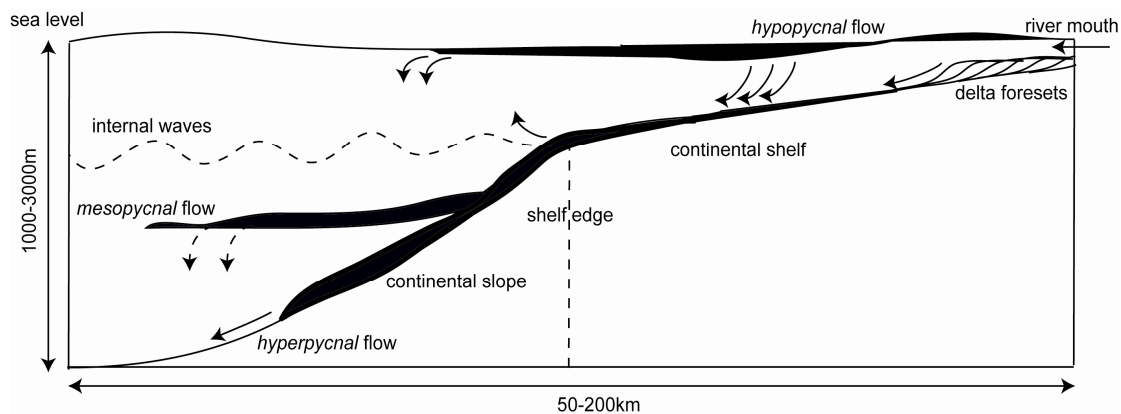


Figure 2.7: Four types of density flow and their occurrence in a continental margin setting. Arrows are used to indicate (direction of) transport, settling and resuspension of suspended material.

Flows with a density lower than that of the ambient water are termed hypopycnal flows. Hypopycnal flows (overflows) primarily occur at river mouths, where sediment is dispersed in buoyant plumes. The negative difference in density ($\rho_f < \rho_w$) between the suspension flow and the ambient water is usually caused by differences in temperature and salinity between the interstitial river water and the saline water in the basin, which, in hypopycnal flows, are more significant than the positive difference in density caused by the transport of sediment.

At some point downstream of the river mouth, a hypopycnal buoyant plume may undergo a transition whereby the density of the flow becomes higher than that of the ambient water. The transition is attributed to mixing of saline ambient water into the flow and temperature decrease of the interstitial river water. Such density flows, with a positive density difference relative to the ambient water ($\rho_f > \rho_w$), are termed hyperpycnal flows (underflows). Hyperpycnal means “above a density threshold”. In modern-day usage, the term hyperpycnal flow is used to refer to low-density sediment-gravity flows generated directly from river mouths, and not for failure-induced sediment-gravity flows generated wholly within a marine basin (Mulder and Alexander, 2001a).

Other types of density flows include homopycnal and mesopycnal flow. Homopycnal flow occurs where density flows of different or similar composition in terms of fluids, solids and solutes have equal densities ($\rho_f = \rho_w$). Homopycnal flow typically occurs in the absence of a temperature contrast between the flow and the ambient fluid, such as where a river flows into a well-mixed lake (Bates, 1953). Mesopycnal flow (intraflow or intrusive flow) occurs if the density of the intrusive flow is between the densities of two layers in a stratified water column so that the flow travels above a pycnocline (Mulder et al., 1997a). Mesopycnal flows are particularly important in strongly stratified marine basins where density differences between water layers are large (Rimoldi et al., 1996). Essentially, hypopycnal and hyperpycnal flows constitute the end members in this classification scheme. Although homopycnal and mesopycnal flows could be regarded as intermediate forms of density flows, they occur only under fairly specific conditions in nature.

2.4.1 Initiation mechanisms

Mechanisms of initiation of turbidity currents are closely related to the position of turbidity currents in the continuum of sediment-transporting density flows. On the one hand, turbidity currents constitute the dilute end member of failure-induced sediment-gravity flows. As such, they may evolve due to progressive dilution of a failure-induced denser flow (e.g. Kelts and Hsu, 1980; Siegenthaler et al., 1987). Initiation of failure-induced sediment-gravity flows is commonly attributed to slope instability, i.e., remobilization of unconsolidated sediment deposited at the shelf break or in the canyon head. Instability may be induced by earthquakes, volcanic activity or intense internal-wave action at or near the shelf break during e.g. storms. Turbidity currents may also arise directly from suspension clouds generated by storm activity on a shelf (Prior et al., 1989).

On the other hand, turbidity currents form at river mouths during periods of high discharge, when a buoyant plume of river water with suspended sediment undergoes a hypopycnal to hyperpycnal transformation whereby the density effectively increases. When the bulk density of the river discharge (mixture of sediment and water) becomes greater than that of the ambient water in the basin, the flow continues from the river onto the floor of the basin in the form of a sediment-gravity flow (Lambert and Giovanoli, 1988). Many turbidite systems, especially modern fan systems, display obvious connections with rivers (Kneller and Buckee, 2000). The growth of turbidite systems occurs when fluvial systems can discharge directly to the shelf break, a direct link generally associated with sea-level lowstands (Mutti, 1985; Shanmugam et al., 1985b; Mutti and Normark, 1991; Posamentier et al., 1991; Normark et al., 1993), but it may also occur during highstands if rates of delta progradation are sufficiently high to reach the shelf break (Burgess and Hovius, 1998).

Rivers that generate hyperpycnal flows are generally characterized by high hinterland relief and exceptionally high suspended loads (e.g. the Var, which drains the south-western French Alps; Mulder et al., 1997b). The potential for hyperpycnal flow is enhanced where the available sediment is fine-grained, such as the loess carried by the Yellow River. Mulder and Syvitski (1995) calculated the likely interval between hyperpycnal flow events for a selection of the world's largest river systems, and conclude that almost half of them could generate hyperpycnal flows with a return

period of 100 years or less. However, it is likely that the rivers supplying large fans (e.g. the Amazon) can never generate hyperpycnal flows under the current (Holocene) hydrological regime. Indeed, most of these fans have been inactive throughout the Holocene (Mulder et al., 2003). Damuth et al. (1988) suggested that sinuous channels on the Amazon Fan, which developed during late Pleistocene lowstands, may have been formed by continuous underflows.

Some turbidity currents are caused by multiple retrogressive foreset failures of sandbars at river mouths when, during flood run-off, sediment concentration at the river mouth is too low to produce a hyperpycnal turbidity current directly. Slope oversteepening of rapidly deposited, underconsolidated sediment produces frequent, retrogressive foreset failures during and just after flood events, which creates small-scale, short-duration turbidity currents. According to Mastbergen and van den Berg (2003), retrogressive failure in fine, non-cohesive sands may occur so gradually as to generate more sustained (quasi-steady) turbidity currents potentially capable of producing massive sandy deposits.

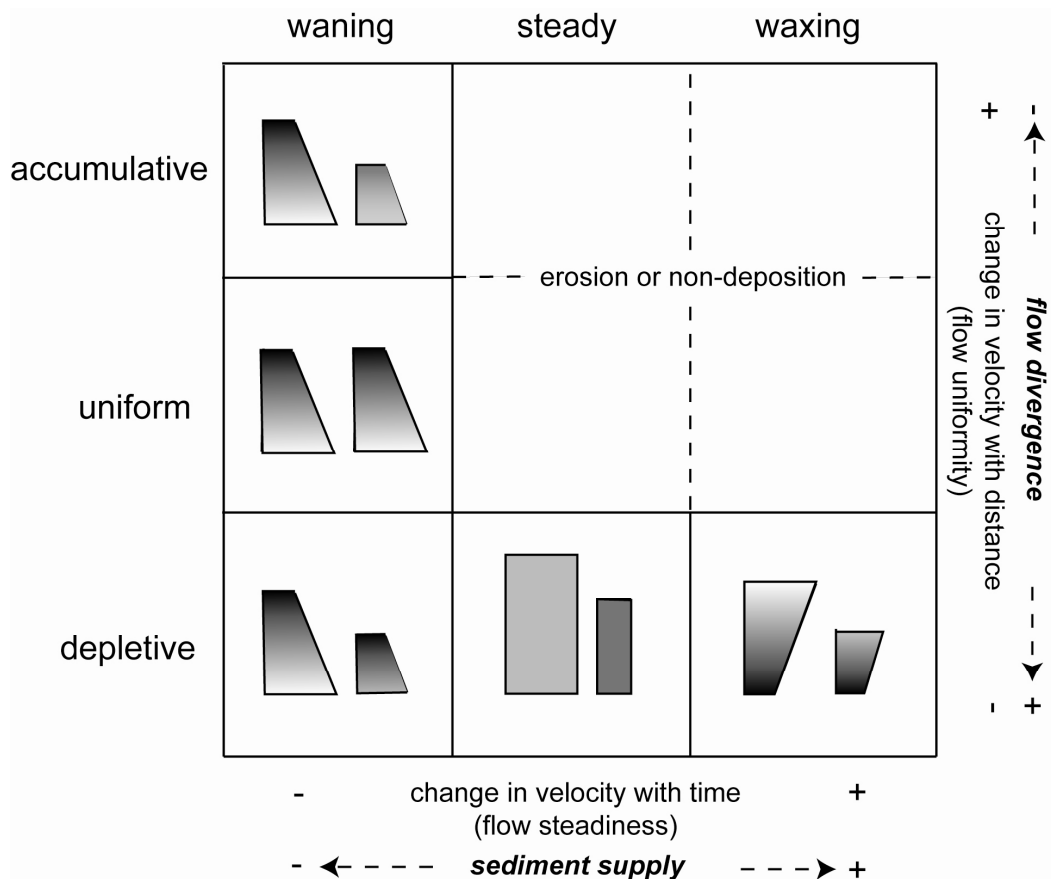


Figure 2.8: The acceleration matrix from Kneller (1995) and Kneller and Branney (1995), illustrating the effect of changes in velocity with distance and with time on the grain-size trend in the deposit. Surges are mostly depletive waning flows; turbidity currents may also be waxing and erosive. Quasi-steady hyperpycnal flows, i.e., turbidity currents generated at river mouths, are depletive flows, but, depending on the shape of the flood hydrograph, may wax and wane (Mulder et al., 2003)

2.4.2 Magnitude and duration

Steady turbulent flow occurs when the mean velocity at a point remains unchanged over a specified time period. In reality, all natural sediment-gravity flows are unsteady but, in some situations, the mean velocity may be nearly constant for a period of hours to days (Shepard et al., 1979). Consequently, turbidity flows can be subdivided into turbid surges and quasi-steady turbidity currents (Mulder and Alexander, 2001a). The main difference between these types of turbidity flow is the duration of the waxing phase, i.e., the phase in which the velocity increases at a point (Figure 2.8). Hence, the distinction between these two types of turbidity flow is based on the duration of the event and the sediment supply.

2.4.2.1 *Turbid surges*

Surges are phenomena of relatively short duration with no permanent sediment supply. The flow is strongly non-uniform, i.e., velocity varies with distance, and the development of a flow body is negligible (Middleton, 1966a). Surges have a distinct flow head, which may be followed by a highly unsteady and non-uniform body. Surges are mainly depositional, and do not usually transport particles with grain sizes larger than sand. Particles are maintained in suspension through the upward component of turbulence and settle gently, with some movement along the bed, producing sedimentary structures and bed forms of typical Bouma T_b - T_d . If particles are sand grade, the flow may reconcentrate to form a concentrated sheet flow spreading along the base as a lobe. Erosion can be produced at the base of turbid surges when the flow is reaccelerated due to e.g. an increase in slope or flow constriction (Mulder and Alexander, 2001a). Individual flows will not produce thick deposits unless the magnitude of the flow is very large or flow is ponded, and, even then, the bed thickness is relatively small compared to the flow size. Most surges are probably initiated through slope instability.

The duration at a point in a surge depends on the scale of the event. Small surges (flow thickness of centimetres to meters) have a duration of seconds to minutes. Bedforms and related sedimentary structures tend to be rare in deposits from small surges, as bedforms take time to develop and the duration of bedform-generating conditions might be too short for recognizable features to form. In contrast, large-scale oceanic surges (scale of tens to hundreds of meters) may last for hours. The Grand Banks event is estimated to have had a duration of over nine hours (Hughes-Clarke et al., 1990). In large-scale surges, a long body may develop, in which flow is non-uniform and unsteady. The head and part of the body are usually waxing and may be erosive, whereas the rest of the body and the tail are waning. These large-scale surges tend to deposit well-developed Bouma T_b - T_d facies.

2.4.2.2 *Quasi-steady turbidity currents*

A current differs from a surge in that it represents a steady motion of a particular body in which no boundary (head or tail) is observed (Mulder and Alexander, 2001a). In a quasi-steady current, the duration of the passage of the head (or flow front) is very short compared to the passage of the body, implying that the head is relatively

insignificant in controlling the nature of the deposits (Kneller and Buckee, 2000). Hyperpycnal turbidity currents are termed quasi-steady, because the flow is fed by prolonged river discharge with a duration of hours to months (Mulder and Syvitski, 1995, 1996), implying that the deposit mostly represents body conditions.

Quasi-steady hyperpycnal turbidity currents frequently develop in lakes where very little suspended sediment is needed to produce excess flow density. Thirty-six to forty-four kilograms per cubic meters of suspended sediment is required to produce a hyperpycnal plume (Mulder and Syvitski, 1995, 1996) when rivers discharge into marine basins, depending on the temperature and salinity at the river mouth. In contrast, turbidity currents generated wholly within the marine environment have saline interstitial water. Hence, sediment concentrations as low as 1-2 kg/m³ may be sufficient to maintain a current on a slope (Mulder et al., 2003). Hyperpycnal turbidity currents have sediment concentrations lower than concentrated density flows and, generally, also lower than many turbid surges that evolve from failure-induced concentrated density flows (Mulder et al., 1998). As a consequence, and assuming the same ambient fluid, hyperpycnal turbidity currents generally have lower velocities than other flow types. A quasi-steady turbidity current can persist for several days or weeks, depending on the flood duration at the river mouth (Skene et al., 1997; Mulder et al., 1998). To an observer at a particular point, the phenomenon appears to be steady for a prolonged period, particularly if the discharge varies gradually. The flow may be uniform or non-uniform over a long distance, depending on the slope and initial momentum. Furthermore, steady and quasi-steady currents may have an element of inherent instability owing to internal waves and eddies (e.g. Düringer et al., 1991).

Quasi-steady turbidity currents have attracted increased attention in the past decade (e.g. Mulder and Syvitski, 1995; Skene et al., 1997; Mulder et al., 2001a; Mutti et al., 2003; Mulder et al., 2003) because it has been recognized that they are potentially capable of producing deposits previously attributed to failure-induced sediment-gravity flows. Variations in discharge and sediment-flux patterns between floods and rivers, together with the variation in conditions with distance from a river mouth result in sedimentary sequences which tend to be more varied than those of other sediment-gravity flow types (Figure 2.8). During the rise of a flood, the rate of velocity increase at a river mouth depends on the origin of the flood (storm, monsoon and prolonged rainfalls), rainfall pattern and catchment behaviour. If the near-shore slope is relatively steep, or if the flow is channelled (lateral flow restriction), the flow is accumulative (Figure 2.8; Kneller, 1995) and reworks its own deposits. In the case of a flash flood, insignificant deposition occurs in areas where the flow is waxing because the initial velocity increases quickly and deposits are immediately reworked. Once past the break-of-slope where the flow is no longer channelled, the flow becomes depletive and almost steady because the increase in initial velocity at the river mouth is attenuated. At these sites, sediments can be deposited and preserved, and a coarsening-up profile is expected during the waxing phase (Figure 2.8; Kneller, 1995). Such a sequence has been described from the Saguenay fjord in Canada (Syvitski and Shafer, 1996). As the flow continues to wax, deposition progrades, and the zone of erosion moves seaward so that areas that were initially depositional may become erosional. As the flood wanes, the site of maximum deposition moves landward. If slopes are steep or the flow is channelled near the river mouth, the flow becomes accumulative and waning. More distally, the flow becomes depletive and

waning. The resulting flow deposits are morphologically identical to those deposited by surges but may be thicker as the waning period may be more prolonged. Depending on the duration of the flood, large amounts of sediment may be deposited. The Saguenay Fjord hyperpycnal turbidite (Syvitski and Shafer, 1996) reaches a maximum thickness of 10-12 m some 37 km from the river mouth.

The depositional signature of quasi-steady turbidity currents ranges from inversely-graded units overlain by a normally-graded sequence to various sequences in which the inversely-graded unit is partly or totally eroded before deposition of a normally-graded unit (Figure 2.8). At locations where the flow is both steady and depletive, thick deposits can form with uniform grain size. Climbing ripples may develop when flow velocities are low, i.e., ranging from a few centimetres to about a meter per second depending on Froude number. Climbing ripples may be a major sedimentary feature of hyperpycnal turbidites, as they represent the steady migration of sedimentary bedforms while sediment supply is maintained (Mulder and Alexander, 2001a).

2.4.3 Anatomy

Turbidity currents are described as having a well-defined head, body and, in some cases, tail. The dynamics of the head are important because they set a boundary condition for the current as a whole (Britter and Simpson, 1978). Both Allen (1971) and Middleton (1993) suggest that the head is a locus for erosion, and therefore sedimentologically important. The head has an overhanging nose as a result of the no-slip condition at the lower boundary and frictional resistance at the upper boundary (Figure 2.9). The no-slip condition requires that the velocity must decrease to zero at the boundary between the fluid and the (stationary) solid. At the rear of the head, a series of transverse vortices are present, identified as Kelvin-Helmholtz instabilities (Britter and Simpson, 1978).

2.4.3.1 *Head*

Middleton (1966b) performed the first comprehensive set of experiments on the heads of brine currents and turbidity currents in the laboratory. He investigated the effects of slope on the velocity and shape of the head, finding that for low slopes ($<2-3^\circ$) the head velocity is adequately described by Keulegan's formula (1957) in which the head velocity is independent of the slope. Further experiments suggest that the dimensionless head velocity is only weakly dependent on slope (for slopes of $5-90^\circ$) because, with increasing slope, higher gravitational forces are counteracted by increased frictional resistance at the upper boundary owing to increased rates of ambient water entrainment (Britter and Linden, 1980). The downstream velocity in the body of the current, which does depend on the slope, has been shown to be up to 30-40% faster than the head velocity (Middleton, 1966b; Kneller et al., 1997, 1999). Consequently, the head height increases with slope, as the body velocity increases and material moves more rapidly from the body into the head (Hopfinger and Tochon-Danguy, 1977; Britter and Linden, 1980; Simpson, 1997).

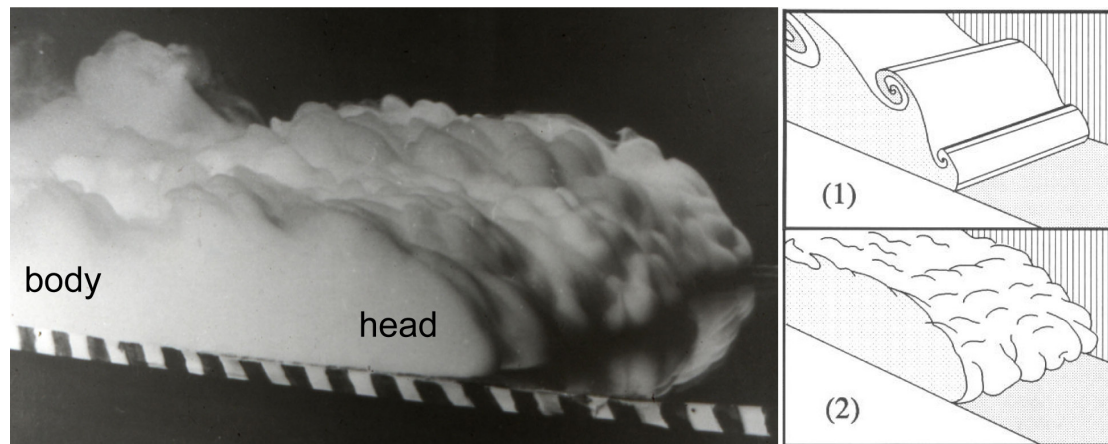


Figure 2.9: Anatomy of an experimental gravity current (Simpson, 1997). K-H billows (1), associated with entrainment of ambient water at the upper interface are best visible in a direction perpendicular to the streamwise direction. Lobes and clefts (2), associated with entrainment of ambient water at the base of the current, are clearly visible at the front.

The primary forces controlling the unidirectional motion of a head in a two-dimensional, sidewall-confined setting (Figure 2.9) are pressure, gravity and friction. The pressure balance of sections in front of the head and in the head yields a net driving force because the pressure force in the head is higher due to the higher density of the gravity current. For gravity currents on an inclined plane an additional driving force is exerted by the component of the gravity force along the bed. This force tends to dominate the motion of the current on large slopes. On steep slopes, the gravity force component is reduced due to entrainment processes in the head. Britter and Linden (1980) assumed that for slopes $> 0.34^\circ$, the buoyancy force downslope counteracts the friction force to produce a steady flow with constant head velocity. For slopes $> 5^\circ$ the influence of bottom drag is less noticeable, but flow velocity remains constant because the buoyancy force is now counteracted by friction at the upper boundary of the flow (increased entrainment). Internal-wave speeds in the body of the gravity current are most often larger than the velocity of the head, and therefore different parts (internal waves) of the current catch up with the front and overtake it to feed the head, which becomes thicker over time.

Bottom drag and interfacial friction become important if propagation processes over longer distances are considered (Figure 2.10). Both interfacial friction and bottom drag increase the level of turbulence in the head region. In a fully turbulent gravity current, entrainment of ambient fluid and associated kinetic energy loss is caused by two major forms of instability. Firstly, at the interface with the overlying ambient fluid, friction causes Kelvin-Helmholtz billows and subsequent entrainment of ambient fluid. Secondly, buoyancy-induced instabilities occur where the head overrides the ambient fluid, which then rises to be entrained in the head. These buoyancy-induced instabilities are responsible for the non-steady lobe and cleft structure (Figure 2.9-2). Interfacial mixing due to K-H instabilities increases when the bottom slope increases, but the front speed remains constant for increasing slope because the larger gravitational force is counterbalanced by the increased entrainment in the head and the flow behind it (e.g. Siegenthaler and Buhler, 1985). Interfacial mixing causes momentum to be imparted to less-dense fluid entrained into the head (Britter and Simpson, 1980), and causes, together with dense inflow from behind, a growth of the head volume and height.

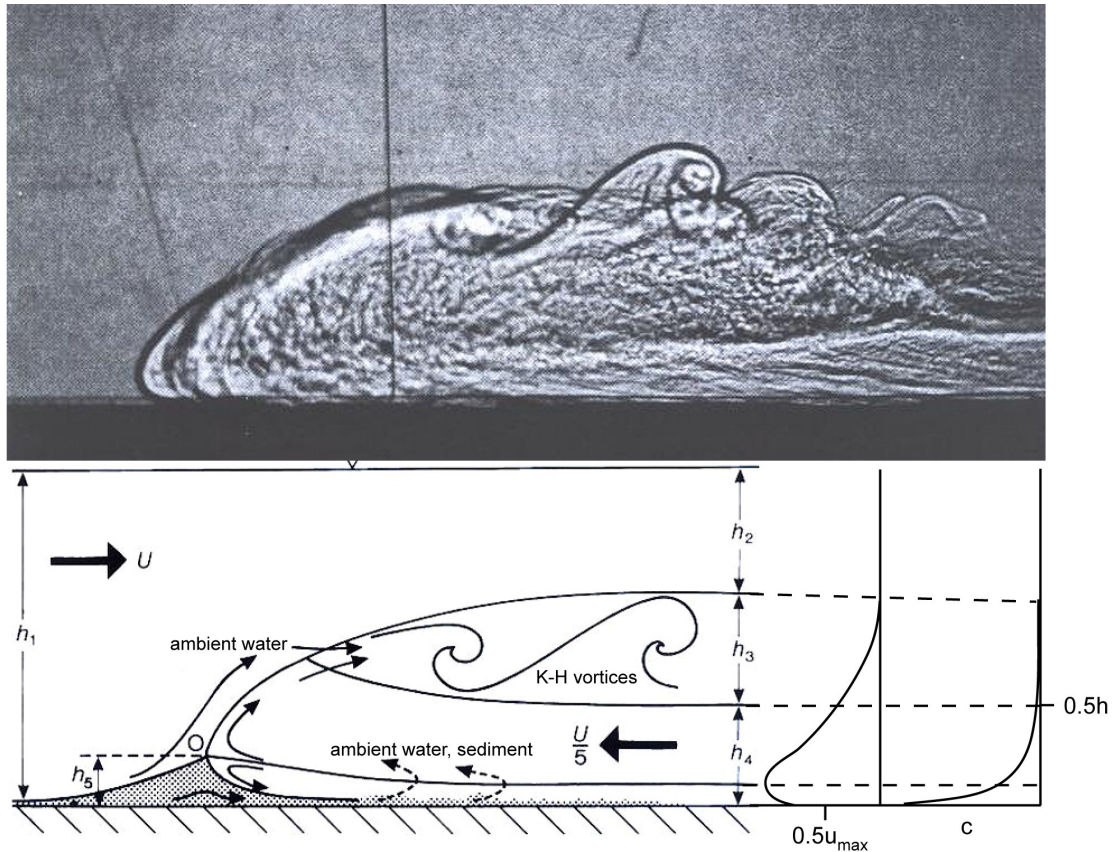


Figure 2.10: Anatomy of a gravity current head. Upper graph: photograph of an experimental saline gravity current (from Simpson, 1997). Lower graph: schematic illustration of the head section of a gravity current (modified from Simpson, 1997), illustrating entrainment of water and sediment, as well as typical vertical profiles of velocity and sediment concentration for a weakly depositional flow (e.g. Altikinar et al., 1996)

The turbulence structure in gravity current heads is dominated by shearing at the upper interface. Data on the turbulence structure in the head of a gravity current have been presented by Kneller et al. (1997, 1999) and Parsons (1998). Time series of instantaneous downstream velocity clearly record the arrival of the head and the passage of large, low-frequency Kelvin-Helmholtz billows superimposed on a period of quasi-steady motion. Instantaneous velocities associated with large eddies, were found to exceed the maximum mean downstream velocity by up to 50%. Garcia and Parsons (1996) and Parsons (1998) demonstrated experimentally that dimensionless mixing rates decrease with decreasing Reynolds number. In currents with high Reynolds number, entrainment is primarily due to secondary instabilities (K-H vortex breakdown) in the upper part of the current, whereas in currents with low Reynolds number, in which not all the turbulent sub-ranges are present, entrainment due to secondary instabilities is less significant because viscous effects become more important. Therefore, care must be taken in laboratory experiments to ensure that the Reynolds number is sufficiently high to minimize such viscous effects because they compromise the scaling. Entrainment of ambient water into the head is a function of the densimetric Froude number (e.g. Ellison and Turner, 1959) and therefore the initial reduced gravity.

2.4.3.2 *Body and tail*

Few physical descriptions of the body and tail exist in the literature. Ellison and Turner (1959) describe the body as a region of steady downstream velocity which has a thin, dense layer of fluid near the base of the current which, with increasing downstream velocity, mixes with the ambient fluid at the upper boundary as an irregular succession of large eddies. In general, the body of gravity currents may be subdivided into two distinct regions: a lower, dense layer, and a region of less dense fluid that has been mixed out of the head of the current (Britter and Simpson, 1978; Simpson and Britter, 1979). Time series of downstream velocity in the body of quasi-steady gravity currents reveal the presence of large coherent structures, associated with internal-wave action, that advect with the current (Kneller et al., 1997; Best et al., 2001). Instantaneous velocities in the body may be up to 40% higher than the time-averaged downstream velocity in the body (Buckee et al., 2001) and therefore equivalent to, or higher than, instantaneous velocities in the head. This suggests that the body of the current may play a significant role in sediment entrainment.

2.4.3.3 *Stratification*

Gravity currents are described as having an inner and outer region divided by the velocity maximum. The inner region, which is bounded at the lower end by the solid-fluid interface, has a positive velocity gradient. The outer region has a negative velocity gradient and is bounded at the upper end by the interface with the ambient fluid. The inner region is generally less than half the thickness of the outer region. The height of the velocity maximum is controlled by the ratio of the drag forces at the upper and lower boundaries. Gravity currents are density stratified, i.e., they possess a vertical concentration gradient, with a dense, poorly mixed heterogeneous basal layer and a less dense, mixed homogeneous region above.

Two main types of sediment concentration profiles have been observed in turbidity currents. A smooth profile is commonly seen in low-concentration, weakly depositional currents (Altikinar et al., 1996; Garcia, 1990, 1994) and in saline gravity currents (Ellison and Turner, 1959). The second class of density distribution has a stepped concentration profile and is commonly observed in erosional currents (Garcia, 1993) or currents interpreted to have a high entrainment rate at the upper boundary (Peakall et al., 2000). Experiments in which vertical grain-size distributions have been measured (Garcia, 1994) show that fine-grained material is more uniformly distributed in the vertical direction than the coarse material, which tends to become concentrated in the lower part of the current. Theoretical and experimental studies of turbidity currents (Stacey and Bowen, 1988a,b; Garcia and Parker, 1993; Garcia, 1994; Altikinar et al., 1996), and limited field data (e.g. Chikita, 1989; Normark, 1989; Zeng and Lowe, 1997) suggest that they have patterns of vertical sediment distribution rather similar to those of shear flows, in which the vertical sediment concentration profile obeys a power-law distribution (given by Rouse, 1937) with an exponent that is directly proportional to the ratio of the current shear velocity to the grain settling velocity (Middleton and Southard, 1984), whereby relatively low values of this ratio u^*/w_s predict high near-bed concentrations of suspended sediment, decaying rapidly upwards. This has two important consequences: firstly, any multiple-grain-size current must be stratified in terms of both density and grain size,

particularly if it is depositional or close to being so, and secondly, the grain-size range near the base of the current is broader than higher up in the current.

From laboratory and field measurements it is possible to define a standard velocity and concentration profile for equilibrium turbidity currents. Sloff (1997) concluded that the location of the velocity maximum for internally supercritical currents differs from that of internally subcritical currents, based on data of turbidity currents generated in a laboratory flume (Garcia, 1990, 1993; Garcia et al., 1986; Garcia and Parker, 1993; Parker et al., 1987), and supplemented with data from turbidity currents in the field (Chikita, 1989; Fan, 1986, 1991) and saline currents (Ellison and Turner, 1959; Garcia, 1990). For internally supercritical currents, i.e., those with a Froude number above unity, the velocity maximum is located at about 15% of the underflow depth (see Figure 2.11, left graph). For internally subcritical currents, i.e., those with a Froude number below unity, the velocity maximum is located at about 40% of the underflow depth (see Figure 2.11, right graph). Principally, concentration profiles of suspended sediment for equilibrium subcritical and supercritical currents are deducible from the fluid diffusion (or turbulence) profile which, in turn, is coupled to the velocity profile. Turbulence damping effects by density gradients must be taken into account by means of the gradient Richardson number Ri_g , defined as:

$$Ri_g = -\frac{g}{\rho_w} \frac{\partial \rho_f / \partial z}{(\partial u / \partial z)^2 + (\partial v / \partial z)^2} \quad (2.1)$$

where g is gravity, ρ_w is the density of the ambient fluid, ρ_f is the density of the flow, and u and v are the lateral components of the local velocity vector. The gradient Richardson number (Ri_g) is calculated with respect to local density gradients and highlights regions that are less stably stratified than the whole (Kneller and Buckee, 2000). As such, it is a well-known measure for the stabilizing effect of stratification on turbulence in a shear flow. The stability threshold for which flow is unstable (turbulent) is usually taken as $Ri_g < 0.25$ (Miles, 1990), but in practical situations, for instance due to boundary mixing, the flow is turbulent for $Ri_g < 0.4$ to 0.6 (Garcia, 1993). Larger density gradients or smaller velocity gradients make the flow more stable.

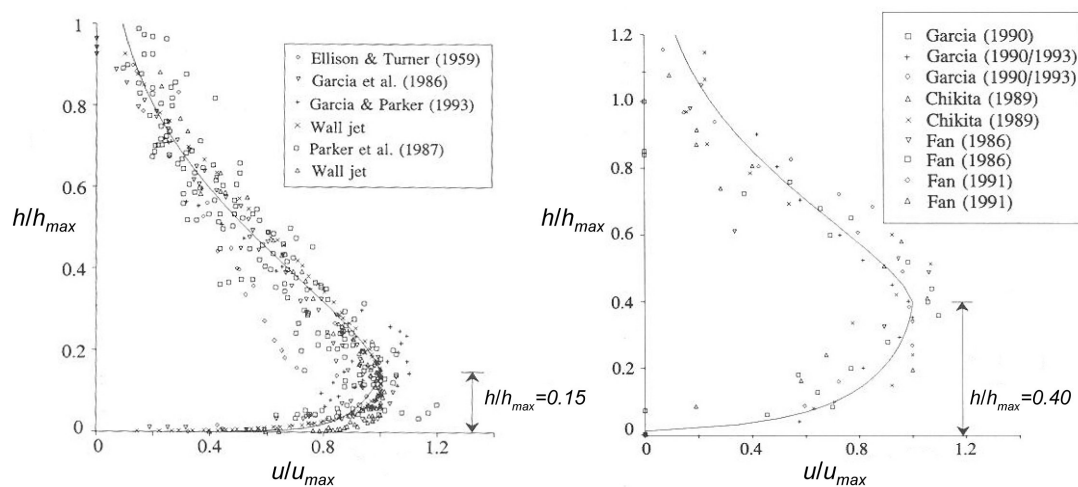


Figure 2.11: Vertical velocity data of experimental supercritical (left graph) and subcritical (right graph) density currents, and fitted velocity profiles (reproduced from Sloff, 1997).

2.5 *Research methods*

Since Kuenen (1937) and Kuenen and Migliorini (1950) first demonstrated experimentally that turbidity currents were the most probable agents of transport of clastic sediment into the deep oceans, research has followed three main lines: the study of ancient and modern turbidite systems, experimental modelling and numerical modelling.

2.5.1 Study of modern and ancient turbidite systems

Outcrop studies can provide sedimentological data at various scales. On a larger scale, vertical sequences, lateral changes in sedimentological characteristics and architectural aspects of sediment bodies can be studied. At the scale of individual beds, information can be acquired on e.g. grain-size distribution, sedimentary structures, and the nature of bed boundaries. Recently, advances in 3D-visualization techniques and the Global Positioning System have aided scientists in making the step from two-dimensional to three-dimensional datasets in areas where exposure allows this (e.g. Skoorsteenberg Formation, Karoo Basin, South Africa: Hodgson et al., 2006; Brushy Canyon Formation, West Texas, USA: Gardner and Borer, 2000).

Outcrop studies are primarily limited in usefulness owing to the degree of exposure. The presence of vegetation commonly biases observations towards the more sandy units, whereas deposits that contain mainly silt and clay also may contain valuable information. Weathering may obscure grain-size trends and sedimentary structures, but may also accentuate features that would otherwise have remained undetected. The main limitations however lie in the fact that outcrops are two-dimensional and of limited extent. As such, only features smaller than the dimensions of the outcrop can be interpreted with certainty. Outcrops provide two-dimensional sections through three-dimensional geological features. Only when the spacing between individual exposures is smaller than the dimensions of the architectural elements of a depositional system, and the total outcrop area is larger than those elements, can a three-dimensional picture of the elements be obtained (Visser, 2005).

Slabbed core is highly suitable for detailed investigation of sedimentological features in a continuous vertical sequence (e.g. Lowe and Guy, 2000; Haughton et al., 2003; Shanmugam et al., 1994). The slabbed core is visually easy to study, and, due to the fresh cut, weathering does not pose a problem. Cores are commonly used for reservoir characterization and serve to validate information from other sources. The limitation of core studies lies in the one-dimensional nature of the material. It is difficult to infer three-dimensional information from core. Limitations of outcrop and core studies, together with the extreme complexity of most turbidite systems, and individual turbidite beds, has precluded the development of quantitative models of turbidity-current behaviour inferred solely from their deposits (Visser, 2005).

2.5.2 Experimental modelling

Middleton (1966a) stated that “a better understanding of turbidity-current dynamics is required to account for the many diverse phenomena reported from modern environments and ancient turbidite systems”. Study of the mechanics of turbidity currents has been limited by the difficulties of studying them in nature. Turbidity currents may reach velocities of tens of meters per second (e.g. Mulder et al., 1997a) and heights of hundreds of meters (Heezen and Ewing, 1952). Even rather modest currents have damaged or destroyed equipment deployed for the purpose of studying them (e.g. Shepard et al., 1979; Zeng et al., 1991). Consequently, most of what is known about large natural turbidity currents, i.e., those significant in terms of sediment transport into the deep sea, has been inferred from indirect sources, such as submarine cable breaks.

Small-scale laboratory experiments are an alternative method to study turbidity-current dynamics. Advances in experimental technology have increased our understanding from broad descriptions of turbidity-current dynamics to the structure of turbulence in these currents (Kneller et al., 1997; Parsons, 1998; Best et al., 2001, Buckee et al., 2001). Furthermore, physical data from field observations, or more practically from experiments, are required to test numerical models.

However, the advantages of experimental models are offset by scaling problems. Scaling of natural gravity currents to a laboratory level is a well-documented issue in fluid dynamics (e.g. Prandtl, 1952; Duncan, 1953; Middleton and Southard, 1984; French, 1985). There are basically four approaches to scaling of physical models: 1:1 replicas of the field prototype, Froude-number similarity, distorted scale modelling, and unscaled experimental analogues. The large scale of turbidity currents in the oceans that produce significant deposits makes them impossible to reproduce at a 1:1 scale. Consequently, scaled laboratory experiments present the best way to study turbidity currents. The results of unscaled experimental analogue models of large turbidity currents (e.g. Alexander and Morris, 1994), although qualitatively informative, are difficult to apply quantitatively. Distorted scale experiments, for example where unrealistically high slopes are used to obtain appropriate bed shear stresses (e.g. Postma et al., 1988) may be the only way of reproducing some aspects of the prototype, but clearly necessitate some circumspection in application of the results.

Froude-scale modelling is based on a similarity approach in which the gravity current is fully characterized by a series of dimensionless variables. As long as the values of the dimensionless variables in laboratory currents are known to be comparable with those of the natural current, the experiment is adequately scaled with respect to the parameters included in that variable, allowing modelling of large-scale phenomena in the laboratory (e.g. Middleton, 1966a). Dimensional analysis depends upon identification of the controlling variables, which are then grouped into a smaller number of dimensionless parameters such as the flow Reynolds number and the Froude number.

The Reynolds number Re is defined as the ratio of inertial to viscous forces:

$$Re = \frac{\rho_f u h}{\mu} \quad (2.2)$$

where u represents flow velocity, g is gravitational acceleration, h is flow depth, ρ_f is fluid density and μ represents the dynamic viscosity of the fluid. The Froude number Fr is defined as the ratio of inertial to gravitational forces acting on a fluid flow:

$$Fr = \frac{u}{\sqrt{gh}} \quad (2.3)$$

Currents that share the same Re and Fr numbers are said to be dynamically similar. In case of Froude-scale modelling, Fr takes the same value as the prototype, but this requirement is not rigorously applied to Re under the assumption that effects of viscosity can be neglected if the current is fully turbulent. Hence, Froude-scale models are only appropriate for turbidity-current modelling if the model is fully turbulent ($Re > 3000$), which is sometimes difficult to achieve in the laboratory. Even then, it assumes that turbulence is self-similar across the range of scales presented by the model and the prototype. In Froude-scale modelling of turbidity currents, the densimetric Froude number is used, since the action of gravity depends upon the fractional density difference between the sediment-laden current (ρ_f) and the ambient fluid (ρ_w):

$$Fr_d = \frac{u}{\sqrt{g' h}} \quad g' = g \left[\frac{\rho_f - \rho_w}{\rho_w} \right] \quad (2.4)$$

In addition, turbidity currents must also be scaled to the natural system. Under the assumption that the settling velocity adequately describes the particle hydrodynamics, a dimensionless settling velocity is used, which is defined as the ratio of terminal settling velocity of the sediment grains to some velocity scale that is considered characteristic of the current (Middleton, 1966a; Laval et al., 1988). However, electrostatic forces may change the correctly scaled settling velocity of very fine sediment in experimental studies. This problem can be solved by using glass beads or silica flour (e.g. Parker et al., 1987; Garcia, 1993). However, all fine sediment experience capillary forces once they have settled. Capillary forces arise from adhesive intermolecular forces between the sediment and the water which, in case of fine sediment, are larger than the cohesive forces between the water molecules (Atkins, 1990). The impact of these capillary forces on substrate erodibility can only be reduced by using larger grain sizes. Settling velocity can also be scaled by using grains of reduced density, but the consequent reduction in the bulk density of the current necessitates an increase in the sediment concentration. Changing sediment concentration or grain size affects particle behaviour, which may no longer scale with the whole current behaviour (Middleton, 1966a; Peakall et al., 1996). Therefore, problems invariably arise in reproducing field-scale flows in a laboratory.

2.5.3 Numerical modelling

Numerical models provide significant insights into current dynamics. They provide a valuable method for understanding and predicting the consequences of the complex relationships and feedback mechanisms involved in turbidity currents. Analytical solutions have been proposed for some aspects of gravity-current behaviour (e.g. Chu et al., 1979), but numerical techniques are by far the most promising tool to understand and predict three-dimensional turbidity-current processes and deposits. Turbidity currents are highly complex phenomena. They are non-uniform, unsteady, non-linear, free boundary flows, driven by a combination of gravitational, body and pressure forces (Allen, 1985). Additionally, the density varies as sediment is eroded or deposited. In most cases, there are more variables than governing equations, and many models rely on simplifying assumptions in order to resolve this. The accuracy of simulated turbidity-current hydrodynamics and sedimentation thus depends on the choice and validity of the assumptions made. Experimental results provide a means of constraining some of these variables as well as providing a test for such models. Numerical modelling of turbidity currents spans the full range from simple hydraulic equations and box models to highly complex turbulence models. Numerical models may be used for a wide range of purposes, from prediction of turbidite geometries and grain-size distributions, to modelling the vertical structure of turbulence in a turbidity current.

Mathematical models may be process-based, rule-based, or a combination of both. A major drawback to building a fully dynamic, process-based stratigraphic model is the complexity involved in breaking down the interacting processes into elementary objects and continua to which Newton's laws can be applied exactly: the deductive, or process-based, approach (Paola, 2000). The large amount of computer power involved in running the complex physics-based algorithms needed to represent the interaction of sediment transport processes with external forces is a related issue. To limit the complexity, and thus the amount of computing power needed, many models are not fully three-dimensional. The extent to which a two-dimensional representation may be considered a valid simplification of reality depends on the system to be modelled. In the case of turbidite fans, in which mass fluxes in the transverse flow direction contribute significantly to the geometry of the fan, a three-dimensional representation is preferred.

An alternative way of dealing with dynamic complexity is to construct a model from rules. Characteristic for such a rule-based or process-response model is the relatively simple description of the processes involved. Instead of a detailed physical description of the processes, their behaviour is translated into rules that capture the essence of the processes. The essence in this context refers to those properties of the process that are responsible for the expected response. The expected response is obtained from a combination of observations such as outcrop studies, seismic, small-scale experiments, and detailed knowledge of the physics behind the processes involved. Rule-based models are common in stratigraphic modelling, because their simplistic definition of sediment-transport and sedimentation processes results in a high computational efficiency, which is desired in modelling the stratigraphic evolution of sedimentary systems. However, in many such models, quantitative validation (to e.g. small-scale experiments) is difficult, because the very basic translation of elementary laws of physics includes an implicit up-scaling step, in which the influence of small-

scale processes on sedimentation is assumed to be negligible. This limits the applicability of process-response models to large spatial and temporal scales. However, at such large scales, input parameter values can only be obtained at the expense of large uncertainties. Consequently, a wide range of possibly valid truth-cases exists, many of which must then be discarded on the basis of other grounds.

2.6 Modelling techniques

In order to model turbidity-current dynamics, a series of equations must be solved: the conservation of fluid mass, the conservation of sediment mass and the conservation of momentum (known as the Navier-Stokes equation). In addition, an equation for conservation of turbulent kinetic energy may be employed (e.g. Parker et al., 1986). The Navier-Stokes equation is a non-linear partial-differential equation which can be solved for turbulent currents, such as gravity currents, by applying simplifying assumptions.

2.6.1 Assumptions and simplifications

The momentum equations for Newtonian fluids are the Navier-Stokes equations. They are non-linear partial differential equations and describe the flow of a fluid whose stress depends linearly on velocity and on pressure. Changes in momentum of fluid particles occur as a result of changes in pressure and viscous forces acting inside the fluid. The unsimplified Navier-Stokes equations do not have a generalized closed-form solution. A closed-form solution is an analytical solution obtained by a bounded number of well-defined operations. As such, the unsimplified Navier-Stokes equations are only of use in computational fluid dynamics, or if they can be simplified.

In problems involving flow and sediment transport, the degree of simplification depends on the scale of interest. At the scale of ripples and dunes, the mechanics of sediment transport must be coupled to the Reynolds-averaged Navier-Stokes equations to properly describe the phenomenon. At larger scales, the *shallow-water* equations (or *St. Venant* equations; Saint-Venant, 1871) provide a suitable starting point. In their derivation the following simplifying assumptions are made:

- *Incompressibility* may be assumed for fluids with negligible pressure-induced density variations. Incompressibility simplifies the Navier-Stokes equations (conservation of momentum and mass) by assuming constant density:

$$\frac{\partial u_x}{\partial t} + u_x \frac{\partial u_x}{\partial x} + u_y \frac{\partial u_x}{\partial y} + u_z \frac{\partial u_x}{\partial z} = -\frac{1}{\rho} \frac{\partial p}{\partial x} + \nu \frac{\partial^2 u_x}{\partial x^2} + \nu \frac{\partial^2 u_x}{\partial y^2} + \nu \frac{\partial^2 u_x}{\partial z^2} + g_x \quad (2.5a)$$

$$\frac{\partial u_y}{\partial t} + u_x \frac{\partial u_y}{\partial x} + u_y \frac{\partial u_y}{\partial y} + u_z \frac{\partial u_y}{\partial z} = -\frac{1}{\rho} \frac{\partial p}{\partial y} + \nu \frac{\partial^2 u_y}{\partial x^2} + \nu \frac{\partial^2 u_y}{\partial y^2} + \nu \frac{\partial^2 u_y}{\partial z^2} + g_y \quad (2.5b)$$

$$\frac{\partial u_z}{\partial t} + u_x \frac{\partial u_z}{\partial x} + u_y \frac{\partial u_z}{\partial y} + u_z \frac{\partial u_z}{\partial z} = -\frac{1}{\rho} \frac{\partial p}{\partial z} + \nu \frac{\partial^2 u_z}{\partial x^2} + \nu \frac{\partial^2 u_z}{\partial y^2} + \nu \frac{\partial^2 u_z}{\partial z^2} + g_z \quad (2.5c)$$

$$\frac{\partial u_x}{\partial x} + \frac{\partial u_y}{\partial y} + \frac{\partial u_z}{\partial z} = 0 \quad (2.5d)$$

Here, the fluid velocity vector is defined as (u_x, u_y, u_z) , the vector of gravitational acceleration is defined as (g_x, g_y, g_z) , p denotes pressure, and ν represents the viscosity of the fluid. As can be seen, in an incompressible fluid, changes in velocity of a fluid particle with time and in space occur as a result of spatial changes in pressure p and viscous forces (ν represents the viscosity of the fluid), combined with the force of gravity g acting on the fluid particle.

- In *Reynolds-averaging*, the velocity and pressure are averaged over the turbulence by decomposing them into a mean and a fluctuating part:

$$u_i = \bar{u}_i + u_i' \quad p_i = \bar{p}_i + p_i' \quad (2.6)$$

where values of i (1, 2, or 3) correspond to x , y , and z . Application of Reynolds-averaging to the incompressible form of the Navier-Stokes equation results in the Reynolds-averaged form of the incompressible Navier-Stokes equations, in which the viscous forces in the momentum equations are decomposed into viscous stresses $\tau_{v,ij}$ and Reynolds stresses $\tau_{R,ij}$, associated with turbulence:

$$\begin{aligned} \frac{\partial \bar{u}_x}{\partial t} + \bar{u}_x \frac{\partial \bar{u}_x}{\partial x} + \bar{u}_y \frac{\partial \bar{u}_x}{\partial y} + \bar{u}_z \frac{\partial \bar{u}_x}{\partial z} = -\frac{1}{\rho} \frac{\partial \bar{p}}{\partial x} + \frac{1}{\rho} \left(\frac{\partial \tau_{v,xx}}{\partial x} + \frac{\partial \tau_{v,xy}}{\partial y} + \frac{\partial \tau_{v,xz}}{\partial z} \right) \\ + \frac{1}{\rho} \left(\frac{\partial \tau_{R,xx}}{\partial x} + \frac{\partial \tau_{R,xy}}{\partial y} + \frac{\partial \tau_{R,xz}}{\partial z} \right) + g_x \end{aligned} \quad (2.7a)$$

$$\begin{aligned} \frac{\partial \bar{u}_y}{\partial t} + \bar{u}_x \frac{\partial \bar{u}_y}{\partial x} + \bar{u}_y \frac{\partial \bar{u}_y}{\partial y} + \bar{u}_z \frac{\partial \bar{u}_y}{\partial z} = -\frac{1}{\rho} \frac{\partial \bar{p}}{\partial y} + \frac{1}{\rho} \left(\frac{\partial \tau_{v,yx}}{\partial x} + \frac{\partial \tau_{v,yy}}{\partial y} + \frac{\partial \tau_{v,yz}}{\partial z} \right) \\ + \frac{1}{\rho} \left(\frac{\partial \tau_{R,yx}}{\partial x} + \frac{\partial \tau_{R,yy}}{\partial y} + \frac{\partial \tau_{R,yz}}{\partial z} \right) + g_y \end{aligned} \quad (2.7b)$$

$$\begin{aligned} \frac{\partial \bar{u}_z}{\partial t} + \bar{u}_x \frac{\partial \bar{u}_z}{\partial x} + \bar{u}_y \frac{\partial \bar{u}_z}{\partial y} + \bar{u}_z \frac{\partial \bar{u}_z}{\partial z} = -\frac{1}{\rho} \frac{\partial \bar{p}}{\partial z} + \frac{1}{\rho} \left(\frac{\partial \tau_{v,zx}}{\partial x} + \frac{\partial \tau_{v,zy}}{\partial y} + \frac{\partial \tau_{v,zz}}{\partial z} \right) \\ + \frac{1}{\rho} \left(\frac{\partial \tau_{R,zx}}{\partial x} + \frac{\partial \tau_{R,zy}}{\partial y} + \frac{\partial \tau_{R,zz}}{\partial z} \right) + g_z \end{aligned} \quad (2.7c)$$

$$\frac{\partial \bar{u}_x}{\partial x} + \frac{\partial \bar{u}_y}{\partial y} + \frac{\partial \bar{u}_z}{\partial z} = 0 \quad (2.7d)$$

In these equations, the average viscous stresses tensor $\tau_{v,ij}$ and the Reynolds stress tensor $\tau_{R,ij}$ are defined as:

$$\tau_{v,ij} = \rho\nu \left(\frac{\partial \bar{u}_i}{\partial x_j} + \frac{\partial \bar{u}_j}{\partial x_i} \right) \quad \tau_{R,ij} = \frac{\partial (-\rho \overline{u_i' u_j'})}{\partial x_j} \quad (2.8)$$

In this so-called tensor notation, indices i and j take values of 1, 2, or 3 to indicate the Cartesian coordinate axes x , y , and z . As such, x_1 corresponds to x , x_2 corresponds to y , and x_3 corresponds to z .

- *Inviscid* flow may be assumed for fluids in which viscous effects are negligible when compared to inertial effects. The Reynolds number is commonly used to determine whether the assumption of inviscid flow is appropriate. High Reynolds numbers indicate that the inertial forces are more significant than the viscous (friction) forces. In such cases, the assumption of inviscid flow (zero viscosity) is appropriate, and the Navier-Stokes equations reduce to the Euler equations, in which the viscous stress terms in the momentum equation are omitted:

$$\frac{\partial \bar{u}_x}{\partial t} + \bar{u}_x \frac{\partial \bar{u}_x}{\partial x} + \bar{u}_y \frac{\partial \bar{u}_x}{\partial y} + \bar{u}_z \frac{\partial \bar{u}_x}{\partial z} = -\frac{1}{\rho} \frac{\partial \bar{p}}{\partial x} + \frac{1}{\rho} \left(\frac{\partial \tau_{R,xx}}{\partial x} + \frac{\partial \tau_{R,xy}}{\partial y} + \frac{\partial \tau_{R,xz}}{\partial z} \right) + g_x \quad (2.9a)$$

$$\frac{\partial \bar{u}_y}{\partial t} + \bar{u}_x \frac{\partial \bar{u}_y}{\partial x} + \bar{u}_y \frac{\partial \bar{u}_y}{\partial y} + \bar{u}_z \frac{\partial \bar{u}_y}{\partial z} = -\frac{1}{\rho} \frac{\partial \bar{p}}{\partial y} + \frac{1}{\rho} \left(\frac{\partial \tau_{R,yx}}{\partial x} + \frac{\partial \tau_{R,yy}}{\partial y} + \frac{\partial \tau_{R,yz}}{\partial z} \right) + g_y \quad (2.9b)$$

$$\frac{\partial \bar{u}_z}{\partial t} + \bar{u}_x \frac{\partial \bar{u}_z}{\partial x} + \bar{u}_y \frac{\partial \bar{u}_z}{\partial y} + \bar{u}_z \frac{\partial \bar{u}_z}{\partial z} = -\frac{1}{\rho} \frac{\partial \bar{p}}{\partial z} + \frac{1}{\rho} \left(\frac{\partial \tau_{R,zx}}{\partial x} + \frac{\partial \tau_{R,zy}}{\partial y} + \frac{\partial \tau_{R,zz}}{\partial z} \right) + g_z \quad (2.9c)$$

$$\frac{\partial \bar{u}_x}{\partial x} + \frac{\partial \bar{u}_y}{\partial y} + \frac{\partial \bar{u}_z}{\partial z} = 0 \quad (2.9d)$$

- The assumption of inviscid flow is implicitly incorporated in the *boundary-layer* or *slender-flow approximation* (Parker et al., 1986). The slender-flow approximation assumes that changes in flow in lateral directions occur much more slowly than in the upward direction normal to the bed. In the equation of conservation of momentum in the upward-normal direction, the mean part of the pressure p is decomposed into a hydrostatic pressure p_h and a dynamic pressure p_d (related to flow):

$$\frac{\partial \bar{u}_z}{\partial t} + \bar{u}_x \frac{\partial \bar{u}_z}{\partial x} + \bar{u}_y \frac{\partial \bar{u}_z}{\partial y} + \bar{u}_z \frac{\partial \bar{u}_z}{\partial z} = -\frac{1}{\rho} \left(\frac{\partial \bar{p}_h}{\partial z} + \frac{\partial \bar{p}_d}{\partial z} \right) + \frac{1}{\rho} \frac{\partial \tau_{R,zj}}{\partial z} + g_z \quad (2.10)$$

where $\tau_{R,zj}$ represents the Reynolds stress in the upward-normal direction. In the absence of flow, Equation 2.10 of upward-normal momentum balance reduces to the equation for hydrostatic pressure which, after integration, reduces to an expression for the pressure deviation from the local atmospheric pressure at the water-surface:

$$-\frac{1}{\rho} \frac{\partial \bar{p}_h}{\partial z} - g = 0 \quad \int \quad \bar{p}_h = \rho g(H - z) \quad (2.11)$$

where H represents flow thickness. Furthermore, when taking into account the scaling considerations for slender flows, the change in dynamic pressure p_d may be considered very small. Hence, the main result of the application of the slender-flow approximation to the momentum balance in the upward-normal direction is to reduce Equation 2.10 to the equation for hydrostatic pressure (Equation 2.11; Parker et al., 1986). Substitution of Equation 2.11 in Equations 2.9a and 2.9b gives:

$$\frac{\partial \bar{u}_x}{\partial t} + \bar{u}_x \frac{\partial \bar{u}_x}{\partial x} + \bar{u}_y \frac{\partial \bar{u}_x}{\partial y} + \bar{u}_z \frac{\partial \bar{u}_x}{\partial z} = -g \frac{\partial H}{\partial x} + \frac{1}{\rho} \frac{\partial \tau_{R,xz}}{\partial z} + gS_x \quad (2.12a)$$

$$\frac{\partial \bar{u}_y}{\partial t} + \bar{u}_y \frac{\partial \bar{u}_y}{\partial y} + \bar{u}_x \frac{\partial \bar{u}_y}{\partial x} + \bar{u}_z \frac{\partial \bar{u}_y}{\partial z} = -g \frac{\partial H}{\partial y} + \frac{1}{\rho} \frac{\partial \tau_{R,yz}}{\partial z} + gS_y \quad (2.12b)$$

$$\frac{\partial \bar{u}_x}{\partial x} + \frac{\partial \bar{u}_y}{\partial y} = 0 \quad (2.12c)$$

Here, g_i has been replaced by $g(S_x, S_y, -1)$ with S_x, S_y representing bed slope. A further advantage of the slender-flow approximation is that the Reynolds stresses $\tau_{R,xx}, \tau_{R,xy}, \tau_{R,yx},$ and $\tau_{R,yy}$ associated to turbulence in horizontal directions may be neglected compared to those in vertical directions ($\tau_{R,xz}, \tau_{R,yz}$).

- An often adopted simplification technique is that of *depth-averaging* of velocity in the vertical direction. In depth-averaging, velocity u , which principally varies with depth in unsteady flows, is assumed to maintain an approximately similar profile in the vertical direction as it changes in time or in the flow. As such, a single depth-averaged flow velocity U can be defined as resulting from the integration of the vertical velocity profile over the thickness H of the underflow layer (*layer integration*):

$$UH = \int_0^H \bar{u} dz \quad (2.13)$$

Together with boundary conditions at the bed ($z=0$) and the surface of the flow ($z=H$), the slender-flow equations (Equations 2.12a, 2.12b, and 2.12c) may be rewritten into the *shallow-water* equations (or *St. Venant* equations; Saint-Venant, 1871) with lateral variation (2-DH form):

$$\frac{\partial(U_x H)}{\partial t} + \frac{\partial(U_x^2 H)}{\partial x} + \frac{\partial(U_x U_y H)}{\partial y} = -gH \frac{\partial H}{\partial x} + gHS_x - \frac{\tau_{b_x}}{\rho} \quad (2.14a)$$

$$\frac{\partial(U_y H)}{\partial t} + \frac{\partial(U_y^2 H)}{\partial y} + \frac{\partial(U_y U_x H)}{\partial x} = -gH \frac{\partial H}{\partial y} + gHS_y - \frac{\tau_{b_y}}{\rho} \quad (2.14b)$$

$$\frac{\partial H}{\partial t} + \frac{\partial U_x H}{\partial x} + \frac{\partial U_y H}{\partial y} = 0 \quad (2.14c)$$

Here, the Reynolds stresses $\tau_{R,xz}$ and $\tau_{R,yz}$ in vertical directions have been replaced by the shear stresses τ_{bxz} and τ_{byz} evaluated at the bed according to:

$$\tau_{b_x} = \tau_{R,xz} \Big|_{z=0} = \rho u_{*x}^2 \quad \tau_{b_y} = \tau_{R,yz} \Big|_{z=0} = \rho u_{*y}^2 \quad (2.15)$$

where u_{*x} and u_{*y} represent the components of the shear velocity vector in x- and y-direction respectively.

The shallow-water equations basically describe shallow flow in rivers and oceans, driven by the force of gravity acting on the fluid. However, in subaqueous sediment-laden flows, the primary driving force is provided by the force of gravity acting on the suspended sediment. In dilute suspension flows, such as turbidity currents, the suspended sediment causes a small density difference with the ambient fluid, but the density of the flow is not constant due to sediment exchange with the bed. In such non-conservative buoyancy-driven flows, the assumption of incompressibility is invalid.

The *Boussinesq approximation* (Boussinesq, 1877) is a commonly used simplification for buoyancy-driven flows, and is complementary to the shallow-water approximation. It states that density differences between two fluids are sufficiently small to be neglected, except where they appear in terms multiplied by the acceleration due to gravity. The essence of the Boussinesq approximation is that the difference in inertia is negligible but gravity is sufficiently strong to make the specific weight appreciably different between the two fluids. The Boussinesq and shallow-flow approximations are applied in the mathematical model of turbidity-current hydrodynamics and sedimentation, presented in Chapter 3.

2.6.2 Reduction of model dimensions

Besides the above-mentioned approximations, the *reduction of the number of dimensions* in a flow problem also drastically simplifies it. In hydrodynamic modelling, depth-averaging reduces the number of dimensions by one, since vertical variations in e.g. flow velocity and suspended sediment concentration are averaged out. As such, a three-dimensional depth-averaged hydrodynamic model is termed 2-DH. In more sophisticated depth-averaged three-dimensional models (2-DV), the flow is usually divided into two or more layers, in which variations in flow variables in the vertical dimension are depth-averaged. Furthermore, in a 1-D model, one horizontal dimension is also omitted, making the assumption that lateral mass fluxes are small when compared to fluxes in the streamwise direction.

Different viewpoints exist with respect to the number of dimensions in a model. In stratigraphic modelling, the stratigraphy is taken as a reference in determining the number of dimensions in a model. As such, a three-dimensional stratigraphic model is one in which the product is modelled in three dimensions. In contrast, a three-dimensional hydrodynamic model is one in which the hydrodynamic behaviour of a flowing fluid is modelled in three dimensions. Consequently, a three-dimensional model of the stratigraphic evolution of a turbidite fan can be based on a 2-DH representation of the process. The model presented in Chapter 3 is an example of such a model.

2.6.3 Parameterization of sediment transport

In turbidity currents, sediment is transported in suspension, i.e., the grains are kept from falling towards the bed by the upward component of turbulence, which is anisotropic in the vicinity of the bed (Bagnold, 1966). Transport of suspended sediment in a turbidity current can be described with the convection-diffusion equation (Equation 2.16, see below) which follows from the conservation of mass for a unit volume (Sloff, 1994; Van Rijn, 1987):

$$\frac{\partial ch}{\partial t} + \underbrace{\frac{\partial u_x ch}{\partial x} + \frac{\partial u_y ch}{\partial y} + \frac{\partial u_z ch}{\partial z}}_{\text{advective transport}} - \underbrace{\frac{\partial}{\partial x} \left(\epsilon_x \frac{\partial ch}{\partial x} \right) - \frac{\partial}{\partial y} \left(\epsilon_y \frac{\partial ch}{\partial y} \right)}_{\text{horizontal diffusion}} = \underbrace{w_s \frac{\partial ch}{\partial z}}_{\text{settling}} + \underbrace{\frac{\partial}{\partial z} \left(\epsilon_z \frac{\partial ch}{\partial z} \right)}_{\text{vertical diffusion}}$$

The sediment-flow interaction is determined by the diffusion coefficients ϵ_x , ϵ_y , ϵ_z , and the particle fall velocity w_s . In modelling of turbidity currents, horizontal advective processes are far more important than horizontal diffusive processes. Therefore, *horizontal diffusion is neglected*, i.e., the horizontal diffusive terms in the equation may be disregarded. Changes in suspended sediment concentration through exchange with the bed are contained in the right-hand side of the equation. For the parameterization of exchange with the bed, several models exist. They may be based on different concepts of suspension transport: *competence-driven* transport and *capacity-driven* transport.

In competence-driven transport, the competence of the flow is the determining factor for transporting sediment. Flow competence is defined as the ability of the flow to carry sediment of a given size. Hence, flow competence is characterized by the largest particle the flow can carry. It is usually parameterized by the ratio of shear velocity u_* to grain-settling velocity w_s , whereby the shear velocity of the flow is related to the mean flow velocity by a drag coefficient. The shear velocity thus obtained is assumed to represent the upward component of turbulence in the flow near the bed. In contrast, capacity-driven transport relates to the capacity of the flow, which is defined as the total amount of sediment (of all different sizes) the flow can transport. The flow capacity concept relates sediment transport to the level of turbulent kinetic energy in the flow as a whole, and not just in the vicinity of the bed.

Parker et al. (1986) explicitly account for erosion and deposition in parameterizing the right-hand side of the convection-diffusion equation, whereby the formulation for erosion (see Chapter 3 for details) is based on experimental data. Their model can be

seen as representing competence-driven transport. An alternative approach to the empirical model of Parker and co-workers (Garcia and Parker, 1993; Wright and Parker, 2004a, 2004b) is that of Galappatti (1983) and Galappatti and Vreugdenhill (1985), adapted for turbidity-current modelling by Sloff (1994a, 1997). Galappatti (1983) substitutes an asymptotic solution of the depth-integrated concentration into the convection-diffusion equation for suspended sediment, instead of estimating the depth-averaged suspended sediment concentration, near-bed sediment concentration and sediment entrainment rate empirically. The depth-averaged concentration is then theoretically determined instead of empirically, since the convection-diffusion equation is actually solved, albeit approximately. In the solution of the depth-averaged concentration, exchange of suspended sediment with the bed (right-hand side of Equation 2.16) is calculated based on the deviation from the depth-averaged equilibrium suspended sediment concentration C_e :

$$\underbrace{w_s \frac{\partial ch}{\partial z}}_{\text{settling}} + \underbrace{\frac{\partial}{\partial z} \left(\varepsilon_z \frac{\partial ch}{\partial z} \right)}_{\text{vertical diffusion}} = \frac{w_s (C_e - C)}{T} \quad (2.17)$$

The dimensionless adaptation time T is a measure of the duration of non-equilibrium conditions in the turbidity current, e.g. the amount of time required to re-establish the equilibrium concentration profile after a perturbation.

The value of the depth-averaged equilibrium concentration is based on the equilibrium concentration profile and the velocity profile, the shape of which highly depend on the hydrodynamic conditions. Sloff (1994a, 1997) approximated these profiles semi-empirically, and successfully tested computed equilibrium concentration and velocity profiles against experimental data measured by Garcia et al. (1986) and Garcia (1990) in a laboratory flume. The model by Sloff (1997) can be seen as representing capacity-driven transport. However, both models require estimation of the near-bed sediment concentration to calculate exchange with the bed. Proper estimation of the near-bed sediment concentration is critically important in obtaining realistic sedimentation rates.

2.6.4 Turbulence modelling

A major challenge in simulating turbulence is that random fluctuations such as eddies and vortices occur on a very wide range of scales, all of which must be taken into account in a realistic model. In the atmosphere, the swirls and eddies of air that make up the overall flow range from several centimetres in diameter to thousands of kilometres. The scales can range over many orders of magnitude, with the number of variables, and thus the computational effort required to keep track of them, increasing rapidly as the range in scales increases. The degree of turbulence in a fluid flow is commonly quantified by the Reynolds number (Equation 2.2). Higher Reynolds numbers correspond to a wider spread in the range of eddy sizes, equivalent to higher levels of turbulence. Models that incorporate turbulence use techniques such as DNS (Direct Numerical Simulation), RANS (Reynolds Averaged Numerical Simulation, and LES (Large Eddy Simulation).

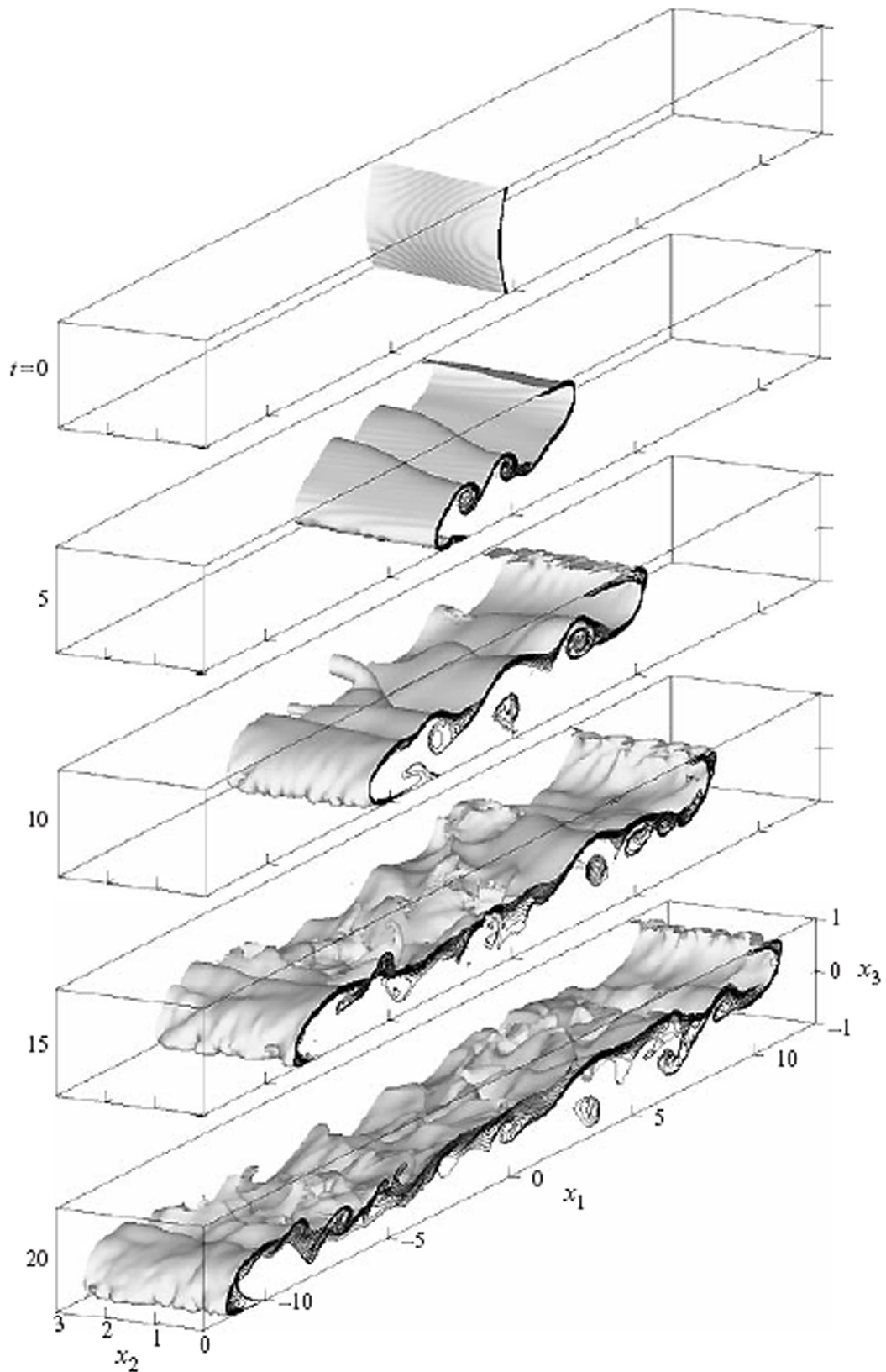


Figure 2.12: Direct Numerical Simulation of a three-dimensional lock-exchange flow between no-slip walls. At time $t=0$, the lock, which separates the heavier fluid in the right part of the box from the lighter fluid in the left part of the box, is released. Flow fields at different times t are visualized by a density isosurface, together with isocontours in the side-plane. Reproduced from Härtel et al. (2000).

Direct Numerical Simulation (DNS) captures all of the relevant scales of turbulent motion. It starts with the fundamental equations of fluid flow (the Navier-Stokes equations) and calculates speed and direction for each fluid particle. Here, “direct” means that velocities are calculated at each time step as the flow progresses, without reliance on experimental data to supply parameters. DNS tracks each particle (for instance the particles in a plume of smoke) as it moves step-by-step within a high-resolution grid. DNS numerically solves the complete turbulent flow field directly, without any form of time or length averaging in the domain (Sengupta, 2004; Bates et al., 2005). DNS is extremely expensive in terms of computing power, and currently only applicable to simple, low Reynolds number flows (Figure 2.12). Hence, there is a need for models that represent the smallest scales of turbulent motion.

Large Eddy Simulation (LES) is a technique in which the smaller eddies are filtered and are modelled using a sub-grid scale model, while the larger energy carrying eddies are simulated. Since the largest eddies contain the most energy and interact most with the mean flow, the LES approach results in a good model of the main effects of turbulence (Sengupta, 2004; Bates et al., 2005). This method generally requires a more refined mesh than a RANS model, but not as fine as that needed for a DNS solution.

The Reynolds-Averaged Navier-Stokes (RANS) equations are the oldest approach to turbulence modelling. In RANS, new apparent stresses known as Reynolds stresses, are introduced to account for viscous effects (loss of energy) due to turbulent eddies and vortices (Sengupta, 2004; Bates et al., 2005). The apparent stresses result from the decomposition of velocity into a mean and a time-averaged part. The introduction of Reynolds stresses adds a second-order tensor of unknowns to which various models (e.g. $k-\epsilon$ closure model, Mellor-Yamada closure model) can provide different levels of closure. The turbulence closure models are valid only as long as the time over which the changes in the mean velocity occur is large compared to the time scales of the turbulent motion containing most of the energy. Considerable progress is being made, also stimulated by the exponential increase in available computing power, in modelling single flows in a controlled environment, such as e.g. lock-exchange flows. However, application of turbulence modelling in stratigraphic models, which require highly efficient algorithms to be of practical use, is not yet feasible, and perhaps not desirable.

2.6.5 Numerical techniques

Mathematical models involving fluid flow commonly consist of a system of non-linear partial differential equations for which no practical analytical solution exists. Therefore, the system of equations is solved numerically. In numerical models, the spatial domain is discretized into small cells to form a volume mesh or grid, and a suitable algorithm is applied to solve the equations of motion (Euler equations for inviscid flow, Navier-Stokes equations for viscid flow). In problems where shocks or discontinuities are present, as in the case of turbidity currents, high resolution, Total Variation Diminishing (TVD) schemes are needed to avoid spurious oscillations in the solution. In the field of computational fluid dynamics (CFD) a large number of methods is available to solve fluid flow problems numerically. With respect to discontinuous flows such as turbidity currents, the development of computational

methods is mainly attributed to aeronautical science. CFD code for the design and analysis of transonic flows past airfoils and wings have become standard tools in the aircraft industry and are readily available in the public domain. The analogy between compressible flows in gas dynamics and open-channel flow has instigated the use of these aeronautical methods in hydraulic engineering. Since the mid-eighties, the progress in computing discontinuous shallow-water flows, also stimulated by increasing computing power, has increased significantly to a level where their application on time scales exceeding decades has become feasible.

Decisions for choosing an appropriate computational method have to consider the physical behaviour of the model, the nature of the solution, the required accuracy and computational efficiency. In modelling of turbidity-current hydrodynamics, the presence of a discontinuous front poses an additional demand on the computational method of choice. From a mathematical point of view, disturbances in the state of a solution travel in the form of waves in numerical flow models. These waves propagate with a characteristic speed along wave paths or “characteristics” in the space-time domain. The amplitude of the waves quantifies the magnitude of the disturbance and directly relates to the fluxes in flow variables. The superposition of all the waves travelling in the computational domain constitutes the state of the solution. The presence of a flow front such as the head of a turbidity current requires that the solution be discontinuous from one grid cell to the next, whereby the discontinuity is characterized by a sharp jump in flow variables at the boundary between two grid cells. Therefore, an accurate representation of a discontinuous front in an otherwise continuous flow requires a special treatment.

Two techniques are available to compute discontinuous flows: shock fitting and shock capturing. Shock fitting is more accurate than shock capturing. In shock fitting, the front is considered to be an internal moving boundary condition in an otherwise continuous computational domain. The internal moving boundary condition is a set of shock relations that describe the behaviour of the solution across the discontinuity. In a 1-D flow model, the use of internal moving boundary conditions requires the definition of a Lagrangian sub-coordinate system on a deformable grid moving with the front. However, in 2-DH flow models, the interaction of the initial shock with additional shocks, such as internal hydraulic jumps that appear during computation, causes disorder because additional moving internal boundary conditions and deforming grids are needed to accurately track the additional shocks.

Shock capturing is a much more robust way of computing discontinuous flows, since continuous flow and shocks are all solved by means of the same scheme without using additional moving boundary conditions for the front. Furthermore, the organization of the computations is not affected by the presence and interaction of additional discontinuities in the computational domain. A potential disadvantage of shock capturing is that the front is less sharp than in shock fitting, because it is smeared over at least one grid cell. However, the length-scale of the head is much smaller than the length-scale of sedimentary basins, which justifies the use of a much simpler shock-capturing scheme. An essential property of shock-capturing techniques is the addition or presence of pseudo-viscosity to damp the non-physical numerical oscillations near the shock. The origin of the non-physical numerical oscillations lies in the numerical treatment of the derivatives in the mathematical equations.

Numerical treatment of derivatives requires that they be replaced by differential quotients. Expansion of a difference equation into a Taylor series results in the original difference equation plus truncated higher-order terms, which arise due to the approximation of the continuous derivative. These truncated higher-order terms together constitute the truncation error. Even-order terms in this truncation error cause physical dissipation, i.e., they act so as to compress waves to a spike. Odd-order terms cause dispersion, whereby the propagation velocity of the waves is altered. The orders of these dissipation and dispersion errors depend on the scheme. A first-order scheme has second-order dissipation and third-order dispersion errors, whereas second-order schemes have fourth-order dissipation and third order dispersion errors. In first-order upwind schemes, dissipation is dominant, and the solution is smoothed. In second-order space-centred schemes, dispersion is dominant. Here, non-physical numerical oscillations occur near discontinuities, which become a fixed source that continuously emanates disturbances. By adding pseudo-viscosity, the solution near the jump in flow variables is smoothed, while in the gradually varied flow region it is at least one order of magnitude smaller than the order of the numerical scheme (Sloff, 1997).

Principally, the choice of scheme is made first, based on a consideration between accuracy and computational efficiency. Although accuracy is an important requirement, it is also costly in terms of computational efficiency. Taking into account the need for computational efficiency in stratigraphic modelling, the merits of a high-order accurate numerical scheme should be weighed against the inherent uncertainty in the geological data from which to extract the initial and boundary conditions for the stratigraphic model. First-order upwind schemes (e.g. Godunov schemes, characteristic difference schemes) establish a relation between the physical propagation of the flow and the direction of differentiation. Although they are dissipative in nature (no pseudo-viscosity required), they achieve only first-order accuracy in continuous flow regions. Extensions to improve the accuracy of first-order upwind schemes require a significant computational effort, especially in solving 2-DH discontinuous flows.

By contrast, centred schemes achieve second-order accuracy in continuous flow regions. However, pseudo-viscosity must be added to schemes of second-order and higher accuracy to keep the solution free of oscillations in the presence of discontinuities. Pseudo-viscosity may be added in the form of “empirical” artificial viscosity or TVD (Total Variation Diminishing concept by Harten, 1983) artificial viscosity. In the empirical artificial viscosity approach, a (second-order) diffusion term is explicitly added to the momentum and continuity equations. The magnitude of this diffusion coefficient is usually a function of the flow variables multiplied by an “empirical” coefficient. A major disadvantage of the empirical artificial viscosity approach is that this coefficient must be estimated for each application. In contrast, TVD artificial viscosity does not require calibration. Second-order schemes produce correct oscillation-free solutions if the total variation, defined as the sum of the fluxes between the cells, diminishes in time. Second-order schemes can be made to satisfy the TVD concept and be oscillation-free by adding a non-linear component to the original solution. If the magnitude of this non-linear term is made equal to the second-order contribution of the original solution responsible for the oscillations, the solution is free of oscillations. In empirical artificial viscosity spurious oscillations are damped, whereas in TVD artificial viscosity, the generation of spurious oscillations is prevented.

2.7 Modelling fan stratigraphy: past and present

Stratigraphic modelling has a long history, dating back to the mid-sixties, when Briggs and Polack (1967) built the first dynamic model of evaporate sedimentation. A few years later, stratigraphic modelling came into its own with the book by Harbaugh and Bonham-Carter (1971), which showed how computational stratigraphic models such as diffusion models, delta evolution models, and carbonate deposition models can be devised. Over the years, increased understanding of processes governing stratigraphy resulted in attempts to replace process-response models by process-based models. Perhaps by lack of better methods, a limited understanding of the processes, or underestimation of the significance of deep-marine sediments in the stratigraphic record, but deep-marine sedimentation processes were somewhat neglected in this process. The transport and deposition of deep-marine sediments was, for a long time, primarily modelled by diffusion.

2.7.1 1D Process-based models

Probably the first process-based model related to turbidity-current hydrodynamics was the one-dimensional model of density currents by Ellison and Turner (1959). It consists of three layer-integrated conservation equations for flow momentum, flow volume and solute mass. The Ellison-Turner model only applies to conservative flows driven by density differences caused by temperature or salinity gradients. However, it can be used as an approximation to estimate the development of a turbidity current laden with fine-grained sediment such as clay and fine silt in the stream direction.

Around the same time, Bagnold (1962) published a “zero-equation” model of turbidity currents, based on the autosuspension concept proposed by Knapp (1938). In the Knapp-Bagnold model, sediment suspends itself in a sense that no net expenditure of energy by the flow is needed in keeping the grains suspended, depending on the ratio of particle fall velocity to the product of mean flow velocity and bed slope:

$$\frac{US}{w_s} > 1 \quad (2.18)$$

where U is mean flow velocity, S is bed slope and w_s represent the fall velocity of the sediment. If the Knapp-Bagnold criterion is satisfied, the concentration, and thus the velocity of the turbidity current might increase indefinitely because the amount of sediment entrained from the bed exceeds the amount of sediment lost through settling. This implies that more energy is fed through sediment entrainment than is consumed in holding it in suspension (Southard and Mackintosh, 1981; Parker et al., 1986). Pantin (1979) and Parker (1982), independently of each other, showed that, in erosive turbidity currents, energy is expended not only in keeping the sediment suspended, but also in entraining sediment and ambient water into the current. In both cases, the potential energy of the suspension increases at the cost of turbulent kinetic energy. Hence, Parker et al. (1986) added a fourth equation to the original layer-averaged three-equation model (conservation of momentum, water volume and sediment mass) of Ellison and Turner (1959) to account for the balance of turbulent kinetic energy when attempting to model erosive turbidity currents. Closure of the three- and four-equation models is achieved through relations for sediment entrainment, water

entrainment, bed friction, and shape factors related to the assumption of similarity of vertical profiles of flow velocity and sediment concentration. The closure-relations are semi-empirical at best, and derived using data from observations of turbidity currents under controlled laboratory conditions (Altinakar et al., 1990, 1996; Parker et al., 1987; Garcia and Parker, 1989, 1993; Garcia, 1993, 1994). A similar layer-integrated three-equation model to that of Parker et al. (1986) has been proposed by Mulder et al. (1998) to model erosion and deposition by hyperpycnal flows at river mouths.

Other one-dimensional modelling efforts in the late 1970s and 1980s include those by Komar (1977) on sedimentation from steady turbidity currents, the one-dimensional spatial evolution of steady turbidity flows in water reservoirs (Akiyama and Stefan, 1986) and the scouring of submarine canyons by swift turbidity currents (Fukushima et al., 1985). More recently, Choi and Garcia (1995) used the three-equation model to study the propagation of a turbidity front along a sloping bottom, and concluded that simulated propagation velocities compared fairly well with the relationship proposed by Britter and Linden (1980) to estimate the speed of density currents fronts and the experimental observations made by Altinakar et al. (1990) for weakly-depositional turbidity currents. In all cases, layer-integrated equations were used.

Recently, Kubo et al. (2005) validated the layer-integrated three-equation model of Parker et al. (1986) against data from a laboratory experiment in which stratigraphy was created from a series of turbidity currents in a small subsiding three-dimensional basin representative of a characteristic salt-withdrawal basin in the Gulf of Mexico (see also Chapter 6, Paragraph 6.3). However, instead of the original competence-based formulation for deposition by Parker et al. (1986), the concept of flow capacity was used as a criterion of deposition from suspension (Hiscott, 1994; Kubo, 2004). Flow capacity is parameterized as the product of flow height, near-bed sediment concentration and a “capacity” parameter. This capacity parameter takes the value of the integral of the vertical profile of relative concentration of suspended sediment, which is obtained by an approximation in which the integral of the vertical profile of relative concentration is related to the Rouse number. For sediment entrainment from the bed, the original formulation by Parker et al. (1986) was used. Although the model of Kubo et al. is essentially a one-dimensional model capable of producing stratigraphy in cross-section, it was integrated in *2D-SedFlux* (see below) whose model architecture accounts for basins whose width varies with distance. A comparison of bed surface profiles generally shows a good agreement between the experimental and model results. Furthermore, individual beds in the modelled stratigraphy can be correlated to their experimental counterparts. However, differences are observed in variation in bed thickness between the model and the experiment (Kubo et al., 2005). Essentially, the validation experiment discussed in Chapter 6 can be regarded as a more sophisticated version of the work by Kubo et al. Here, the same experimental data are used to validate a 2-DH model of turbidity-current hydrodynamics and sedimentation capable of producing stratigraphy in three dimensions.

The one-dimensional four-equation model of Parker et al. (1986), which includes the balance of turbulent kinetic energy, was numerically solved by Pratson et al. (2001) in a Lagrangian reference frame (a reference frame moving with the flow). This model, called “*BANGID*”, was used to compare the behaviour of turbidity currents against that of debris flows (Pratson et al., 2000). Reportedly, simulations compare well to

experimental data of turbid flows (Pratson et al., 2001). Furthermore, a sensitivity test of the model revealed that a constraint must be placed on the erosive power of the flow. In line with earlier propositions by Parker et al. (1986), this is accomplished by coupling the frictional shear at the base of the flow to its turbulent kinetic energy.

A “one-and-a-half” or 1-DV model was developed by Sloff (1997) to investigate sedimentation from turbidity currents in storage reservoirs. In such shallow reservoirs, the intrusion of a turbidity current produces a countercurrent in the ambient water above (Lambert and Luthi, 1977). Hence, the upper ambient water layer must be treated separately to account for the influence of the upper layer on the hydrodynamics of the intruding turbidity current. In this depth-averaged two-layer model, baroclinic and barotropic flow are treated separately, whereby for the baroclinic flow front, shock-capturing is applied to properly model the propagation speed. Results indicate that the overall behaviour of turbidity currents and saline current is satisfactorily represented by the model. Computed front propagation speeds are sufficiently accurate for engineering purposes (Sloff, 1997).

However, the complexity of flow in turbidity current fronts cannot be captured by the layer-integrated three- or four- equation models. Bradford et al. (1997) used the method of characteristics to extract analytical solutions from the layer-integrated three-equation model of Parker et al. (1986), and concluded that, for turbid surges flowing into quiescent water, the speed of the propagating front could be obtained by either including a turbulent entrainment term in the continuity equation as suggested by Choi and Garcia (1995) or by specifying a finite acceleration of the wave front.

2.7.2 2D Process-based models

From a mathematical point of view, the one-dimensional layer-integrated three- and four-equation models by Parker et al. (1986) can be extended to include transverse variations in the flow. However, publications regarding such 2-DH models and their performance in terms of a (quantitative) comparison of model results to experimental data are scarce. Bradford and Katopodes (1999a, 1999b) developed a two-dimensional version of the layer-integrated three-equation model to simulate bed aggradation due to sediment deposition, channel avulsion, and channelization resulting from unsteady turbidity current action on submarine fans. The numerical solution is obtained with a finite-volume method and includes shock-capturing to ensure a sharp front. The closure relations include the sediment entrainment function for non-uniform bed sediment (Garcia and Parker, 1991) as well as an empirical expression to estimate the near-bed sediment concentration of a given size fraction to the depth-averaged concentration (Garcia, 1994). Validation of the model was achieved by comparing simulated results to data of partially confined turbidity currents generated during a radial lock-exchange experiment conducted by Bonnecaze et al. (1995). Obstruction of the channel due to localized aggradation and subsequent avulsion was found to depend on grain size, sediment concentration and channel slope (Bradford and Katopodes, 1999b). The model was applied in studies of the morphological evolution of the Reserve Fan and Rupert Inlet, both of which are characterized by low-density hyperpycnal inflow. Hence, the simulated turbidity currents were actually thin sustained turbid underflows, characterized by very small initial flow thickness (<0.5m) and concentrations (1.5% by volume) at the shelf-edge. Ignition of these thin

turbid underflows into turbidity currents was found to depend on the value of the drag coefficient, which, in the model, influences both sediment entrainment and flow speed.

Imran et al. (1998) used essentially the same 2-DH model in conjunction with the Exner (1920, 1925) equation for bed sediment continuity to study the onset of channelization in submarine fans resulting from sustained steady turbidity currents. However, and in contrast to the numerical implementation of the 2-DH model by Bradford and Katapodes (1999a), no shock-capturing is applied in this numerical approach. Imran et al. (1998) motivate this deficiency by reasoning that the time necessary for the front to reach the end of the computational domain is very short in comparison to the time needed to build significant morphology on the bed. Hence, the influence of deficiencies associated with the numerical treatment of the head of the turbidity current is not expected to affect long-term evolution of bed morphology. With the help of numerical experiments, a search was conducted for the optimum conditions for channelization, which confirmed that a wide range of conditions exists for which turbidity currents debouching from a canyon onto a fan spontaneously self-channelize (Imran et al., 1998). More recently, the model was applied to study the influence of along-shelf currents on hyperpycnal flow and sedimentation patterns observed near the mouth of the Eel river (Imran and Syvitski, 2000) and on the Adriatic shelf near the mouth of River Tronto (Khan et al., 2005). In the latter case, a commercially available three-dimensional hydrodynamic model (*FLUENT*) was used to obtain the necessary input conditions for the model by simulating the transformation of a river flow into a hyperpycnal plume through the plunge process, which cannot be realistically done with depth-averaged models. It was found that along-shelf currents can significantly change the direction and spreading pattern of a hyperpycnal plume, and its resultant sedimentation pattern (Khan et al., 2005).

Above-mentioned models have not been specifically developed for use in stratigraphic modelling on geologic timescales. In the field of quantitative stratigraphy, modelling usually takes a holistic approach, whereby all the processes that affect the evolution of stratigraphy at continental margins are taken into account, a so-called source-to-sink approach. Noteworthy examples of such stratigraphic models are *SEDSIM* and *2D-SedFlux*. *SEDSIM* (Tetzlaff and Harbaugh, 1989; Martinez and Harbaugh, 1993; Griffiths et al., 2001) was developed in the mid-eighties at Stanford. It is a three-dimensional stratigraphic forward modelling program in which the core flow and sedimentation algorithms are linked to modules including subsidence, sea level change, wave transport, compaction, slope failure and carbonate deposition. *SEDSIM* models erosion, transport and deposition, and thus it “predicts” clastic sediment distribution on an arbitrary bathymetric surface. Similar to the objectives of this thesis, it simulates turbidity-current flow and resulting sedimentation patterns on geologic timescales. A closer look into the hydrodynamics that make up the core of the *SEDSIM* program reveals that it is essentially a two-dimensional flow model, in which the depth-averaged Navier-Stokes equations are solved in a Lagrangian reference frame. Fluid flow modelling is performed by allowing fluid elements to travel over a topographic grid. The fluid elements are treated as discrete points having a fixed volume (“marker-in-cell” method), and react to changes in slope, flow density and the density of the medium (e.g. air, sea water, fresh water) through which they are passing. As in other depth-averaged models, an important assumption is the similarity in vertical profiles of velocity and

concentration and their uniformity in streamwise and transverse flow directions. *SEDSIM* is commonly regarded as the most advanced stratigraphic modelling package around. Unfortunately, information on the workings of the model is scarce, and dates back mostly to the early versions developed by Tetzlaff and Harbaugh (1989) and Martinez and Harbaugh (1993). Although successful applications have been published (Griffiths et al., 2001), no well-constrained tests of the validity of the model's fluid dynamics or morphodynamics appear to have been carried out (Paola, 2000).

2D-SedFlux is a process-response basin-fill model, aimed at simulating the transport and delivery of sediment on continental margins over time-scales of up to tens of thousands of years using daily time steps (Syvitski and Hutton, 2001). It combines individual process-response models into one fully interactive model, which delivers a multi-size sediment load onto and across a continental margin. It can simulate basin stratigraphy and variations therein in a vertical plane, with a typical vertical resolution of 0.01-0.25 m. *2D-SedFlux* includes, amongst others, modules that simulate river-mouth dynamics, buoyant surface plumes, hyperpycnal and failure-induced low-density turbidity currents, and debris flows. The model allows for the deposit to compact, and to experience tectonic processes (faults, uplift) and isostatic subsidence from the sediment load. Turbidity-current modelling in *2D-SedFlux* is based on the work by Kubo et al. (2005), which has been reviewed previously. As such, it is essentially one-dimensional in its representation of hydrodynamics, because layer-integrated equations for conservation of momentum and mass of water and sediment are used. A hydrodynamically two-dimensional (2-DH) version of *2D-SedFlux*, capable of simulating three-dimensional stratigraphy, is underway.

2.7.3 Models including turbulence

Turbidity-current models that include turbulence are at present two-dimensional at best, i.e., they describe flow variations in a vertical plane. Instead of assuming similarity in vertical profiles of velocity and concentration, as in depth-averaged models, these models compute the velocity field and distribution of suspended sediment in the streamwise and upward-normal direction. In the past, turbidity-current models including turbulence have been applied to gain insight into the vertical structure of density and turbidity currents (Stacey and Bowen, 1988a, 1988b; Brørs and Eidsvik, 1989; Choi and Garcia, 2002), and to investigate the conditions for self-acceleration or "ignition" (Eidsvik and Brørs, 1989). Most, if not all, models employ the $k-\varepsilon$ turbulence closure model. The results of these studies have been used to assess the validity of the assumption of similarity in profiles of velocity and sediment concentration, on which depth-averaged one- and two-dimensional models are based. Furthermore, rates of ambient water entrainment were also found to agree well with empirical water entrainment relations used in depth-averaged models (e.g. Parker et al., 1986; Sloff, 1997).

Recently, Felix (2001, 2002) has used the Mellor-Yamada level 2.5 second-order turbulence-closure scheme in a two-dimensional model for turbidity currents, with the aim to include the effect of sediment-induced stratification on the vertical structure of turbidity currents. The influence of the presence of the particles on the turbulence other than the buoyancy was parameterized through a drag term leading to an extra dissipation term in the turbulent kinetic energy equation and in the equation of the

length scale of the turbulence. To validate the model, it was applied to historical flows in Bute Inlet and the Grand Banks turbidity current. The flows show a clear interaction between velocity, turbulence and sediment distribution in both the streamwise and upward-normal direction. Numerical tests revealed that flows with fine-grained sediment have low vertical and high horizontal gradients of velocity and sediment concentration. Furthermore, they show little increase in flow thickness and decelerate slowly. Changes in velocity and concentration in time and space are comparable, i.e., their vertical profiles remain approximately similar as the fine-grained flow evolves. In contrast, flows with coarse-grained sediment have high vertical velocity gradients, low horizontal velocity gradients and high horizontal concentration gradients. According to Felix (2001, 2002), these flows grow considerably in thickness and decelerate rapidly. Changes in velocity and concentration in time and space are not comparable, i.e., their vertical profiles change as the coarse-grained flow evolves.

Three-dimensional flow models including turbulence are available in the form of semi-commercial packages (*DELFT3D*, *FLOW3D*), which were not specifically designed for research on turbidity-current hydrodynamics and sedimentation. Even in these models, a degree of depth-averaging is often applied in three-dimensional flow simulations to keep the computational time within practical bounds. The degree of depth-averaging is determined by the number of discrete layers into which the flow is divided in the upward-normal direction.

A limitation of the use of turbulence models in general is that the methods are at present very costly in terms of computer power and time. In many cases, the desired model output (such as grain-size distribution or deposit thickness) does not warrant the computational power required, given the uncertainties of initial conditions of turbidity currents in natural environments, and a more simple depth-averaged model would serve most modelling purposes (Kneller and Buckee, 2001).

2.7.4 The *FanBuilder* model

The aim of the *FanBuilder* model, described in this thesis, is to simulate the long-term stratigraphic evolution of turbidite fans, which includes features such as channelization, channel aggradation, avulsion and lobe switching. None of the two-dimensional models mentioned in the preceding review have been developed specifically for use in studies of the stratigraphic evolution of turbidite fans on a field-scale. However, depth-averaged models developed by Parker et al. (1986), Sloff (1997), Bradford and Katapodes (1999a, 1999b) and Imran (1998), have shown to be promising in simulating the above-mentioned essential features. Hence, the mathematical model of turbidity-current hydrodynamics and sedimentation, which lies at the heart of the *FanBuilder* model, is essentially based on these depth-averaged models. In the numerical implementation, computational efficiency has been an important consideration in choosing the most suitable numerical scheme. The chosen combination of the explicit fractional-step MacCormack scheme in operator-split form, with a high-resolution shock-capturing technique is simple, robust and computationally efficient. Furthermore, it ensures second-order accuracy in space and time, which is deemed sufficient in the context of modelling stratigraphy.

3 MATHEMATICAL FORMULATION

3.1 Introduction

In this chapter, a generic process-based model is proposed to simulate turbidity-current flow and sedimentation over arbitrary topography in three dimensions. It combines theoretical formulations on density flow (Parker et al., 1986) and sediment transport (Garcia and Parker, 1991, 1993; Wright and Parker, 2004a, 2004b) and numerical techniques (MacCormack, 1969; Garcia and Kawahita, 1986; Sloff, 1997; Wang et al., 2000), in a numerical simulation model. The purpose of the model is to serve as a tool in qualifying and, where possible, quantifying the impact of changes in forcing parameters (flow density, grain size and sorting of the suspended sediment, slope) on the stratigraphic evolution of turbidite fans. The objective of this chapter is to explain the model from a physical and mathematical point of view. The numerical implementation is discussed in Chapter 4. Validation of the model to a wide range of experimental conditions (e.g. variations in flow density, variations in grain size and sorting of the suspended sediment, flow around obstacles, and multiple successive flows) will be discussed in Chapter 5 and Chapter 6 of this thesis.

3.2 Mathematical model

3.2.1 Configuration

Figure 3.1 illustrates the configuration of the model. A situation is modelled in which a turbidity current (brown) flows over a surface representing topography, thereby exchanging sediment with the bed (yellow). The body of water through which the turbidity current flows is assumed to be quiescent, infinitely deep and unstratified. The assumption of an infinitely deep medium allows the use of the “single-layer” formulation, which accurately describes the hydrodynamics of turbid underflows in situations where the thickness of the underflow is much smaller than the depth of the ambient fluid (Huppert and Simpson, 1980). The coordinate system in the model is defined with reference to the local bed slope. The vertical component (z -axis) is upward-normal to the bed, and both the streamwise (y -axis) and the transverse (x -axis) components are parallel to the bed. Consequently, the unit upward vertical vector, which, in a standard Cartesian reference frame, is defined as $(0, 0, 1)$, is here defined as $(\sin\theta_x, \sin\theta_y, 1)$, with θ_x, θ_y representing bed slope angle in x - and y -direction respectively. The vector of gravitational acceleration is defined as $-g(\sin\theta_x, \sin\theta_y, 1)$, where g denotes the magnitude of gravitational acceleration. Under the assumption that slope angles θ_x, θ_y are small, the sine of the slope angle is approximately equal to bed slope (S_x, S_y) :

$$\sin\theta_x \approx S_x = -\frac{\partial\eta}{\partial x} \quad \sin\theta_y \approx S_y = -\frac{\partial\eta}{\partial y}$$

where $\eta(x, y, t)$ denotes (true) vertical bed elevation. Hence, the vector of gravitational acceleration is approximated as $g(S_x, S_y, -1)$.

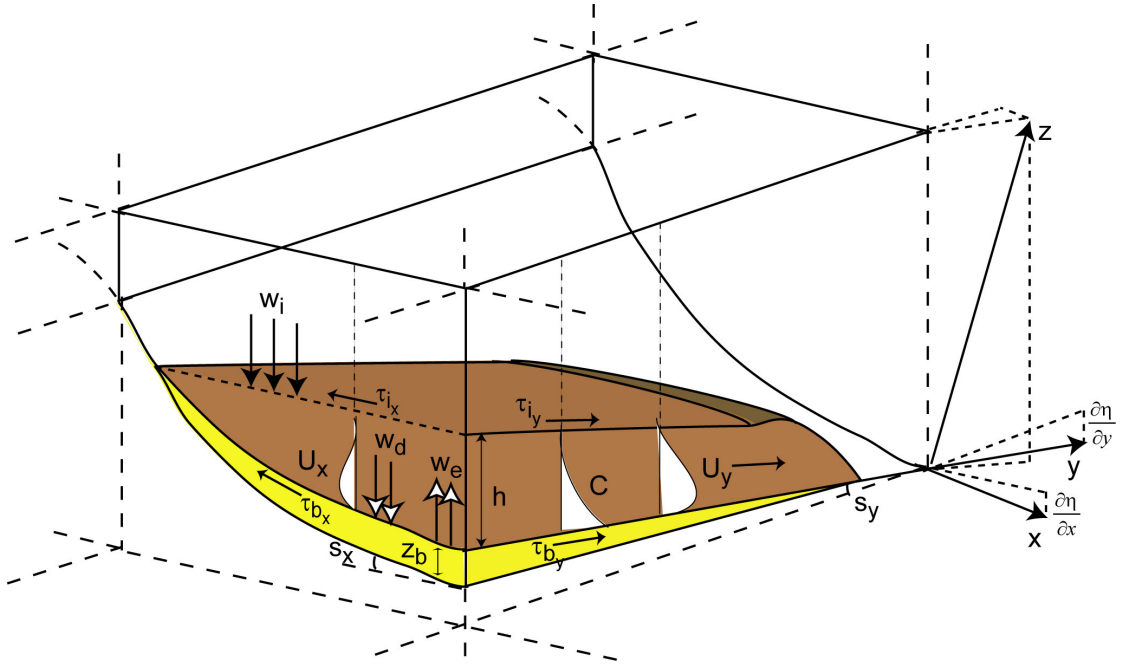


Figure 3.1: Model configuration sketch, showing the frontal part of a turbidity current (brown) flowing over a sloping surface (basin-floor topography), covered with unconsolidated sediment (yellow). See main text or appendix for list of parameters.

The turbidity current, with thickness h , volumetric suspended sediment concentration c , and streamwise and transverse velocities u_x , u_y respectively, is assumed to be sufficiently dilute to justify the use of the Boussinesq (1877) approximation, in which variations in density ρ_f only contribute significantly to the buoyancy term. This assumption is valid for flows with concentrations of suspended sediment that do not exceed 5% by volume. Higher densities notably affect internal wave speeds, flow stability and bed morphology (Sloff, 1993a, 1993b). The value for kinematic viscosity ν is taken equal to that of clear water. The instantaneous velocity of the sediment phase is taken equal to the sum of the (horizontal) fluid velocity and the sediment fall velocity in quiescent water. Concentrations are assumed to be low enough for hindered settling not to occur.

The turbidity current is assumed to be fully turbulent ($Re > 3000$), with streamwise and transverse variations in flow variables assumed to be significantly smaller than variations in the upward-normal direction. This allows the use of the slender-flow or boundary-layer approximation, in which the pressure field throughout the flow is considered hydrostatic. A further advantage of the slender-flow approximation is that Reynolds stresses associated to turbulence in horizontal directions may be neglected compared to those in vertical directions (Parker et al., 1986). Hence, the only turbulence-related terms retained are those quantifying turbulence-induced viscous dissipation of momentum. Assuming similarity of the vertical profiles of the streamwise and transverse velocity components (u_x , u_y) and concentration (c) as they change in time or in any of the horizontal directions (no helicoidal flow), and neglecting horizontal diffusion, these primary flow variables, along with the depth h , can be layer-averaged to obtain a single value for each position in space at any given time. Although the assumption of similarity is rather severe, results from experimental work and (turbulence-included) modelling studies have shown that the similarity

assumption is valid for a wide range of conditions (Garcia, 1985; Stacey and Bowen, 1988a, 1988b; Brørs and Eidsvik, 1989; Choi and Garcia, 2002).

Changes in concentration occur through entrainment of ambient water at the top of the turbidity current, deposition of sediment from the turbidity current and erosion of sediment from the bed by the turbidity current. The rate of entrainment of ambient water (w_i in Equation 3.8) is related to the bulk Richardson number (Ri_b in Equation 3.10). Rates of deposition (w_d in Equation 3.21) and erosion of sediment (w_e in Equation 3.14) are related to the level of shear stress (τ_{bx} , τ_{by}) at the bed. Bed-load transport is not taken into account, because small-scale bed morphology changes, such as e.g. current ripples, do not significantly alter the evolution of the turbidity current at the much larger scale under consideration. Furthermore, the sediment in suspension and on the bed is assumed to be non-cohesive. This is a rather severe assumption, since, in natural sediment, small amounts of clay are sufficient to increase the resistance of sediment to erosion by current action. Therefore, some measure of bed strength was incorporated into the model to represent the effect of consolidation on the rate of erosion.

3.2.2 Governing equations

The layer-averaged equations of balance of fluid mass, sediment mass and momentum, derived by e.g. Parker et al. (1986), describe variations in the primary flow variables in the streamwise and upward-normal direction for a turbidity current of low density. Here, these equations are used in their extended form, and include transverse variations in primary flow variables, as well as support for transport of multiple grain-size classes in the flow and exchange of multiple grain-size classes with the bed. The five equations thus obtained define a two-dimensional horizontal hydrodynamic problem, and are written as:

$$\frac{\partial h}{\partial t} + \frac{\partial U_x h}{\partial x} + \frac{\partial U_y h}{\partial y} = e_w U \quad (3.1)$$

$$\frac{\partial U_x h}{\partial t} + \frac{\partial U_x^2 h}{\partial x} + U_y \frac{\partial U_x h}{\partial y} = -\frac{1}{2} Rg \frac{\partial Ch^2}{\partial x} + RgChS_x - u_{x*}^2 + \nu \frac{\partial^2 U_x}{\partial x^2} + \nu \frac{\partial^2 U_x}{\partial y^2} \quad (3.2)$$

$$\frac{\partial U_y h}{\partial t} + \frac{\partial U_y^2 h}{\partial y} + U_x \frac{\partial U_y h}{\partial x} = -\frac{1}{2} Rg \frac{\partial Ch^2}{\partial y} + RgChS_y - u_{y*}^2 + \nu \frac{\partial^2 U_y}{\partial x^2} + \nu \frac{\partial^2 U_y}{\partial y^2} \quad (3.3)$$

$$\frac{\partial C_{(i)} h}{\partial t} + \frac{\partial U_x C_{(i)} h}{\partial x} + \frac{\partial U_y C_{(i)} h}{\partial y} = w_{s(i)} (b_{(i)} e_{s(i)} - C_{b(i)}) \quad (3.4)$$

$$(1 - \phi) \frac{\partial \eta}{\partial t} = \sum_{i=1}^n w_{s(i)} (C_{b(i)} - b_{(i)} e_{s(i)}) \quad (3.5)$$

Here, h , U_x , U_y , C , and η are the primary variables of the system. The variable h represents flow thickness, U_x and U_y are the layer-averaged flow velocities in the horizontal directions, C is the layer-averaged total volumetric concentration of suspended sediment in the flow, and η denotes true vertical bed elevation. Furthermore, U represents the length of the composite flow velocity vector, which is defined as $(U_x, U_y, 0)$, and ν denotes the kinematic viscosity of the suspension, which, at low concentrations of suspended sediment, may be considered to be approximately equal to the kinematic viscosity of clear water. The layer-averaged concentration C is equal to the sum of the concentrations $C_{(i)}$ of the n individual grain-size fractions in the flow:

$$C = \sum_{i=1}^n C_{(i)} = \sum_{i=1}^n f_{(i)} C \quad (3.6)$$

Here, $f_{(i)}$ represents the fraction of suspended material in the i th size range present in the flow, i.e., the grain-size distribution. The parameter $C_{b(i)}$ represents the near-bed sediment concentration of the i th grain size. Likewise, the parameter b_i represents the fraction of material in the i th size range present in the bed (Paragraph 3.2.3.6). Parameters S_x and S_y are the bed slopes in the horizontal directions, which are assumed to be small, and ϕ is the porosity of the sediment upon deposition.

The parameter R denotes the submerged specific gravity of the sediment, which, together with C and g , can be used to calculate the submerged specific gravity of the suspension:

$$R = \frac{\rho_s}{\rho_w} - 1 \quad RCg = \left[\frac{\rho_f - \rho_w}{\rho_w} \right] g = g' \quad (3.7)$$

where ρ_s represents the density of the sediment, usually taken as 2650 kg/m^3 , ρ_w represents the density of the ambient fluid, and ρ_f denotes the density of the suspension.

The system of equations (3.1) to (3.5) constitutes a system of quasi-linear hyperbolic partial-differential equations when the kinematic viscosity ν is zero (second-order terms effectively vanish). Here, the value of ν is very small ($\approx 1.0e^{-6}$), such that the system is only slightly parabolic in some regions. Nonetheless, in general, the system conserves its hyperbolic nature, even with such small non-zero values of ν , so that it admits weak solutions, such as shock waves with height discontinuities characteristic of turbidity currents (Garcia and Kahawita, 1986). In numerical models this kinematic viscosity parameter is often taken as measure of the dissipation of momentum due to turbulent eddies. As such, it is used as a tuning parameter to enhance the numerical stability.

3.2.3 Closure relations

Assumptions for the shear velocities u_{x*} , u_{y*} , water entrainment coefficient e_w , near-bed concentration ratio r_0 , and sediment entrainment coefficient e_s are required to close the set of equations stated above. Transport of suspended sediment by the turbidity current is described with the convection-diffusion model, which follows from the conservation of mass for a unit volume (Sloff, 1994a, van Rijn, 1987). In

partial-differential form, and with appropriate values for diffusion coefficients, flow velocities and boundary conditions, this model can be solved to obtain the average density at each point in the turbidity current. In practice, this fully three-dimensional model is often simplified by means of layer-averaging, whereby the adjustment of vertical profiles of concentration is replaced by a sediment entrainment function, which governs the exchange of suspended sediment between the turbidity current and the bed. In this empirical or semi-empirical function, the near-bed sediment concentration C_b is a key parameter (Paragraph 3.2.3.3).

3.2.3.1 Shear velocity

The shear velocities u_{x*} , u_{y*} are a measure of the shear stress exerted on the bed by the flow. In the absence of bedforms, the shear velocity is assumed to be proportional to the square of the layer-averaged velocity of the flow:

$$u_{x*}^2 = c_D U_x U \quad u_{y*}^2 = c_D U_y U \quad (3.8)$$

Here, c_D is a dimensionless drag coefficient. The drag coefficient parameterizes the intensity of the turbulence in the flow, which is generated due to the combined effect of skin friction (friction between a fluid and a solid) and form drag (friction due to bed forms) at the interface of the flow with the bed. In reality, its value is variable and difficult to determine exactly. Its value may be considered to be a function of, amongst others, the ratio of bedform height (height of the boundary layer) to flow depth. A higher ratio implies that the boundary layer occupies a larger part of the total flow depth; hence the amount of drag exerted by the flow on the bed is larger, and values of c_D are higher. In the model its value is taken to be constant and given a value between 0.002 and 0.06 (Parker et al., 1986), depending on the spatial scale of the simulation. Higher values of c_D must be imposed for small-scale simulations because of the smaller flow depths involved.

3.2.3.2 Ambient-water entrainment

The rate of entrainment of ambient water at the interface between the turbidity current and the body of water through which it flows is associated with buoyancy-induced instabilities (e.g. Kelvin-Helmholtz instabilities) that occur when the thicker head of the turbidity current is swept back over the thinner body of the current:

$$w_i = e_w U \quad (3.10)$$

Here, the parameter w_i represents the rate of ambient-water entrainment at the density interface, and the parameter e_w is a dimensionless water entrainment coefficient. Parker et al. (1987) derived an empirical relation for the water entrainment rate from experimental data of turbidity currents and conservative saline currents:

$$e_w = \frac{0.075}{(1 + 718 Ri_b^{2.4})^{0.5}} \quad (3.11)$$

where Ri_b is the bulk Richardson number, which is a measure of stratification in the flow, and related to the square of the densimetric Froude number:

$$Ri_b = \frac{RgCh}{U^2} = \frac{g'h}{U^2} = \frac{1}{Fr_d^2} \quad (3.12)$$

Values of Ri_b close to zero indicate highly unstratified, supercritical flow with a maximum entrainment rate of 0.075, whereas high values of Ri_b occur for subcritical flows with stable stratification in which entrainment of water is small.

3.2.3.3 Near-bed sediment concentration

The near-bed sediment concentration ratio r_0 is a shape factor that relates the near-bed sediment concentration C_b to the layer-averaged concentration of suspended sediment in the flow:

$$C_{b(i)} = r_{0(i)} C_{(i)} \quad (3.13)$$

Garcia (1994) derives an expression for r_0 from experimental data on turbidity currents laden with poorly sorted sediment:

$$r_{0(i)} = 0.40 \left(\frac{D_{s(i)}}{D_{sg}} \right)^{1.64} + 1.64 \quad (3.14)$$

where $D_{s(i)}$ denotes grain size and D_{sg} denotes the geometric mean size of the sediment mixture, given by:

$$\ln(D_{sg}) = \frac{\sum C_{(i)} \ln(D_{s(i)})}{\sum C_{(i)}} \quad (3.15)$$

3.2.3.4 Erosion

The rate of erosion of sediment from the bed by the turbidity current is parameterized as follows:

$$E = \sum_{i=1}^{i=n} w_{e(i)} = \sum_{i=1}^{i=n} e_{s(i)} w_{s(i)} \quad (3.16)$$

Here, E represents the total rate of erosion of sediment, $w_{e(i)}$ represents the rate of erosion of sediment of the i th size fraction, and $e_{s(i)}$ denotes a dimensionless erosion coefficient. As can be seen, the rate of erosion of grains of a given size is assumed to be related to the fall velocity $w_{s(i)}$, which in turn can be seen as a measure of the near-bed turbulence intensity needed to suspend a grain. The semi-empirical formulation for sediment mixtures (Garcia and Parker, 1991, 1993), which was derived from laboratory data and tested with field data for small rivers, relates the dimensionless

erosion coefficient $e_{s(i)}$ of sediment of a given grain size $D_{s(i)}$ to the ratio $\mu_{(i)}$ of shear velocity to settling velocity:

$$e_{s(i)} = \frac{A(\zeta Z_{(i)})^5}{1 + \frac{A}{0.3}(\zeta Z_{(i)})^5} \quad (3.17a)$$

where $A=1.3 \cdot 10^{-7}$. The parameter ζ is a straining parameter, defined as:

$$\zeta = 1 - 0.288\sigma_\phi \quad (3.18)$$

It represents a possible hiding effect, according to which the presence of grains of different sizes alters the mobility of a grain of a given size. It is assumed to be dependent on the standard deviation σ (on a phi-scale) of the sediment mixture on the bed, which characterizes the non-uniformity of the sediment (Garcia and Parker, 1991).

The parameter $Z_{(i)}$ is defined as:

$$Z_{(i)} = \alpha_1 \frac{u_*}{w_{s(i)}} R_{p(i)}^{\alpha_2} \left(\frac{D_{s(i)}}{D_{s50}} \right)^{0.2} \quad R_{p(i)} = \frac{(RgD_{s(i)})^{0.5} D_{s(i)}}{\nu} \quad (3.19a)$$

Here, $R_{p(i)}$ represents the Reynolds particle number. It is a measure of the flow regime (laminar vs. turbulent) surrounding a particle and, consequently, the associated amount of drag exerted by the flow on the particle. Assuming a value of 1.65 for the submerged specific gravity R of the sediment, and a value of $1.0e^{-6}$ for the kinematic viscosity ν of water, a value of $R_{p(i)}$ of 2.36 corresponds to a grain size of 0.07 mm (3.8 on the phi-scale).

The parameter u_* represents the shear velocity due to skin friction, i.e., in the absence of bedforms, and $w_{s(i)}$ denotes the particle fall velocity according to Dietrich (1982). Furthermore, the parameter D_{50} denotes the median grain size of the mixture, and the constants α_1 and α_2 are given by:

$$(\alpha_1, \alpha_2) = \begin{cases} (0.586, 1.23), & R_{p(i)} \leq 2.36 \\ (1.0, 0.6), & R_{p(i)} > 2.36 \end{cases}$$

Values of α_1 and α_2 are based on observations of eroding density currents made by Garcia and Parker (1993), which showed that a dependency on the Reynolds particle number must be included to limit over-suspension of fine-grained material.

Recently, Wright and Parker (2004b) published a modified version of the erosion relation that includes a bed slope dependency, which became evident when applying the relations to data from large, low-gradient rivers. The modified expressions for erosion rate $e_{s(i)}$ and parameter $Z_{(i)}$ become:

$$e_{s(i)} = p_{bc} \frac{B(\zeta Z_{(i)})^5}{1 + \frac{B}{0.3} (\zeta Z_{(i)})^5} \quad (3.17b)$$

$$Z_{(i)} = \alpha_1 \frac{u_*}{w_{s(i)}} R_{p(i)} \alpha_2 S_f^{0.08} \left(\frac{D_{s(i)}}{D_{s50}} \right)^{0.2} \quad (3.19b)$$

Here, $B=7.8 \cdot 10^{-7}$ and S_f denotes a friction slope which, in the context of turbidity currents, takes the following form (Kostic and Parker, in press):

$$S_f = \frac{c_D}{Ri_b} \quad (3.20)$$

The parameter p_{bc} represents a measure of bed strength, associated with consolidation (Kostic and Parker, 2006). It takes values between zero for non-erodible material, and unity for easily erodible unconsolidated material. Equations 3.17a and 3.19a will be used for simulations on experimental scale, whereas equations 3.17b and 3.19b will be used for field-scale studies.

3.2.3.5 Deposition

The rate of deposition of sediment from the turbidity current is parameterized as follows:

$$D = \sum_{i=1}^{i=n} w_{d(i)} = \sum_{i=1}^{i=n} C_{b(i)} w_{s(i)} \quad (3.21)$$

Here, D represents the total rate of deposition of sediment, and $w_{d(i)}$ represents the rate of deposition of sediment of the i th size fraction. Similar to the parameterization of the rate of erosion of sediment, the rate of deposition of sediment is assumed to be related to the fall velocity $w_{s(i)}$ of sediment of a given size.

3.2.3.6 Bed change

Equation 3.22 describes exchange of suspended sediment between the turbidity current and the bed. In the absence of bed load transport, it takes the following form:

$$(1 - \varphi) \frac{\partial \eta}{\partial t} = \sum_{i=1}^n w_{s(i)} (C_{b(i)} - b_{(i)} e_{s(i)}) \quad (3.22)$$

Here, η is bed elevation, φ represents the initial porosity of the bed sediment, and n denotes the number of grain size fractions in the sediment mixture. The parameter $b_{(i)}$ represents the fraction of material in the i th size range present in the bed:

$$\eta_b = \sum_{i=1}^n \eta_{b(i)} = \sum_{i=1}^n b_{(i)} \eta_b \quad (3.23)$$

where η_b represents total bed thickness. The value of $b_{(i)}$ is also subjected to change in time, as entrainment by and deposition from the passing turbidity current change the composition of the bed. The change in $b_{(i)}$ can be expressed as follows:

$$(1 - \varphi)\eta_b \frac{\partial b_{(i)}}{\partial t} = w_{s(i)}(r_{0(i)}C_{(i)} - b_{(i)}e_{s(i)}) - b_{(i)} \frac{\partial \eta_b}{\partial t} \quad (3.24)$$

3.3 Head region

As a turbidity current advances over the sediment bed, its hydrodynamic anatomy is characterised by a raised head section, which precedes the main body of the flow, and a dilute tail section that trails the body of the flow (Chapter 2, Figures 2.9 and 2.10). The motion of the head plays an important role in the hydrodynamic evolution of a turbidity current. Proper parameterization of the processes active in this head region and their role in the local energy balance at the head is imperative in ensuring accurate run-out length of a turbidity current and, consequently, a realistic geometry of the deposit it produces.

In general, there are two approaches to modelling the complex behaviour of turbidity-current fronts (Sloff, 1997). One approach is to use the relations derived by Benjamin (1968) from observations on head motion of turbidity currents that have reached a steady-state, which are quite common in nature. However, models based on Benjamin's work were all designed to eliminate discrepancies between observed and predicted front velocities, are all empirical and therefore require calibration and verification. Furthermore, application of the results of these theories in 2-DH numerical models requires complex techniques (shock-fitting, moving boundaries) that are not practical for the purpose of long-term stratigraphic modelling.

An alternative approach, adopted by Sloff (1997) in a 2-DV model of turbid underflows in shallow reservoirs, is to treat the head of the turbidity current as a discontinuous solution to the shallow-water equations evolving from a state of rest. In this approach, the head is considered to be a wave that attained maximum steepness to a point where it is essentially a shock wave. By doing this, the turbidity current can be regarded as a dam-break wave of dense fluid collapsing into an ambient fluid, in which the front depth and velocity downstream of the head are assumed to be very small. The advantage of this approach is that only one algorithm is required to compute both internal bores and fronts. Furthermore, it allows the use of efficient numerical shock-capturing techniques that are well-established in dam-break modelling. Therefore, taking into account the requirement for the model to be efficient when used in long-term stratigraphic modelling studies, the approach by Sloff (1997) was chosen for modelling the head of a turbidity current.

The basic equations (see Equations 3.1 to 3.5) that govern the motion of a turbidity current are conservative with respect to mass, momentum energy and entropy for the continuous part of the turbidity current. However, kinetic energy is lost at the head and in hydraulic jumps in the form of turbulent motion, a process which is irreversible. Therefore, locally, at jumps (head, internal bores, hydraulic jumps) the assumptions are that only mass and momentum are conserved, and that the amount of

energy lost is exactly the amount needed to satisfy the laws of conservation of mass and momentum (Sloff, 1997). Since at discontinuities the basic equations do not hold, shock relations are derived to serve as internal boundary conditions for the system of equations to ensure that mass and momentum are conserved at jumps. Here, these relations are formulated and numerically implemented (Chapter 4) along the lines of the *Rankine-Hugoniot jump condition*, which has to be satisfied for the relations to be conservative in terms of mass and momentum. A small balance region in the direct vicinity of the head is defined, and, under the assumption that the source terms (friction forces, entrainment, horizontal gravity forces and residual pressure forces) may be averaged over the jump, in 1-D, the system of equations reduces to:

$$\frac{\partial \mathbf{u}}{\partial t} + \frac{\partial \mathbf{f}(\mathbf{u})}{\partial x} = 0 \quad (1.24)$$

where \mathbf{u} is the vector of conservative variables and \mathbf{f} constitutes the mass and momentum flux vector. In the limit, i.e., when the length of the balance region is taken to be a single point, integration and subtraction gives:

$$c_{front} (\mathbf{u}_{left} - \mathbf{u}_{right}) = \mathbf{f}_{left} - \mathbf{f}_{right} \quad (1.25)$$

where \mathbf{u}_{left} and \mathbf{u}_{right} are the solutions (in terms of conservative variables) left and right of the jump, \mathbf{f}_l and \mathbf{f}_r are the mass and momentum fluxes left and right of the jump, and c_{front} is the propagation speed of the head. An important requirement for a shock to be physically admissible is that it has positive celerities (internal wave speeds) left and right of the shock going into it, which is expressed in the entropy condition (Lax, 1957, Courant and Hilbert, 1962, Le Veque, 1990):

$$\phi_{(1),left} \geq c_{front} \geq \phi_{(1),right} \quad (1.26)$$

where $\phi_{(1)}$ denotes the positive internal wave speed (characteristic celerity) of the continuous flow left and right of the shock respectively. This entropy condition is revisited in the section on numerical formulation.

The 1-D formulation above was extended to 2-DH radial flow (e.g. Sloff, 1997; Bradford et al., 1997) by considering that only quantities normal to the front are discontinuous, while in the tangential direction all quantities remain continuous. By means of a coordinate transformation of the basic equations to s, n coordinates tangential and normal to the front respectively, the 2-DH system reduces to a 1-D system with a single front celerity normal to the front in the n -direction. However, the need for this more complex formulation in (s, n) coordinates was circumvented by means of a numerical operator splitting technique, whereby the differential operators in the basic equations are split according to their directionality in a Cartesian coordinates (Chapter 4).

3.4 Analytical solutions

The mathematical model formulated describes low-density turbidity-current hydrodynamics and sedimentation based on, amongst others, the Boussinesq and shallow-water approximations, and incorporates a means of dealing with the complex processes and associated energy losses that occur in the head. Although the full two-dimensional model (i.e., including the source terms that parameterize bed friction, ambient-water entrainment and exchange of sediment with the bed) is too complicated to be solved analytically, an analytical solution can be derived by considering the one-dimensional version of the system of equations, i.e., without transverse flow. Moreover, by assuming conservative density flow without bed friction, ambient-water entrainment and exchange with the bed, a one-dimensional self-similar solution can be derived. In a self-similar solution, the distributions of flow variables remain similar to themselves with time, hence they only change as a result of changes in scale. Consequently, the flow can be described with only one independent variable, and the system of partial-differential equations changes into a system of ordinary differential equations, which simplifies it considerably. Analytical and self-similar solutions allow us to explore the behaviour of the model, thereby gaining insight into the sensitivity of the model to initial conditions and other variables that may govern the behaviour of the solution. Furthermore, they may serve as a truth-case in assessing the accuracy of numerically obtained results in the absence of appropriate data.

Parker et al. (1986) derived an analytical solution of their one-dimensional model of turbidity-current hydrodynamics and sedimentation, by assuming steady flow developing in the streamwise direction. This simplified model, which consists of three ordinary differential equations, was used to explore the mechanism of self-acceleration (ignition) which is thought to play an important role in the transformation from small turbid underflows to true turbidity currents. It was found that, if initial values of velocity U_y and sediment transport rate $U_y Ch$ are sufficiently large, the turbid underflow strongly self-accelerates (Parker et al., 1986). In this process of self-acceleration, at some point, the amount of suspended sediment is such that the energy expended in keeping it suspended far exceeds the level of turbulent-kinetic energy in the flow. As such, sustained self-acceleration of small, principally low-density, turbid underflows in the three-equation model leads to physically impossible flows. Since our two-dimensional mathematical model is essentially an extension of the one-dimensional three-equation model of Parker et al. (1986), the mechanism of self-acceleration due to sustained entrainment of sediment must be taken into account in studies where (strongly) erosive currents are modelled (Chapter 7, Paragraph 7.2).

Bradford et al. (1997) used the method of characteristics to transform the one-dimensional three-equation model of Parker et al. (1986) to a system of ordinary differential equations to which they obtained solutions by means of integration. Their aim was to derive analytical solutions to be potentially used in verifying numerical models, and to gain further insight into the behaviour of the equations. For the one-dimensional model, simplified analytical solutions were derived by excluding bed friction, ambient-water entrainment and exchange of sediment with the bed. A comparison of the analytical solution to a numerically computed one showed that the propagation of a discontinuity in an approximate numerical solution is sensitive to the state of the solution downstream of it, defined by the initial conditions. To obtain the correct propagation speed of the front, a zero depth must be specified downstream of

the head of the turbidity current, and the ambient-water entrainment term must be included in the solution at the front. Numerical computations incorporating ambient-water entrainment and bed friction showed that entrainment has a profound effect on the speed and shape of the front. It significantly decreases the flow velocity at the front, which may have a profound effect on the flow's competence to entrain sediment. The influence of bed friction was much smaller (Bradford et al., 1997).

A characteristic decomposition was also attempted by Bradford et al. (1997) to obtain analytical solutions for a two-dimensional model of turbidity-current hydrodynamics and sedimentation similar to the one presented in this thesis. However, no analytical solutions were found, since the two-dimensional system of equations cannot be transformed into ordinary differential equations. Hence, they can not be integrated exactly. Nonetheless, by solving the two-dimensional system of equations numerically using a high-resolution finite-volume method, Bradford et al. (1997) illustrate the same sensitivity of the behaviour of the front to initial underflow thickness and ambient-water entrainment as in the one-dimensional version.

4 NUMERICAL IMPLEMENTATION

4.1 Introduction

In this chapter, a generic process-based numerical model is proposed, which is capable of simulating turbidity-current flow and sedimentation over varying topography in three dimensions. It combines theoretical formulations on density flow (Parker et al., 1986) and sediment transport (Garcia and Parker, 1991, 1993; Wright and Parker, 2004a, 2004b) and numerical techniques (MacCormack, 1969; Garcia and Kawahita, 1986; Sloff, 1997; Wang et al., 2000) in a simulation model with the purpose to serve as a tool for qualifying and, where possible, quantifying the impact of forcing parameters (flow density, grain size and sorting of the suspended sediment, slope) on the stratigraphic evolution of turbidite fans. The objective of this chapter is to provide insight into the numerical implementation of the model. Validation of the model to a wide range of experimental conditions (e.g. variations in flow density, variations in grain size and sorting of the suspended sediment, flow around obstacles, and multiple successive flows) will be discussed in Chapter 5 and Chapter 6 of this thesis.

4.2 Conservative vs. non-conservative form

The governing equations for two-dimensional turbidity-current hydrodynamics and sedimentation, driven by a non-uniform sediment mixture, have been stated in Chapter 3, but will be reproduced here for reference:

$$\frac{\partial h}{\partial t} + \frac{\partial U_x h}{\partial x} + \frac{\partial U_y h}{\partial y} = e_w U \quad (4.1)$$

$$\frac{\partial U_x h}{\partial t} + \frac{\partial U_x^2 h}{\partial x} + U_y \frac{\partial U_x h}{\partial y} = -\frac{1}{2} Rg \frac{\partial Ch^2}{\partial x} + RgChS_x - u_{x*}^2 + \nu \frac{\partial^2 U_x}{\partial x^2} + \nu \frac{\partial^2 U_x}{\partial y^2} \quad (4.2)$$

$$\frac{\partial U_y h}{\partial t} + \frac{\partial U_y^2 h}{\partial y} + U_x \frac{\partial U_y h}{\partial x} = -\frac{1}{2} Rg \frac{\partial Ch^2}{\partial y} + RgChS_y - u_{y*}^2 + \nu \frac{\partial^2 U_y}{\partial x^2} + \nu \frac{\partial^2 U_y}{\partial y^2} \quad (4.3)$$

$$\frac{\partial C_{(i)} h}{\partial t} + \frac{\partial U_x C_{(i)} h}{\partial x} + \frac{\partial U_y C_{(i)} h}{\partial y} = w_{s(i)} (b_{(i)} e_{s(i)} - C_{b(i)}) \quad (4.4)$$

$$(1 - \phi) \frac{\partial \eta}{\partial t} = \sum_{i=1}^n w_{s(i)} (C_{b(i)} - b_{(i)} e_{s(i)}) \quad (4.5)$$

Equations 4.1, 4.2 and 4.3 describe the conservation of mass and momentum of the fluid. Equation 4.4 describes conservation of suspended sediment, with $i=1, n$. In the case of non-uniform sediment mixtures ($n>1$), an equation is needed for each separate grain-size fraction the flow. Hence, the system of equations that govern conservation

of mass and momentum of the turbidity current actually consists of $3+n$ equations, where n represents the number of grain-size fractions in the sediment mixture. The $3+n$ equations constitute a system of coupled, first-order, quasi-linear and non-homogeneous partial-differential equations (PDE). The PDEs contain time derivatives representing the change in primary flow variables in time at locations in the flow, space derivatives representing advection of mass (fluid, suspended sediment) and momentum (energy), and source terms representing loss or gain of momentum (gravity, friction), fluid mass (ambient water entrainment) and sediment mass (erosion, deposition).

Equations 4.1, 4.2, 4.3 and 4.4 may be rewritten in flux vector form (Hirsch, 1990) as:

$$\frac{\partial \mathbf{u}}{\partial t} + \frac{\partial \mathbf{f}(\mathbf{u})}{\partial x} + \frac{\partial \mathbf{g}(\mathbf{u})}{\partial y} = \mathbf{q}(\mathbf{u}) \quad (4.6)$$

where $\mathbf{u}(h, U_x h, U_y h, C_1 h, \dots, C_n h)$ is the vector of conservative variables, $\mathbf{f}(\mathbf{u})$ and $\mathbf{g}(\mathbf{u})$ are the flux vectors in x- and y-direction respectively, and $\mathbf{q}(\mathbf{u})$ is the vector containing the source terms:

$$\mathbf{f} = \begin{pmatrix} U_x h \\ U_x^2 h + \frac{1}{2} RCgh^2 \\ U_x U_y h \\ U_x C_1 h \dots \\ \dots U_x C_n h \end{pmatrix} \quad \mathbf{g} = \begin{pmatrix} U_y h \\ U_y U_x h \\ U_y^2 h + \frac{1}{2} RCgh^2 \\ U_y C_1 h \dots \\ \dots U_y C_n h \end{pmatrix} \quad \mathbf{q} = \begin{pmatrix} e_w U \\ -RCghS_x - c_D U U_x \\ -RCghS_y - c_D U U_y \\ w_{s(1)}(b_1 e_{s(1)} - r_{0(1)} C_1) \dots \\ \dots w_{s(n)}(b_n e_{s(n)} - r_{0(n)} C_n) \end{pmatrix} \quad (4.7)$$

In this form, the system of equations is conservative in terms of mass and momentum. Alternatively, a non-conservative form of the system of equations can be formulated, in which the vector of primitive variables \mathbf{v} is defined as $\mathbf{v}(h, U_x, U_y, C_1, \dots, C_n)$. In this non-conservative form, the mass and momentum conservation equations are combined to obtain a system which is conservative in terms of mass and velocity. Both systems give identical solutions in continuous flows, but differences arise in the solution of discontinuities. From a physical point of view, the only meaningful weak solutions are those that follow from the system of equations in conservative form (e.g. Abbot, 1979). However, in the computation of gravity-current fronts, the conservative form does not perform well because it gives a poor representation of a real front. The difference is due to the different forms of the momentum equations, which, in non-conservative form, give a much better (sharper) representation of discontinuities. This effect is also known in dam-break models (e.g. Stoker, 1957). By comparing computed and measured frontal velocities for both conservative and non-conservative numerical solutions, Sloff (1997) concluded that the latter gives a markedly better representation of a gravity-current front.

The superiority of the non-conservative form is further illustrated in Figure 4.1, which displays the evolution of flow thickness in time for a conservative gravity current (no entrainment and no exchange of sediment with the bed). In the version based on the non-conservative form, the front is limited to a region spanning only a few grid cells,

and may be considered discontinuous, whereas in the version adopting the conservative form, the front of the gravity current is considerably smeared over a much larger number of grid cells. Therefore, our numerical implementation is based on the system of equations in non-conservative form, i.e., with the momentum equations in non-conservative form. The mass balance equations are in conservative form to ensure that they are congruent in discretized form.

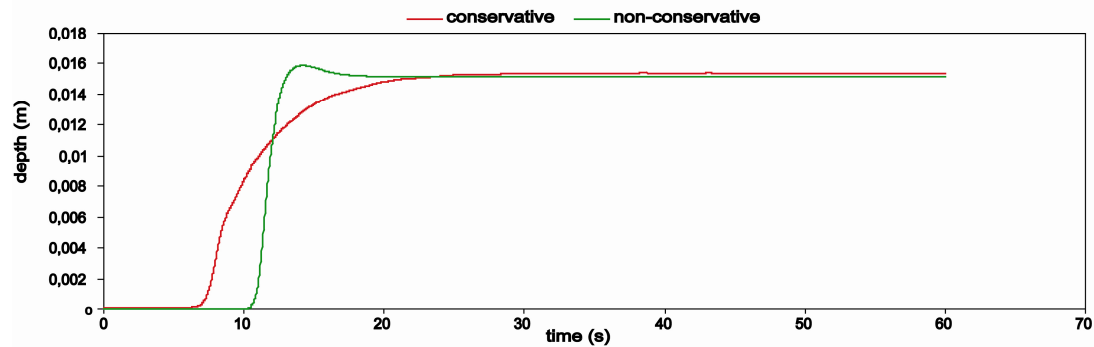


Figure 4.1: Evolution of flow thickness in time for a simulated experimental conservative gravity current. Red line is flow depth computed using a conservative formulation, whereas the green line represents the flow depth computed using a non-conservative formulation.

4.3 Solution method

4.3.1 Requirements and conditions

The complexity of the mathematical model requires that a solution is found by means of integration in time and space with an appropriate numerical discretization technique. A wealth of numerical techniques is available in the field of Computational Fluid Dynamics (CFD) and, more specifically, in the field of computing discontinuous shallow flow, to which type of flow turbidity currents can be assumed to belong. A short list of numerical techniques applicable to modelling of discontinuous shallow flow has already been reviewed in Chapter 2 (Paragraph 2.6.5) of this thesis, to which the reader is referred to for background information.

The selection of a numerical scheme for discretizing and solving the model is dependent on the conditions needed by the model in order to be considered a practical tool for investigating the stratigraphic evolution of turbidite fans. Stratigraphic modelling is often done at time scales of thousands to tens of thousands of years, during which hundreds of individual turbidity currents may occur. This requires very high computational efficiency, a condition often in direct conflict with the level of detail (accuracy) of the model. Moreover, the inherent uncertainty in the estimation of the initial and boundary conditions in reconstructing field-scale flows responsible for observed stratal patterns must be taken into account in the trade-off between the desired level of detail and computational efficiency. A second-order numerical scheme has been chosen to ensure a reasonable level of detail in simulating continuous flow regions. Furthermore, the numerical scheme must facilitate the use of a shock-capturing technique, which implies that the scheme conserves mass and momentum across the shock.

A related choice to be made is to use either an explicit or an implicit method for solving for the $3+n$ flow variables. The advantage of an implicit method is that it is unconditionally stable, whereas the stability of an explicit method is conditional, and depends on the velocity of flow, the length of the time step and the grid-cell size. Stability requires that the Courant Number (udt/dx) is less than or equal to unity. A time step and grid-cell size can be chosen which, in combination with an estimate of flow velocity, ensure that the Courant Number does not exceed unity. Moreover, unconditional stability is at odds with the requirement of computational efficiency, and, in some cases, accuracy. Implicit methods require iteration to converge to a stable solution, and, in cases where no solution is apparent, produce a distorted solution that is inaccurate. Therefore, an explicit method is preferred over an implicit one.

Other conditions for the numerical scheme include robustness, and the possibility to easily incorporate a shock-capturing technique. Here, preference lies with schemes that have proven strong in computing both slowly varying as well as rapidly varying shallow flows that contain shocks and discontinuities.

4.3.2 MacCormack scheme

The finite-difference scheme adopted here is the MacCormack (1969) scheme, originally derived from the basic Lax-Wendroff (1960, 1964) scheme. The MacCormack scheme is a simple and robust explicit scheme of second-order accuracy in time and space, which satisfies the requirements stated in the previous paragraph. Originally designed for use in studies on compressible gases, it was successfully applied in the computation of dam-break problems in open-channel flows, and open-channel flows containing hydraulic jumps and bores (Garcia-Navarro et al., 1992; Yang et al., 1993a, 1993b; Wang et al., 2000).

The MacCormack scheme is a two-step ‘predictor-corrector’ scheme. Its simple and straightforward treatment of non-linear fluxes sets it apart from other schemes in the Lax-Wendroff family of schemes. However, in the linear case, to which the presented mathematical model can be reduced (Appendix A.3.2), it becomes identical to other Lax-Wendroff schemes, which allows for the use of results from linear numerical analysis of the Lax-Wendroff scheme with respect to stability and accuracy (Sloff, 1997). The ‘predictor’ step in the scheme is a first-order forward discretization in space, which is unstable for positive celerities (propagation speed of internal waves), whereas the ‘corrector’ step is unstable for negative celerities. However, the overall combined scheme is stable and of second order due to cancellation of truncation errors in each step (Hirsch, 1990).

The two-dimensional five-point form of the MacCormack scheme for a quasi-linear system with source term \mathbf{q} and artificial viscosity terms \mathbf{d}_x , \mathbf{d}_y is as follows:

$$\mathbf{v}_{(i,j)}^P = \mathbf{v}_{(i,j)}^t - \frac{\Delta t}{\Delta x} \left[\Delta_x \mathbf{f}_{(i,j)}^t \right] - \frac{\Delta t}{\Delta y} \left[\Delta_y \mathbf{g}_{(i,j)}^t \right] + \Delta t \mathbf{q}_{(i,j)}^t + \frac{\Delta t}{\Delta x} \mathbf{d}_{x(i,j)}^t + \frac{\Delta t}{\Delta y} \mathbf{d}_{y(i,j)}^t \quad (4.8a)$$

$$\mathbf{v}_{(i,j)}^C = \mathbf{v}_{(i,j)}^t - \frac{\Delta t}{\Delta x} \left[\nabla_x \mathbf{f}_{(i,j)}^P \right] - \frac{\Delta t}{\Delta y} \left[\nabla_y \mathbf{g}_{(i,j)}^P \right] + \Delta t \mathbf{q}_{(i,j)}^P + \frac{\Delta t}{\Delta x} \mathbf{d}_{x(i,j)}^P + \frac{\Delta t}{\Delta y} \mathbf{d}_{y(i,j)}^P \quad (4.8b)$$

where $\mathbf{v}_{(i,j)}$ denotes the vector of primitive variables at grid point $(i\Delta x, j\Delta y)$, \mathbf{f} and \mathbf{g} are the discretized flux vectors applied to local values of \mathbf{v} , \mathbf{q} is the vector of source terms containing e.g. friction and entrainment terms, and vectors $\mathbf{d}_x, \mathbf{d}_y$ are artificial viscosity terms, to be added to prevent the occurrence of spurious oscillations near discontinuities (Paragraph 4.3.4 and 4.3.5). The operators Δ_x, Δ_y and ∇_x, ∇_y are the first-order forward and backward difference operators respectively, defined as:

$$\Delta_x \mathbf{f}_{(i,j)}^t = \mathbf{f}(\mathbf{v}_{(i+1,j)}^t) - \mathbf{f}(\mathbf{v}_{(i,j)}^t); \quad \Delta_y \mathbf{g}_{(i,j)}^t = \mathbf{g}(\mathbf{v}_{(i,j+1)}^t) - \mathbf{g}(\mathbf{v}_{(i,j)}^t) \quad (4.9a)$$

$$\nabla_x \mathbf{f}_{(i,j)}^P = \mathbf{f}(\mathbf{v}_{(i,j)}^P) - \mathbf{f}(\mathbf{v}_{(i-1,j)}^P); \quad \nabla_y \mathbf{g}_{(i,j)}^P = \mathbf{g}(\mathbf{v}_{(i,j)}^P) - \mathbf{g}(\mathbf{v}_{(i,j-1)}^P) \quad (4.9b)$$

The superscripts t, P (for predictor) and C (for corrector) indicate the time level of the solution, whereby the predictor and corrector solutions are considered to be intermediate solutions which by themselves are not valid, stable solutions, but, when combined as in Equation 4.9c, constitute the solution at time level t+1:

$$\mathbf{v}_{(i,j)}^{t+1} = \frac{1}{2}(\mathbf{v}_{(i,j)}^P + \mathbf{v}_{(i,j)}^C) \quad (4.9c)$$

4.3.3 Operator splitting

To stretch the computational efficiency of the model, the operator-splitting technique by Strang (1968) was adopted, in which the two-dimensional discretized space operators are split into products of one-dimensional operators that are solved in sequence. Referring to system of equations in flux vector form (Equations 4.6 and 4.7), the two one-dimensional systems are defined as:

$$\frac{\partial \mathbf{u}}{\partial t} + \frac{\partial \mathbf{f}(\mathbf{u})}{\partial x} = \mathbf{q}_x(\mathbf{u}) \quad \frac{\partial \mathbf{u}}{\partial t} + \frac{\partial \mathbf{g}(\mathbf{u})}{\partial y} = \mathbf{q}_y(\mathbf{u}) \quad (4.10)$$

By doing this, the stability properties of the scheme are further improved, and the amount of computational work is reduced. Moreover, since the two-dimensional system is split into two one-dimensional systems along x- and y-directions, the implementation of a shock-capturing method is facilitated because there is no need to transform the basic equations into coordinates tangential and normal to the discontinuity. However, care must be taken in defining the one-dimensional operators as well as in putting them in sequence, to ensure that the overall scheme maintains second-order accuracy (Hirsch, 1990). As shown in Equations 4.8a and 4.8b the MacCormack scheme combines forward and backward differences in separate predictor and corrector steps. Four different schemes can be defined through various combinations of one-sided differences of the flux components \mathbf{f} and \mathbf{g} (Hirsch, 1990; see Equations 4.9a, b and Figure 4.2).

Garcia and Kahawita (1986) defined two sets of operators, in which backward and forward differencing is alternated, and to put them in a $2\Delta t$ sequence as follows:

$$\begin{aligned} \mathbf{u}_{(i,j)}^{t+1} &= \mathbf{OP}_{y,1} \left(\frac{\Delta t}{2} \right) \mathbf{OP}_{x,1} \left(\frac{\Delta t}{2} \right) \mathbf{u}_{(i,j)}^t \\ \mathbf{u}_{(i,j)}^{t+2} &= \mathbf{OP}_{x,2} \left(\frac{\Delta t}{2} \right) \mathbf{OP}_{y,2} \left(\frac{\Delta t}{2} \right) \mathbf{u}_{(i,j)}^{t+1} \end{aligned} \quad (4.11)$$

where operators $\mathbf{OP}_{x,1}$, $\mathbf{OP}_{y,1}$, $\mathbf{OP}_{x,2}$ and $\mathbf{OP}_{y,2}$ all contain a complete predictor-corrector sequence. Operators $\mathbf{OP}_{x,1}$ and $\mathbf{OP}_{y,1}$, are backward-differenced in the predictor step and forward-differenced in the corrector step, and operators $\mathbf{OP}_{x,2}$ and $\mathbf{OP}_{y,2}$ are forward-differenced in the predictor step and backward-differenced in the corrector step.

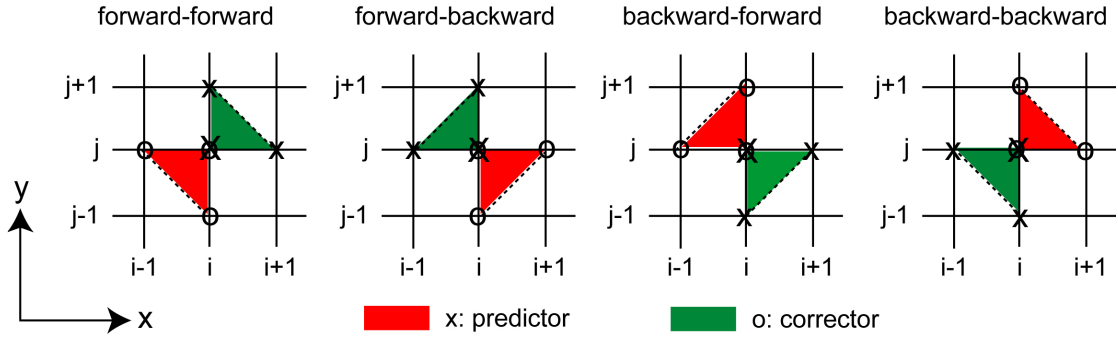


Figure 4.2: Computational molecules for the MacCormack scheme (after Hirsch, 1990)

Starting from the system of equations in non-conservative form, i.e., with the vector of primitive variables defined as $\mathbf{v}(h, U_x, U_y, C_1, \dots, C_n)$, the one-dimensional operator for x-differenced terms ($\mathbf{OP}_{x,1}$ and $\mathbf{OP}_{x,2}$) is defined as:

$$\begin{aligned} \frac{\partial h}{\partial t} + \frac{\partial U_x h}{\partial x} &= (1 - \alpha_{STD}) [e_w U] \\ \frac{\partial U_x}{\partial t} + U_x \frac{\partial U_x}{\partial x} + RgC \frac{\partial h}{\partial x} + \frac{Rgh}{2} \frac{\partial C}{\partial x} &= -RgC \frac{\partial z_b}{\partial x} - \frac{(c_D + e_w) U U_x}{h} \\ \frac{\partial U_y}{\partial t} + U_x \frac{\partial U_y}{\partial x} &= 0 \\ \frac{\partial C_{(i)}}{\partial t} + U_x \frac{\partial C_{(i)}}{\partial x} &= (1 - \alpha_{STD}) \left[\frac{w_{s(i)} (b_{(i)} e_{s(i)} - r_{0(i)} C_{(i)}) - e_w U}{h} \right] \\ \frac{\partial \eta_{b(i)}}{\partial t} &= (1 - \alpha_{STD}) \left[\frac{w_{s(i)} (C_{b(i)} - b_{(i)} e_{s(i)})}{1 - \phi} \right] \end{aligned} \quad (4.12a)$$

The one-dimensional operator for y-differenced terms ($\mathbf{OP}_{y,1}$ and $\mathbf{OP}_{y,2}$) is defined as:

$$\begin{aligned}
 \frac{\partial h}{\partial t} + \frac{\partial U_y h}{\partial y} &= \alpha_{STD} [e_w U] \\
 \frac{\partial U_x}{\partial t} + U_y \frac{\partial U_x}{\partial y} &= 0 \\
 \frac{\partial U_y}{\partial t} + U_y \frac{\partial U_y}{\partial y} + RgC \frac{\partial h}{\partial y} + \frac{Rgh}{2} \frac{\partial C}{\partial y} &= -RgC \frac{\partial z_b}{\partial y} - \frac{(c_D + e_w)UU_y}{h} \quad (4.12b) \\
 \frac{\partial C_{(i)}}{\partial t} + U_y \frac{\partial C_{(i)}}{\partial y} &= \alpha_{STD} \left[\frac{w_{s(i)} (b_{(i)} e_{s(i)} - r_{0(i)} C_{(i)}) - e_w U}{h} \right] \\
 \frac{\partial \eta_{b(i)}}{\partial t} &= \alpha_{STD} \left[\frac{w_{s(i)} (C_{b(i)} - b_{(i)} e_{s(i)})}{1 - \phi} \right]
 \end{aligned}$$

Here, the bed slopes S_x and S_y have been replaced by their equivalent derivative notation. The parameter α_{STD} is introduced to divide the source terms representing interfacial friction and sediment exchange with the bed over the one-dimensional operators. They are calculated for a complete time step Δt for each cell, based on cell-average values of the primitive variables U_x , U_y , $C_{(i)}$ and h , hence they must be manipulated to prevent them from being added twice during each x - y operator cycle. The value of the source term divider α_{STD} is taken proportional to the ratio of the averaged magnitude of the velocity components U_x and U_y , and recalculated prior to each new time step. In practice, this implies that the contribution of the source terms during a computational cycle is largest in the operator parallel to the largest component of the flow velocity vector.

A full discretization of these operators according to the MacCormack scheme can be found in Appendix A.2.

4.3.4 Empirical artificial viscosity

The MacCormack scheme generates spurious oscillations around sharp discontinuities (e.g. head of a gravity current, internal bores, hydraulic jumps). These high-frequency oscillations, generated by the truncation error of the second-order scheme and characterised by large mass-flux errors around discontinuities, cause the solution to lose its conservative nature. Hence, the accuracy of the solution is affected. To overcome this problem, these high-frequency spurious oscillations must be taken care of. One way of doing this, is by adding a diffusive term to the flux terms in the scheme, which damps the oscillations near discontinuities, whereas in continuous regions the flow is not affected. In this conventional artificial viscosity approach, first introduced by Von Neumann and Richtmeyer (1950), diffusive terms are added to the MacCormack scheme at predictor and corrector time levels (terms \mathbf{d}_x , \mathbf{d}_y in Equations 4.8a, 4.8b), which, for e.g. the predictor time level in the MacCormack scheme, are defined as:

$$\begin{aligned} \mathbf{d}_{x(i,j)}^t &= (\mathbf{d}_{x(i+\frac{1}{2},j)}^t - \mathbf{d}_{x(i-\frac{1}{2},j)}^t) = \delta_{x(i+\frac{1}{2},j)}^{v,t} (\Delta_x \mathbf{v}_{(i,j)}^t) - \delta_{x(i-\frac{1}{2},j)}^{v,t} (\nabla_x \mathbf{v}_{(i,j)}^t) \\ \mathbf{d}_{y(i,j)}^t &= (\mathbf{d}_{y(i,j+\frac{1}{2})}^t - \mathbf{d}_{y(i,j-\frac{1}{2})}^t) = \delta_{y(i,j+\frac{1}{2})}^{v,t} (\Delta_y \mathbf{v}_{(i,j)}^t) - \delta_{y(i,j-\frac{1}{2})}^{v,t} (\nabla_y \mathbf{v}_{(i,j)}^t) \end{aligned} \quad (4.13)$$

Corrector time level terms are similar in form, but use values of \mathbf{v} from the predictor time level. The parameter δ^v is a tuning parameter which determines the height of the diffusive terms and is defined as (MacCormack and Baldwin, 1975):

$$\delta_{x(i+\frac{1}{2},j)}^{v,t} = \max(\varepsilon_{EAV(i,j)}^t, \varepsilon_{EAV(i+1,j)}^t) \quad \delta_{x(i-\frac{1}{2},j)}^{v,t} (\varepsilon_{EAV(i-1,j)}^t, \varepsilon_{EAV(i,j)}^t) \quad (4.14)$$

The parameter ε_{EAV} contains a tuning parameter that implicitly determines the height of the diffusive term, and is defined as:

$$\varepsilon_{EAV(i,j)} = \alpha_{EAV} \left(\frac{|h_{(i+1,j)}^t - 2h_{(i,j)}^t + h_{(i-1,j)}^t|}{h_{(i+1,j)}^t - 2h_{(i,j)}^t + h_{(i-1,j)}^t} \right) \quad (4.15)$$

where h denotes flow height, and α_{EAV} is a non-physical tuning parameter, which has to be adjusted empirically for each individual application. This is highly impractical in modelling a sequence of flows that are slightly different in terms of initial and boundary conditions. Moreover, this empirical artificial viscosity method damps rather than eliminates oscillations (Hirsch, 1990; Sloff, 1997), which still introduces an unsatisfactory amount of inaccuracy in the solution.

4.3.5 TVD artificial viscosity

A more robust method of eliminating the spurious oscillations near discontinuities is through limitation of the (numerical) fluxes through the interfaces between cells. In second-order numerical schemes (e.g. MacCormack's scheme), the fluxes through the cell interfaces are first-order approximated to obtain the averaged values of the variables within the cells. If the slope of the fluxes in a cell exceeds the difference in mean values of the fluxes between adjacent cells, over- and undershoots (oscillations) are generated in the numerical solution. Therefore, the scheme must be controlled at each time step and within each cell, so as to keep the gradients of the fluxes within proper bounds. By doing this, the generation of oscillations is prevented, as opposed to conventional artificial viscosity methods, which damp oscillations that already exist (Hirsch, 1990). This is the added value of TVD (Total Variation Diminishing) schemes, which are named so as to reflect that the total variation of the discrete numerical solution (the sum of all the inter-cell fluxes) diminishes in time.

The TVD concept may be adapted to quasi-linear systems, such as presented in Paragraph 4.2 (see Equations 4.6, 4.7), provided a technique is applied to approximate the fluxes at the cell interfaces. To this end, the two-dimensional system must be numerically reformulated in flux-conservative form as follows:

$$\mathbf{v}_{(i,j)}^{t+1} - \mathbf{v}_{(i,j)}^t = -\frac{\Delta t}{\Delta x} (\mathbf{f}_{(i+\frac{1}{2},j)}^t - \mathbf{f}_{(i-\frac{1}{2},j)}^t) - \frac{\Delta t}{\Delta y} (\mathbf{g}_{(i,j+\frac{1}{2})}^t - \mathbf{g}_{(i,j-\frac{1}{2})}^t) + \Delta t \mathbf{q}_{(i,j)}^t \quad (4.16)$$

In this formulation, the numerical fluxes \mathbf{f} and \mathbf{g} are discretized at cell interfaces, and not, as in Equations 4.9a, 4.9b, at cell centres. Since fluxes of primitive variables \mathbf{v} are defined at cell centres, they must be averaged to obtain values of fluxes at the interfaces between cells. Considering a one-dimensional system for the sake of simplicity, the flux at a cell interface is calculated as follows:

$$\mathbf{f}_{(i+\frac{1}{2},j)}^t = \frac{1}{2}(\mathbf{f}_{(i+1,j)}^t + \mathbf{f}_{(i,j)}^t) - \frac{1}{2} \frac{\Delta t}{\Delta x} \mathbf{A}_{(i+\frac{1}{2},j)}^t (\mathbf{f}_{(i+1,j)}^t - \mathbf{f}_{(i,j)}^t) \quad (4.17a)$$

with \mathbf{A} representing the Jacobian matrix, associated with the linearization of the flux vector $\mathbf{f}(\mathbf{v})$ by:

$$\frac{\partial \mathbf{f}(\mathbf{v})}{\partial x} = \frac{\partial \mathbf{f}}{\partial \mathbf{v}} \frac{\partial \mathbf{v}}{\partial x} = \mathbf{A} \frac{\partial \mathbf{v}}{\partial x} \quad (4.18)$$

An important property of the Jacobian is that its eigenvalues constitute the positive and negative celerities of the system of equations, which represent the propagation velocity of perturbations (fluxes) in primitive variables \mathbf{v} through the computational domain. Decomposition of the fluxes (see Equation 4.17a) into positive (+) and negative (-) parts, corresponding to these positive and negative propagation velocities (celerities), results in the following modified form (4.17b) of Equation 4.17a (Sloff, 1997):

$$\mathbf{f}_{(i+\frac{1}{2},j)}^t = \underbrace{\mathbf{f}_{(i+1,j)}^{-t} + \mathbf{f}_{(i,j)}^{+t}}_{\text{upwind flux}} + \underbrace{\frac{1}{2} \left(1 - \frac{\Delta t}{\Delta x} \mathbf{A}_{(i+\frac{1}{2},j)}^{+t} \right) \Delta_x \mathbf{f}_{(i+\frac{1}{2},j)}^{+t} - \frac{1}{2} \left(1 + \frac{\Delta t}{\Delta x} \mathbf{A}_{(i+\frac{1}{2},j)}^{-t} \right) \Delta_x \mathbf{f}_{(i+\frac{1}{2},j)}^{-t}}_{\text{correction term}}$$

As can be seen, the numerical flux through a cell interface is composed of an upwind flux (first two terms on the right-hand side), which consists of the parts of the fluxes, defined at cell centres left and right of the cell interface that propagate towards the cell interface, supplemented with a correction to render the scheme second-order accurate. In TVD schemes, the gradients of the fluxes are kept within proper bounds by limiting the magnitude of this correction term with a flux limiter. By limiting the magnitude of the correction term near discontinuities, the scheme is locally reduced to first-order, thus becoming dissipative instead of dispersive.

The TVD-limited flux is defined as:

$$\mathbf{f}_{(i+\frac{1}{2},j)}^{\text{TVD},t} = \mathbf{f}_{(i+\frac{1}{2},j)}^t - \mathbf{d}_{x(i+\frac{1}{2},j)}^t \quad (4.19)$$

As can be seen, the difference between the original flux \mathbf{f} and the TVD-limited flux \mathbf{f}^{TVD} is the TVD version of the artificial viscosity term \mathbf{d}_x , and quantifies to which amount the original correction term (see equation 4.17b) is to be limited (Sloff, 1997):

$$\mathbf{d}_{x(i+\frac{1}{2},j)}^t = \frac{1}{2} \left(1 - \Psi_{(i+\frac{1}{2},j)}^+ \right) \left(1 - \frac{\Delta t}{\Delta x} \mathbf{A}_{(i+\frac{1}{2},j)}^{+t} \right) \Delta_x \mathbf{f}_{(i+\frac{1}{2},j)}^{+t} - \frac{1}{2} \left(1 - \Psi_{(i+\frac{1}{2},j)}^- \right) \left(1 + \frac{\Delta t}{\Delta x} \mathbf{A}_{(i+\frac{1}{2},j)}^{-t} \right) \Delta_x \mathbf{f}_{(i+\frac{1}{2},j)}^{-t}$$

The parameter Ψ is the limiter function, which should be close to zero around discontinuities, and unity in continuous regions. Since the TVD condition requires

that the gradients of the fluxes are to be kept within proper bounds, Ψ itself is defined as a function of ratios of consecutive variations of these fluxes:

$$\Psi_{(i+\frac{1}{2},j)}^+ = \Psi\left(\mathbf{f}_{(i+\frac{1}{2},j)}^+, \mathbf{f}_{(i+\frac{3}{2},j)}^+\right) \quad (4.21)$$

Various limiter functions (e.g. Minmod, Superbee) have been defined (see e.g. Hirsch, 1990; Le Veque, 1990), some of which have a smoothing effect on discontinuities whereas others compress them. Details on the definition of the flux ratios, and on the limiter functions used, can be found in Appendix 1.4.

As mentioned before, the TVD method can be adopted for the non-linear system of equations presented here by a local linearization technique to approximate the fluxes at cell interfaces. This can be achieved by means of applying Roe's (1981a, 1981b) characteristic decomposition of the fluxes, obtained from Roe's approximate Riemann solver (Hirsch, 1990; LeVeque, 1990). Roe's technique extends the theory of linear wave decomposition to non-linear systems, whereby any variation in fluxes $\Delta \mathbf{f}$ can be expressed as a sum of simple waves \mathbf{r}_k with amplitudes $\Delta \mathbf{w}$, multiplied by their propagation velocity (celerity ϕ):

$$\Delta \mathbf{f} = \mathbf{A} \Delta \mathbf{v} = \sum_{k=1}^{k=m} \phi_k \Delta \mathbf{w}_k \mathbf{r}_k \quad (4.22)$$

Each fraction $\Delta \mathbf{f}_k$ represents the contribution from the k^{th} wave with propagation velocity ϕ_k to the total flux variation $\Delta \mathbf{f}$ (Hirsch, 1990), which can be individually limited to control the scheme around discontinuities. Through substitution of (4.22) into (4.20), the TVD artificial viscosity term \mathbf{d}_x can be expressed as (Sloff, 1997):

$$\mathbf{d}_{x(i+\frac{1}{2},j)}^t = \frac{1}{2} \sum_{k=1}^{k=m} \left(1 - \Psi_{k,(i+\frac{1}{2},j)}^t\right) \cdot \left| \hat{\phi}_{k,(i+\frac{1}{2},j)}^t \right| \cdot \left(1 - \frac{\Delta t}{\Delta x} \hat{\phi}_{k,(i+\frac{1}{2},j)}^t\right) \cdot \left(\Delta_x \mathbf{w}_{k,(i+\frac{1}{2},j)}^t\right) \cdot \hat{\mathbf{r}}_{k,(i+\frac{1}{2},j)}^t \quad (4.23)$$

The vector of characteristic variables \mathbf{v} , the eigenvalues ϕ_k , and the right-eigenvectors \mathbf{r}_k can be found through analysis of the Jacobian \mathbf{A} . The circumflex sign (^) is used to indicate that the linearized form of the Jacobian \mathbf{A} is to be used. Details on Roe's technique, the linearization of the Jacobian matrices, and the application to the system of equations (Equations 4.6 and 4.7) presented here to describe turbidity-current hydrodynamics and sedimentation, can be found in Appendix A.3.

In the TVD version of the applied MacCormack scheme, the artificial viscosity terms \mathbf{d}_x , \mathbf{d}_y are calculated at the beginning of a time step (at time t), based on values of primitive variables \mathbf{v} at time t , and added to the original predictor-corrector solution (see Equation 4.9c):

$$\mathbf{v}_{(i,j)}^{t+1} = \frac{1}{2} \left(\mathbf{v}_{(i,j)}^P + \mathbf{v}_{(i,j)}^C \right) + \frac{\Delta t}{\Delta x} \left(\mathbf{d}_{x(i+\frac{1}{2},j)} - \mathbf{d}_{x(i-\frac{1}{2},j)} \right) + \frac{\Delta t}{\Delta y} \left(\mathbf{d}_{y(i,j+\frac{1}{2})} - \mathbf{d}_{y(i,j-\frac{1}{2})} \right) \quad (4.24)$$

This concludes the numerical formulation of the mathematical model. However, to solve the system of equations in numerical form, boundary conditions must be imposed at the edges of the computational domain.

4.3.6 Boundary conditions

Since a numerical grid is always bounded, every numerical model needs boundary conditions. The treatment of boundary conditions is an essential part of the numerical model, because eventually information from the boundaries covers the full computational domain. Hence, an incorrect treatment of the boundaries results in an inaccurate or unstable model. It has already been shown (see Equation 4.22 and Appendix A.3) that the solution to the system of equations consists of a superposition of $3+n$ waves, propagating independently and with speed ϕ_k along the $3+n$ characteristics of the system. At the boundaries, the information carried by these waves either enters or exits the computational domain, and supplementary information must be provided in the form of boundary conditions to calculate the values of the dependent variables at the boundary. In a well-posed system, the information on the incoming and outgoing waves can be recovered from the imposed conditions, leading to a bounded solution (Sloff, 1997). The imposed conditions can be physical, i.e., prescribed at the beginning of the simulation or time step, or numerical, i.e., defined from the interior flow field.

The intended use of the *FanBuilder* model in stratigraphic modelling studies requests that the region of interest is unbounded, i.e., open to outflow. Information may reach the boundaries of the computational domain in the form of small disturbances of the initial state. Such small disturbances may render the solution inaccurate or even unstable. Therefore, non-reflective open outflow boundaries will be used in the numerical model, which ensure that information can freely exit the computational domain without causing disturbances of the solution. Furthermore, inflow boundary conditions are needed at points where the turbidity current is fed into the computational domain.

In case of the system of equations presented here, $3+n$ boundary conditions have to be imposed, in accordance with the number of characteristics. As for the traditional shallow-water equations of which the model is essentially an extension, the number of physical boundary conditions to be imposed depends on the flow regime (Garcia and Kahawita, 1986; Hirsch, 1990). In case of two-dimensional horizontal subcritical suspension flow, $2+n$ physical boundary conditions must be imposed at inflow boundaries (U_x , U_y , C_i) whereas only one is needed at outflow boundaries (h). In case of 2-DH supercritical suspension flow, $3+n$ boundary conditions must be imposed at inflow boundaries (U_x , U_y , h , C_i), whereas none are needed at outflow boundaries. The remaining numerical boundary conditions are to be determined from the interior flow field (see tables in Figures 4.3 and 4.4). To impose the boundary conditions, ghost-points are defined. The ghost-points, which lie one space increment outside the computational domain, are imaginary points that contain the missing information needed to compute the values of the primitive variables $\mathbf{v}(h, U_x, U_y, C_1, \dots, C_n)$ at the points along the boundaries of the computational domain (see Figures 4.3 and 4.4).

Various alternatives exist for calculation of the values of the primitive variables $\mathbf{v}(h, U_x, U_y, C_1, \dots, C_n)$ at the boundaries. Sloff (1997), who evaluated the mathematically more appropriate but more complex characteristic-variable extrapolation against a simple extrapolation (zero order, first order) of dependent variables, concluded that the latter worked better, especially in combination with rapid flow changes.

inflow boundary procedure

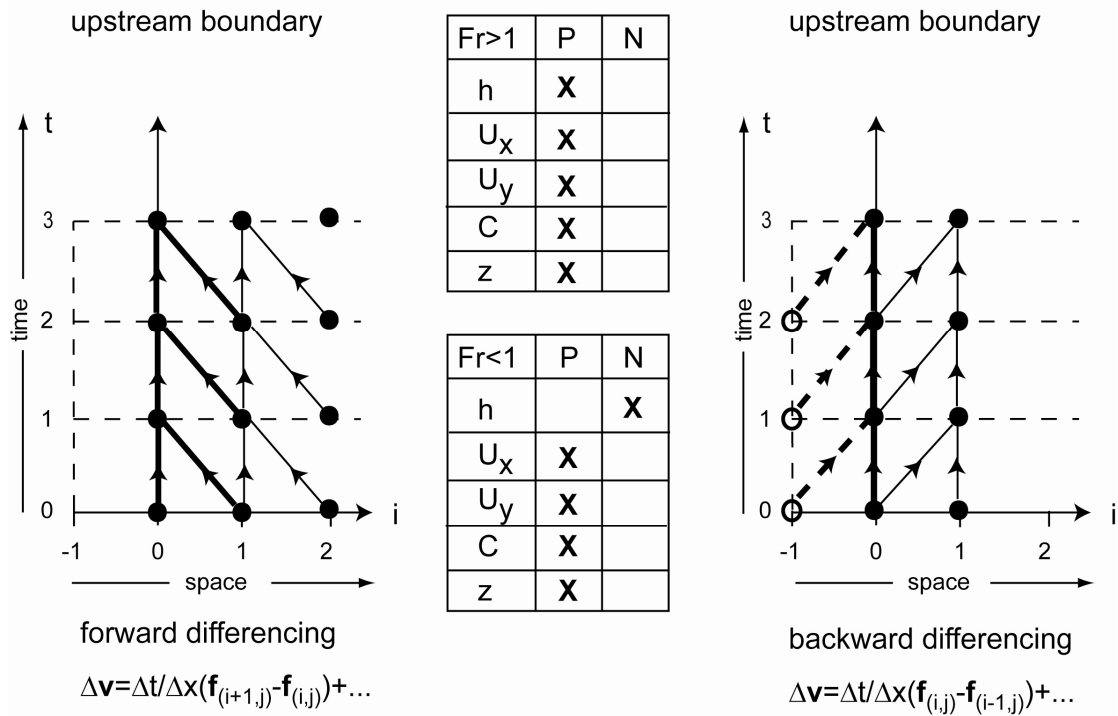


Figure 4.3: Space-time diagrams illustrating boundary procedure at inflow points. Horizontal axes represent the space domain, with values of index i denoting grid points. Index i ranges from zero at the inflow boundary to n at the outflow boundary of the grid, where n denotes the number of grid points. Grid points inside the computational domain are indicated with solid circles; imaginary ghost-points outside the computational domain are indicated with open circles. Vertical axes represent the time domain, with values of index t denoting the time-level of the solution, i.e., $t=2$ indicates the solution after 2 time steps Δt . In the table headers, P stands for “Physical” and N stands for “Numerical”.

In general, to maintain the accuracy of the scheme, the adopted boundary extrapolation can be one order below the order of the interior scheme (Gustafsson, 1975). For the second-order MacCormack scheme a combination of zero- and first-order extrapolation methods gave the best results in terms of stability and accuracy. In case of subcritical flow at the boundary, ghost-point values (see Figures 4.3 and 4.4) are determined by means of zero-order extrapolation, whereas for supercritical flow ghost-point values are determined by means of first-order extrapolation. As the conventional artificial viscosity terms are essentially second-order diffusive terms, their calculation follows the combined zero- and first-order boundary procedure described above. However, in the calculation of the TVD artificial viscosity terms, zero-order extrapolation is sufficient to maintain the accuracy of the scheme, since the TVD approach locally reduces the scheme to first-order accuracy.

Numerical boundary values use ghost-point values obtained by means of extrapolation of numerically computed values from the boundary and the interior, whereas physical boundary values use ghost-point values obtained by means of extrapolation of boundary values at complete time steps. In practice, each operator sequence $\mathbf{OP}_x\text{-}\mathbf{OP}_y$ (see Equation 4.11) advances the solution by Δt (Paragraph 3.3.3 and Appendix A.2) and consists of two one-dimensional operators (\mathbf{OP}_x and \mathbf{OP}_y) that contain a complete predictor-corrector sequence.

outflow boundary procedure

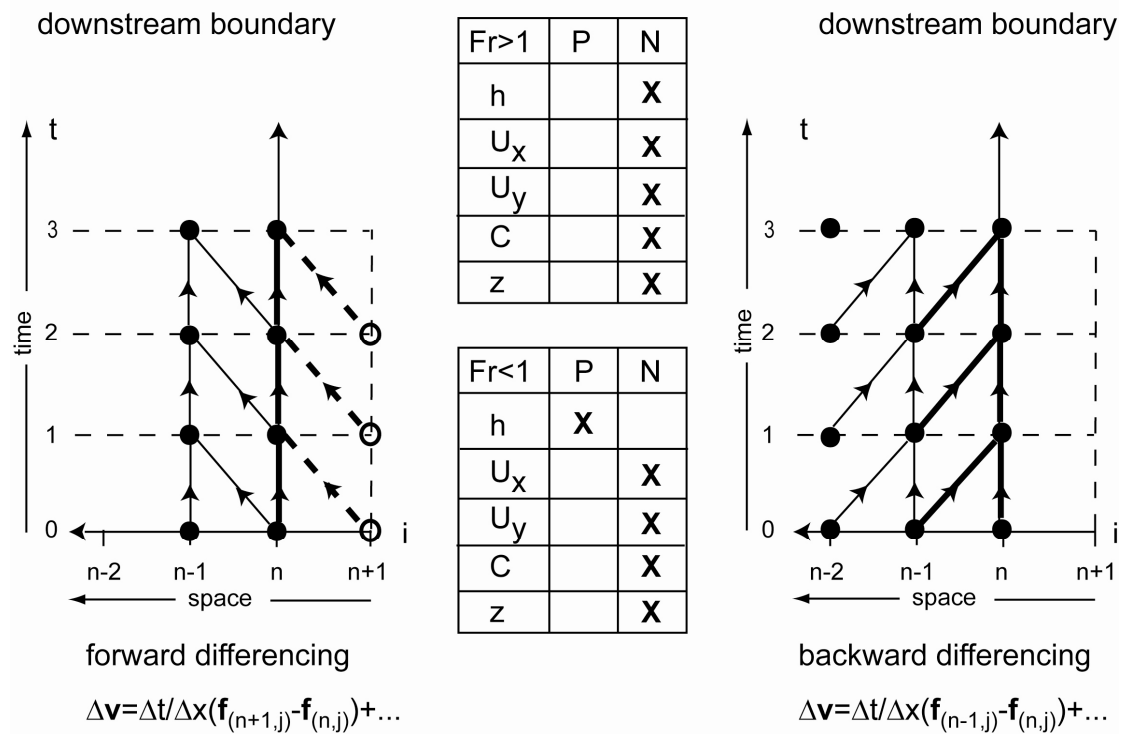


Figure 4.4: Space-time diagrams illustrating boundary procedure at outflow points. Horizontal axes represent the space domain, with values of index i denoting grid points. Index i ranges from zero at the inflow boundary to n at the outflow boundary of the grid, where n denotes the number of grid points. Grid points inside the computational domain are indicated with solid circles; imaginary ghost-points outside the computational domain are indicated with open circles. Vertical axes represent the time domain, with values of index t denoting the time-level of the solution, i.e., $t=2$ indicates the solution after 2 time steps Δt . In the table headers, P stands for “Physical” and N stands for “Numerical”.

At the predictor time level, numerical boundary conditions are based on values of dependent variables from the previous operator, whereas at the corrector time level, numerical boundary conditions are based on values of dependent variables from the predictor time level. In contrast, physical boundary conditions are always based on values of dependent variables from the previous operator sequence.

The flow regime can change rapidly from supercritical and subcritical and vice versa between predictor and corrector steps, due to the presence of shocks in the solution. Because the boundary conditions are different for subcritical and supercritical flow, a Froude number check is needed to ensure that the correct boundary conditions are imposed. The Froude number check is done at both predictor and corrector time levels, and includes not only the boundary points themselves but also the first mesh point upstream (Sloff, 1997). Inflow at the boundary is considered subcritical if at either of the two points at or near the inflow boundary the Froude number is less than or equal to one. At outflow boundaries the flow is considered subcritical only if at both points the Froude number is less than or equal to one. In all other cases, the flow regime at the boundary is considered supercritical. This approach ensures second-order accuracy of the scheme and leads to stable solutions.

4.3.7 Initial conditions

The initial conditions describe the state of the system at time $t=0$. From a mathematical point of view, the system converges to a solution through transfer of information along the characteristics, starting from the initial state. As such, the choice of initial conditions influences the final solution of the system. Care must be taken in defining initial conditions that accurately define the initial physical state of the system to ensure a physically meaningful solution. On the other hand, the initial conditions must be chosen such that the stability is ensured throughout the simulation.

The initial state is represented by a computational mesh representing initial basin-floor topography. At the onset of inflow of a turbidity current into the basin (time $t=0$), the initial physical state of the model is known as a “dry-bed” state, which means the underflow (turbidity current) is absent everywhere on the computational mesh. From a physical point of view, the initial conditions should reflect this dry-bed state. However, when taking into account the stability of the model, a dry-bed state is not a good choice, because very small disturbances in the values of dependent variables may lead to negative flow depths and, consequently, stability problems.

Here, an alternative approach is adopted, which is often used in dry-bed problems (e.g. dam-breaks). In this so-called “wet-bed” approach, dry cells are covered with a very thin uniform layer of water, with flow thickness h and discharge q_x, q_y orders of magnitude smaller than those of the turbidity current. Physically, the density of this underflow layer should be equal to that of the ambient water, i.e., the volume concentration of suspended sediment should be zero. However, a better front representation is obtained when the density of this underflow layer (dry cell) is manipulated such that it equals the density of the flow front. This will be shown in the next paragraph. It is an essential requirement that the underflow layer is very thin when compared to the overriding turbidity current, to prevent significant violation of the dry-bed front relation (Toro, 2001) and, consequently, inaccurate frontal propagation velocities. A detailed analysis of the dry-bed and wet-bed states can be found in e.g. Bradford et al. (1997) and in Toro (2001).

To prevent non-physical propagation of information ahead of the front and, consequently, disturbance of the solution, the dry-bed values of the dependent variables are multiplied by a tolerance parameter. By doing this, small disturbances in the dry-bed state can not accumulate to disturb the solution. At the end of each predictor-corrector step, dependent variable values of cells for which the disturbance falls within the tolerance range are reset to dry-bed conditions.

4.3.8 Head region

The head of a turbidity current is characterized by strong gradients, not only in depth and velocity, but also in concentration since, downstream of the head, the suspended sediment concentration is effectively zero. The implemented shock-capturing scheme (Paragraph 4.3.5) should reproduce the magnitude and position of the jumps in flow depth, velocity and concentration. Bradford et al. (1997) investigated the behaviour of the solution at the front by means of characteristic analysis. At the cell-interface between the front-cell of the turbidity current and the first unoccupied cell

downstream of the front, the solution evolves in analogy with the classical shock tube problem (Appendix A.3). The solution evolves differently depending on the state of the unoccupied cell, which is defined by the initial state of the model. If the unoccupied cell is covered with a thin, low-discharge underflow layer with ambient fluid, the propagation velocity of the front is much higher than in the case of a thin, low-discharge underflow layer with turbid fluid (Chapter 3, Paragraph 3.4). However, the computed front is a poor representation of a real front.

To illustrate this, figures 4.5 and 4.6 display solutions for conservative (density) flow and turbidity flow respectively. The upper graphs of figures 4.5 and 4.6 display the solutions for an unoccupied cell covered with ambient fluid. In the case of conservative flow (Figure 4.5, upper graph), in which source terms (erosion, deposition, entrainment) are zero, the concentration (blue line) should be constant right up to the jump in flow depth (green line), which represents the front of the flow. However, the concentration decreases gradually to zero over a section spanning several cells, to which the solution responds by increasing the flow depth. Similar behaviour is displayed by the solution with non-zero source terms (see Figure 4.6, upper graph).

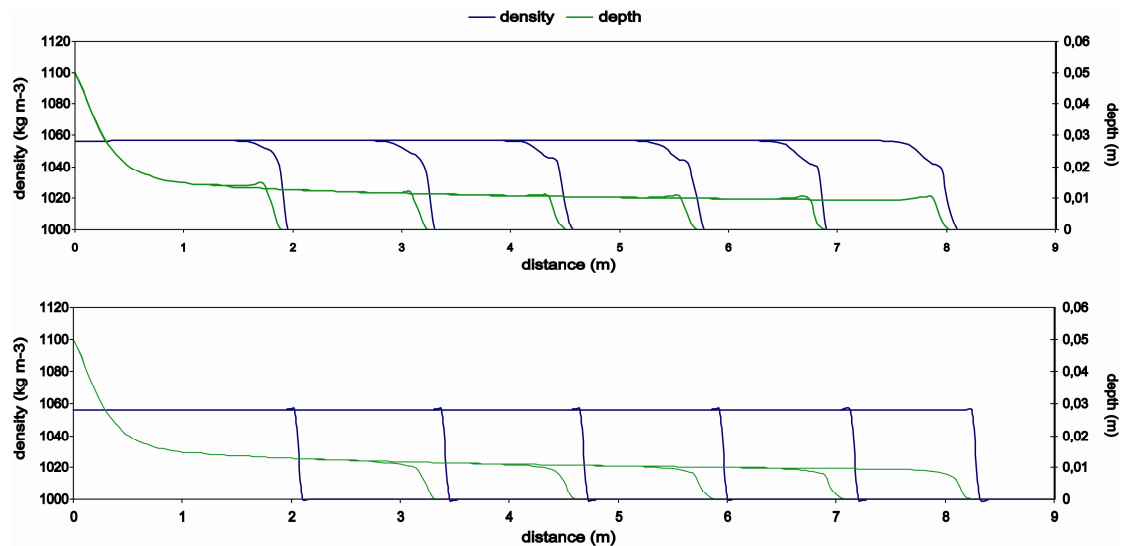


Figure 4.5: 2-DH flow depth and density profiles for a conservative density current in cross-section parallel to the streamwise flow direction. Upper graph: flow depth and density, computed without extrapolation of concentrations into the front region. Lower graph: flow depth and density, computed with extrapolation of concentrations into the front region (bed slope= 5°, $c_D = 0.031$, Van Albada limiter).

To overcome the physically unrealistic increase in flow thickness at the front, Sloff (1997) replaced the concentration equation at the front with a simple zero-order extrapolation of the concentration upstream of the front into the front region. Although this requires the front position to be tracked, a task which is cumbersome in two dimensions, alternative approaches (e.g. shock fitting) are even more demanding in terms of computational effort. To track the front position, a criterion must be defined that indicates the exact position of the front. Here, an additional advantage of adopting the operator-splitting method of Strang (1968) becomes apparent.

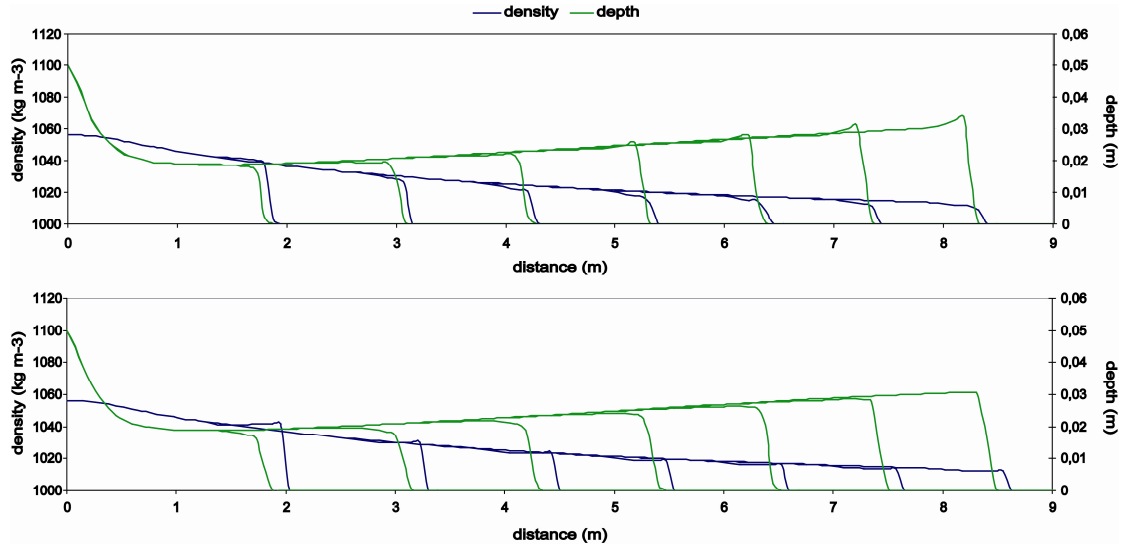


Figure 4.7: 2-DH flow depth and density profiles for an experimental turbidity current (see next paragraph for details) in cross-section parallel to the streamwise flow direction. Upper graph: flow depth and density, computed without extrapolation of concentrations into the front region. Lower graph: flow depth and density, computed with extrapolation of concentrations into the front region (bed slope = 5°, $c_D = 0.031$, Van Albada limiter).

Operator splitting essentially reduces the two-dimensional shock tracking problem to a one-dimensional problem, and allows the use of the definition of the location of the front proposed by Sloff (1997) for his one-dimensional two-layer model (2-DV). However, to ensure the front is propagating in the direction which corresponds to the gradient in depth, an additional velocity criterion is added:

$$\zeta_{\text{front}, x(i,j)} = \frac{h_{(i-\text{sign}(U_{x(i,j)}),j)} - h_{(i+\text{sign}(U_{x(i,j)}),j)}}{h_{(i,j)}} \quad C_{(i,j)} = C_{(i-\text{sign}(U_{x(i,j)}),j)} \quad \text{if } \zeta_{\text{front}, x(i,j)} > \zeta_{\text{crit}} \quad (4.25)$$

where ζ_x denotes the front gradient, h and C denote flow depth and concentration respectively and $\text{sign}(U_x)$ is plus or minus one, depending on the sign of the velocity. The parameter ζ_{crit} is the critical value of the front gradient above which the flow is considered to be discontinuous.

The numerical implementation of the procedure to extrapolate the concentrations into the front region is as follows. At the start of each operator (\mathbf{OP}_x , \mathbf{OP}_y), prior to the predictor-corrector sequence, the position of the front is determined and stored, and concentrations are extrapolated. Since numerically the front (discontinuity) is smeared over more than one cell, the front region is assumed to start at the first cell that complies with the front criterion. Then, during the predictor and corrector steps, the concentrations are updated normally, up to the cell where the front is located. From thereon, the conventional concentration equation is switched off and concentrations are extrapolated downstream up to and including the first dry cell. The concentration value used is the value of the cell just upstream of the first cell that complies with the front criterion.

The effect of this procedure on the solution is illustrated in the lower graphs of Figures 4.5 and 4.6. Instead of the gradual decline in density at the head of the current, the density now remains constant throughout the front region of the current. At the cell interface separating the first wet cell of the front of the flow from the undisturbed dry cells, the gradient in density is now zero; hence the concentration is not manipulated by the flux limiter and the physically unrealistic increase in flow depth at the discontinuity is largely suppressed. It must be remarked that this solution only works when used in combination with the right-eigenvector matrices derived from the system of equations in non-conservative form (Appendix A.3.2), since, in flux-conservative form, the concentration is coupled to the depth of the flow. Consequently, it is manipulated by the flux limiter whenever a jump in flow depth occurs, regardless of the difference in concentration across a cell interface.

4.3.9 Stability

Numerical stability is related to the behaviour of the solution as the time step is increased. The MacCormack solution scheme is an explicit scheme, and therefore it is conditionally stable. The condition for stability is the Courant-Friedrichs-Lewy (CFL) criterion. The CFL criterion for the two-dimensional operator-split MacCormack scheme is defined as (Wang et al., 2000):

$$\Delta t < CFL \frac{\min(\Delta x, \Delta y)}{\max(|U_x| + \sqrt{RCgh}, |U_y| + \sqrt{RCgh})} \quad 0 < CFL \leq 1 \quad (4.26)$$

where *CFL* is the *Courant number*. This is a more favourable condition than that of the original two-dimensional MacCormack scheme, i.e., without operator splitting (see e.g. Hirsch, 1990). Potentially, the time step on a computational mesh with e.g. a field-scale space increment of 100 meters and maximum velocities in the order of e.g. 5 meters per second would be about 20 seconds. However, the stability of the solution is also sensitive to the magnitude of the source terms \mathbf{q} , which is directly related to the length of the time step. Large source terms lead to large variations in values of dependent variables and distort the system beyond recovery.

There is no stability criterion to limit the length of the time step to the magnitude of the source terms. For maximum accuracy, the time step should be chosen such that the Courant number is as close to unity as possible (Sloff, 1997), but the magnitude of the source terms should be such that the solution remains stable throughout the simulation. In practice, the sensitivity of the source terms to the length of the time step must be assessed by means of trial and error.

4.3.10 The *FanBuilder* model

The *FanBuilder* model is a process-based stratigraphic model capable of simulating the evolution of stratal patterns from multiple successive turbidity currents over arbitrary basin-floor topography. The core of the *FanBuilder* model consists of the numerical implementation of the process-based model of turbidity-current hydrodynamics and sedimentation. A sequence of turbidity-current events can be

simulated, based on inflow parameter values that may be either user-specified or stochastically determined based on user-defined based on (user-specified) probability-density functions of event magnitude and recurrence frequency. During quiet intervals between two turbidity-current events, the length of which is defined by the recurrence interval, user-specified tectonic activity can alter the basin-floor topography, and background sedimentation can cover the previously deposited turbidite deposits.

The diagram below gives a step-by-step overview of the workflow followed during a simulation involving multiple events. The left part of the diagram is the *stratigraphy loop*, in which, upon *start* of a simulation, turbidity currents (*events*) are generated as long as the amount of time involved in the events does not exceed the *period* of geological time to be simulated. Each event has a period of *quiescence* (recurrence interval, *sampled* from a user specified distribution) coupled to it, during which only background sedimentation occurs. For each event, the size (volume of sediment) is *sampled* from a user-specified distribution, whereas the discharge characteristics are drawn from user-specified ranges of velocity, depth and concentration of suspended sediment. This, together with the user-specified composition of the sediment (discretized grain-size distribution), fully specifies the turbidity current upon entrance into the model domain. The model domain is defined by a user-specified (three-dimensional) surface representing initial topography (basement), which may already be covered with sediment prior to inflow of the first event, and altered due to user-specified tectonic activity. All user-specified initial parameter values are read from an *input* file.

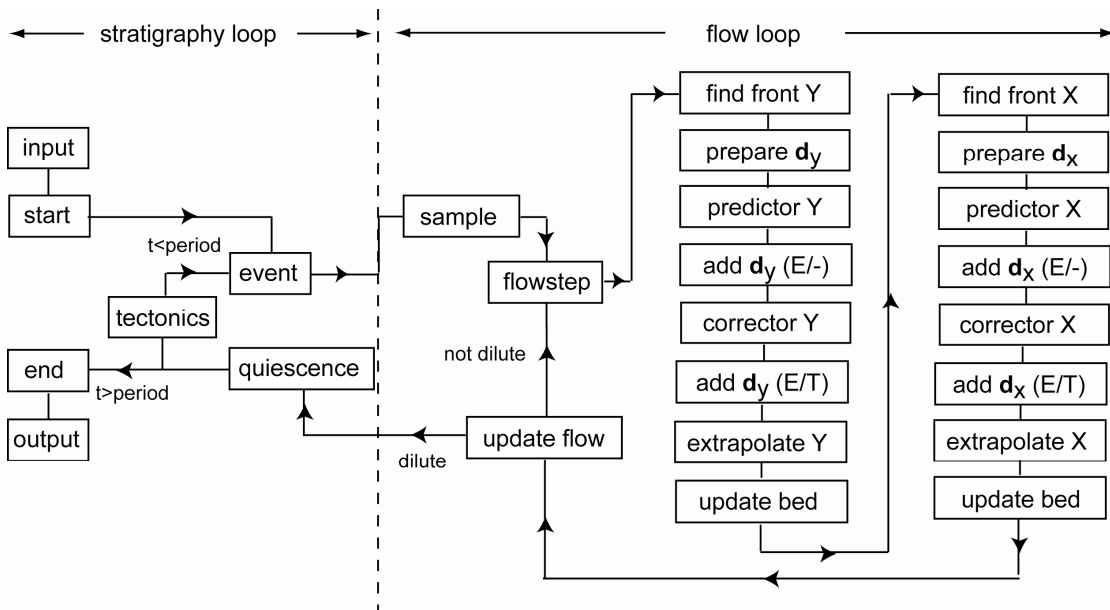


Figure 4.8: Flow diagram of the FanBuilder model

The right part of the diagram is the *flow loop*. This part of the program contains the algorithms that simulate turbidity-current hydrodynamics and sedimentation. Starting from the *event* box, turbidity-current size (volume of sediment, concentration) and discharge per time step (inflow velocity, inflow depth) are *sampled*, and used to initialise the new event. The duration of inflow for the turbidity current is calculated from the size (total discharge) and the discharge per time step. Once started, the

program iterates *flow steps* as long as the concentration of suspended sediment of the turbidity current is above a user specified *dilution limit*.

Each flow step consists of an operator sequence, whereby the solution is advanced first in y-direction and then in x-direction. To enhance stability and minimize accumulation of truncation errors, two sets of operators have been developed, which differ in their sequence of direction of differentiation in space, i.e., either forward in space in predictor, and backward in space in corrector, or vice versa. The program continuously switches between these two sets of operators.

Essentially, for each operator, the same operations are performed. Before each operator, the location of the front is determined in *find front x*, *find front y*. Next, the parameters needed later on in the calculation of the artificial viscosity terms are prepared in *prepare d_x*, *prepare d_y*. Then, the predictor (*predictor x*, *predictor y*) and corrector (*corrector x*, *corrector y*) steps are performed, whereby the equation governing suspended sediment concentration is skipped for cells that have been identified earlier as belonging to the front section of the flow. In case of empirical artificial viscosity (denoted “E”), the viscosity terms are added after both the predictor and the corrector step, whereas in case of TVD artificial viscosity (denoted “T”), viscosity is only added after the corrector step (*add d_x*, *add d_y*).

Having added the viscosity terms, the concentration of the cell that has been identified as the first (upstream) front cell is extrapolated (*extrapolate x*, *extrapolate y*) into the cells which are part of the front region of the flow. Also, at this point in the sequence, the stratigraphy is updated, i.e., the contents of the beds (fractions of grain sizes present, is updated as the sum of changes that have occurred during the operator predictor-corrector sequence (*update bed*). At the end of a flow step, i.e., after a complete operator sequence, the primary flow variables are updated to a new time level $t+1$.

5 QUANTITATIVE VALIDATION EXPERIMENTS

5.1 Introduction

In this chapter, results are presented from the first of three series of validation experiments, which are performed to assess the capabilities of the *FanBuilder* model (Chapter 3) to simulate turbidity-current hydrodynamics and sedimentation. In these validation experiments, simulated hydrodynamic behaviour (depth, velocity, and density of flows), deposit geometry and spatial distribution of grain sizes are compared to experimental data. The selection of laboratory experiments includes simulations of flows with different hydrodynamic behaviour (this chapter), simulations of flows interacting with topography (Chapter 6) and simulations in which multiple successive flows over the same bed create stratigraphy in a subsiding mini-basin (Chapter 6).

The experiments performed by Luthi (1980a, 1980b, 1981) focus on the behaviour of non-channelized turbidity currents in the vicinity of the point of origin, and their deposits. As such, the natural setting for these experimental flows is near river mouths, where suspensions of river water and sediment flow out into a large body of water (lakes, oceans) in the form of a hyperpycnal flow. Under the assumption that the exit point of submarine canyons may be considered a point of origin for turbidity currents travelling down the continental slope, the experimental turbidity currents are representative small-scale analogues for unconfined submarine turbidity currents spreading out onto a semi-horizontal basin floor. In the first part of this chapter, simulated modelling results from quasi-steady and waning turbidity currents are quantitatively compared to experimental data (Luthi, 1980a, 1980b, 1981). In the second part, the sensitivity of the *FanBuilder* model to time-step length and grid-cell size will be evaluated by comparing the validated modelling results to results of simulations in which a different spatial and temporal resolution is used.

5.2 Experimental set-up

The experimental set-up is displayed in Figure 5.1. Small-scale turbidity currents were generated by releasing a thoroughly mixed suspension of freshwater and solid particles from a mixing tank (A) through an entry gate into a basin (E) with an adjustable ramp (expansion table). The ramp (F) was 9 m long and 5 m wide and, in the majority of the experiments, had a constant inclination of 2.3° or 5°. The basin itself was 10 m long, 6 m wide and 1 m deep, and was filled with clear water to the upper edge of the entry gate (to upper right of hose D), which had a width of 30 cm and a height of 5 cm. Water depth in the basin increased from 5 cm near the entry gate to 85 cm near the lower edge of the ramp. Suspension discharge rate in all experiments was kept constant at 3.5 l/s. During an experiment, the additional influx of the suspension was compensated by a relay-controlled drainage system (G) in order to keep the water level in the basin constant (Luthi, 1981). This prevented the generation of a counter-current in the suspension-free layer above the turbidity current.

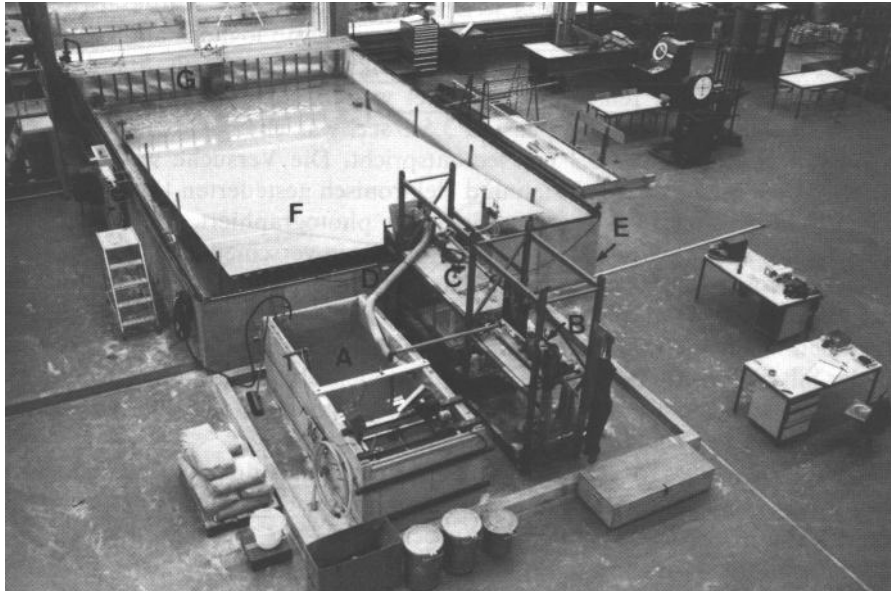


Figure 5.1: View on the experimental installation (Luthi, 1980b)

Two sets of experiments were conducted, using different sediment mixtures, resulting in distinctly different flows in terms of hydrodynamic behaviour and sedimentation patterns. In the first set of experiments, the suspended sediment consisted of chalk powder with a mean grain diameter of approximately $3\ \mu\text{m}$ and maximum size of $10\ \mu\text{m}$. The use of chalk powder, in combination with constant discharge (inflow velocity $0.233\ \text{m/s}$) resulted in quasi-steady flows with virtually no deposition (Luthi, 1981). Published results for these experiments include contour maps displaying the propagation of the front in time through the basin, together with measurements of flow velocity and density through time at several locations in the basin.

In the second set of experiments, the suspended sediment consisted of quartz silt with an almost lognormal size distribution. Mean grain size of this material was $4.76\ \Phi$ ($37\ \mu\text{m}$) with a standard deviation of $0.52\ \Phi$. The hydrodynamic behaviour of the flows was characterised by fairly rapid loss of sediment, i.e., rapidly waning flow. Since, for this set of experiments, the focus was on the deposits, published data also include measurements of deposit thickness, mean grain size, standard deviation and skewness of the deposit, and a description of observed sedimentary structures. Figure 5.2 is a photograph of a deposit of one of these quartz-silt experiments. The entry gate is in the upper left corner of the photography and flow evolved from upper left to lower right of the photograph. Characteristic features of the deposit include an area of non-deposition near the entry gate, which is bounded to left and right by levee-like ridges, the current ripples on the surface of the deposit and the lobe-like shape of the deposit. Furthermore, just downstream of the area of non-deposition, the deposit quickly attains its maximum thickness, which gradually decreases away from the entry gate.



Figure 5.2: Photograph of deposit from a silt-laden experimental turbidity current (Luthi, 1980b)

5.3 Quasi-steady flow

In the first set of (in total) four experiments, quasi-steady turbidity currents were generated, each laden with very fine chalk powder at different concentrations. To determine the grain size to be used in the simulations, the reported settling velocity of 0.004 cm/s of the chalk powder was taken as a reference, because, in the model, settling velocity directly counteracts shear velocity in keeping the grains suspended. In the absence of information on the density of the chalk, a density similar to that of quartz (2650 kg/m^3) is assumed. Using Dietrich's formula (Dietrich, 1982) in the inversion of the settling velocity, a grain size of $7.5 \text{ }\mu\text{m}$ for the chalk powder is obtained. This value lies between the approx. $3 \text{ }\mu\text{m}$ and more than $10 \text{ }\mu\text{m}$ reported by Luthi (1980b, 1981). Other initial conditions follow directly from the experimental set-up. The initial flow depth is taken to be 5 cm, which corresponds to the height of the entry gate. The cross-sectional area of the entry gate is 0.015 m^2 , which, together with the discharge of 3.5 l/s, leads to an initial flow velocity of 0.233 m/s. The initial concentration of suspended sediment determines the density of the flow, and was varied between the four experiments. Other initial model parameters include the depth (0.00001 m), velocity (0.00001 m/s) and concentration (0.001 % by volume) of the underflow layer (see Chapter 4, Paragraph 4.3.7 on initial conditions), the choice of flux limiter function (Superbee) and the value of the drag coefficient c_D , the importance of which will be illustrated below. Based on a model sensitivity evaluation (Paragraph 5.5), the grid resolution for all the simulations was set at 181 by 100 cells, which corresponds to a (square) grid-cell size of 5 cm. The time-step length was set at 0.1 seconds.

Figure 5.3 displays the front propagation of a quasi-steady turbidity current with an initial density of 1010.4 kg/m^3 , which corresponds to a suspended sediment concentration of 0.788% by volume.

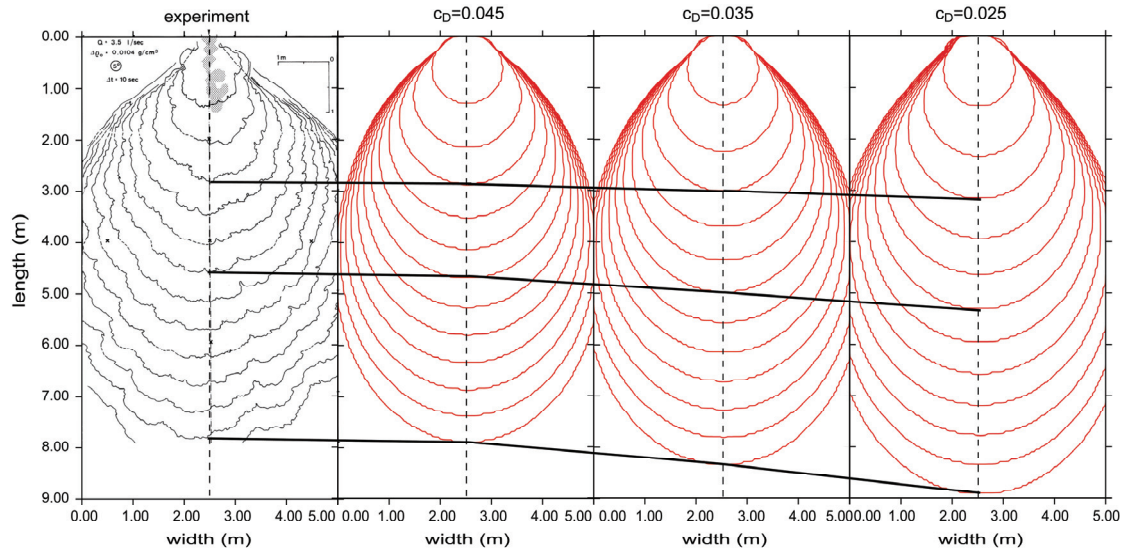


Figure 5.3: Comparison of simulated front propagation to measured data for an experimental quasi-steady turbidity current with initial density of 1010.4 kg/m^3 (CP run 1 of Luthi). Leftmost graph: measured front propagation contours, published in Luthi (1980b). Other graphs: simulated front propagation contours with different values of the drag coefficient (c_D). All contours drawn at 10 s intervals

The leftmost graph is taken from Luthi (1980b, CP run 1) and displays the measured front propagation for this experimental turbidity current. The location of the front of the turbidity current is represented by contours, drawn at 10 s intervals. The distance between the contours stabilizes after approximately 30 s, at which point the flow velocity is near-constant and the flow is quasi-steady.

The other three graphs display the simulated front propagation with different values of the drag coefficient c_D . The drag coefficient parameterizes the intensity of the turbulence in the flow, which is generated due to the combined effect of skin friction (friction between a fluid and a solid) and form drag (friction due to bed forms) at the interface of the flow with the bed. In reality, its value is variable and difficult to determine exactly. Its value may be considered to be a function of, amongst others, the ratio of bedform height (height of the boundary layer) to flow depth. A higher ratio implies that the boundary layer occupies a larger part of the total flow depth; hence the amount of drag exerted by the flow on the bed is larger, and values of c_D are higher. In the model its value is taken to be constant and given a value between 0.002 and 0.06, depending on the spatial scale of the simulation, whereby higher values of c_D must be imposed for small-scale simulations (smaller flow depths).

As can be seen in Figure 5.3, the value of c_D has a significant effect on the propagation velocity of the front of the simulated turbidity currents. A value of c_D of 0.045 gives the best match with the measured data, whereas lower values lead to higher propagation velocities. However, in all three simulated cases, the turbidity current attains a quasi-steady state (distance between the contours almost stabilizes). This hydrodynamic behaviour is to be expected given the constant initial conditions (discharge, density) and the very fine chalk powder sediment with its excellent suspension characteristics.

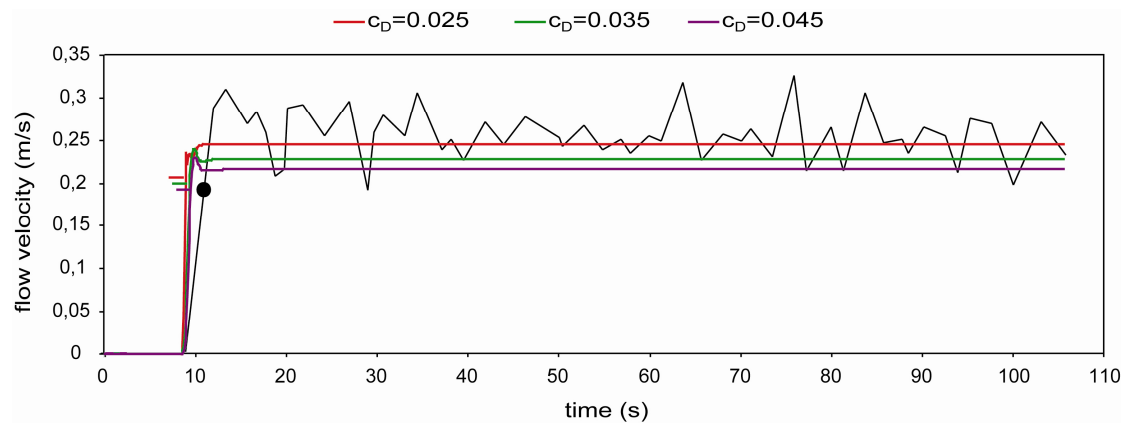


Figure 5.4: Comparison of simulated flow velocities to measured data for an experimental turbidity current laden with chalk powder and initial density of 1044 kg/m^3 . Black line represents measured flow velocity reproduced from Luthi (1980b). Coloured lines represent simulations with different values of the drag coefficient (c_D). Black dot indicates the velocity of the front of the turbidity current, as measured in the experiment; short coloured lines indicate velocity of the front in the simulations. The measurement station is located 2m downstream of the entry gate.

Figure 5.4 displays the evolution of flow velocity with time at a fixed location for an experiment in which the inclination of the expansion table is set at 20° , which is much steeper than in all other experiments. Measurements were taken two metres downstream of the entry gate, which is at base of the ramp, just before the point where the inclination abruptly changes from 20° to 0° . Originally, this experiment was part of a set of experiments to test the hypothesis that the velocity of the body of the turbidity current is higher than the head, as proposed by, amongst others, Middleton (1966a). The black line represents the velocity measurements. The velocity of the body of the flow fluctuates around an average value of approximately 27 cm/s, probably due to turbulence. The passage of the head of the turbidity current is marked in the graph by a black dot and has a velocity of 19 cm/s, a value which is lower than that of the body of the flow.

The simulated flow velocities (coloured lines in Figure 5.4) display similar behaviour, irrespective of the value of the drag coefficient. However, in all three simulated cases, flow velocities of the body, although constant, are somewhat lower than the average of the measured velocities. This suggests that a value of c_D lower than 0.025 would give a better fit to the data, whereas in the experiment discussed earlier, with significantly lower flow velocities, a value of c_D of 0.045 gives the best fit. Furthermore, the head velocities of the simulated turbidity currents are slightly higher than the measured head velocity.

Figure 5.5 displays measured and simulated frontal velocities for three experimental turbidity currents with different densities and sediment composition. Simulated results for the low-density quasi-steady turbidity current with initial density of 1004 kg/m^3 match well with measured values for a value of c_D of 0.025 (lowest two lines in graph). In the case of the higher-density quasi-steady turbidity current of 1104.6 kg/m^3 , simulated frontal velocities are somewhat higher than measured velocities in the vicinity of the entry gate, but decrease more rapidly to fall just below measured velocities for the remainder of the duration of the experiment.

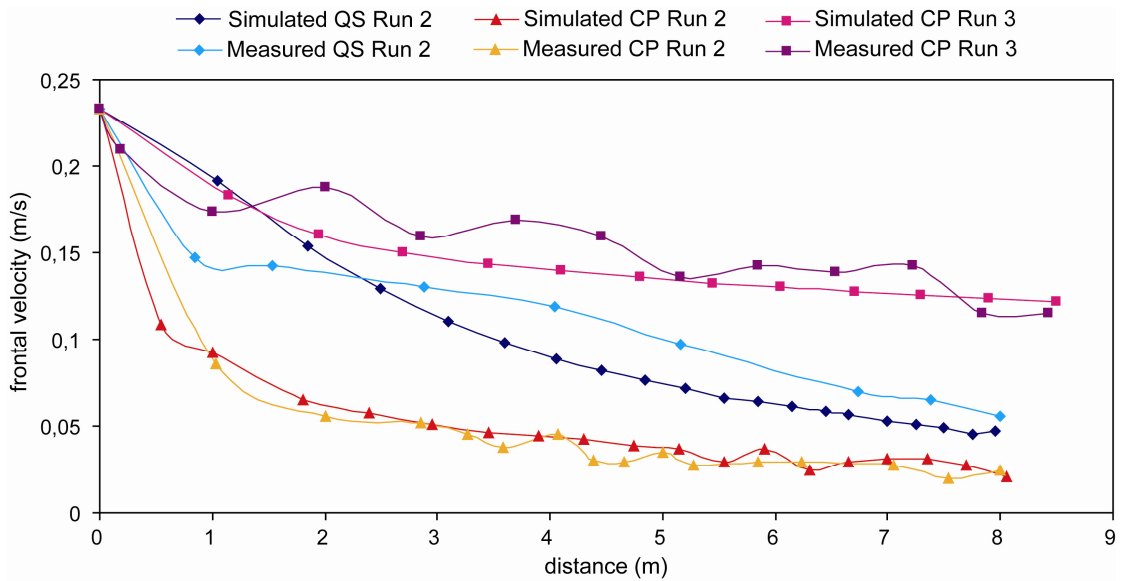


Figure 5.5: Comparison of simulated frontal velocities to measured data (Luthi, 1980b) for three different experiments. QS run 2: rapidly waning silt-laden turbidity current, initial density 1067.5 kg/m^3 . CP run 2: quasi-steady turbidity current laden with chalk powder, initial density 1004.0 kg/m^3 . CP run 3: quasi-steady turbidity current laden with chalk powder, initial density 1104.6 kg/m^3 . Value of drag coefficient (c_D): 0.025.

Likewise, in case of the rapidly waning turbidity current laden with quartz-silt, initially simulated frontal velocities are higher than measured velocities, and decrease to a level below measured velocities for the remainder of the experiment. The likely reason for this discrepancy between measured and simulated flow behaviour is to be found in the assumption that the momentum lost through friction with the bed, quantified through u_* , is related to the depth-averaged velocity of flow by a constant value of c_D . In reality, the momentum lost through friction with the bed also depends on other parameters, such as the ratio of bed roughness length to flow depth, and the viscosity of the suspension, which requires that it be parameterized in a non-linear relationship which also takes into account these factors (see also Chapter 7, Paragraph 7.2).

5.4 Waning flow

In a second set of four experiments, waning turbidity currents were generated, each laden with quartz silt at different concentrations. The mean size of the quartz-silt grains used in the experiments was 4.76Φ ($37 \mu\text{m}$), with a standard deviation of 0.52Φ (Luthi, 1980b, 1981). This grain-size distribution is discretized into a distribution with three classes (bins) with size $53.2 \mu\text{m}$ (probability 0.278), $37.1 \mu\text{m}$ (probability 0.444) and $21.1 \mu\text{m}$ (probability 0.278), which corresponds to the mean size and the mean size plus and minus the standard deviation. The settling velocity of the mean size, calculated using Dietrich's formula (Dietrich, 1982), is 11.8 cm/s , a value which is slightly lower than the 13 cm/s reported by Luthi (1980b, 1981). Other initial conditions (inflow depth, inflow velocity, underflow depth, underflow velocity, underflow density, inclination of the expansion table and choice of limiter) were taken equal to the values used in the simulations of the quasi-steady turbidity currents.

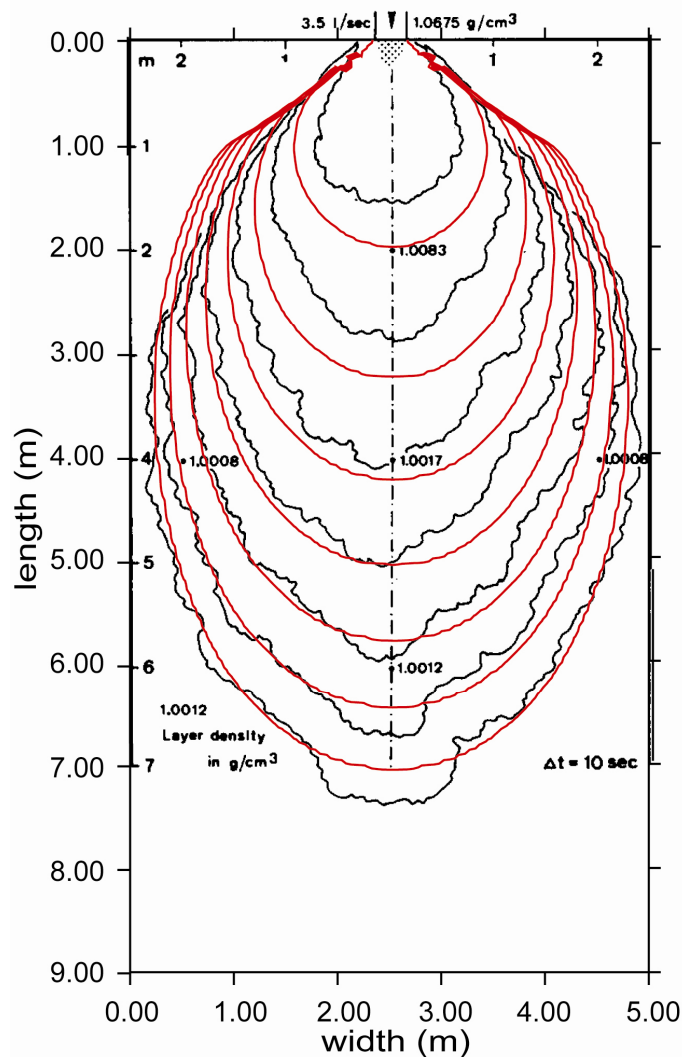


Figure 5.6: Comparison of simulated front propagation contours (red) to measured data (black) for a silt-laden turbidity current with an initial density of 1067.5 kg/m^3 (QS run 2 of Luthi). Measured data reproduced from Luthi (1981). Value of drag coefficient (c_D): 0.020. Contours drawn at 10 s intervals.

The duration of the experiments is constrained by the front of the turbidity current reaching the distal end of the expansion table, which took one minute in case of the highest-concentration turbidity current, and four minutes in case of the lowest-concentration turbidity current.

Figure 5.6 displays the front propagation of a rapidly waning turbidity current, laden with quartz-silt, with initial density of 1067.5 kg/m^3 . Black lines and red lines represent the location of the front of the experimental and simulated turbidity current respectively, measured at 10s intervals (Luthi, 1981). As discussed earlier, the value of c_D influences the simulated hydrodynamic behaviour. Here, a value of 0.020 gives an excellent fit to measured data, except for a zone near the entry gate, where the velocity of the simulated turbidity current is higher than that of the experimental turbidity current, a limitation which has already been discussed. Other discrepancies between the simulated and measured front contours must be attributed to processes that are not explicitly taken into account in the model, such as the formation of turbulent eddies and instabilities related to the entrainment of water into the turbidity current (K-H instabilities, lobes, clefts).

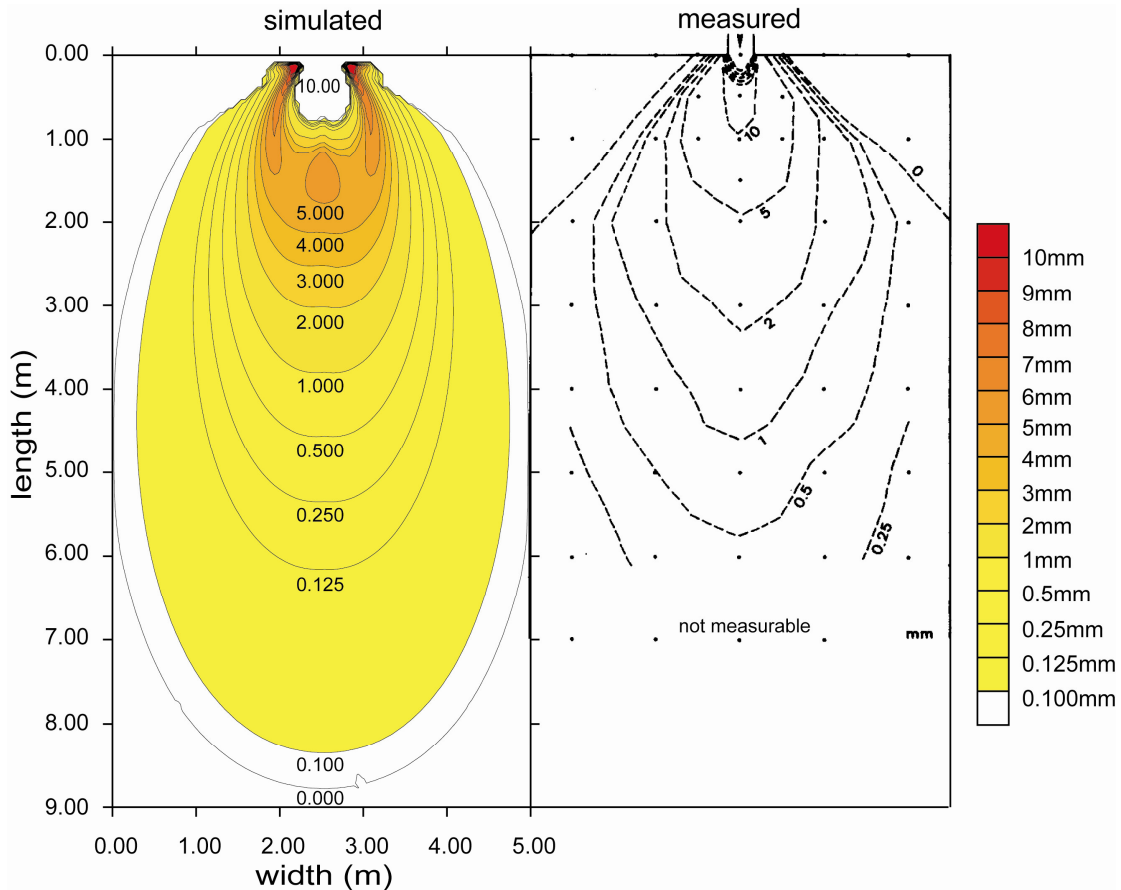


Figure 5.7: Comparison of simulated deposit thickness to measured data for a rapidly waning silt-laden turbidity current with initial density of 1067.5 kg/m^3 (QS run 2 of Luthi). The white area between the 0.0 mm contour and the 0.1 mm contour represents the part of the deposit which is less than a grain thick. Measured data reproduced from Luthi (1981). Value of drag coefficient (c_D): 0.020 .

A comparison between simulated and measured deposit thickness for this experiment (QS run 2 of Luthi) is made in Figure 5.7. The graph to the left is a contour map of the simulated deposit, based on thickness values of 1991 points (181 by 101 points). The graph to the right is reproduced from Luthi (1981) and displays the thickness of the experimental deposit measured at 35 locations. A value of 0.4 was used in the simulation for the initial porosity of the freshly deposited sediment. Shape and thickness of the simulated and experimental deposit are very similar; visually there is a good match between the simulated deposit and the experimental deposit. Quantitatively, there is some discrepancy in the position of the contours of equal thickness. The 2 mm and 5 mm contours closely match, but other contour positions differ. Near the entry gate, the experimental deposit is thicker than the simulated deposit, whereas the zone of non-deposition in the experimental deposit seems to be smaller. Furthermore, the levees seem to be more pronounced in the simulated deposit. Notwithstanding the quality of the published data, a more detailed quantitative analysis is not pursued here, given the large difference in the number of sample points between the simulations and the experiments.

A comparison between simulated and measured deposit thickness for a second experiment (QS run 1 of Luthi) is made in Figure 5.8. In this experiment, the initial density of the turbidity current was 1023.8 kg/m^3 , which is significantly lower than the value of 1067.5 kg/m^3 in run 2. Consequently, the deposit is thinner, and the

length to width ratio is smaller for both the simulated and the experimental deposit (compare figures 5.7 and 5.8). Again, the qualitative match between simulated and experimental deposit is good; the deposits are similar in shape and thickness. Main discrepancies in thickness occur in the distal part of the deposit and near the entry gate. However, the magnitude of the difference in thickness between the simulated and the experimental deposit at the distal end is much larger than in the previous example.

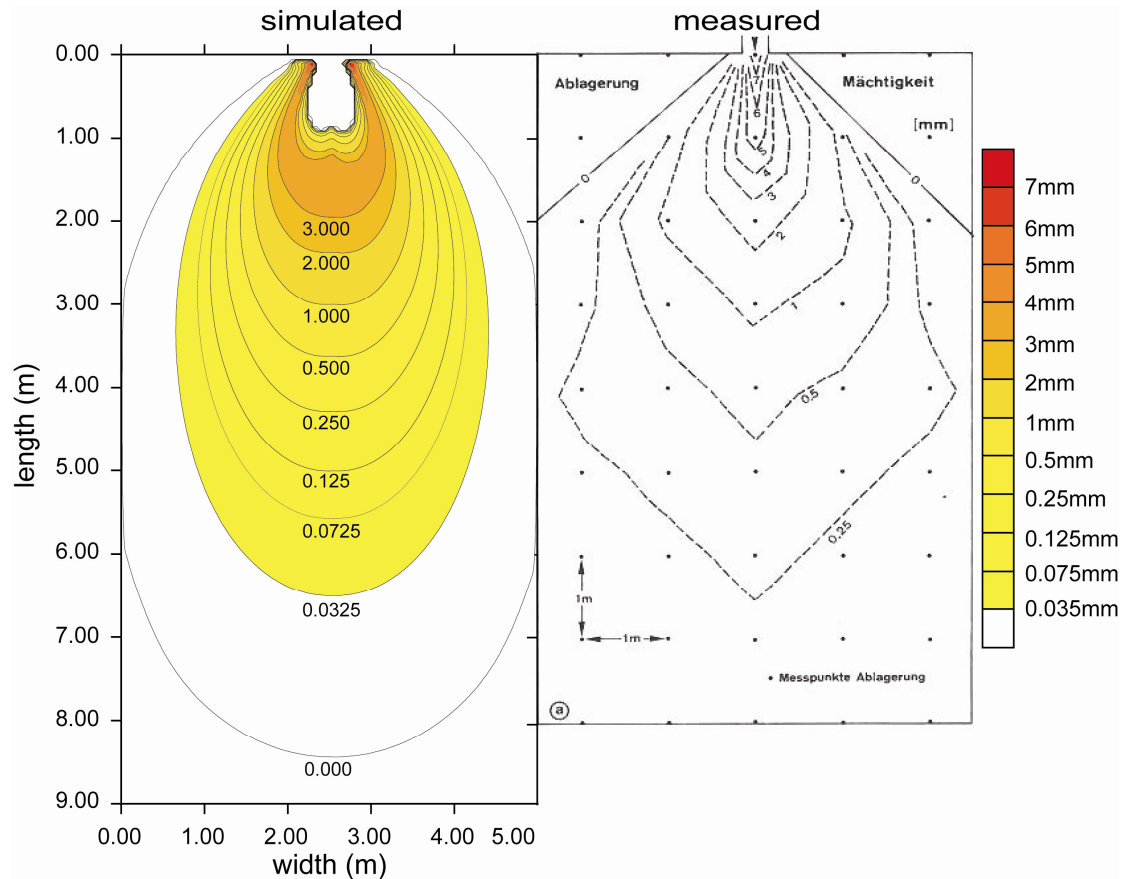


Figure 5.8: Comparison of simulated deposit thickness to measured data for a rapidly waning silt-laden turbidity current with initial density of 1023.8 kg/m^3 (QS run 1 of Luthi). The white area between the 0.0mm contour and the 0.0325mm contour represents the part of the deposit of which the thickness is less than the mean grain size. Measured data reproduced from Luthi (1980b). Value of drag coefficient (c_D): 0.020.

A possible explanation for this larger difference is that, due to the longer duration of the lower-density experiment (QS run 1), the turbidity current was partially ponded in interacting with the sidewalls of the basin. Further evidence to support this hypothesis is found in the shape of the 0.25mm contour of the experimental deposit. Contrary to all other contours, the 0.25mm contour widens again 3m downstream of the entry gate. This possible ponding effect is not reproduced by the model on account of the open non-reflective model boundaries. Other sources of this discrepancy must be sought in the relatively small number of sample points in the experimental deposit and the discretization of the grain-size distribution, with the volume fraction of the three classes likely to be somewhat different from the continuous grain-size distribution of the sediment itself.

A comparison of the mean grain size of the simulated deposit versus the measured mean grain size of the experimental deposit is displayed in Figure 5.9. The mean grain size of the experimental deposit ranges between 36 μm and 44 μm , which implies that the finer fraction (roughly the sediment with a size less than the mean size of 37 μm) of the sediment does not settle out of suspension in the experimental turbidity current. By contrast, in the simulated deposit, the mean size ranges between 22 μm and 42 μm , indicating that the finest fraction of the three (21.1 μm) does settle out of suspension in the simulation. The simulated mean deposit grain size displays a distinct fining trend with distance away from the entry gate, similar to the trend in mean grain size of the experimental deposit.

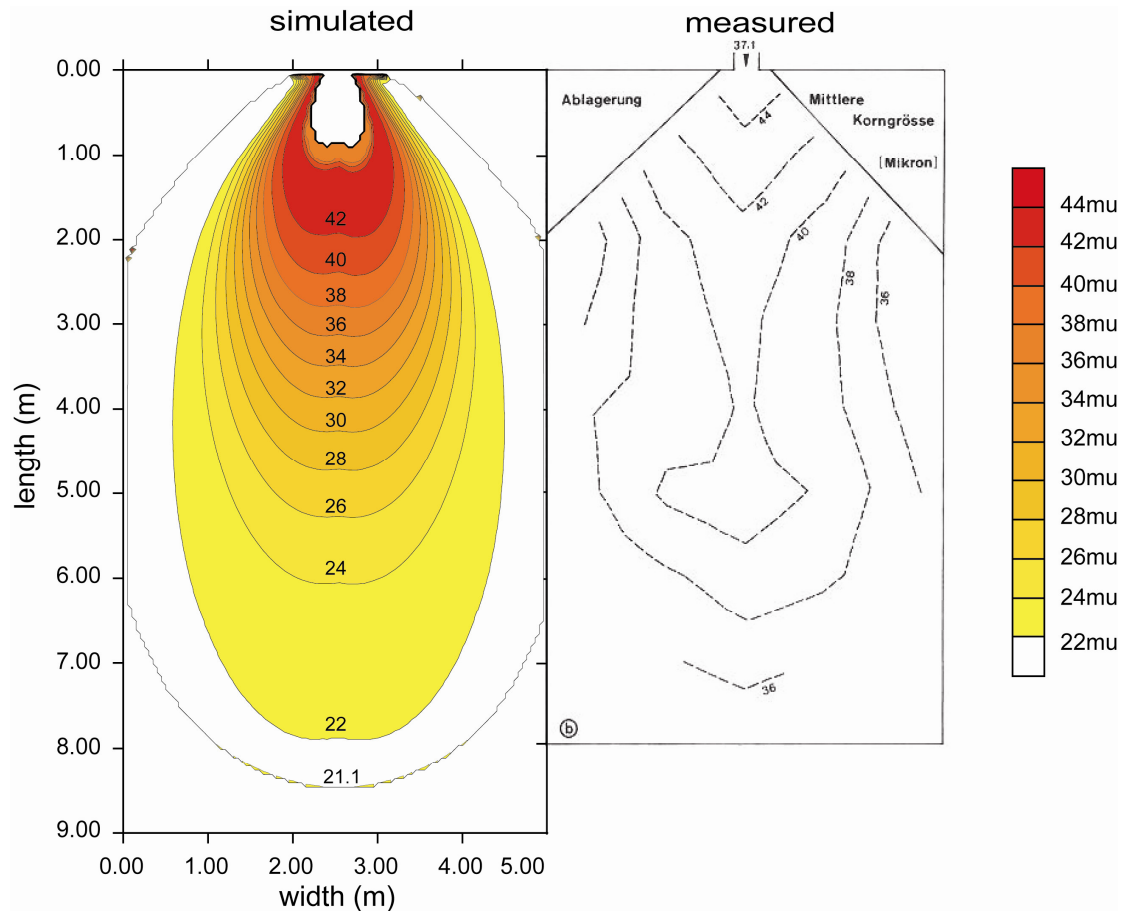


Figure 5.9: Comparison of mean grain size of simulated deposit to measured data for a rapidly waning silt-laden turbidity current with initial density of 1023.8 kg/m^3 (QS run 1 of Luthi). Measured data reproduced from Luthi (1980b). Value of drag coefficient (c_D): 0.020.

Furthermore, as already observed by Luthi, transport of suspended sediment seems to be confined to a zone in the turbidity current which is narrower than the turbidity current itself, an observation confirmed by the elongated form of the contours of equal mean grain size of the simulated deposit. However, the actual contour pattern of the mean grain size of the experimental deposit is not reproduced by the model (Figure 5.9, right graph). More specifically, the 40 μm contour suggests that for the runs with quartz-silt, flow velocities in the axial part of the experimental turbidity current were significantly higher than flow velocities calculated by the model. This conclusion is further supported by the pattern of the contours of the front propagation of the experimental turbidity current as shown in Figure 5.6, which clearly display the presence of a “nose” at the front of the current, which is not reproduced by the model.

5.5 Sensitivity to temporal and spatial resolution

In the field of numerical modelling, accuracy is defined as the level to which the approximate numerical solution converges to the exact analytical one. However, an analytical solution to the two-dimensional mathematical model that includes the source terms cannot be obtained. As such, an alternative approach was adopted by validating simulated results to measured data for laboratory-scale turbidity currents. With the results of these validation experiments, presented in the previous paragraph, a measure of accuracy of the model has been obtained. However, the accuracy that was aimed for was obtained at the cost of computational efficiency, because the experiments were simulated at high spatial and temporal resolutions. In stratigraphic modelling studies, computational efficiency is an important requirement, which must be weighed against the level of accuracy desired. If the level of accuracy is deemed acceptable at lower resolution, then this lower resolution would be preferred since it ensures that simulations can be performed quicker. To gain insight into the behaviour of the solution at different resolutions, the sensitivity of the solution (depth, velocity, and density of flow, deposit thickness and grain size) is evaluated by comparing the validated high-resolution solution, to solutions obtained using lower spatial and temporal resolution. In a first set of tests, the time-step length is varied, while keeping a constant grid-cell size, whereas in a second set of tests, the grid-cell size is varied, while keeping a constant time-step length.

5.5.1 Sensitivity to length of computational time step

5.5.1.1 Quasi-steady flows

Figure 5.10 illustrates the sensitivity of the solution to the length of the computational time step for quasi-steady flow.

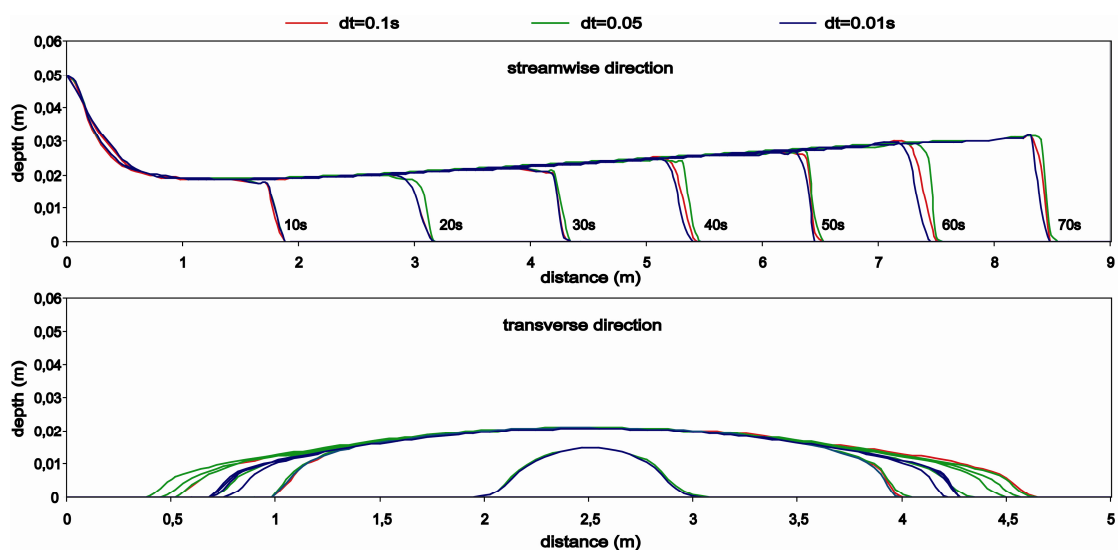


Figure 5.10: Computed solutions with **different time-step lengths** for **quasi-steady flow** (chalk powder, uniform grain size distribution). Upper graph displays depth of flow at 10s intervals along axis parallel to the streamwise flow direction. Lower graph displays depth of flow at 10s intervals along axis parallel to the transverse flow direction, and located 2m from the entry gate. In the transverse direction, the effect of stagnating spreading causes the lines of flow depth for a single solution (e.g. green lines) to overlap.

In the profile parallel to the streamwise flow direction (upper graph), differences in depth of flow are very small, and only visible at the front of the flow. In the profile perpendicular to the streamwise flow direction (lower graph), the flow has a somewhat smaller spread for the solution with highest time resolution (blue lines terminate closer to inflow location than red and green lines). The mass conservative property of the solution is evaluated by means of the volumetric error, which is defined as:

$$\text{vol}_{\text{error}} = \left[\frac{\text{vol}_{\text{inflow}} - \text{vol}_{\text{outflow}} - \text{vol}_{\text{flow}} - \text{vol}_{\text{bed}}}{\text{vol}_{\text{inflow}}} \right] \times 100 \quad (5.1)$$

Here, $\text{vol}_{\text{inflow}}$ represents the volume of sediment discharged into the computational domain, $\text{vol}_{\text{outflow}}$ represents the volume of sediment exiting the computational domain through outflow at the boundaries, vol_{flow} represents the volume of sediment in suspension in the flow, vol_{bed} represents the volume of sediment in the deposit, and $\text{vol}_{\text{error}}$ represents the error in volume, i.e., the volume of sediment which is lost due to numerical deficiencies. As can be seen in Figure 5.11, the mass conservative property of the solution depends not only on the time-step length, but also on the choice of limiter. The Superbee limiter clearly performs best in this respect, with a volume error of about 2 %. Nonetheless, the error in volume stabilizes in time, regardless of the choice of limiter. As the time resolution increases, the volume error decreases.

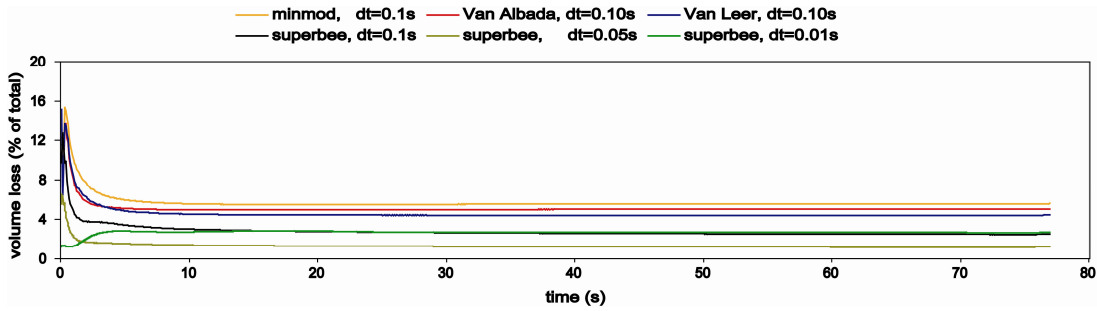


Figure 5.11: Sensitivity of *volume error* (Equation 5.1) to *time-step length* for *quasi-steady flow* (chalk powder, uniform grain size distribution).

Taking into account the purpose of the model as a tool for use in stratigraphic modelling studies, the true focus of the model is on the geometry and grain size of the deposit. Figure 5.12 (next page) illustrates the sensitivity of the solution to time-step length for quasi-steady flow. Upper graphs display contour maps of the thickness of the deposits for solutions with different time-step length. Visually, the difference between the solutions is small. Lower graphs in Figure 5.12 display contour maps of difference grids obtained by subtracting a reference grid (the truth-case) from the solutions at different time-step lengths. The reference grid is the solution with the highest temporal resolution, i.e., with a time-step length of 0.01 s. The difference is calculated as:

$$\Delta\eta_{b(i,j)} = \left| \eta_{b(i,j)} - \hat{\eta}_{b(i,j)} \right| \quad (5.2)$$

where η_b is the thickness of the deposit of the solution for which the difference to the truth-case $\hat{\eta}_b$ is evaluated, and $\Delta\eta_b$ is the absolute difference.

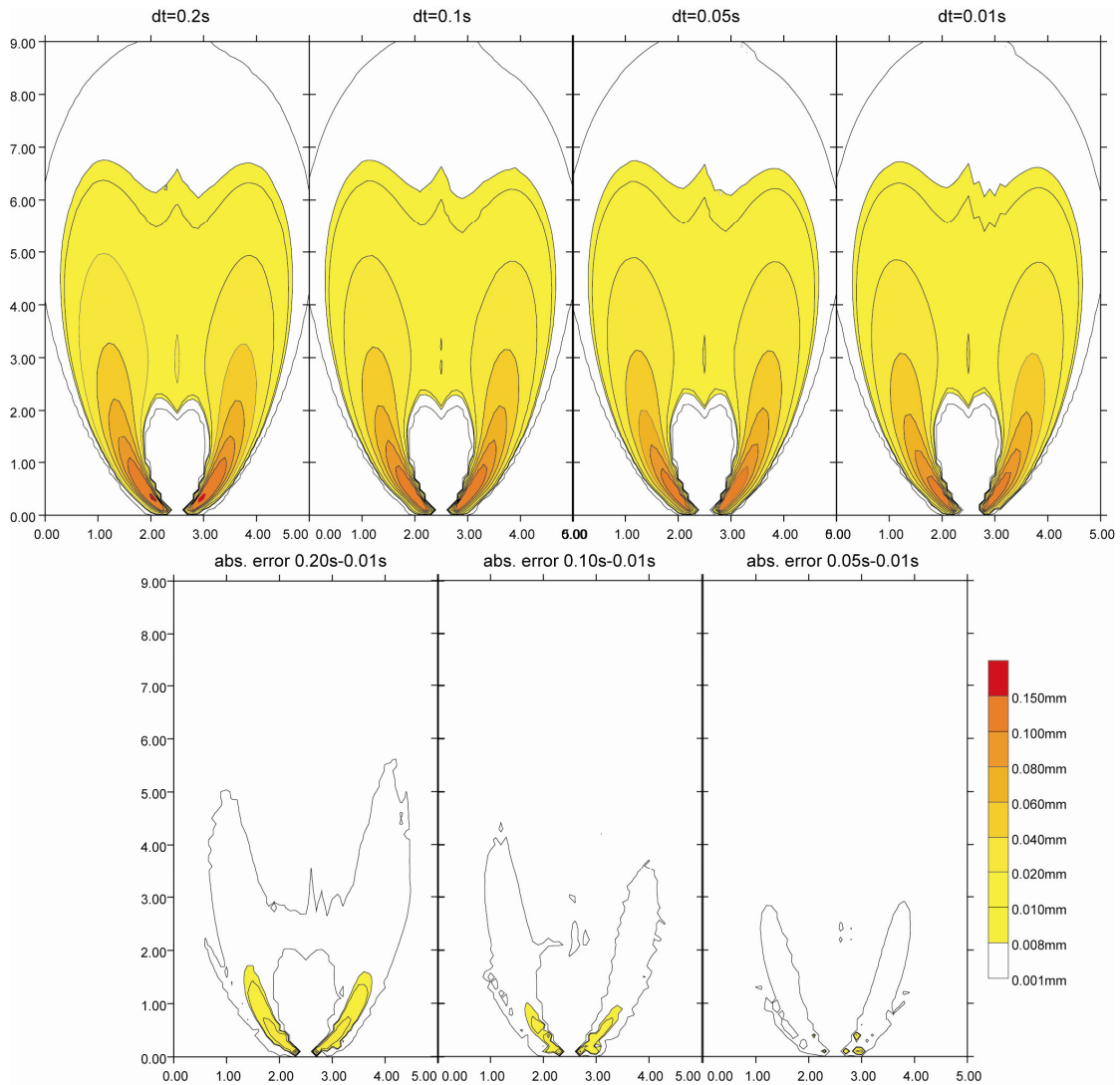


Figure 5.12: Sensitivity of **deposit thickness** to **temporal resolution** for **quasi-steady flow** (chalk powder, uniform grain size distribution). Upper graphs: deposit thickness for different time-step lengths. Lower graphs: absolute difference (Equation 5.2) between the truth-case with time-step length of $0.01s$ and solutions with larger time steps.

All contour maps are based on the same ranges, i.e., the legend to the right is valid for all contour maps. The area between the outer contour line ($\eta_b=0.001mm$) and the contour line of $0.008mm$ is not coloured, since thicknesses in this range fall below the diameter of the grain size ($7.5\mu m$), i.e., the deposit is less thick than the grain size. As can be seen, substantial differences in deposit thickness are confined to the area in the vicinity of the inflow point, and are largest in the levees.

5.5.1.2 Waning flows

Figures 5.13 and 5.14 illustrate the sensitivity of the model to time-step length for waning flows. The density of the flow (upper graph, left) decreases from an initial value of $1067.5 kg/m^3$ to the value of the surrounding tap water ($1000 kg/m^3$), which indicates complete flow dilution approximately 7.5 meters from the entry point.

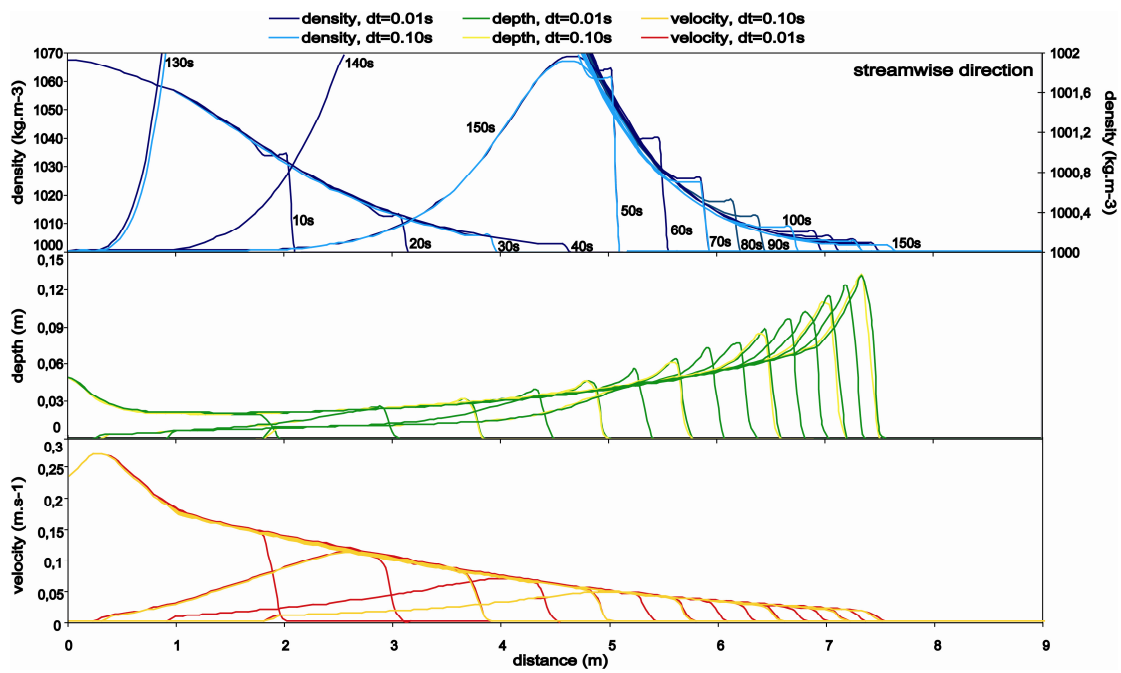


Figure 5.13: Computed solutions with **different time-step lengths** for **waning flow** (quartz silt, uniform grain-size distribution). Graphs display values of flow variables at 10s intervals along axis parallel to the streamwise flow direction. Upper graph: flow density; first 4 lines from the left scaled to left y-axis, rest scaled to right y-axis. Middle graph: flow depth. Lower graph: flow velocity. Inflow stops after 120s.

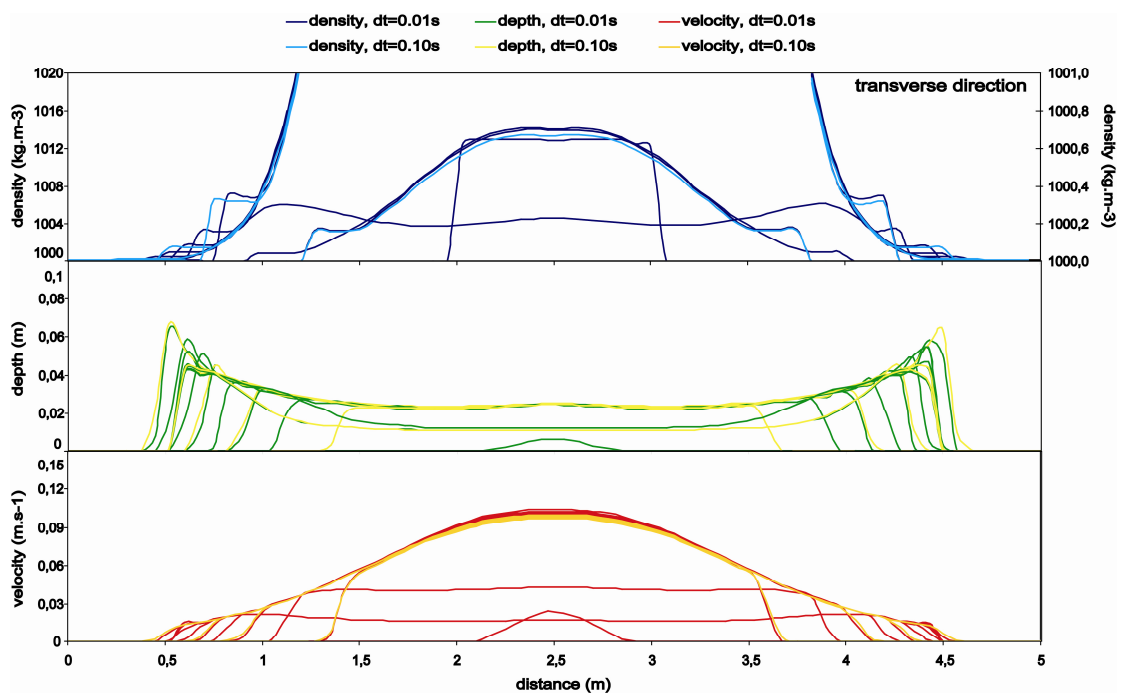


Figure 5.14: Computed solutions **with different time-step lengths** for **waning flow** (quartz-silt, uniform grain-size distribution). Graphs display values of flow variables at 10s intervals along axis parallel to the transverse flow direction, and located 2m downstream of the entry gate. Upper graph: flow density; inner lines scaled to left y-axis, outer lines scaled to right y-axis. Middle graph: flow depth. Lower graph: flow velocity. Inflow stops after 120s. Spreading progressively stagnates, which causes the individual time lines of a solution to overlap.

As the flow progressively dilutes, the depth of flow increases (middle graph) and the velocity decreases (lower graph). The difference between the solutions is small. Strikingly, the entire flow is confined to the expansion table, i.e., no outflow occurs at the downstream boundary. In contrast, in the original experiment with three size fractions, as well as in the simulated case, outflow at the downstream boundary does occur due to the fact that the finest fraction is still suspended. Again, the volume error stabilizes rapidly to values between 4% for Minmod and almost 0% for Superbee with time-step length of 0.01s (Figure 5.15).

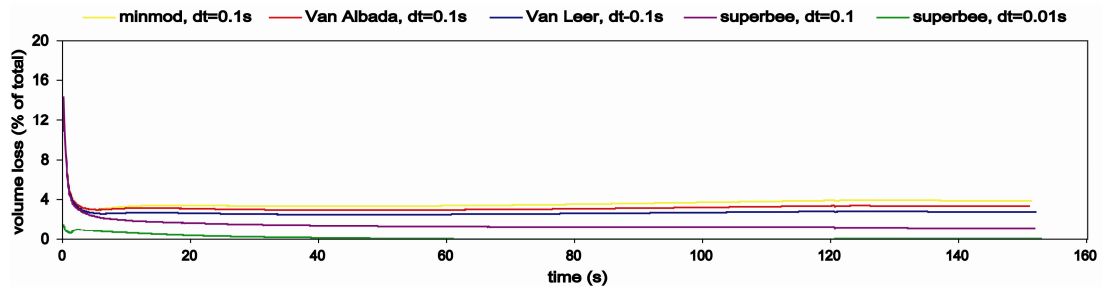


Figure 5.15: Sensitivity of *volume error* (Equation 5.1) to *time-step length* for *waning flow* (quartz-silt, uniform grain-size distribution).

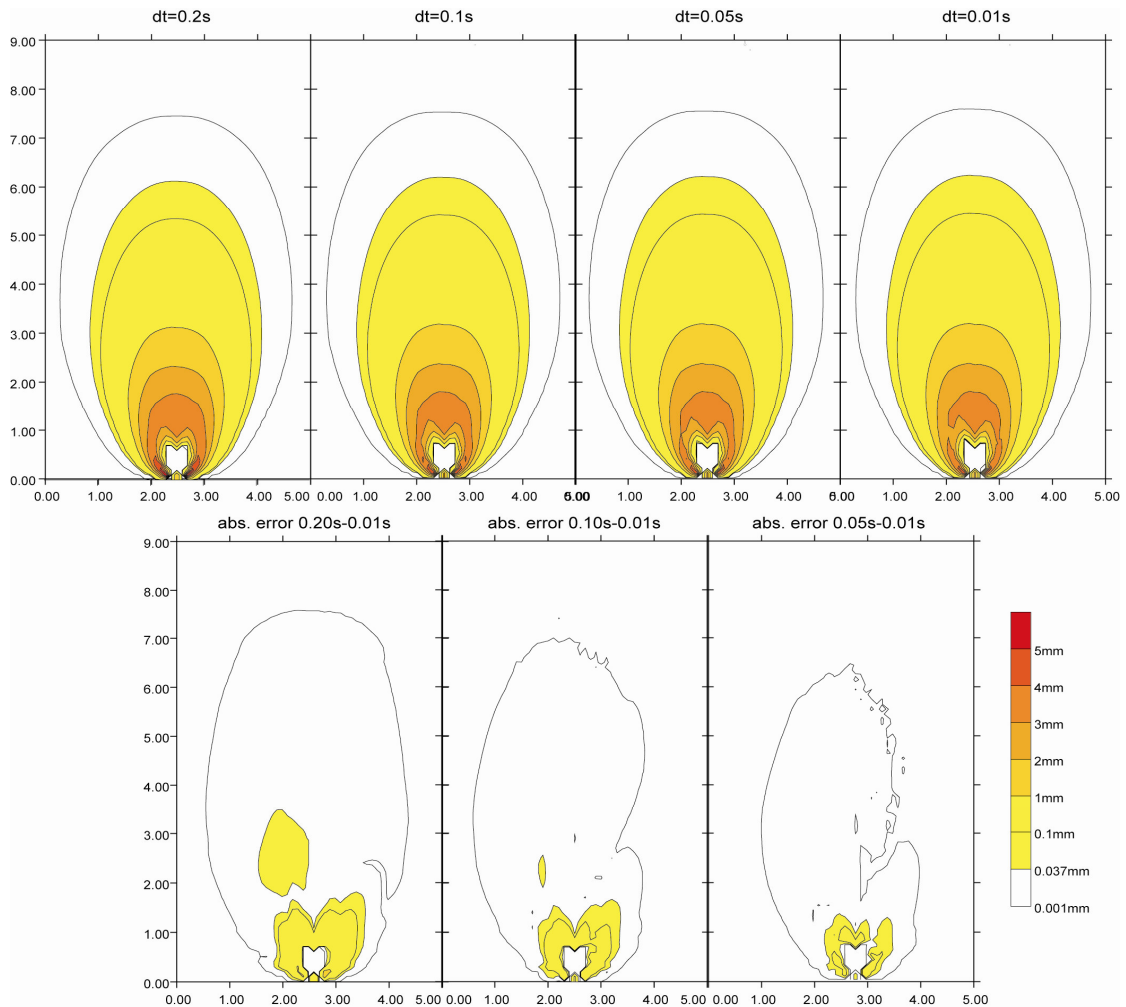


Figure 5.16: Sensitivity of *deposit thickness* to *temporal resolution* for *waning flow* (quartz-silt, uniform grain-size distribution). Upper graphs: *deposit thickness* for different time-step lengths. Lower graphs: *absolute difference* (Equation 5.2) between the truth-case with time step-length of 0.01s and solutions with larger time steps.

Figure 5.16 illustrates the sensitivity of the model to time-step length for waning flow. A difference in time resolution does not significantly alter the geometry of the deposit or the distribution. However, as noticed before, small differences in deposit thickness occur near the inflow point. Furthermore, the difference is largest between the solutions with lowest and highest temporal resolution (lower left graph in Figure 5.16). As before, the grain-size diameter of, in this case, $37\ \mu\text{m}$ is taken as the cut-off thickness in the definition of the outer contour range.

5.5.2 Sensitivity to grid-cell size

5.5.2.1 Quasi-steady flows

Figure 5.17 illustrates the sensitivity of the solution to spatial resolution for quasi-steady flow. Differences are most notable in the profile perpendicular to the main flow direction in the discontinuous part of the flow, i.e., at the front, which steepens as resolution increases.

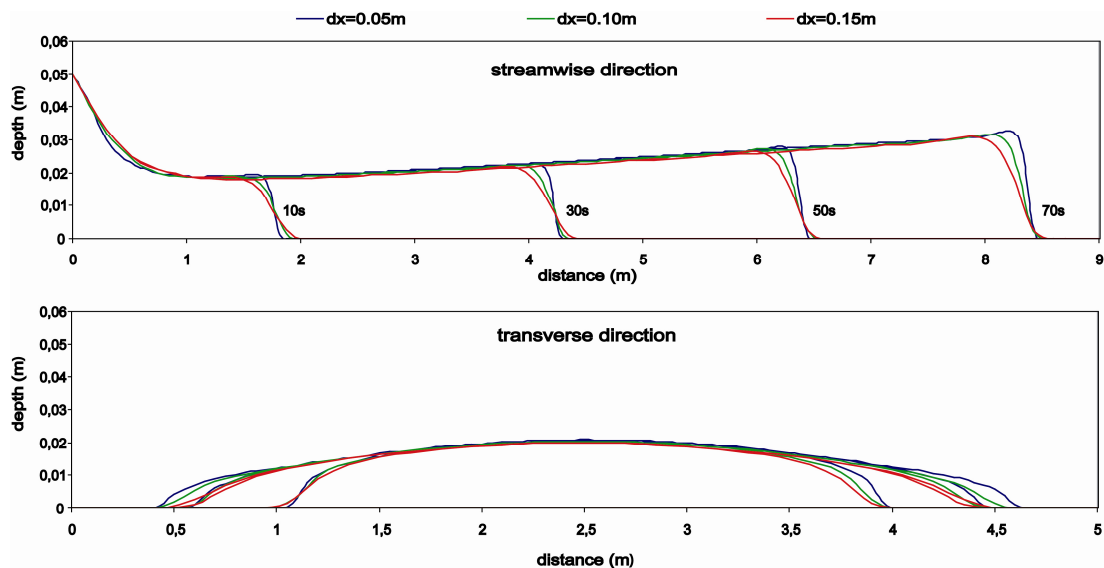


Figure 5.17: Computed solutions with **different spatial resolutions** for **quasi-steady flow** (chalk powder, uniform grain-size distribution). Upper graph displays depth of flow at 20 s intervals along axis parallel to the streamwise flow direction. Lower graph displays depth of flow at 20 s intervals along axis parallel to the transverse flow direction, and located 2m from the entry gate. In the transverse direction, the effect of stagnating spreading causes the lines of flow depth for a single solution (e.g. green lines) to overlap.

The sensitivity of the volume error to spatial resolution and choice of limiter for a quasi-steady flow is displayed in Figure 5.18. Again, the Superbee limiter is superior to the Minmod limiter, but, after an initially high volume error at the start of inflow into the computational domain, the volume error decreases rapidly to stabilize below 4% in all cases. The volume error decreases with increasing spatial resolution.

Figure 5.19 illustrates the sensitivity of the model to grid-cell size for quasi-steady flow. The difference in spatial dimensions of the deposit (length, width) between the solutions with grid-cell size Δx of 0.05m, 0.1m and 0.15m is small.

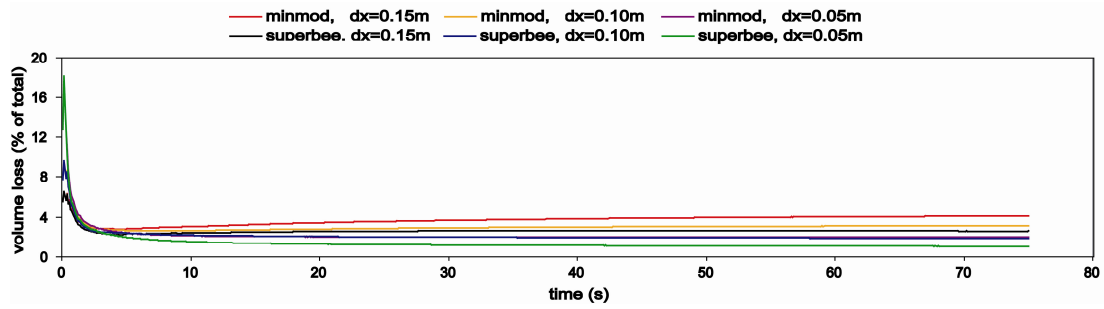


Figure 5.18: sensitivity of *volume error* (Equation 5.1) to *spatial resolution* for *quasi-steady flow* (chalk powder, uniform grain-size distribution).

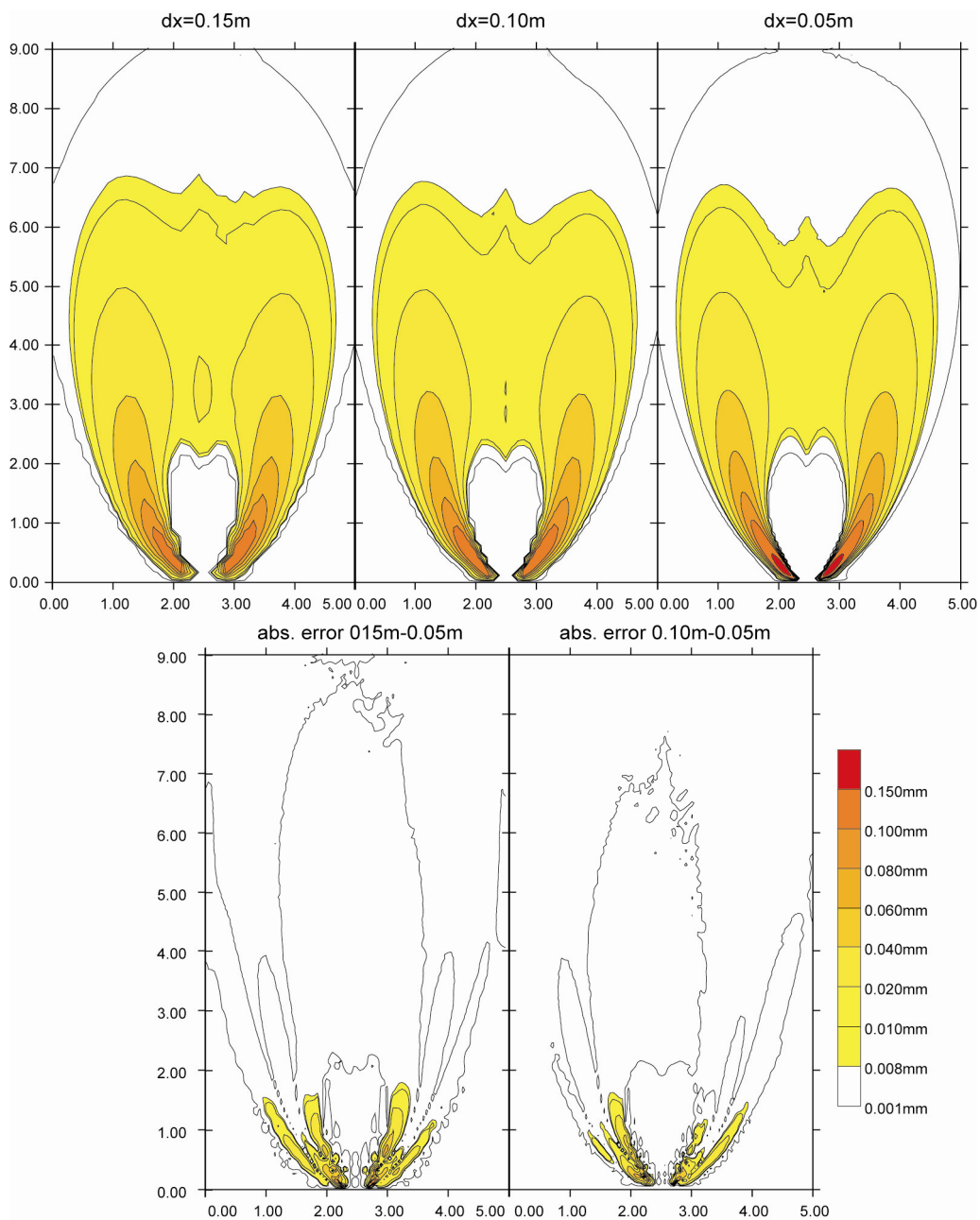


Figure 5.19: Sensitivity of *deposit thickness* to *spatial resolution* for *quasi-steady flow* (chalk powder, uniform grain-size distribution). Upper graphs: deposit thickness for different grid-cell sizes. Lower graphs: absolute difference (Equation 5.2) between the truth-case with grid-cell size of 0.05 m and solutions with larger grid-cell sizes.

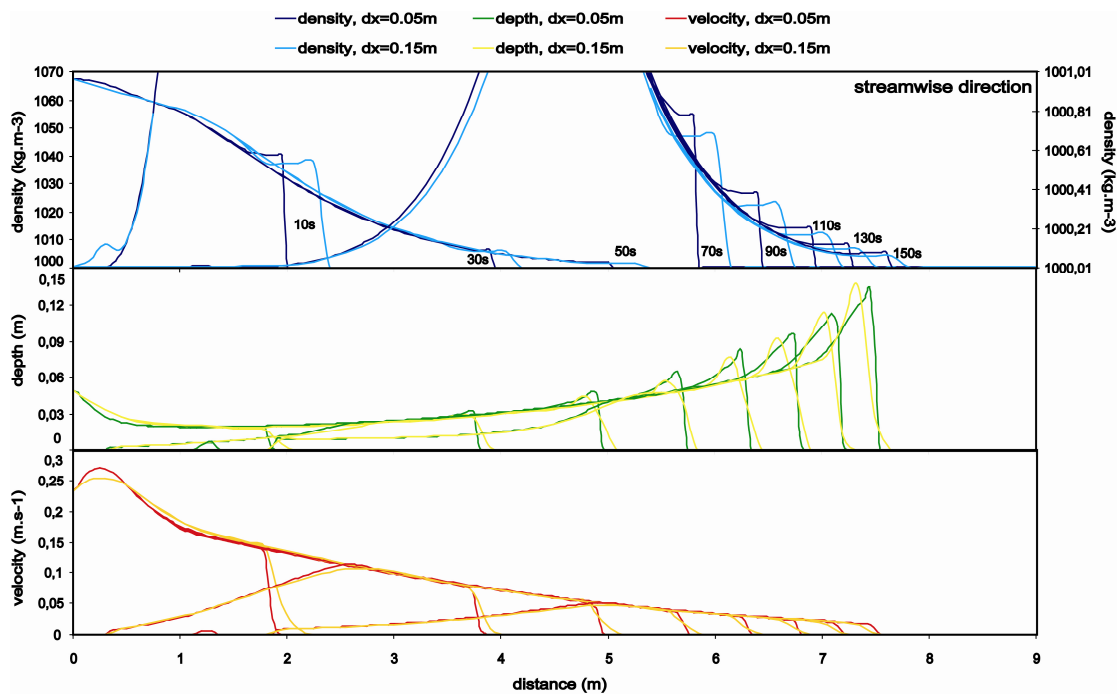


Figure 5.20: Computed solutions with *different spatial resolutions* for *waning flow* (quartz-silt, uniform grain-size distribution). Graphs display values of flow variables at 20s intervals along axis parallel to the streamwise flow direction. Upper graph: flow density; first 4 lines from the left scaled to left y-axis, rest scaled to right y-axis. Middle graph: flow depth. Lower graph: flow velocity. Inflow stops after 120s.

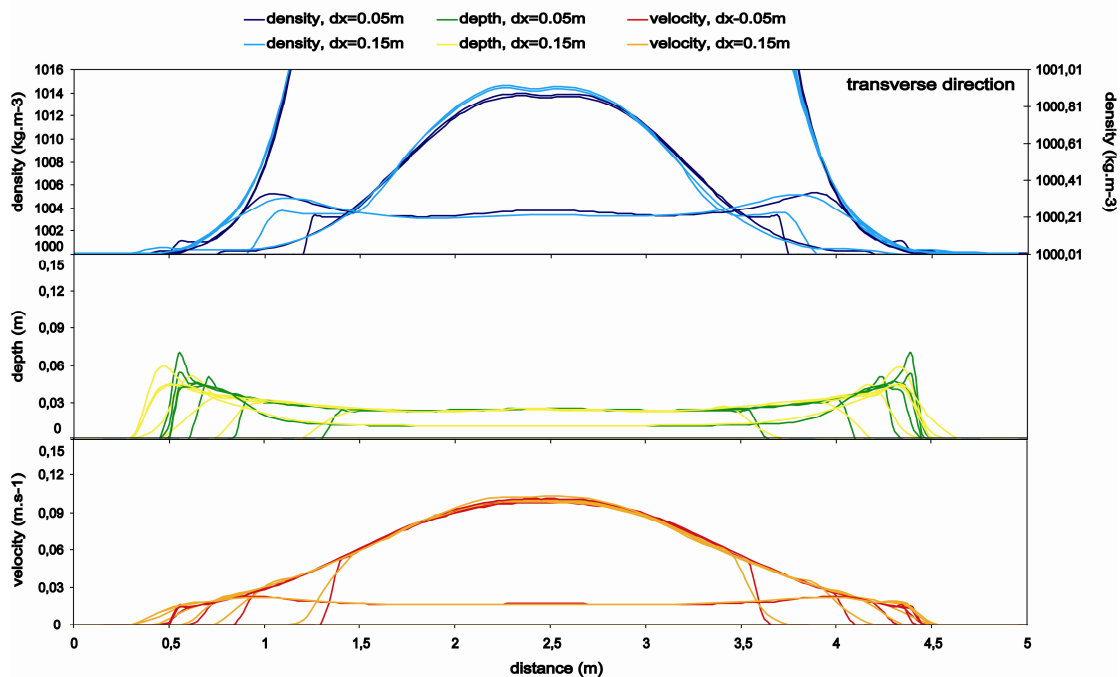


Figure 5.21: Computed solutions with *different spatial resolutions* for *waning flow* (quartz-silt, uniform grain-size distribution). Graphs display values of flow variables at 20s intervals along axis parallel to the transverse flow direction, and located 2m downstream of the entry gate. Upper graph: flow density; inner lines scaled to left y-axis, outer lines scaled to right y-axis. Middle graph: flow depth. Lower graph: flow velocity. Inflow stops after 120s. Spreading progressively stagnates, which causes the individual time lines of a solution to overlap.

There is a small visible difference in thickness (upper graphs) near the entrance of the flow into the computational domain, where high gradients in velocity in a direction perpendicular to the main flow direction cause rapid fallout of sediment and, consequently, levee-like features. These levee-like features are wider and slightly thinner in the solution with a grid-cell size of 0.15m than in the (truth-case) solution with a grid-cell size of 0.05m (compare lower left and lower right graphs in Figure 5.19).

5.5.2.2 Waning flows

The sensitivity to spatial resolution in the case of waning flow is illustrated in figures 5.20 and 5.21, in which the somewhat larger difference in flow densities (upper graphs) is most apparent. As mentioned, dilution to almost the density of the surrounding water causes the depth of the flow to increase and the velocity to decrease. At this point, the model seems to lose some of its accuracy, as is apparent by comparing low-resolution and high-resolution solutions, especially in profiles perpendicular to the main flow direction. Nonetheless, with values around 2% for the Superbee limiter, volume errors are acceptable (Figure 5.22).

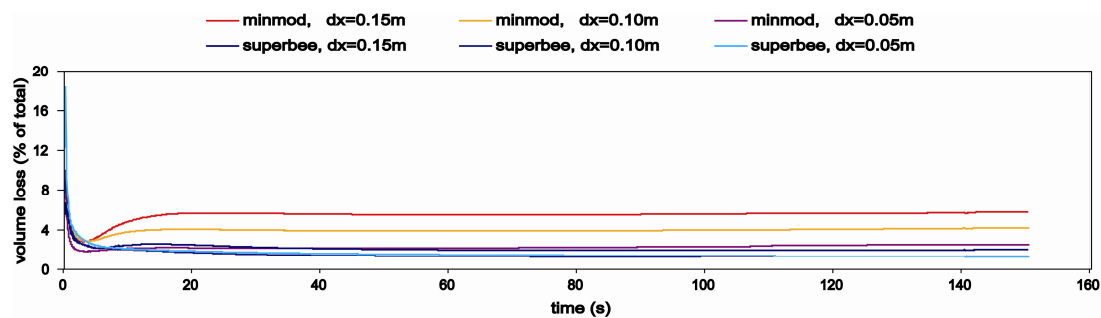


Figure 5.22: Sensitivity of *volume error* (Equation 5.1) to *spatial resolution* for waning flow (quartz-silt, uniform grain-size distribution)

Figure 5.23 illustrates the sensitivity of deposit thickness to spatial resolution for waning flow. Visibly, the geometry of the deposits is very similar, but differences in thickness between the deposits, although still largest in the vicinity of the entry point, occur over a larger area than in the case of solutions for waning flow with different temporal resolution (Figure 5.16). Nonetheless, absolute differences are still less than 1 mm (< 20% of the maximum thickness) in all but the most proximal parts of the deposits. Furthermore, a slight asymmetry in deposit geometry can be observed in the solution at low resolution (upper left graph) relative to the solution at high resolution (upper right graph).

Figure 5.24 illustrates the sensitivity of the model to spatial resolution when applied to experiments with multiple grain-size fractions. Differences in resolution do not significantly alter the spatial distribution of grain sizes (compare upper graphs). Differences in mean grain size occur at the fringes of the deposit, which are very thin, as well as near the inflow point (lower graphs), where the levees are most pronounced in the solution with the highest spatial resolution.

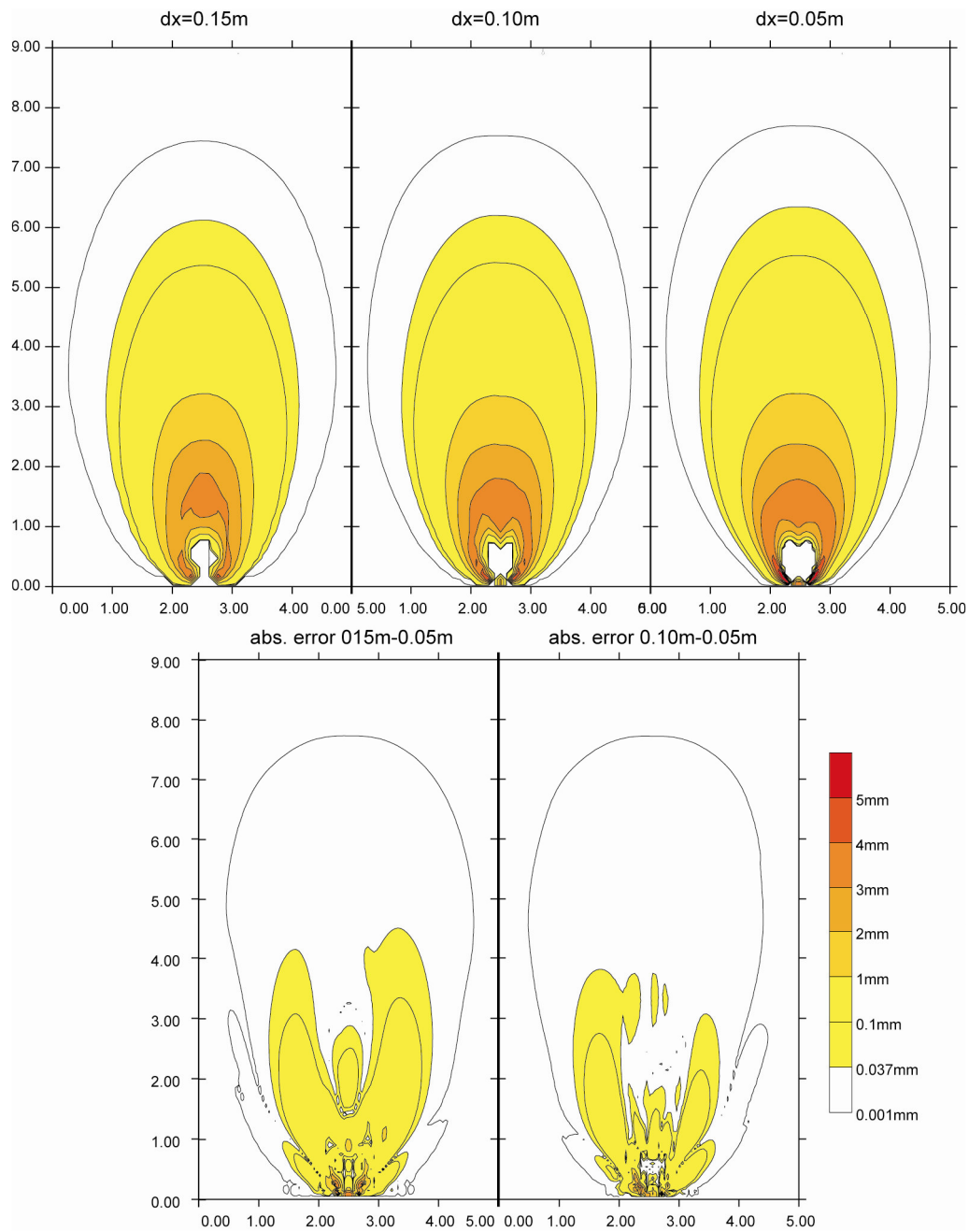


Figure 5.23: Sensitivity of **geometry of deposit** to **spatial resolution** for **waning flow** (quartz-silt, uniform grain-size distribution). Upper graphs: deposit thickness for different grid-cell sizes. Lower graphs: absolute difference (Equation 5.2) between the truth-case with grid-cell size of 0.05m and solutions with larger grid-cell sizes.

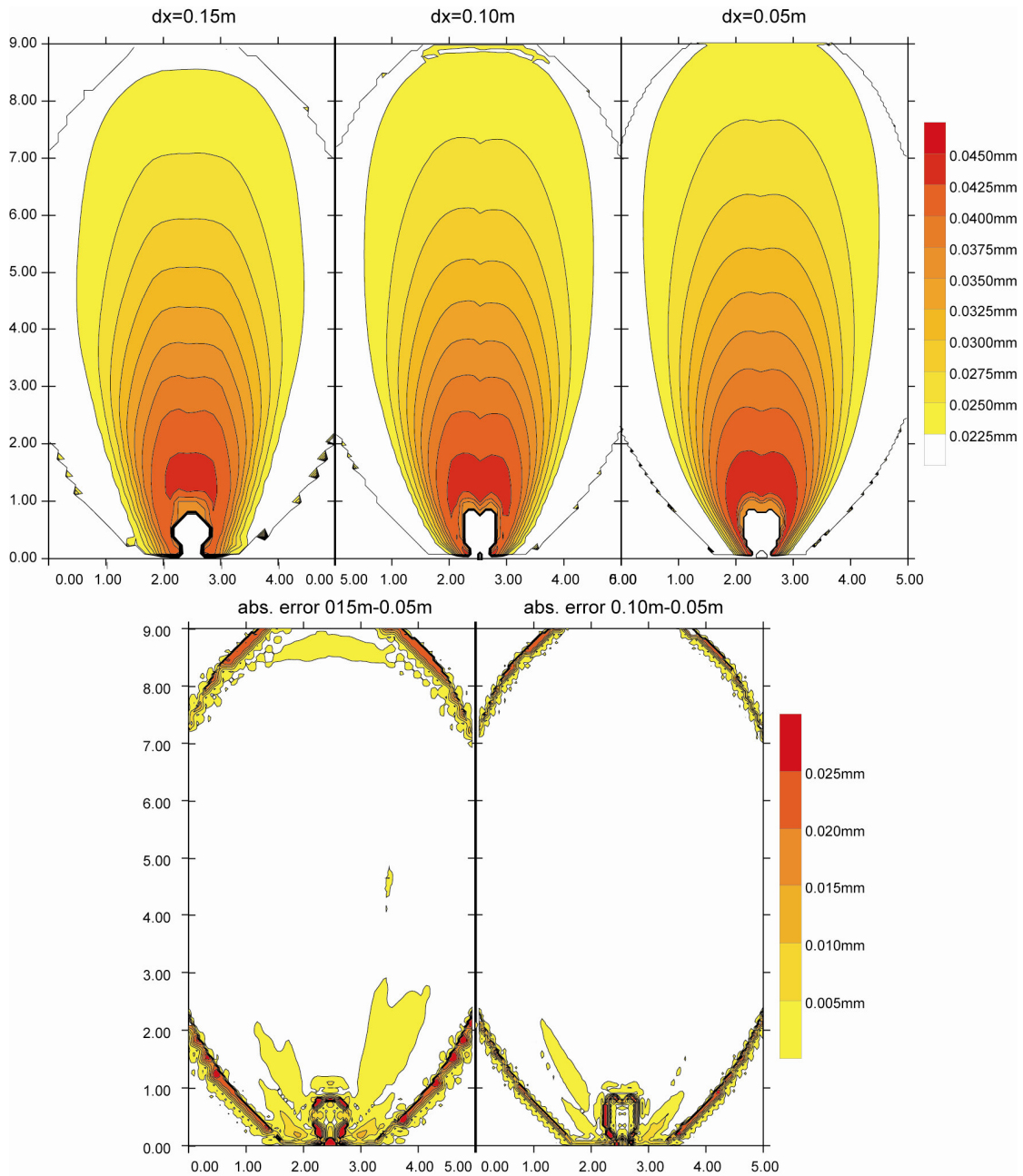


Figure 5.24: Sensitivity of mean **grain size of deposit** to **spatial resolution** for waning flow (quartz silt, three grain-size fractions). Upper graphs: mean grain size of deposit for different grid-cell sizes. Lower graphs: absolute difference (Equation 5.1) between the truth-case with grid-cell size of $0.05m$ and solutions with larger grid-cell sizes.

5.6 Discussion

Based on the results of the quantitative comparison between simulated results and data of the expansion table experiments of Luthi (1980a, 1980b, 1981), presented in the first part of this chapter, it seems justified to conclude that the accuracy of the model is very acceptable for laboratory-scale simulations. Simulated hydrodynamic behaviour and geometry of deposits are very similar to their experimental counterparts. Discrepancies in flow hydrodynamics and deposits are attributed to the following factors:

- The upstream part of the experimental basin, which does not comply with the assumption of an infinitely deep basin postulated in the model to adopt the “single-layer” formulation (Chapter 3, Paragraph 3.2.1).
- The large difference in the number of sample points between the simulations and the experiments.
- Possible irregularities in the experiments such as e.g. small differences in slopes.
- The discretization of the grain size distribution used in the experiments. The volume fraction of the three classes is likely to differ somewhat from the (continuous) grain-size distribution of the sediment itself. This has consequences for deposit geometry and the spatial distribution of grain sizes.
- Processes that are not explicitly taken into account in the model, such as the formation of turbulent eddies and instabilities related to the entrainment of water into the turbidity current (K-H instabilities, lobes, clefts).
- The sensitivity of model outcome to the drag coefficient c_D , the value of which must be estimated from a wide range (0.002-0.06) based on empirical data.

To gain insight into the behaviour of the solution at different resolutions, the sensitivity of the solution (depth, velocity, and density of flow, deposit thickness and grain size) was evaluated by comparing the validated high-resolution solution to solutions obtained using lower spatial and temporal resolution. From a hydrodynamic point of view, loss of accuracy seems more prominent for differences in spatial resolution than for differences in time resolution, especially at lower resolutions, i.e., with grid-cell size of 0.15m. Loss of accuracy mainly occurs in areas of discontinuous flow, with the largest differences in position, velocity and density of the flow occurring in areas where the flow spreads perpendicular to the main flow direction. Furthermore, in situations where the density of the flow approaches that of the surrounding fluid, flow depth increases to unrealistic values. Volumetric errors (Equation 5.1) remain within acceptable limits in all cases for which results are presented, with values ranging from around 0% to 4% when using the Superbee limiter. To further assess the sensitivity of the modelled deposits to differences in temporal and spatial resolution, absolute and relative volumetric errors between the high-resolution reference solution and solutions at lower resolution are calculated.

The absolute error between two solutions is calculated as the sum of the absolute errors at grid points:

$$\sum_i \sum_j \Delta \eta_{b(i,j)} = \sum_i \sum_j \left| \eta_{b(i,j)} - \hat{\eta}_{b(i,j)} \right| \quad (5.3)$$

where η_b is the thickness of the deposit of the solution for which the difference to the truth-case $\hat{\eta}_b$ is evaluated, and $\Delta \eta_b$ is the (absolute) difference.

Parameters i and j denote indices of grid cells in x- and y-directions respectively. The relative error between two solutions is calculated as:

$$\frac{\sum_i \sum_j \Delta \eta_{b(i,j)}}{\sum_i \sum_j \hat{\eta}_{b(i,j)}} = \frac{\sum_i \sum_j \left| \eta_{b(i,j)} - \hat{\eta}_{b(i,j)} \right|}{\sum_i \sum_j \hat{\eta}_{b(i,j)}} \quad (5.4)$$

Absolute and relative errors for solutions with different temporal resolution are plotted in Figure 5.25. Although the absolute errors for solutions involving quasi-steady and waning flow differ, the difference between the relative errors is small, even at low temporal resolution. The large difference in absolute error between the solutions for quasi-steady and waning flow is to be expected, because they constitute solutions to different experiments with different deposits. Interestingly, absolute and relative errors increase almost linearly with decrease in temporal resolution (Figure 5.25).

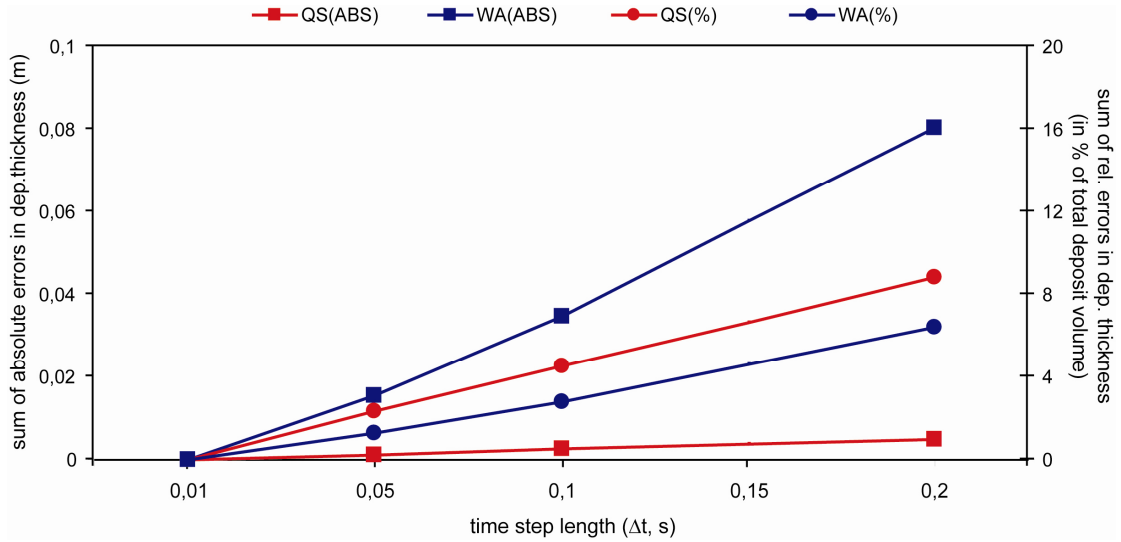


Figure 5.25: Absolute (Equation 5.3) and relative (Equation 5.4) errors in deposit thickness for solutions with time-step lengths of 0.2, 0.1, 0.05 and 0.01s. Lines connecting squares indicate absolute errors (left y-axis); lines connecting circles indicate relative errors (right y-axis). Red lines indicate errors of solutions for quasi-steady flow; blue lines indicate errors of solutions for waning flow.

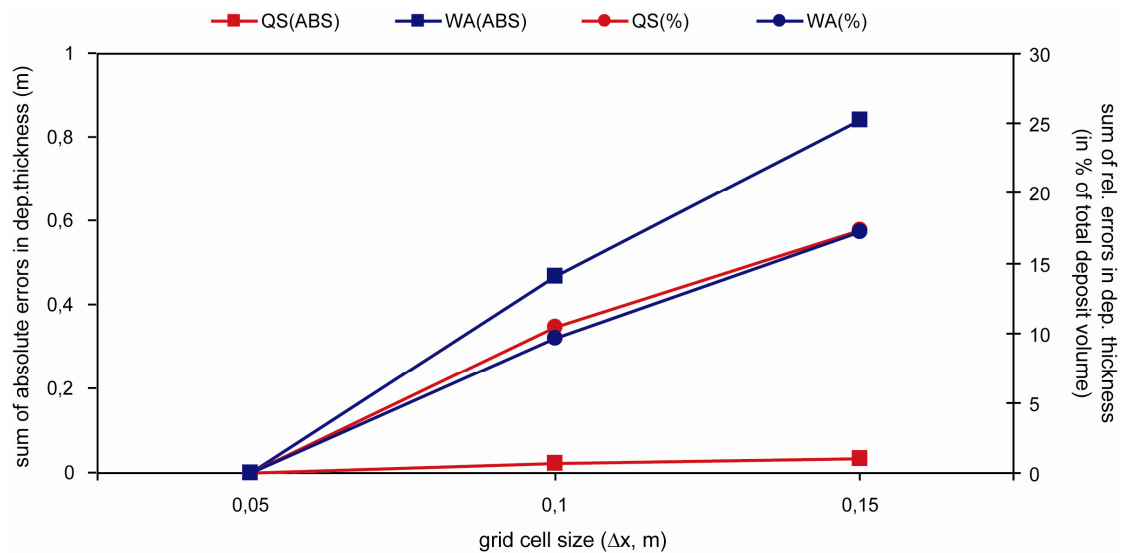


Figure 5.26: Absolute (Equation 5.3) and relative (Equation 5.4) errors in deposit thickness for solutions with grid-cell sizes of 0.15, 0.10, and 0.05m. Lines connecting squares indicate absolute errors (left y-axis); lines connecting circles indicate relative errors (right y-axis). Red lines indicate errors of solutions for quasi-steady flow; blue lines indicate errors of solutions for waning flow.

Similar error behaviour is displayed in Figure 5.26, in which absolute and relative errors for solutions with different spatial resolution are plotted. The absolute and relative errors increase almost linearly with a decrease in spatial resolution. Recognition of this trend is an important step in gaining insight into the behaviour of the model. It allows an estimation of the absolute and relative errors of a simulation which, in case of stratigraphic models involving multiple turbidity-current events, helps to decide upon the temporal and spatial resolution to be used.

6 QUALITATIVE VALIDATION EXPERIMENTS

6.1 *Introduction*

In this chapter, results are presented from two series of validation experiments, which were done to assess the capabilities of the model (Chapter 3) to simulate turbidity-current hydrodynamics and sedimentation. In these validation experiments, simulated hydrodynamic (flow depth, velocity, density) and sedimentation (deposit geometry, grain-size distribution) values were compared to data from small-scale experimental turbidity currents. The laboratory experiments were selected to test the model under conditions ranging from simple to complex while keeping in mind that the ultimate aim is to use the model to simulate the evolution of fan stratigraphy on geologic time scales in natural settings at the field scale.

The first set of validation experiments focuses on hydrodynamics and sedimentation patterns in the presence of complex topographic features, such as lateral and transverse flow obstructions, circular obstacles and flow constrictions. Experimental data published by Kneller (1995) and Kneller and McCaffrey (1995) allow for a qualitative assessment of simulation results.

The second set of validation experiments also involves complex topography. The initial topography has the form of a bowl-shaped basin that is characteristically formed by salt-withdrawal, and is further accentuated during the experiment due to simulated tectonic activity reflecting continued salt-withdrawal. In the validation experiment, simulated results are compared to data from an experiment (Violet et al., 2005), in which stratigraphy is created that is meant to be representative of a subsiding basin with a turbidite fan system such as found e.g. in the Gulf of Mexico. This experiment may be regarded as the ultimate validation test for the model because it combines a sequence of flows with different initial depths, velocities and densities with complex topography that changes in time. Furthermore, the grain-size distribution of the sediment contains three size fractions. The aim of this second validation experiment is to compare the hydrodynamic behaviour of simulated turbidity currents to observations, and to compare the simulated stratigraphy to experimental data, based on geometry and grain size of individual beds and bed successions.

6.2 *Complex topography*

Simulation of turbidity currents that flow over natural topography containing complex features commonly encountered in reservoir characterization studies, such as lateral and transversal (basin-bounding) slopes, diapirs and constrictions, is notoriously difficult. The experiments of Kneller (1995) and Kneller and McCaffrey (1995) will be used to compare simulated results to measured data. These experiments were conducted to investigate the effects of changes in topographic gradient and confinement on flow behaviour (acceleration, deceleration) and on depositional patterns (Kneller, 1995).

6.2.1 Experimental set-up

Figure 6.1 is a sketch of the experimental set-up. A mix of brine and solid grains, brought in suspension through stirring, was released from a mixing tank (lock box) by lifting of a lock gate. Upon release, the suspension flow travelled through the horizontal supply channel and onto the expansion table, where the flow spread radially. Part of the sediment was deposited in the lock box and the supply channel, which complicates a quantitative volumetric comparison of the simulated deposits with measured data. This would require data on the actual release of the suspension from the lock box as well as the flow through the supply channel in the simulations. As the volume of sediment actually discharged onto the expansion table is not specified in the publication, the region of interest of the model is limited to the tank floor only (i.e., it excludes the lock box, the supply channel and the moat around the expansion table).

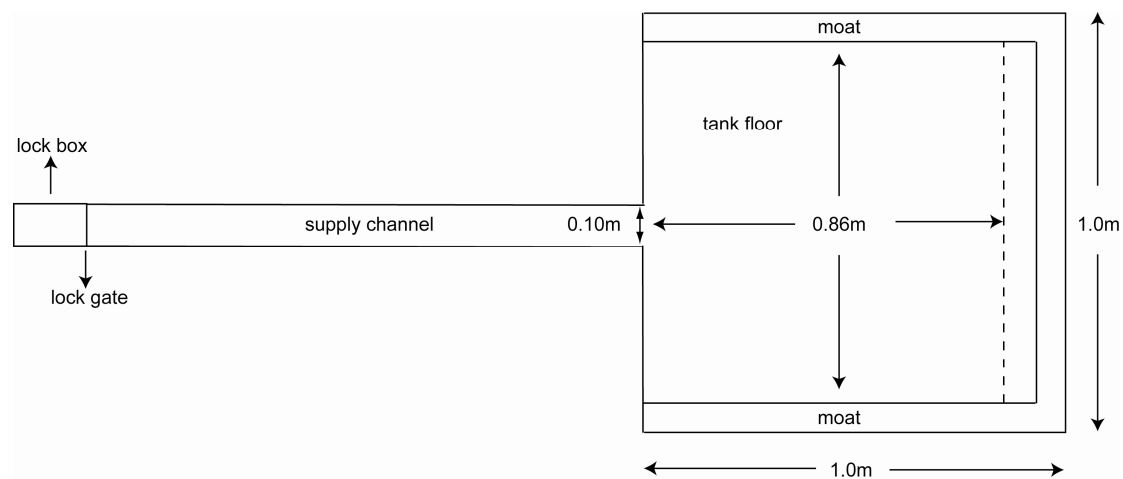


Figure 6.1: Experimental set-up (Kneller, 1995).

The mix of brine and solid grains is somewhat unconventional in experimental work on turbidity currents. By using brine, the settling velocity of the grains is slower due to the higher density (1090 kg/m^3) and viscosity of the brine. Furthermore, the grains consist of acryl with a density which is much lower than that of quartz (1180 kg/m^3). The use of an interstitial fluid with a density different from the tap water in the tank through which the turbidity current propagates is not supported by the model, i.e., the model was not designed to be used in situations where the interstitial fluid differs in density from the ambient fluid. Since a detailed quantitative comparison is difficult because of insufficient data on the volumetrics of the deposits on the tank floor versus the volumes deposited in the supply channel and the lock box, we decided to scale the flows such that they are similar in densimetric Froude number to the experimental flows. Furthermore, the velocities and head heights of the simulated flows were “conditioned” to measured values specified by Kneller (1995).

Initial parameters values used in our simulations are listed in Table 6.1, together with the original experimental values. The median grain size of $96.7 \mu\text{m}$ of the sediment (quartz) in the model was calculated using Dietrich’s formula (Dietrich, 1982), using the settling velocity of 0.68 cm/s specified by Kneller for the sediment analogue in brine of 1090 kg/m^3 density. Furthermore, to preserve the hydrodynamic

characteristics (e.g. densimetric Froude number) of the experimental flows, the density of the simulated flows was made equal to the density of the experimental flows, i.e., 1103.7 kg/m^3 . Although the total discharged volume of the suspension is made equal to that of the experimental flows, the volume of sediment transported by the simulated flows (6.28 % by volume) is smaller than that of the experimental flows (15.22 % by volume), since natural sediment is much denser than the sediment analogue used in the experiments. Therefore, and for reasons previously stated, a detailed quantitative comparison of deposit thicknesses is not possible. The objective of this validation experiment is to assess the capabilities of the model in reproducing patterns in deposits that develop when turbidity currents interact with complex topographic features. Hence, this validation experiment is qualitative in nature rather than quantitative.

parameter	$\rho_w(\text{kg/m}^3)$	$\rho_s(\text{kg/m}^3)$	$\rho_f(\text{kg/m}^3)$	$C_{in}(\%)$	$W_s(\text{cm/s})$	$D_{50}(\text{mm})$	$U_{in}(\text{m/s})$	$h_{in}(\text{m})$	$h_{0.11}(\text{m})$	$h_{0.71}(\text{m})$
model	1000.00	2650.00	1103.68	6.28	0.680	96.7	0.12	0.12	0.0489	0.0385
experiment	1090.00	1180.00	1103.69	15.22	0.680	600	?	?	0.0490	0.037

Table 6.1: Initial conditions for experiment and model simulations

The flow depth and velocity at the channel mouth have not been specified by Kneller (1995). An approximate head velocity of 0.20 m/s was mentioned along the centreline of the flow, but the precise location of the velocity measurement is not specified. Head heights were measured at 0.11 m and 0.71 m from the channel mouth. The initial velocity and flow depth used in the simulations were chosen such that flow depths coincide with measured values at specified locations. As such, an initial flow depth of 0.12 m and velocity of 0.12 m/s, together with the initial suspended sediment concentration of 6.28 % by volume, result in a densimetric Froude number of 0.34 at the channel mouth. The initial Reynolds number of the simulated flows is calculated to be $1.3 \cdot 10^4$, with the value of kinematic viscosity of the suspension determined from the empirical relation given by Davidson et al. (1977) for the dynamic viscosity of clay-free suspensions:

$$\mu_s = \mu(1 - 1.35C)^{-2.5} \quad (6.1)$$

These values of Froude and Reynolds number are roughly equal to the values of 0.3 and $1.0 \cdot 10^4$ respectively, mentioned by Kneller (1995), which implies that the simulated flows are properly scaled to the experimental flows. Furthermore, the height of the head of the flow, in relation to the height of the obstacle, is a measure of the potential of the flow to either overcome an obstacle or be diverted by it. Care was taken to ensure that simulated head heights were equal to specified values upon collision with the obstacle. In all simulations, the grid resolution was 43 by 43 cells, which corresponds to a (square) grid-cell size of 2 cm. The time-step length was set to 0.1 seconds, and the initial porosity of the deposit was set to 0.4.

6.2.2 Unobstructed flow

Prior to evaluating simulation results for turbidity currents flowing over complex topography, a comparison is made for unobstructed flow. Figure 6.2 displays contour maps of the three simulated deposits and the experimental base case. The simulated deposits relate to flows with different values of the drag coefficient c_D . As previously noted, the model outcome is quite sensitive to the value of c_D . Major differences in deposit geometry between the simulations include the size of the non-depositional area, the presence of levee-like rims in the vicinity of the entry point into the model domain and the length-to-width ratio of the deposit, which decreases as c_D increases. A higher value of c_D increases the competence of the simulated flows to keep grains suspended, even though it has a negative effect on the velocity of the flow.

Furthermore, in the deposit simulated with $c_D=0.018$, the area of non-deposition is actually traversed by a narrow ridge of sediment, a feature which is much less pronounced in the deposit simulated with $c_D=0.028$. This feature is caused by density differences in the flow. In a waning turbidity current, the density is highest in the central part of the turbidity current and decreases towards the edges in all directions. Because the suspension fall-out rate is proportional to suspended sediment concentration, the rate of deposition is highest in the central part of the turbidity current, provided the shear velocity allows for deposition to occur. For high values of c_D in the model, this will not be the case, whereas for low values of c_D the magnitude of the shear velocity is such that deposition occurs everywhere in the simulated turbidity current. For intermediate values of c_D , the narrow ridge of sediment is caused by subtle density differences in the flow. This ridge-like feature is also visible in the experimental deposit; it separates two areas of non-deposition, similar to the deposit simulated with an intermediate value of $c_D=0.018$.

Other features present in both the experimental and the simulated deposit are the levee-like rims to the left and right of the entry point and the lobe-like geometry of the deposit. When the hydrodynamic constraints are taken into account, i.e., measured flow depths at 0.11 m and 0.71 m from the entry point, the simulation with $c_D=0.015$ produces the best fit to measured data (Figure 6.3). However, the shape of the simulated deposit is still markedly different from the experimental deposit. In fact, and contrary to the simulated deposit, the experimental deposit does not have the lobe-like geometry which is characteristic of a turbidity current. As such, it is questionable as to whether the experimental flow may be considered a turbidity current, i.e., with turbulence as the primary particle-support mechanism. Upon release of the suspension from the lock-box, the concentration is about 16%. At such concentrations, particle interactions probably contribute significantly to keeping the grains in the flow, especially when they are coarse and uniform in size, as is the case in the experiment. Furthermore, the higher viscosity of the brine, which is used as interstitial fluid, also hampers turbulence development. Therefore, it seems justified to conclude that turbulence may not have been the primary particle-support mechanism. This severely limits the ability of the model to simulate the experimental flow, since the model is based on particle-support by turbulence alone.

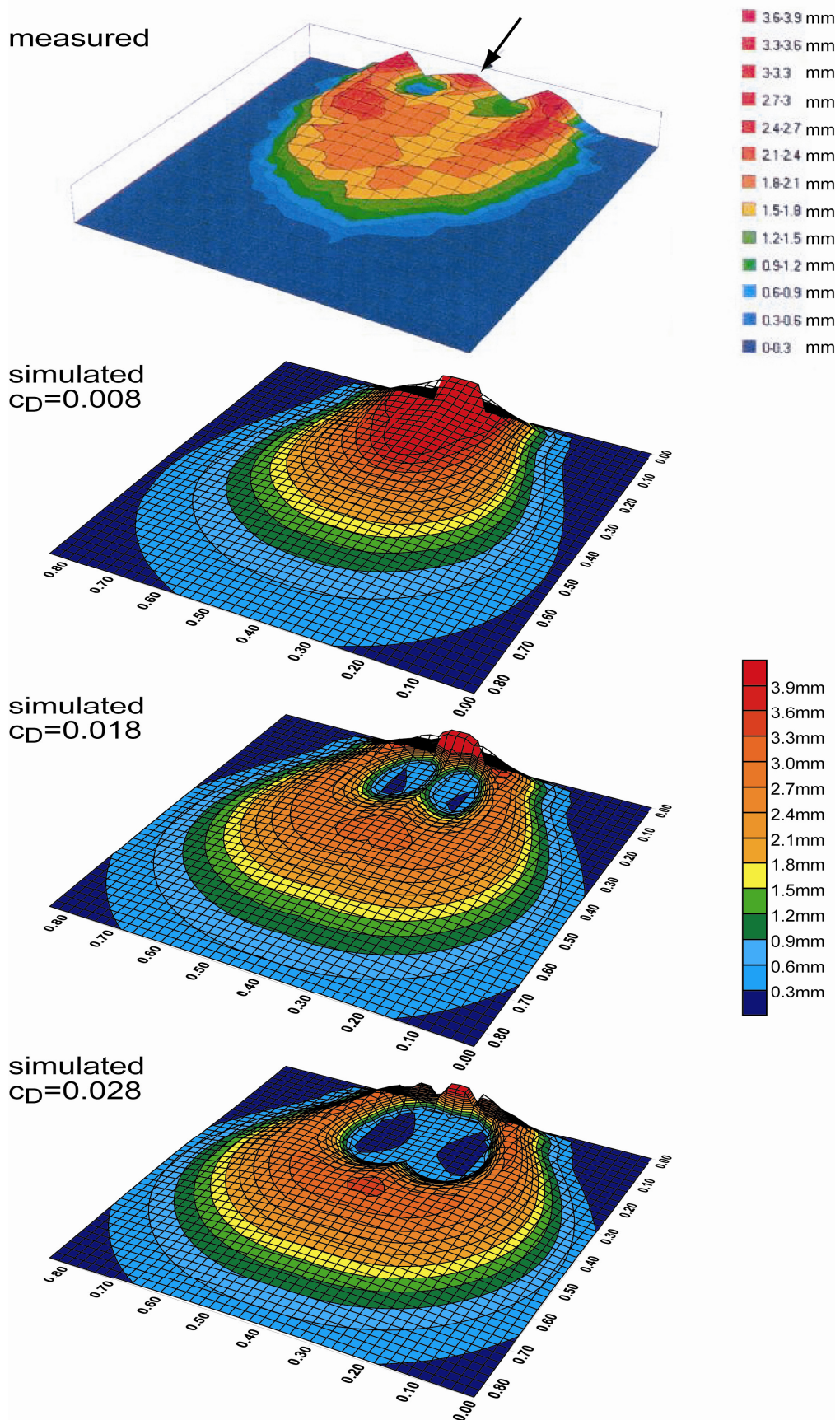


Figure 6.2: Comparison of simulated deposit thickness to measured data for unobstructed flow with different values of c_D . The figure at the top of the page is the contour map of the experimental deposit (Kneller, 1995).

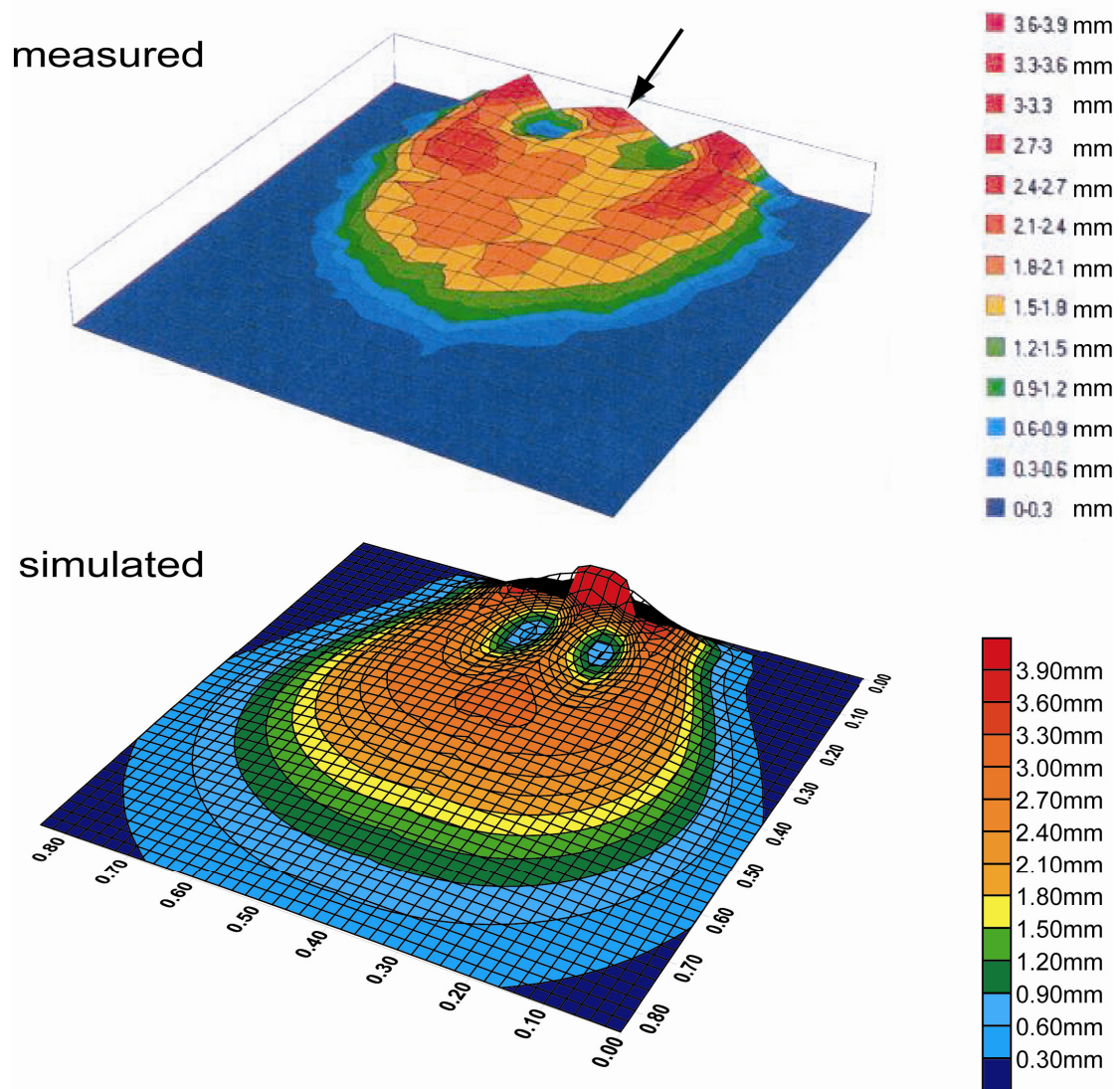


Figure 6.3: Comparison of simulated deposit thickness to measured data (Kneller, 1995) for unobstructed flow. $c_D=0.015$.

A remark must also be made on the value of approximately 0.3 of the densimetric Froude number given by Kneller (1995). When calculating the densimetric Froude number using values given by Kneller (1995) for flow depth, velocity, density of the sediment analogue and the brine, and volumes of solid and fluid released, densimetric Froude numbers well above unity are obtained ($Fr \approx 2.5$). To obtain a densimetric Froude number of 0.3, flow velocities must be about 10 times lower than the 0.2 m/s given by Kneller. Since the values of flow depth, velocity and density used to calculate the reported Froude number are not specified, the scaling must be considered tentative.

6.2.3 Perpendicular obstacle

Figure 6.4 displays contour maps of simulated and measured deposit thicknesses for a turbidity current encountering a transverse linear obstacle. The simulated topographic setting is that of a confined linear sub-basin with a lateral entry point opposite a frontal slope (Kneller, 1995). The height of the obstacle (62.5 mm) is approximately 1.5 times the height of the head as it first encounters the obstacle. The hydrodynamic evolution of the turbidity current is illustrated in six shaded-relief maps (see figure 4.14), which represent snap shots of the flow at 0.5 s intervals. The shaded-relief maps are essentially aerial views of the flow, with a light source from the northwest at an angle of 45° to the horizontal plane.

As can be seen, the evolution of the turbidity current (Figure 6.5) is similar to that of the unobstructed flow situation, up to the point where it reaches the obstacle. While trying to cross the obstacle, the flow velocity decreases and the head height increases. Prior to reaching the crest of the obstacle, the turbidity current gets deflected backwards and sideways. A small part of the total discharged volume overflows the obstacle to reach the downstream part of the model domain. This development of the turbidity current is reflected in the deposit (Figure 6.4). The bulk part of the sediment is deposited upstream of the obstacle, with a maximum thickness near the upstream edge of the obstacle. Both the simulated and the measured deposit display a ridge-like locus of deposition parallel to the linear obstacle.

From the published contour map (Kneller, 1995), it is difficult to assess if the experimental deposit is also partly draped over the upstream part of the obstacle, as is the case for the simulated deposit. Furthermore, Kneller (1995) observed narrow areas of non-deposition immediately upstream and downstream of the obstacle, which, in the upstream case, can also be observed in the simulated deposit (rightmost contour map of Figure 6.4, and Figure 6.6).

The effect of obstacle height on deposition is illustrated in Figure 6.6. As the obstacle height increases relative to the height of the head of the turbidity current, less sediment is transported into the model domain downstream of the obstacle. Upstream of the obstacle, and lateral to it, deposition increases. The narrow areas of non-deposition (white arrows in Figure 6.6) can only be observed in the simulations with obstacle heights of 62.5 mm and 93.3 mm, which suggests that they are associated to the magnitude of the topographic gradient of the upstream side of the obstacle. Possibly, normal incidence of the flow to the obstacle in combination with a low aspect ratio (obstacle width:obstacle height) results in strong reflection to a point where the velocity of the reverse flow is sufficiently high to prevent deposition and, in some cases, erode the bed.

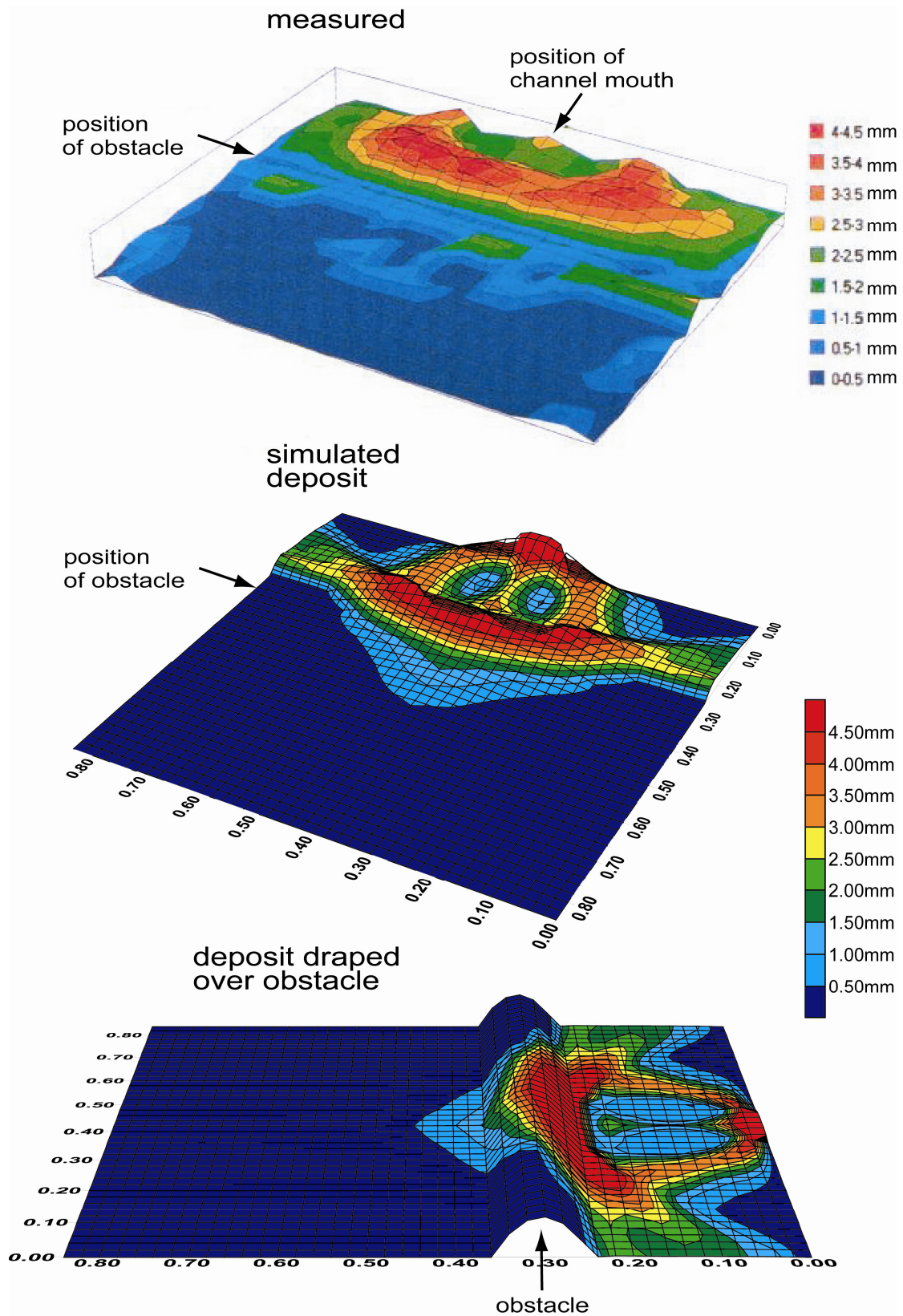


Figure 6.4: Comparison of simulated deposit thickness to measured data for a linear obstacle perpendicular to the main flow direction. Top: contour map of measured deposit thickness (Kneller, 1995). Middle: contour map of deposit thickness of simulated deposit. Bottom: topographic surface (incl. obstacle) partially covered by the simulated deposit. Obstacle height: 62.5mm, obstacle width: 11.7mm, ratio height of obstacle/height of head: 1.45, $C_D = 0.015$

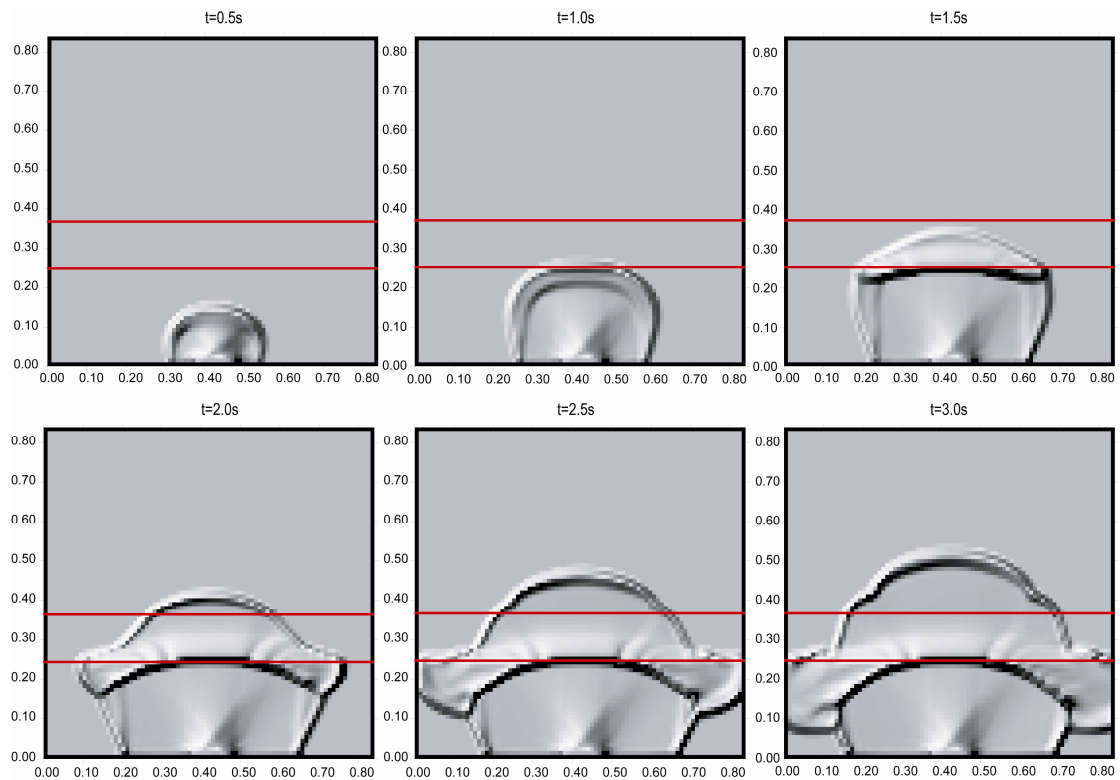


Figure 6.5: Shaded-relief maps of flow depth, illustrating the hydrodynamic evolution of the simulated turbidity current as it interacts with the transverse linear obstacle. Outer edges of obstacle are marked by red lines

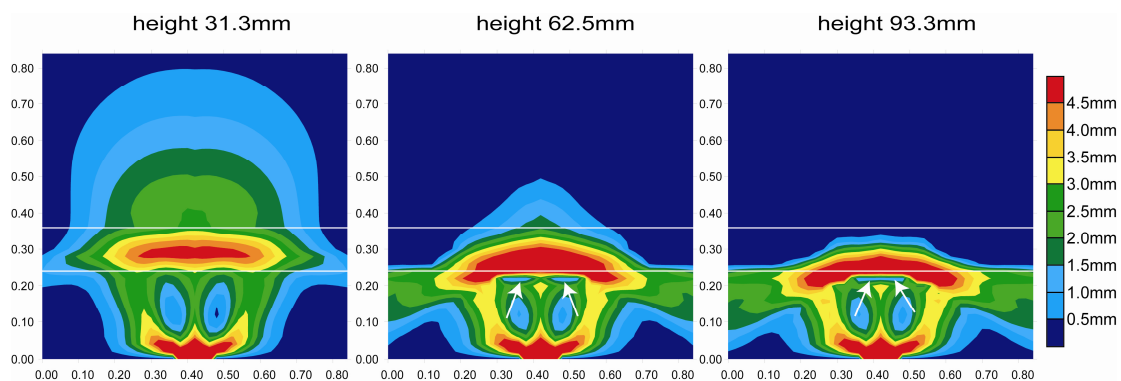


Figure 6.6: Effect of obstacle height on deposition, for obstacle heights of 31.3 mm (0.73 times head height), 62.5 mm (1.45 times head height) and 93.3 mm (2.17 times head height). Outer edges of obstacle are marked by white lines. White arrows indicate narrow areas of non-deposition (see main text).

6.2.4 Circular obstacle

Figure 6.7 displays the contour maps of simulated and measured deposit thickness for a turbidity current interacting with a circular obstacle. The simulated topographic setting is that of a seafloor deformed by salt diapirism, such as e.g. in the Gulf of Mexico.

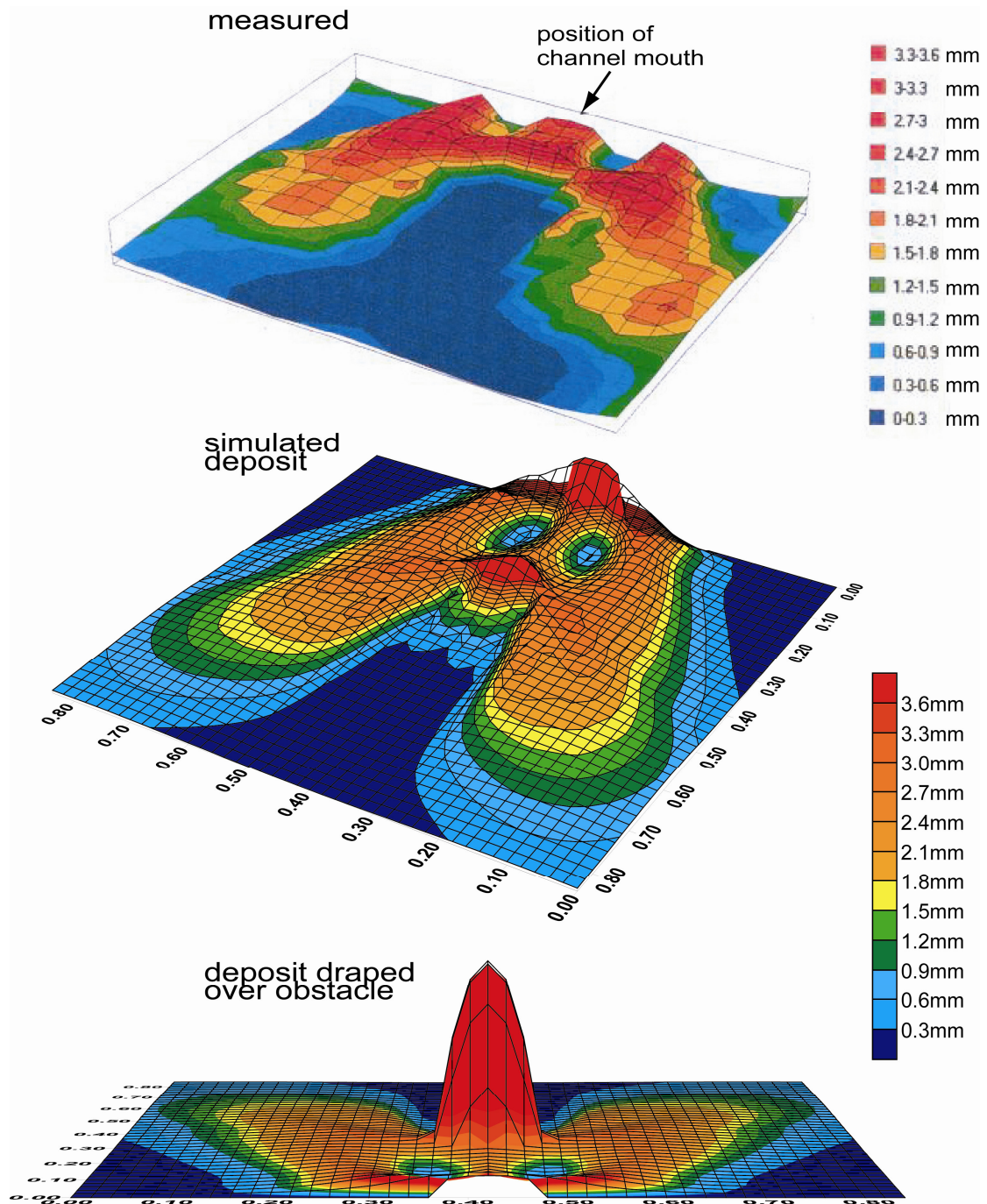


Figure 6.7: Comparison of simulated deposit thickness to measured data for a turbidity current encountering a circular obstacle. Top: contour map of measured deposit thickness (Kneller, 1995). Middle: contour map of deposit thickness of simulated deposit. Bottom: topographic surface (incl. obstacle) partially covered by the deposit. Obstacle height: 62.5 mm, obstacle width: 117 mm, ratio height of obstacle/height of head: 1.45, $C_D = 0.015$.

The graph at the top is a contour map of measured deposit thicknesses (Kneller, 1995). Obstacle height in this particular experiment was 62.5 mm (approx. 1.5 times the head height) and width of the obstacle was 117 mm. Qualitatively, the match between simulated deposit and the experimental “ground truth” case is acceptable. The overall deposit geometry is similar, with an area of non-deposition on the lee-side of the obstacle, a maximum deposit thickness just upstream of the obstacle, and lobe-like areas of high deposition adjacent to the obstacle.

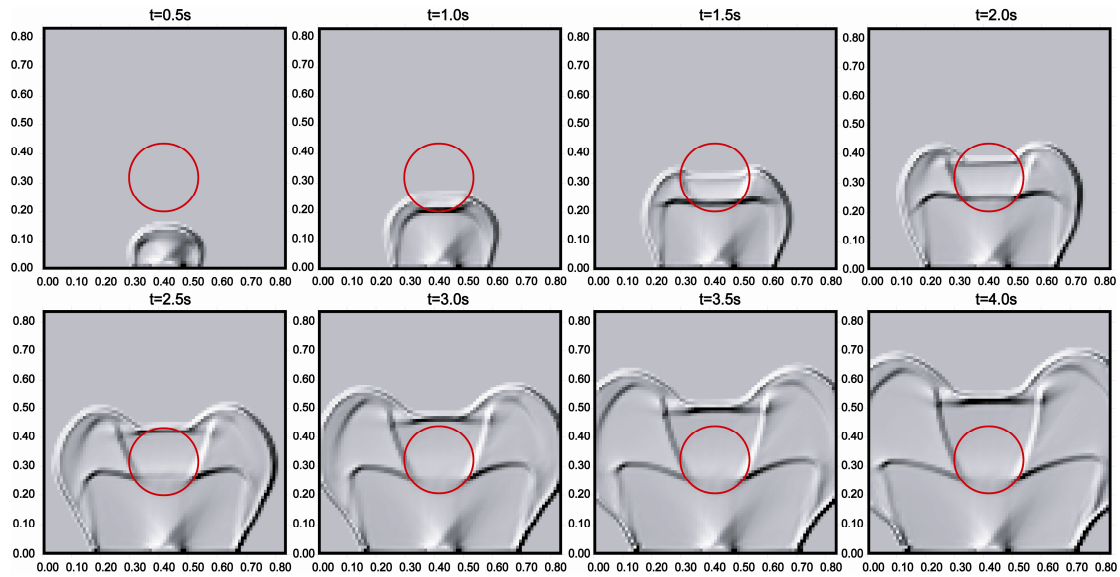


Figure 6.8: Shaded-relief maps of flow depth, illustrating the hydrodynamic evolution of the simulated turbidity current as it interacts with a circular obstacle of height 62.5 mm and width 117 mm. Outer edge of obstacle is marked by red circle

The hydrodynamic evolution of the simulated turbidity current is illustrated in Figure 6.8. Upon collision with the circular obstacle, the flow is split up and deflected. Whether the flow is partially or completely deflected depends on the height of the obstacle in relation to the height of the head of the turbidity current. The effect of obstacle height on flow deflection may be inferred from Figure 6.9. As the height of the obstacle increases, the angle between the loci of deposition adjacent to the obstacle increases, as does the area of non-deposition on the lee-side of the obstacle. For an obstacle height of more than twice the height of the head (rightmost graph in Figure 6.9), the turbidity current is unable to surmount the obstacle, as is evidenced by the absence of sediment on the lee-side of the obstacle.

The angle of deflection depends not only on the height of the obstacle, but also on the width. This is best illustrated by comparing the simulated deposit in Figure 4.16 with a width of 117 mm (aspect ratio of 1.87) to that in Figure 4.18 with equal height of 62.5 mm (second graph from the right) but with a width of 225 mm (aspect ratio of 3.6). In the latter case, the angle between the lobe-like deposits adjacent to the obstacle is much wider, implying that the angle of deflection increases with aspect ratio. Further observations reported by Kneller (1995) include the presence of areas of non-deposition in separation zones on the downstream quarters of the obstacle. Evidence for this feature is also present in the simulated deposits for obstacle heights of 31.3 mm, 62.5 mm and 93.3 mm. It is probably best visible in the rightmost graph of Figure 6.9, in which small blue spots to the left and right of the obstacle indicate close to zero deposit thickness.

Simulations of turbidity currents encountering obstacles with heights of 93.3 mm and higher reveal other interesting features. One such feature is a ridge of sediment upstream of the obstacle, which extends at an angle of almost 90° to the angle of incidence of the flow (white arrows in Figure 6.9). When comparing the four graphs in Figure 6.9, the ridge may be considered a logical continuation of the depositional trend that is observed upstream of the obstacle.

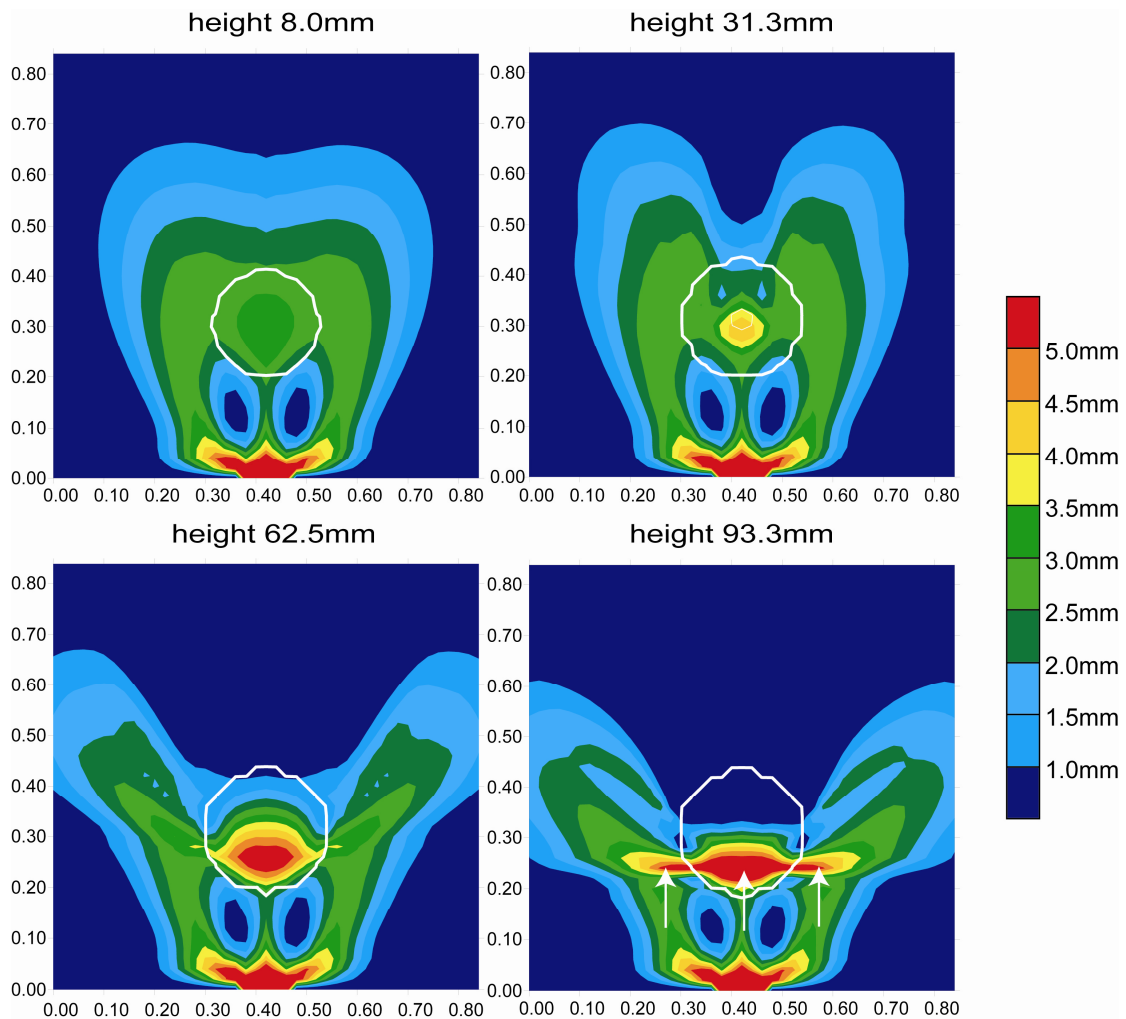


Figure 6.9: Effect of obstacle height on deposition, for obstacle heights of 8 mm (0.19 times head height), 31.3 mm (0.73 times head height), 62.5 mm (1.45 times head height) and 93.3 mm (2.17 times head height). Outer edge of obstacle is marked by white circle. Ridge of sediment upstream of obstacle indicated with white arrows. Obstacle width 225 mm, $c_D = 0.015$.

As the obstacle height increases, the angle between the loci of deposition adjacent to the obstacle increases. At some point, these loci of deposition merge with the one upstream of the obstacle to form a ridge.

6.2.5 Flow constriction

Figure 6.10 displays the contour maps of simulated and measured deposit thickness for a turbidity current passing through a narrow gap in a transverse linear obstacle. This situation might be representative of turbidity current encountering the distal end of a confined linear sub-basin where previous flows have already begun carving out a canyon towards a sub-basin further downstream. The graph at the top is a contour map of measured deposit thicknesses (Kneller and McCaffrey, 1995). Obstacle height was 62.5 mm, which is sufficiently high to prevent the bulk part of the flow from overflowing it (see also Figure 6.6).

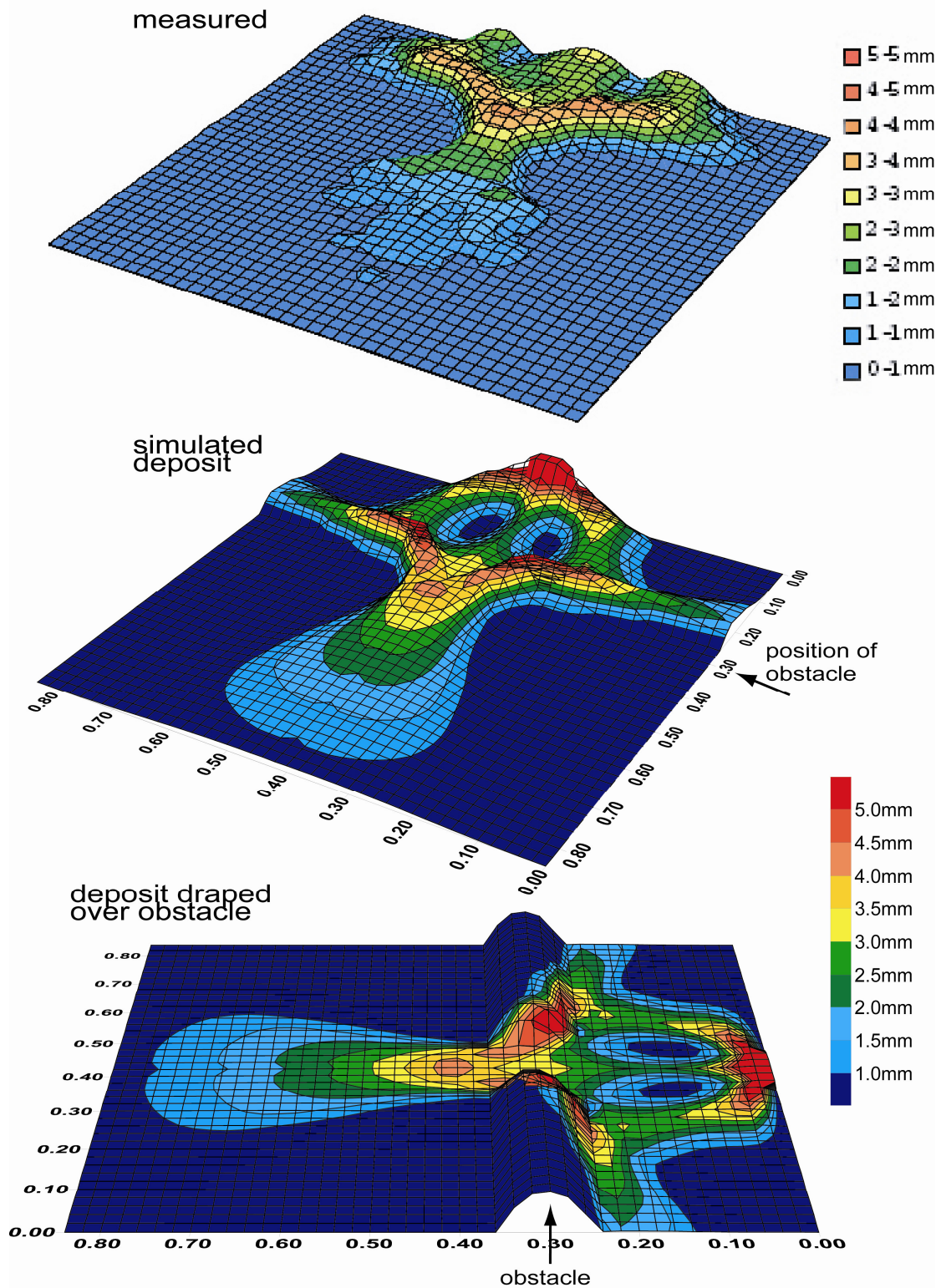


Figure 6.10: Comparison of simulated deposit thickness to measured data for a turbidity current encountering a constricting obstacle. Top: contour map of measured deposit thickness (Kneller and McCaffrey, 1995). Middle: contour map of deposit thickness of simulated deposit. Bottom: topographic surface (incl. obstacle) partially covered by the deposit. Obstacle height: 62.5 mm, obstacle width: 117 mm, ratio height of obstacle/height of head: 1.45, $c_D = 0.015$

Visually, the simulated deposit matches well with the experiment. Areas of non-deposition and high deposition are reproduced, albeit not in exactly the same position. A major difference that may highlight a possible model deficiency is in the position of the area of maximum sediment thickness induced by the constriction. Kneller and McCaffrey (1995) report the location of this area to be in the upstream half of the constriction, suggesting an inferred ability of a turbidity current to “sense” what is happening to the fluid in front of it.

In the simulated deposit the area of maximum sediment thickness is located immediately downstream of the constriction, but shifts progressively upstream when higher values of c_D are used. In the model, the net rate of deposition at any given location in the flow mainly depends on the local concentration of suspended sediment and the value of c_D (flow competence). Higher values of c_D result in faster flow deceleration and lower velocities upon reaching the obstacle. Furthermore, higher values of c_D also allow grains to be kept in suspension longer after inflow into the model domain; hence the local concentration upon reaching the constriction is higher. The combined effect results in the observed upstream shift of maximum deposit thickness.

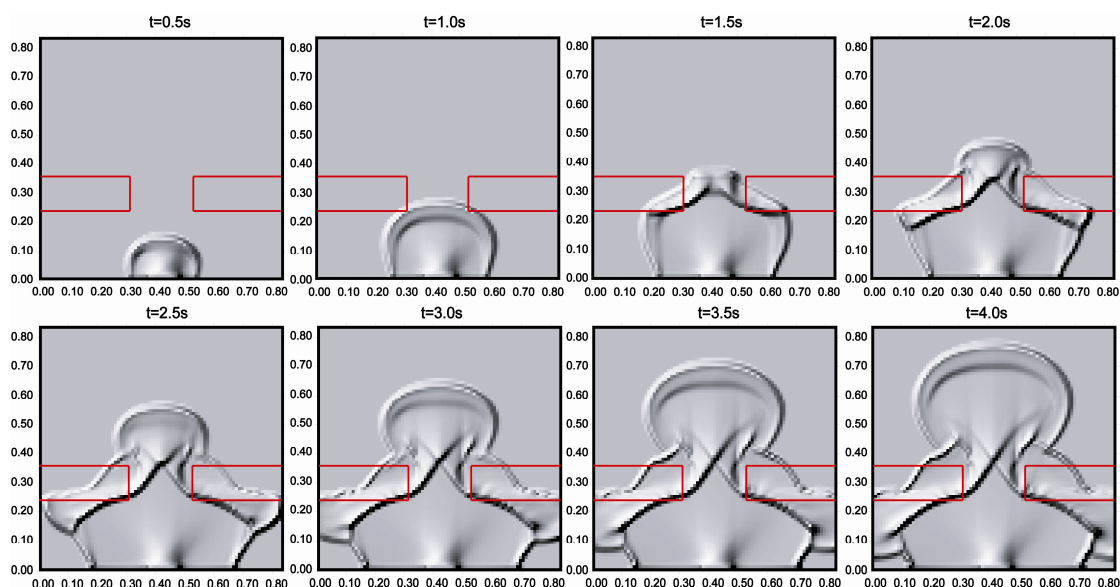


Figure 6.11: Shaded-relief maps of flow depth, illustrating the hydrodynamic evolution of the simulated turbidity current as it interacts with the obstacle. Outer edge of obstacle is marked by red lines

6.2.6 Parallel obstacle

Figure 6.12 illustrates the effect of a flow obstruction aligned in a direction parallel to the main flow direction. The obstruction is formed by an upslope section of the topography with gradients of 5°, 10°, 15°, 30° and 45° normal to the main flow direction. The simulated topographic setting is that of a seafloor deformed by e.g. folding or, in case of larger gradients, faulting. Although this experiment was not actually physically performed, and no experimental data are available to validate the simulated deposits, the validation results presented so far allow a qualitative comparison.

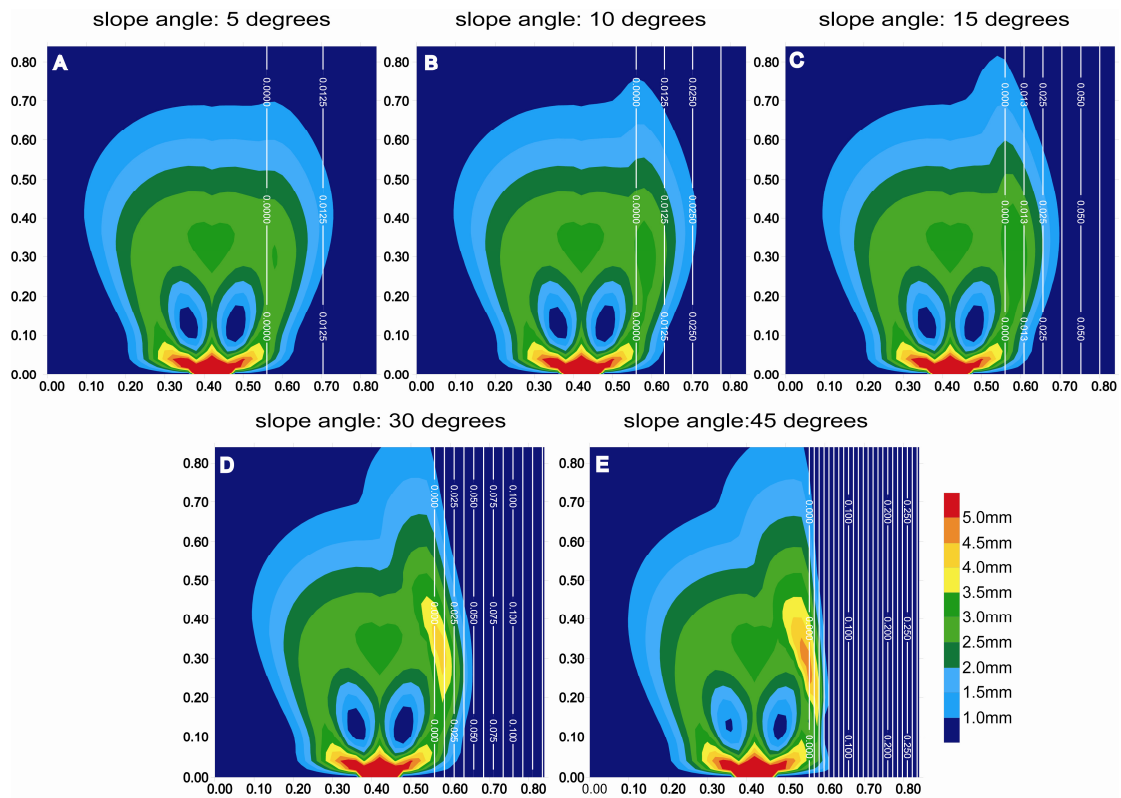


Figure 6.12: Effect of slope angle of lateral flow obstruction on deposition, for slope angles of 5, 10, 15, 30 and 45 degrees. Contour maps represent deposit thickness. Thin white lines are contour lines of topographic height. $C_D = 0.015$

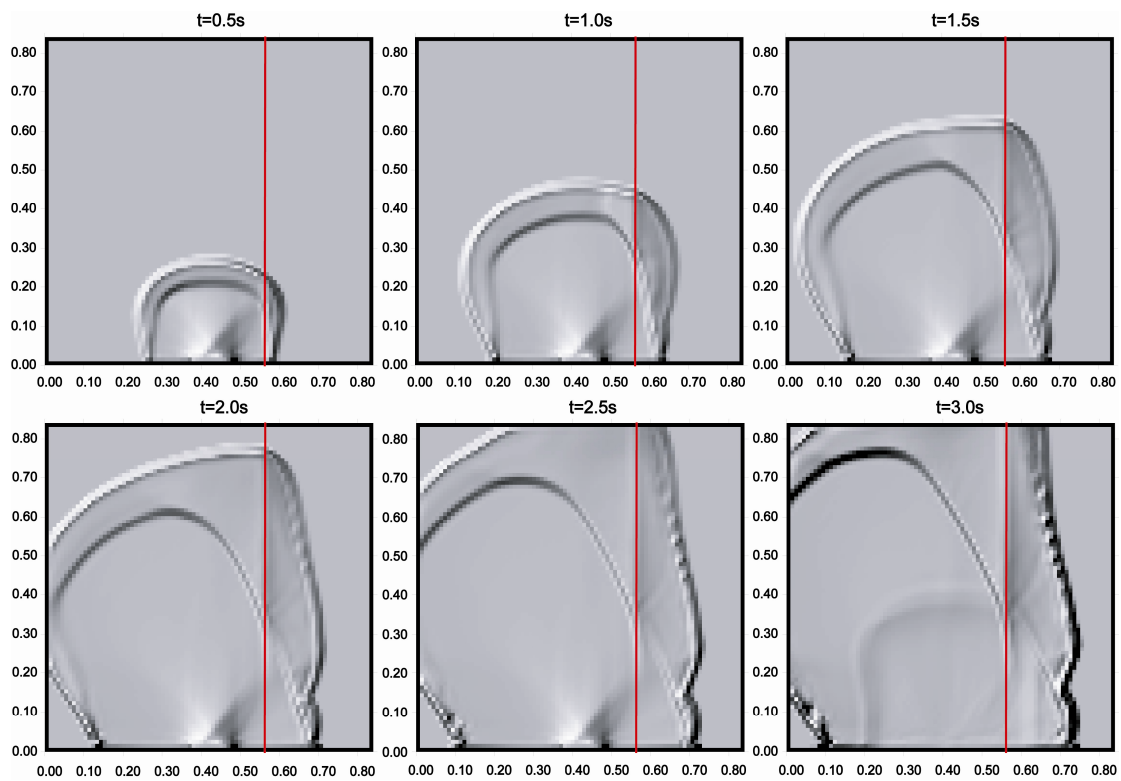


Figure 6.13: Shaded-relief maps of flow depth, illustrating the hydrodynamic evolution of the simulated turbidity current as it interacts with a lateral obstacle with a gradient of 10° . Break in slope is marked by red lines

In all five contour maps of simulated deposit thickness, the effect of the flow-restricting lateral obstruction is discernible in the form of a local thickening of the deposit at the break in slope. As the gradient of the lateral obstruction increases (from left to right and top to bottom in Figure 6.12), the local thickening becomes more pronounced. The relation between deposit and flow evolution is clearly visible when comparing contour map B in Figure 6.12 to the shaded-relief maps of Figure 6.13. Both figures pertain to a simulation in which a turbidity current is partially confined by a lateral obstruction with a gradient of 10° . The radial spreading of the flow is restricted by the obstacle, while discharge remains unchanged. Consequently, the flow-velocity vectors become parallel to the break in slope, and deposition is confined to an area adjacent to the break in slope. Because discharge (inflow) persists, the restricted section of the turbidity current increases in depth, and “overtakes” the head. This causes the protrusion along the break in slope, which increases in intensity as the slope angle increases.

6.3 Experiments in a small subsiding basin with a turbidite fan system

In this paragraph, the capabilities of the model are assessed in simulating multiple flows in sequence. The experiment done by Violet et al. (2005) has been selected to compare simulated results to measured data. Originally, the experiment was conducted to gain insight into the infill history of confined turbidite basins such as found e.g. in the Gulf of Mexico. The validation results encompass a comparison of the hydrodynamic behaviour of simulated turbidity currents to observations, and a qualitative comparison (geometry, trends in thickness and mean grain size) of simulated stratigraphy to experimental data, based on geometry (lateral extent, thickness) and mean grain size of individual beds and bed successions.

6.3.1 Experimental set-up

The experiment was performed in the eXperimental EarthScape (XES) facility at St. Anthony Falls laboratory, University of Minnesota. An important feature of this facility is the ability to apply arbitrary patterns of spatial and temporal variations in subsidence rate. This feature allows for an experiment in which small-scale stratigraphy can be produced in a subsiding basin representative of turbidite reservoirs in the Gulf of Mexico. For a detailed description of the experimental facility, the reader is referred to Violet et al. (2005).

Figure 6.14 displays the topographic configuration at the start of the experiment (right contour map), as well as the discretized version (left contour map) adopted in the simulations. The grid resolution of the discretized bathymetry is 31 by 44 cells, which corresponds to a (square) grid-cell size of 10 cm. The time-step length was set to 0.1 seconds, and the initial porosity of the sediment was set to 0.4. The proximal part of the experimental basin (bottom part of the contour map) represents a confined inlet and was created by building out two subaqueous deltas of crushed coal.

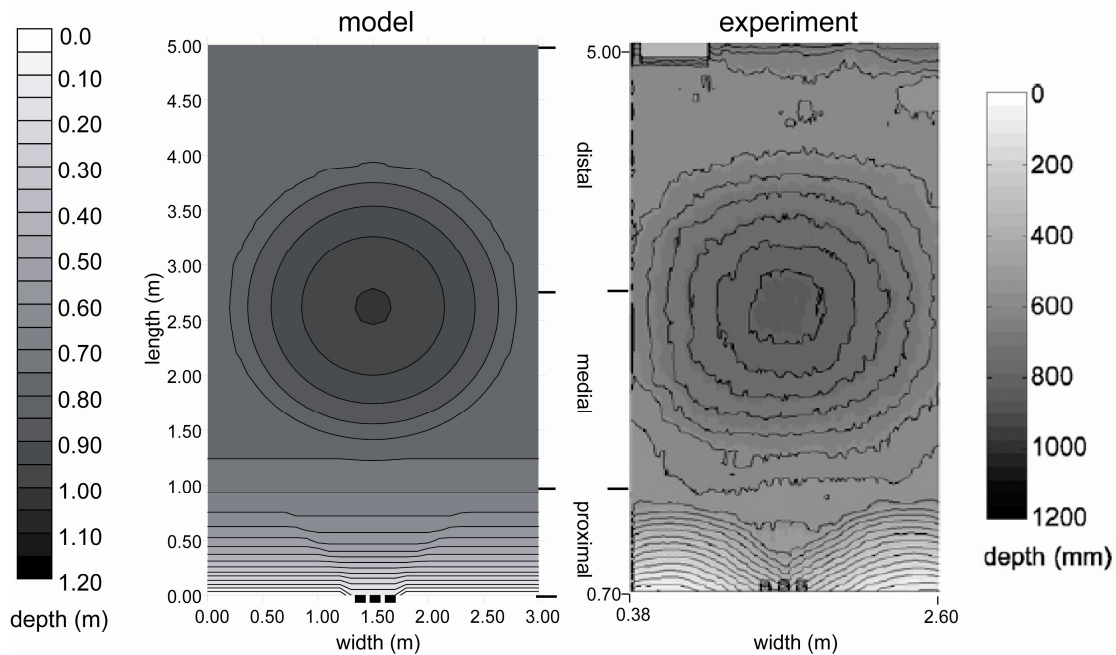


Figure 6.14: Contour maps of initial bathymetry in simulation (left) and experiment (right; Violet et al., 2005). Proximal, medial and distal regions defined after Violet et al., to facilitate comparison of simulated results to experimental data. Grid resolution= 31 by 44 cells, grid cell size=10 cm by 10 cm.

The confined inlet simulates a slope channel or canyon through which the turbidity currents flow on their way to the downstream part of the experimental basin, which contains an (initially) bowl-shaped depression. This bowl-shaped depression represents a generic scale model of a typical salt-withdrawal basin on the north slope of the Gulf of Mexico (Pratson and Ryan, 1994). Initial relief between the outer edges of the basin and the lowest point was 200 mm. Water depth over the lowest part of the basin was 0.80 m, but increased as the basin gradually subsided during the experiment.

The tank has no moats to minimize flow reflections. To minimize flow reflection due to the collision of the turbidity currents with the downstream wall of the basin, a suction mechanism was placed underwater at the downstream end of the basin. Turbid fluid was sucked out through a manifold pipe at a rate at least as high as the inflow rate of the incoming turbidity currents. To maintain the free surface level of the water in the tank, water was constantly fed into the basin at a rate equal to the rate of removal.

Turbidity currents were generated by allowing inflow to occur from one or all of the three inlet pipes, depending on the type of event. The downstream tips of the inlet pipes are visualised in the contour maps of initial bathymetry (Figure 6.14). Three types of turbidity-current flow events were generated: small-pulse flows with an inlet discharge of 1.5 l/s and a duration of 111 seconds, large-pulse flows with an inlet discharge of 4.5 l/s and a duration of 229 seconds, and continuous flows, with an inlet discharge of 1.5 l/s and a duration of 2160 seconds. For the low discharge flows, one inlet pipe was used, whereas for the high discharge flows, all three pipes were used. A mixture of three grades of silica flour consisting of 40% 20 μm material, 45% 45 μm material and 15% 120 μm material was used as a sediment analogue.

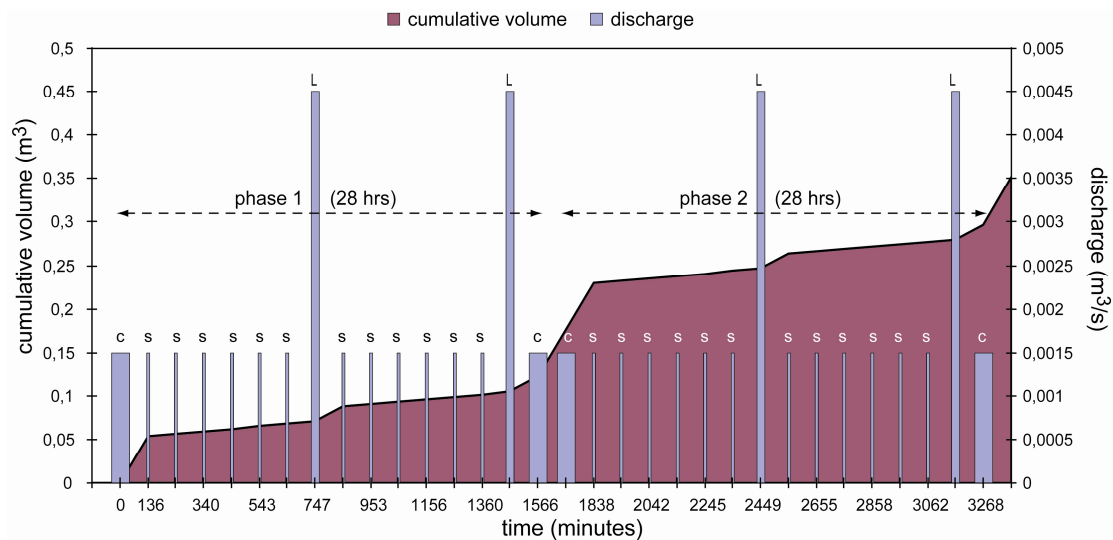


Figure 6.15: Sequence of turbidity-current events generated during experiment (after Violet et al., 2005) Blue bars represent suspension discharge in m^3/s . Dark red area represents the cumulative volume of suspension discharged into the tank .C: continuous event, duration 36 min.; S: small pulse, duration 2 min.; L: large pulse, duration 4 min. Settling time between individual events is 100 min.

Figure 6.15 illustrates the sequence of 32 flows produced during the experiment. During the first phase of the experiment, 2 continuous events, 12 small-pulse events and 2 large-pulse events were generated, all with an initial suspended sediment concentration of 5% by volume. Meanwhile, the deepest point in the basin subsided at a rate of 9 mm/hour from an initial depth of 200mm to a depth of 450 mm at the end of phase one, which had a duration of 28 hrs. The accommodation volume thus created equalled the total amount of sediment discharged into the basin during phase one.

During the second phase of the experiment, which also had a duration of 28 hrs, the sequence of 16 flow events of phase one was repeated, but with no further subsidence applied to the basin. However, during the last 8 flow events, the coarsest grade of silica flour was removed from the sediment mixture to prevent an unintended flow-impact structure from breaching the water surface (see below).

The experimental conditions described above were largely copied in the numerical simulations. Differences in initial conditions between the experiment and the simulations include the initial bathymetry, the location of inflow, the initial flow depth of the events, and the grain-size distribution of the sediment. In the experiment, the initial substrate consisted of a thin erodible layer of sand (grain size not specified) which contains small irregularities, whereas, in the numerical simulations, the initial substrate is completely smooth (Figure 6.14). In the experiment, the erodibility of this sand layer, together with the point-source-like configuration of the inlet pipes, caused the creation of an unintended flow-impact structure just downstream of the inlet. This scour led to an unintended build-up of sediment of (mainly) the coarsest grade of silica flour just downstream of the scour that started to breach the water surface during the third large-pulse flow event (Violet et al., 2005). The influence of this flow-impact structure on deposition in the area around the inlet pipes will be discussed later in this chapter.

Although the diameter of the inlet pipes was given as 7.62 cm (Violet et al., 2005), the initial flow depth of the events in the experiments is difficult to determine, since the flow immediately expands upon leaving the pipes. Furthermore, the use of a single inflow point in the model is sensitive to numerical instabilities during the simulations. Therefore, it was decided to spread the inflow over three points, and to match the discharge of the flow events and the inflow velocity of 0.33 m/s given by Violet et al. (2005) to that in the experiment. Consequently, the initial flow depths for the low-discharge and high-discharge events are different from the experimental values. For the high-discharge (large-pulse) flow events, a flow depth of 4.6 cm is used, and for the low-discharge (small-pulse, continuous) flow events a flow depth of 1.51 cm is used. These flow depth, together with the above mentioned inflow velocity, result in discharge values which are similar to those in the experiment, under the assumption that the cross-sectional flow area has a rectangular instead of circular shape.

6.3.1 Hydrodynamics

Figure 6.16 illustrates the hydrodynamic evolution of the first continuous event during the first 75 seconds of inflow, with the shape of the initial bathymetry indicated in red. In all three types of flow events, Violet et al. (2005) observed an upstream migrating bore.

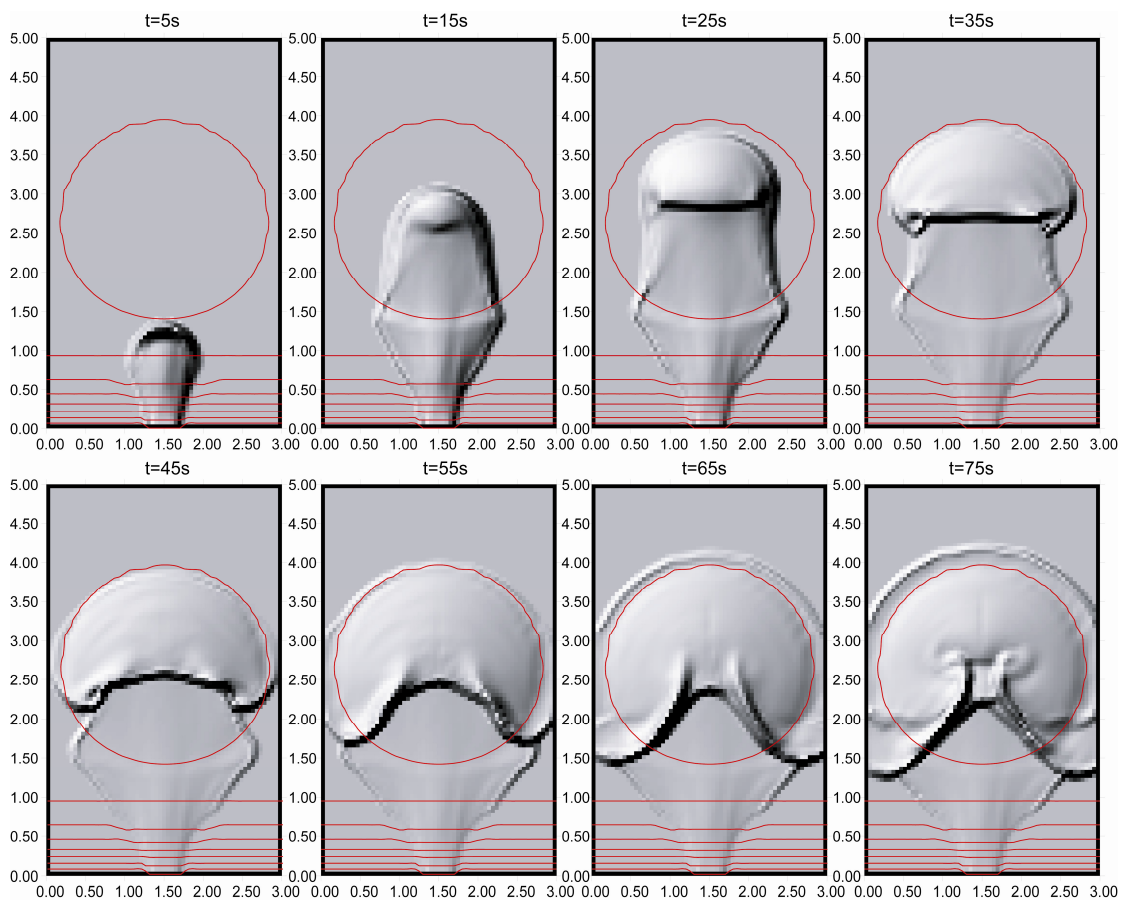


Figure 6.16: Shaded-relief maps of flow depth, illustrating the hydrodynamic evolution of a simulated continuous turbidity current interacting with the initial basin bathymetry. Contour lines (red) represent topography, $c_D = 0.035$

The formation of this bore is attributed to the collision of the turbidity current with the downstream wall of the experimental facility, which contains no moats. In the model, which has open (non-reflective) boundaries, an upstream migrating bore forms as the turbidity current climbs the slope at the downstream end of the basin. The bore marks the transition from supercritical to subcritical flow, and, in both the simulation and the experiment, stabilizes at the upstream end of the basin to form a hydraulic jump. Whether the turbidity current is completely or partially ponded depends on the depth of the basin and the discharge and duration of the event. In the case of the small-pulse flow events, the bore does not stabilize, i.e., no ponding occurs, whereas in the case of the large-pulse and continuous flow events, the bore stabilizes to a hydraulic jump at slightly different locations at the upstream end of the basin. During phase one, subsidence of the basin prevented the occurrence of complete ponding, whereas during phase two, ponding occurred more and more often as the basin was gradually filled with sediment. The simulated hydrodynamic behaviour was also observed by Lamb et al. (2004) during experiments in a two-dimensional version of the basin experiment done by Violet et al. (2005).

6.3.2 Geometry of deposit

The geometry of the deposits from the three types of flow events reflects their hydrodynamic evolution. This is illustrated in Figure 6.17, which contains contour maps of simulated deposit thickness for the three types flow events, all with an initial bathymetry similar to that in the experiment, including the 2 cm thick erodible bed. Since no information is given on the composition of this substrate layer, the grain-size distribution of this bed is taken to be similar to that of the sediment transported by the flows.

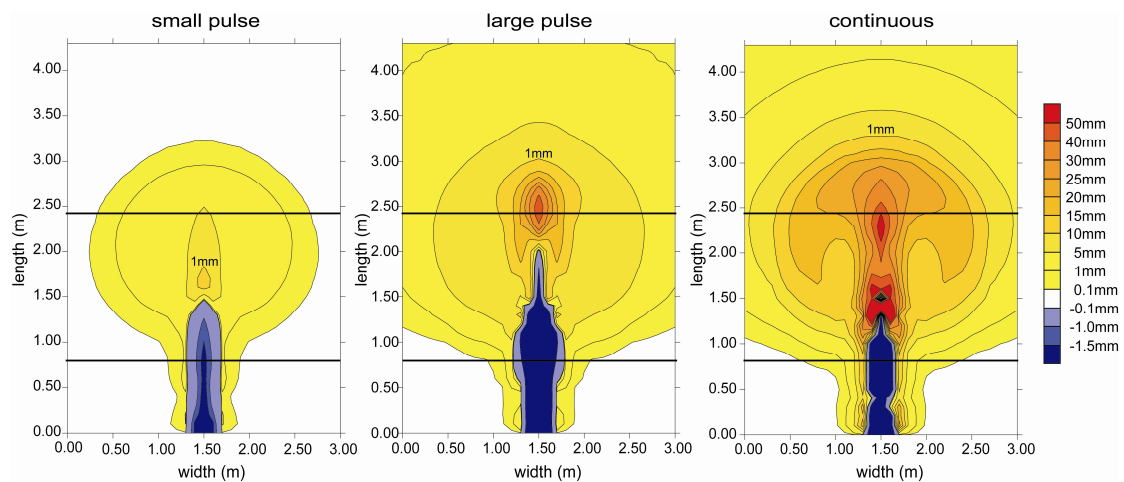


Figure 6.17: Contour maps of deposit thickness for single small-pulse, large-pulse and continuous flow events over an erodible bed with composition similar to that of the sediment in suspension. Blue colours indicate erosion of underlying substrate; yellow-red colours indicate net deposition. Thicker black lines indicate position of boundaries between proximal, medial and distal regions. $C_D=0.035$

The deposit from a small-pulse flow event is broad and thin, except for an elongated central section extending from the point of inflow (m) to the centre of the basin. The upstream part of this section is characterised by erosion of the underlying substrate, up to a point where the gradient of the upstream rim of the basin is no longer

sufficient to support the velocity of flow needed to keep the coarsest grains suspended. Downstream of this point, the deposit reaches its maximum thickness. Levees form on both sides of the erosive part of the section. Similar observations were reported by Violet et al (2005).

The formation of this channel-like structure with levees is also visible in the deposits resulting from the large-pulse and continuous flow events, although the length, width and depth of the section in which erosion occurs differ. In the deposit resulting from the large-pulse flow event, the erosive section is wider, longer and deeper, and hence its potential for erosion is higher than that of the small-pulse flow events. A widening of the erosive channel occurs at the rim of the basin, where the subtle confinement becomes too shallow to contain the large-pulse flow. Furthermore, the point of maximum deposit thickness is located further downstream than the depocentres of the small-pulse and continuous flow events. This is in agreement with experimental observations reported by Violet et al (2005).

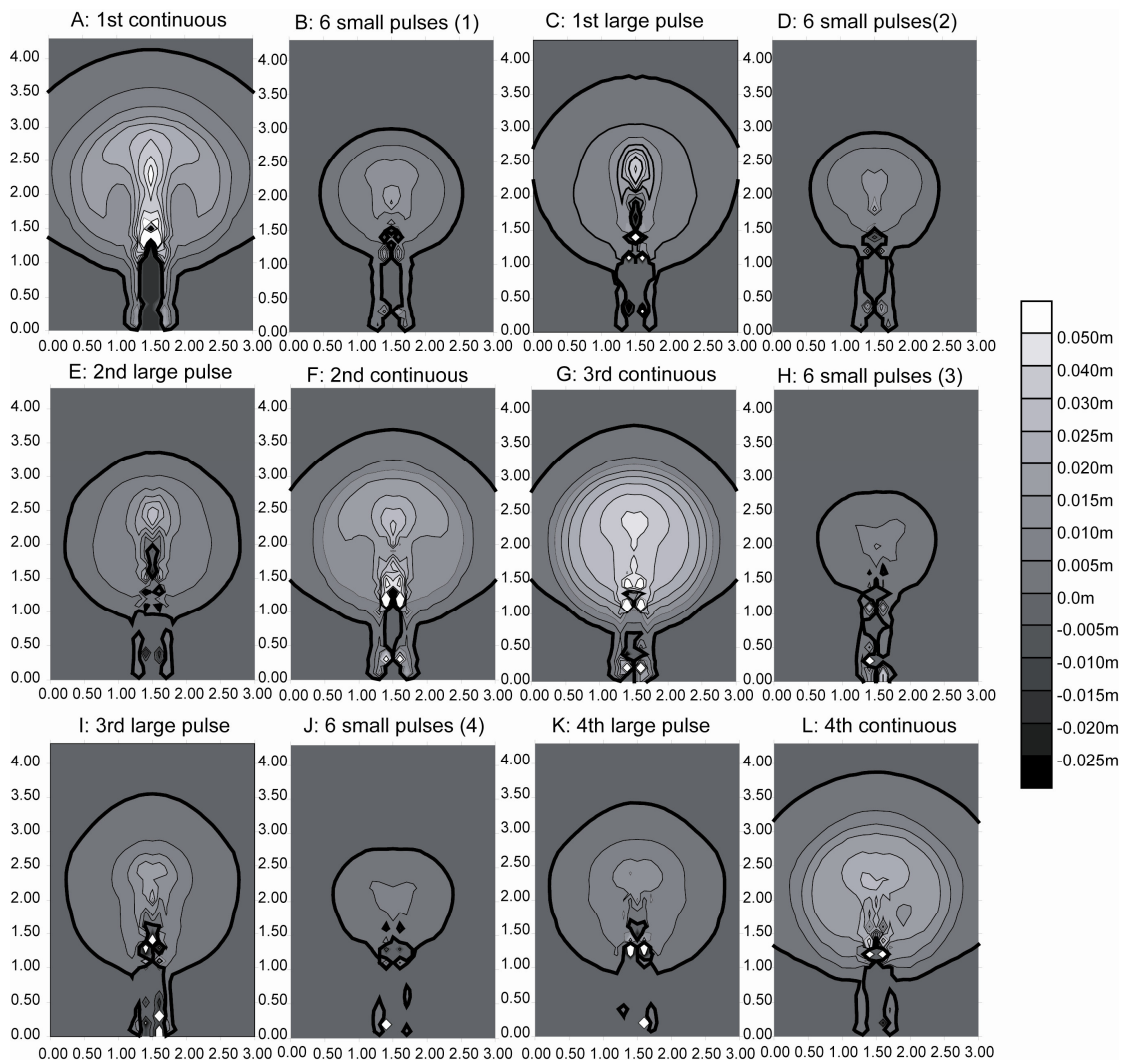


Figure 6.18: Isopach maps of simulated deposits from the four large-pulse and continuous flow events, and for the four sets of six small-pulse flow events. Positive values correspond to net deposition (lighter shades of grey), whereas negative values correspond to erosion (darker shades of grey). Thick line marks the boundary between areas of erosion and deposition. $C_D=0.035$

In the deposit resulting from the continuous flow event, the erosive part of the channel is shortest and deepest, and levees are highest. The point of maximum deposit thickness is located directly downstream of the end of the erosive section, which is likely due to the position of the hydraulic jump. A second depocentre is located a little further downstream, and illustrates how the large spread in grain sizes causes (extreme) grain-size segregation in the deposit. In the experiment, there is a small spread of grain sizes around the mean for each of the three size classes, which is likely to have reduced this effect.

Figure 6.18 illustrates the contribution of the three types of flow events to the evolution of the deposit. Isopach maps are presented for the four large-pulse and continuous flow events, and for the four sets of six small-pulse flow events. For the continuous flow events in the experiment, substantial erosion was only reported in the first event. Similarly, in the simulation, substantial erosion is only visible in the contour map of the first continuous event. Furthermore, and in agreement with experimental observations (Violet et al., 2005), sediment increasingly bypasses the proximal region during stage two.

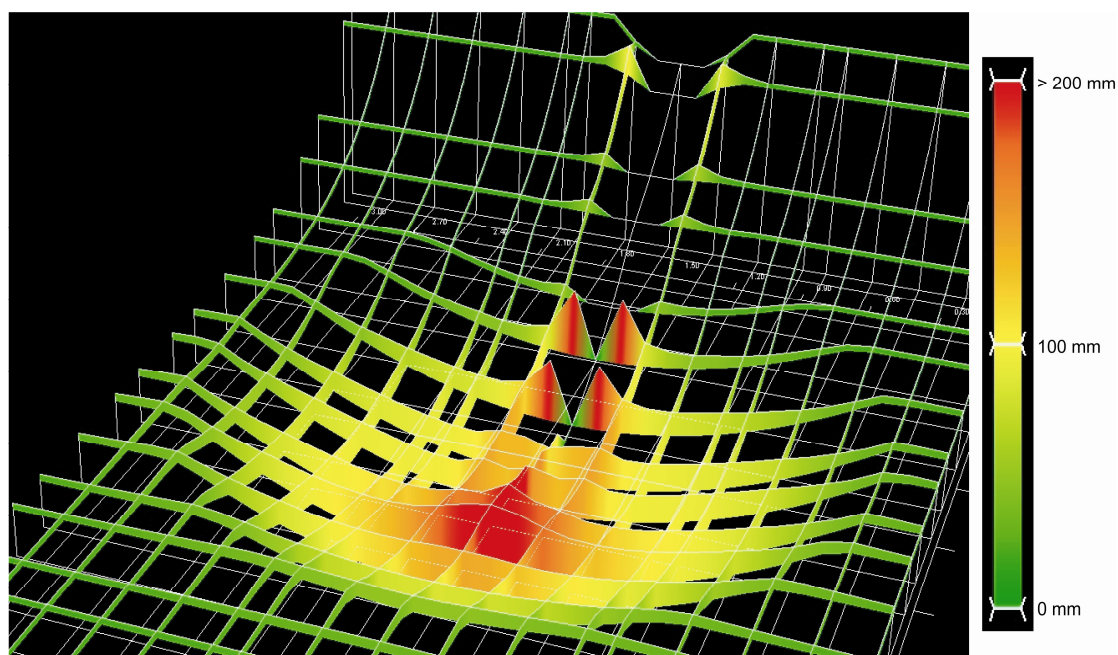


Figure 6.19: 3D view of deposit at the end of the simulation, i.e., after 32 events. Porosity of the deposit is 0.4.

When comparing the geometry of the modelled deposit after 32 flow events (Figure 6.19) to that of the experiment, the most striking difference is in the thickness of the deposit in the proximal zone. The thickness of the experimental deposit is much larger than that of the simulated deposit. In the experiment, the leveed channel, which formed during the first continuous event, was filled by the set of small-pulse flow events and the large-pulse flow event that followed. After infill, aggradation continued for the remainder of the experiment, although to a lesser extent in the second phase than in the first phase. In the simulation, the leveed channel persists throughout the complete duration of the simulation (see also Figures 6.20, 6.22), implying that the simulated flows were (much) more erosive in the proximal region.

This is likely due to the value of the drag coefficient c_D , which has a fairly high value of 0.035. Realisations with other values of c_D show that, as c_D decreases, the erosive power of the flows decreases. Consequently, the termination point of the erosive zone shifts upstream, and the probability for infill of the leveed channel increases. Infill of the channel causes a decrease of the local gradient, which instigates deposition further. Another reason for discrepancies in deposit thickness must be sought in the difference in boundary conditions between the experimental facility and the model. Although measures were taken in the experimental setup to prevent flow reflection at the downstream end of the tank, the turbidity currents can only exit the tank at the downstream end. This may have caused excessive ponding of the turbidity currents to a level where they were completely drowned, as was indeed observed by Violet et al. (2005). By contrast, in the model, open boundaries on all sides allow the turbidity currents to leave the computational domain virtually unobstructed.

6.3.3 Stratigraphy

Figure 6.20 displays a 3D internal view of the complete deposit at the end of the simulation. The colour coding represents the mean grain size of the deposit, with a minimum value of 20 μm (purple) and a maximum value of 100 μm or larger (red). Trends in the simulated stratigraphy resemble that of a turbidite fan, fed by a single supply channel, with largest mean grain sizes in the channel, levees and proximal part of the fan, and lowest mean grain sizes at the fringes of the fan. The initial substrate (lowermost blue layer) covers the initial bathymetry everywhere, except for areas where it has been eroded such as e.g. in the upstream part of the channel.

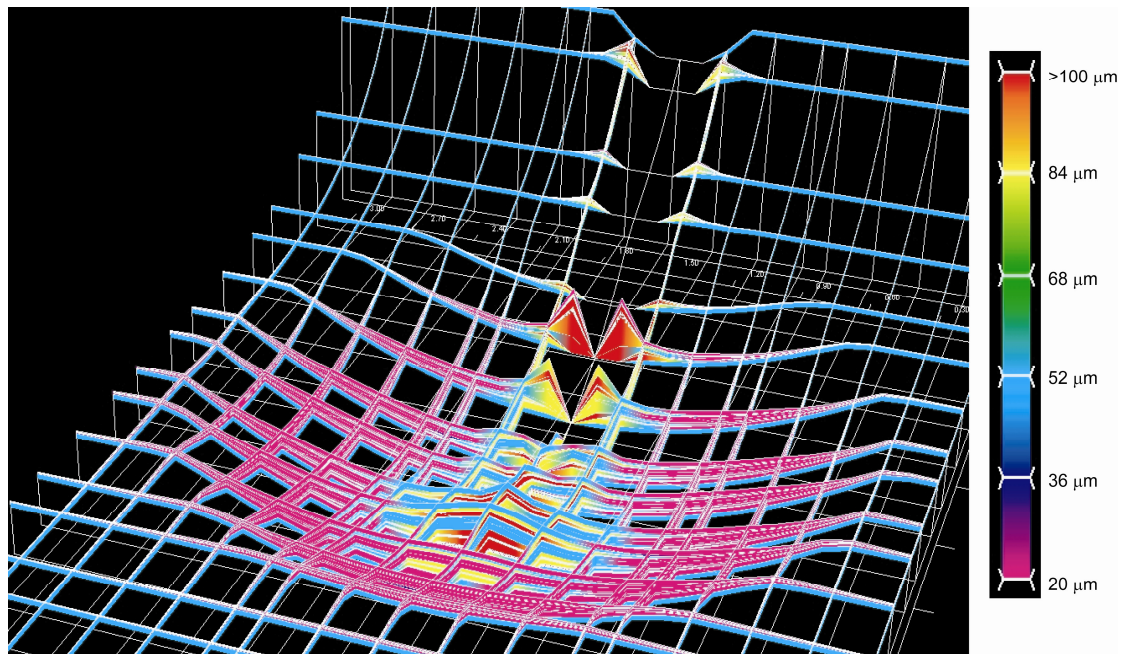


Figure 6.20: 3D internal view of deposit at the end of the simulation, i.e., after 32 events. Porosity of the deposit is 0.4.

Vertical variations in mean grain size, as observed in the central thicker part of the deposit, are caused by differences in transport distance of individual grain-size classes between the three types of flow events. To illustrate this, Figure 6.21 displays contour

maps of mean grain size for deposits from the small-pulse, large-pulse and continuous flow events (see Figure 6.17 for deposit thicknesses). In general, the coarsest deposits are found in the parts of the levees immediately adjacent to the channel and in the area just downstream of the position where the flow regime in the channel changes from erosive to depositional. Furthermore, the large-pulse flow events are capable of transporting coarse material farther into the basin than the small-pulse and continuous flow events. Absence of grain-size measurements in the experimental deposits does not permit a detailed comparison between simulation and experiment.

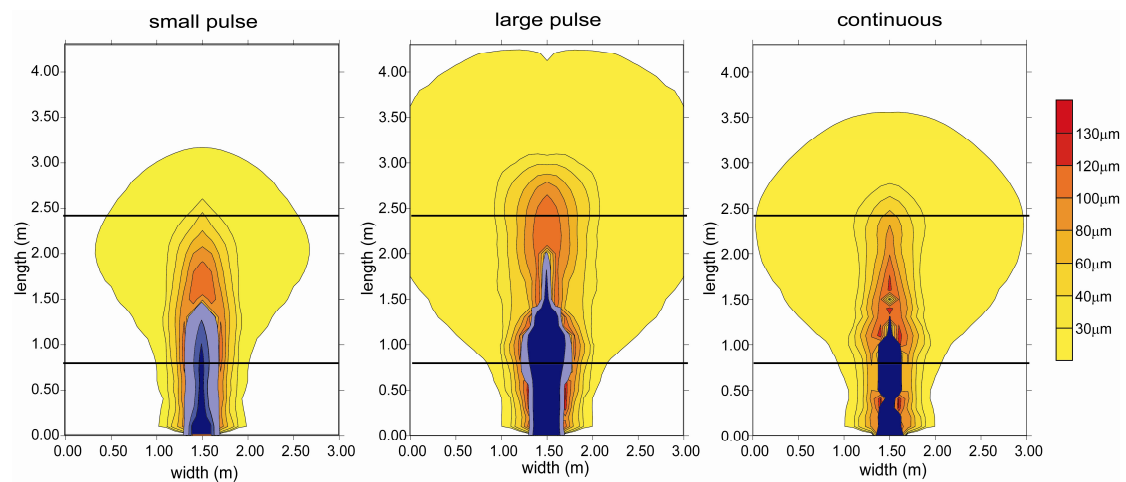


Figure 6.21: Contour maps of mean grain size of simulated deposit for single small-pulse, large-pulse and continuous flow events over an erodible bed with composition similar to that of the sediment in suspension. Blue colours indicate erosion of underlying substrate. Thicker black lines indicate position of boundaries between proximal, medial and distal regions. Porosity=0.4, $c_D = 0.035$

A more detailed analysis of the stratigraphy in terms of bed successions may be carried out by comparing cross-sections through the simulated stratigraphy to photographs of three cross-sectional slices through the experimental deposit (Figure 6.22). The cross-sections were taken at 1.0, 1.6 and 2.4 m from the inflow point. In the photographs, the black line approximately marks the boundary between stages one and two of the experiment. In the experiment, deposition was much higher in the proximal and upstream half of the medial area. The leveed channel is clearly visible in both the experimental and the simulated deposit. In the experiment, it was created during the first continuous event, and filled by the set of six small-pulse flow events and the large-pulse flow event that followed. In the simulation, the infill is absent, a discrepancy which is attributed to a high value of c_D , which enlarges the erosive power of the simulated flow events. Furthermore, in the simulated deposit, the leveed channel is more pronounced at 1.6 m from the source than in the experiment, probably for the same reason.

A comparison of the lower part of the stratigraphy of the experiment at 1.0 m from the source to that of the simulated deposit at 1.6 m from the source gives a better fit. This can be supported by the fact that the zone where the transition from erosion to deposition takes place is shifted downstream in the simulation relative to the experiment. A comparison of the cross-sections at 2.4 m from the source illustrates this. Here, the simulated deposit is notably thicker in the central part of the basin than at the rims, a trend which is absent in the experimental deposit.

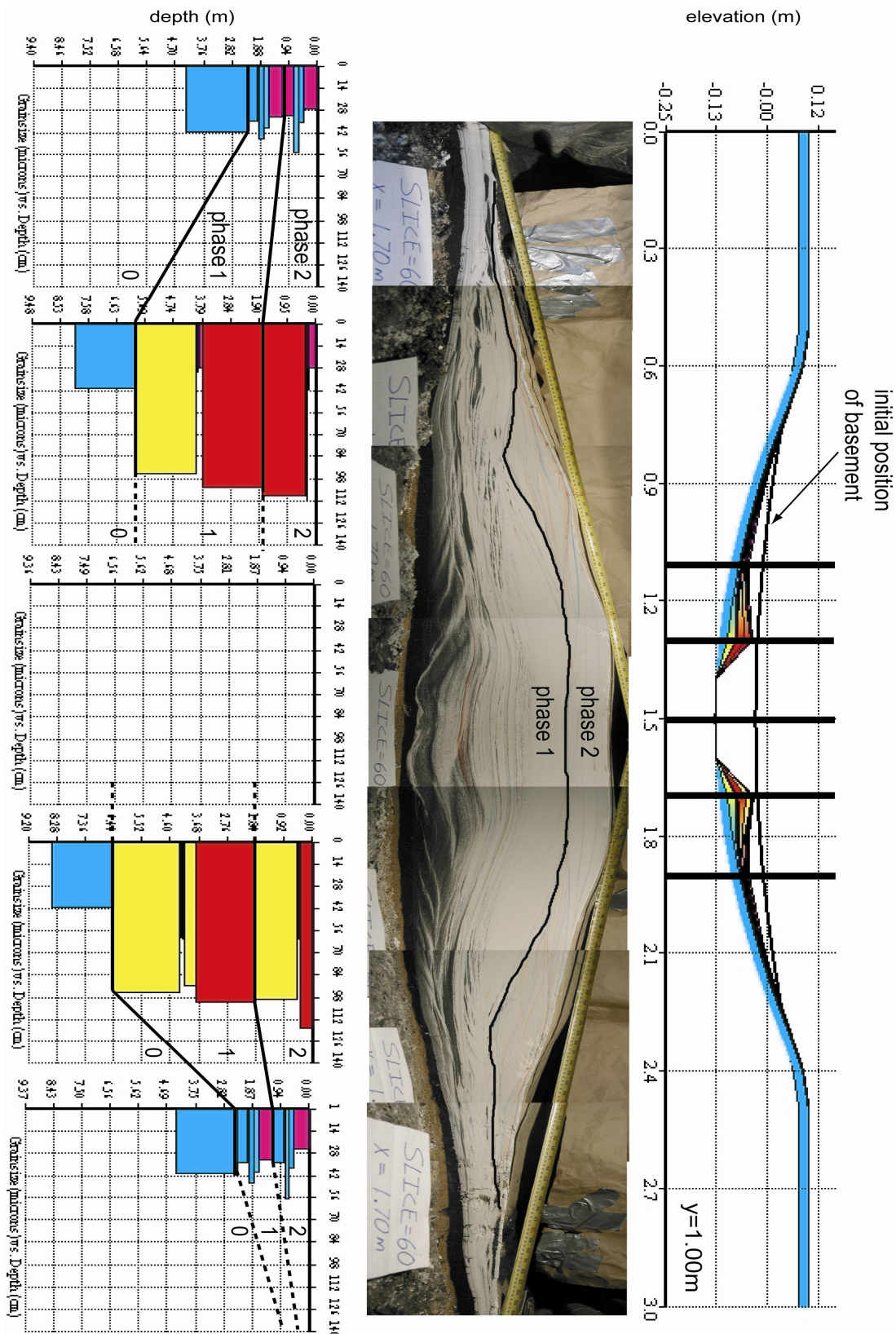


Figure 6.22: Comparison of simulated stratigraphy to experimental stratigraphy (middle) for a cross-section located 1.0m from the source, and taken in the direction perpendicular to the streamwise direction of the flows. Colour coding (see Figure 6.20 for definition) is based on mean grain size of deposit. Porosity=0.4, $c_D=0.035$. Photographic panels reproduced from Violet et al. (2005). Access to data provided by the National Centre for Earth-surface Dynamics Data Repository (http://www.nced.umn.edu/data_archives.html)

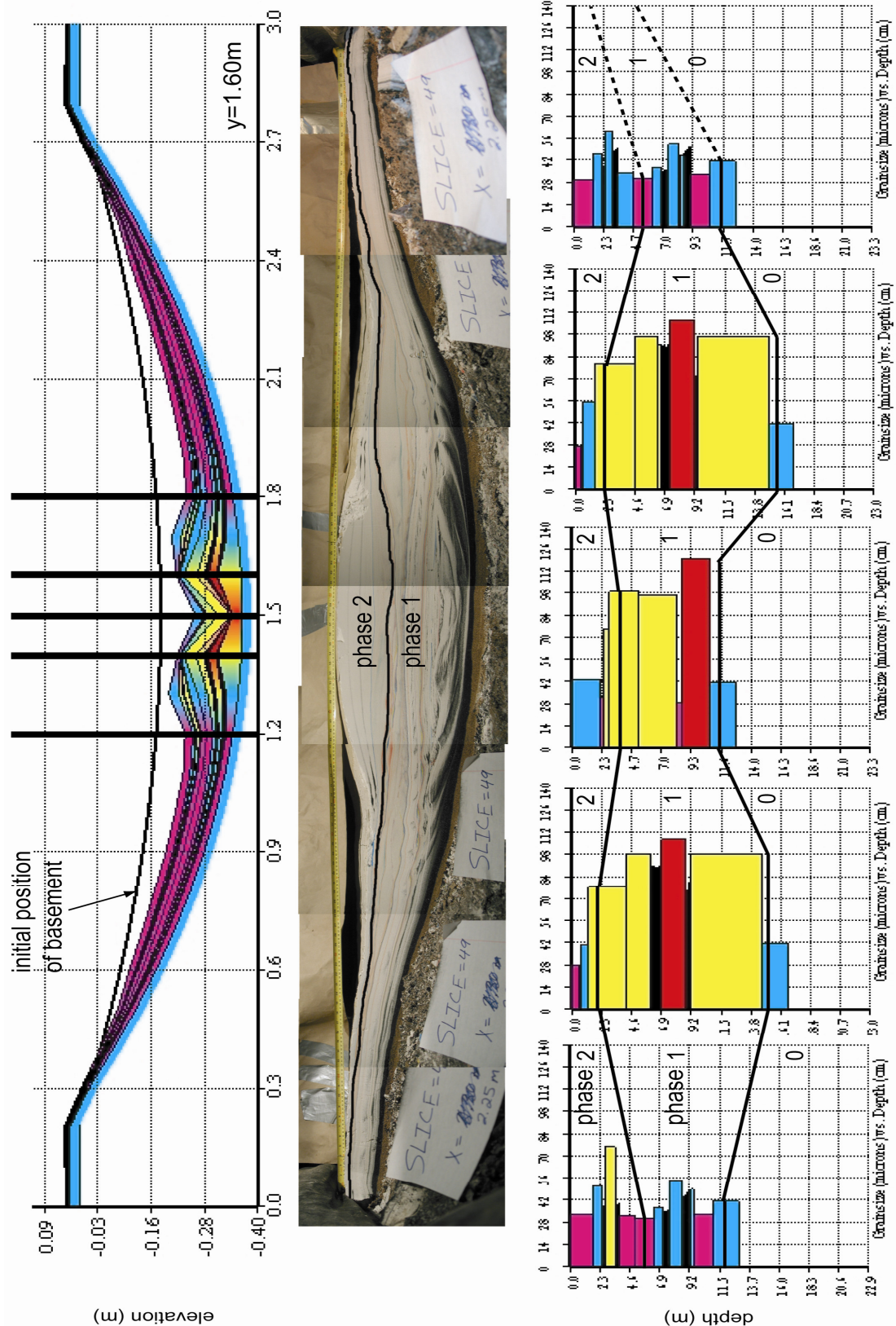


Figure 6.23: Comparison of simulated stratigraphy to experimental stratigraphy (middle) for a cross-section located 1.6m from the source, and taken in the direction perpendicular to the streamwise direction of the flows. Colour coding (see Figure 6.20 for definition) is based on mean grain size of deposit. Porosity=0.4, $c_D = 0.035$. Photographic panels reproduced from Violet et al. (2005). Access to data provided by the National Centre for Earth-surface Dynamics Data Repository (http://www.nced.umn.edu/data_archives.html)

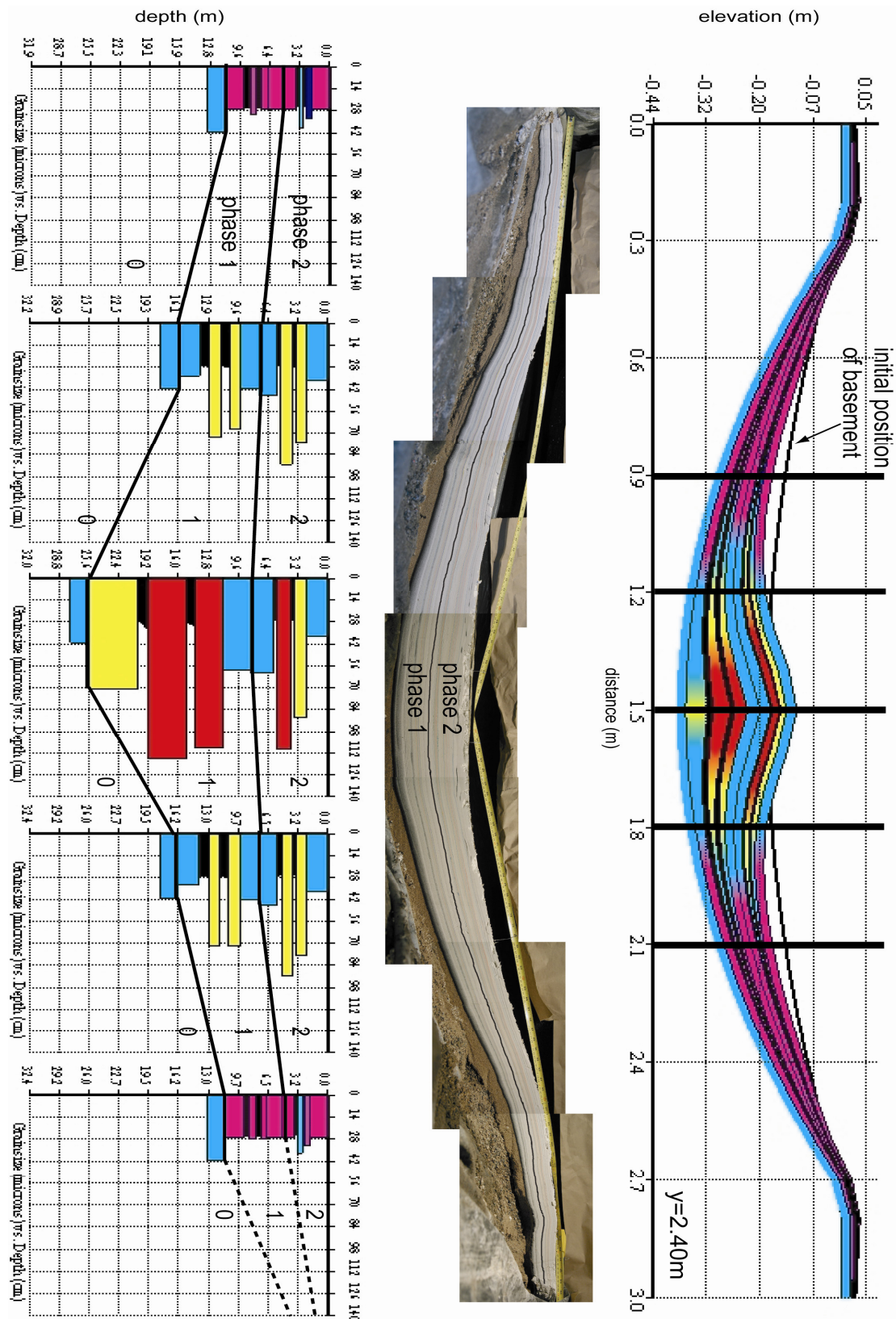


Figure 6.24: Comparison of simulated stratigraphy to experimental stratigraphy (middle) for a cross-section located 2.4m from the source, and taken in the direction perpendicular to the streamwise direction of the flows. Colour coding (see Figure 6.20 for definition) is based on mean grain size of deposit. Porosity=0.4, $c_D=0.035$. Photographic panels reproduced from Violet et al. (2005). Access to data provided by the National Centre for Earth-surface Dynamics Data Repository (http://www.nced.umn.edu/data_archives.html)

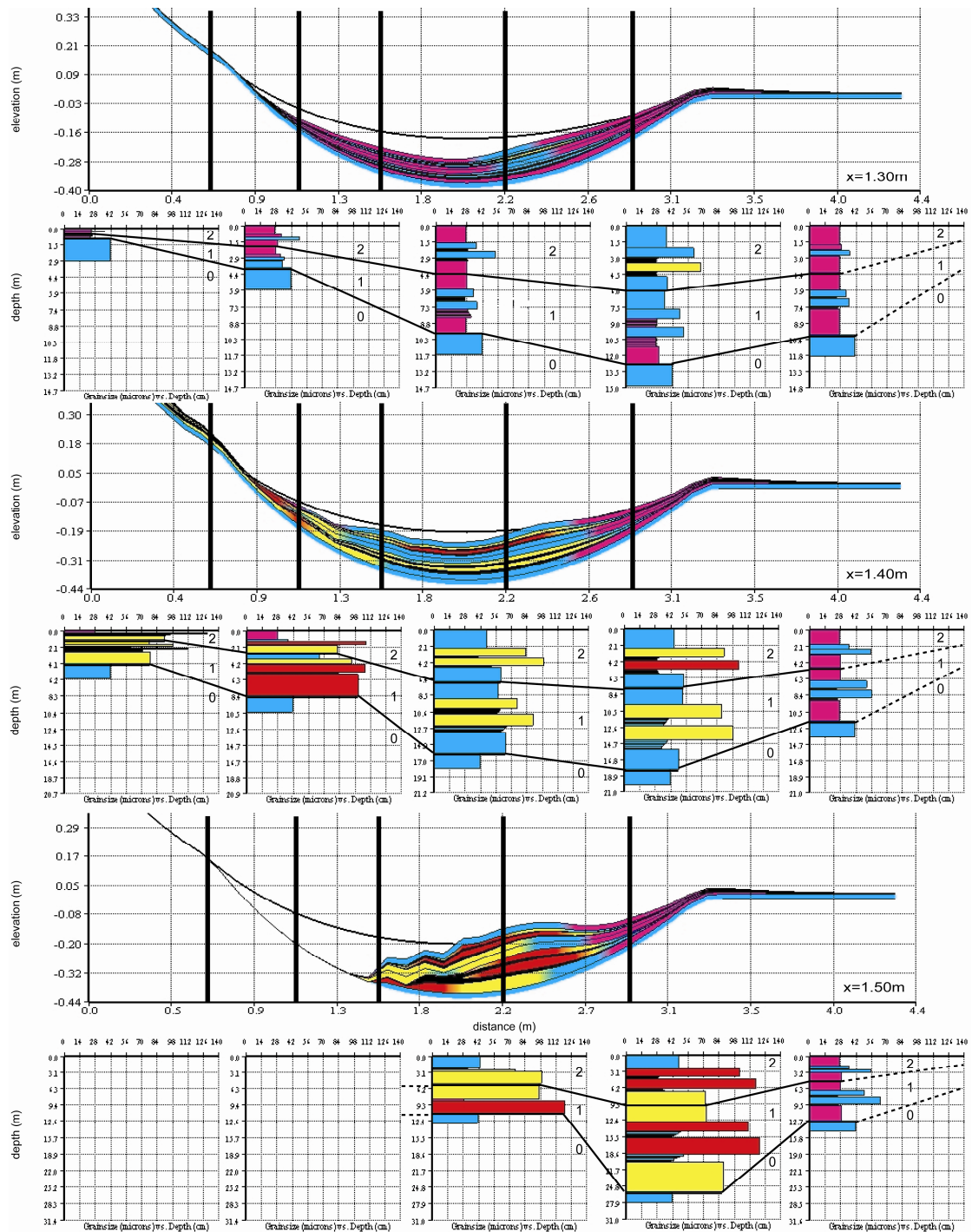


Figure 6.25: Panel of cross-sections through the simulated deposit after 32 events. Cross-sections are taken in the direction parallel to the streamwise direction of the flows. Colour coding is based on mean grain size of deposit (see Figure 6.20 for definition). Porosity=0.4, $c_D = 0.035$

The likely reason for this is that, in the experiment, part of the sediment is already deposited in the proximal and upstream part of the medial region, whereas, in the simulation, this region was largely bypassed.

A comparison of the stratigraphy deposited during phase two supports the assumption that, in the simulation, a part of the total volume of sediment discharged into the basin bypassed the basin and left the computational domain via the open model boundaries, whereas, in the experiment, the sediment was contained in the tank. During phase one, bypass was limited due to the creation of new accommodation space by means of subsidence, whereas during phase two, when subsidence had halted, the basin was progressively filled, and sediment increasingly bypassed the basin. Notwithstanding the aim of this validation exercise, a change in model boundary procedure to cope with closed, reflective boundaries was not considered since, in natural (field-scale) settings, boundaries are basically absent, i.e., they are open and non-reflective.

6.4 Discussion

Results have been presented of validation experiments, which were performed to assess the capabilities of the model to simulate flow behaviour of and sedimentation from turbidity currents in complex settings commonly encountered in turbidite reservoirs. The first set of validation experiments focussed on the interaction of turbidity currents with complex topography. The comparison between simulated results and experimental data (Kneller, 1995; Kneller and Branney, 1995) was limited to a qualitative comparison, i.e., the aim was to assess the capabilities of the model in reproducing patterns (trends in deposit thickness) in deposits which evolve when turbidity currents interact with complex topographic features. A quantitative comparison, which would have been preferred, was impossible due to the unconventional use of brine as an interstitial fluid, which constituted a second fluid in the experiment, since the receiving basin was filled with tap water. Because the model is not designed to cope with an interstitial fluid which is different from the ambient water, the experiments were modelled with tap water as ambient fluid, and initial parameters in the model were manipulated so as to obtain a Froude-scaled version of the experiment. However, this resulted in sediment analogues with different density and, consequently, different volumetric concentrations of suspended sediment. Hence, only a qualitative comparison was possible.

Notwithstanding the differences between the simulated and the experimental flows, the simulated depositional patterns mostly compare well qualitatively with depositional patterns observed in the experiments. For linear obstacles oriented perpendicular to the streamwise flow direction, the ratio of obstacle height-to-head height determines if and to what extent the turbidity current surmounts the obstacle. As the obstacle height increases relative to the height of the head of the turbidity current, less sediment is transported into the part of the model domain downstream of the obstacle. Upstream of the obstacle, and lateral to it, deposition increases. Narrow areas of non-deposition, comparable to experimental observations, can be observed in simulations with obstacle heights of 62.5 mm and 93.3 mm, suggesting that they are likely associated with flow reversal due to a large topographic gradient in a direction parallel to flow.

For circular obstacles, the match between simulated deposit and the experimental “ground truth” case is acceptable. The overall deposit geometry is similar, with an area of non-deposition on the lee-side of the obstacle, a maximum deposit thickness just upstream of the obstacle, and lobe-like areas of high deposition adjacent to the

obstacle. Whether the flow is partially or completely deflected by the circular obstacle depends on the height of the obstacle in relation to the height of the head of the turbidity current. The angle of deflection depends on the aspect ratio (width:height) of the obstacle. Simulations of turbidity currents encountering obstacles with heights well in excess of the height of the head revealed that a ridge of sediment evolves upstream of the obstacle, which extends at an angle of almost 90° to the angle of incidence of the flow. The ridge may be considered a logical continuation of the depositional trend that is observed upstream of the obstacle. As the obstacle height increases, the angle between the loci of deposition adjacent to the obstacle increases. At some point, these loci of deposition merge with the one upstream of the obstacle to form a ridge.

An interesting case is that of a turbidity current flowing through a constriction, such as may be encountered when turbidity currents erode a canyon at the distal rim of an intra-slope basin. The simulated deposit matches well with the experimental “ground truth” case, and areas of non-deposition and high deposition are reproduced, albeit not in exactly the same position. The location of the area of maximum sediment thickness induced by the constriction was found to depend on the drag coefficient c_D . Higher values of c_D result in faster flow deceleration and lower velocities upon reaching the obstacle, and allow grains to be kept in suspension longer after inflow into the model domain. Hence, the local concentration upon reaching the constriction is higher. The combined effect results in the observed upstream shift of maximum deposit thickness. In reality, the net rate of deposition (or erosion) is intimately related to the level of turbulence, and not directly to the (layer-averaged) velocity of flow via a constant. An extension to the model, which couples the capacity of the flow to suspend sediment to the level of turbulent kinetic energy (e.g. Parker et al., 1986), may have the potential to diminish the dependency of the model to c_D (Chapter 7)

For flows obstructed by linear obstacles oriented parallel to the streamwise flow direction, no experimental data were found to validate the simulated deposits. In the simulations, the obstruction is formed by an upslope section of the topography, representative of a seafloor deformed by e.g. folding or, in case of larger gradients, faulting. In the deposit, the effect of the flow-restricting parallel obstruction is discernible in the form of a local thickening at the break in slope. As the gradient of the lateral obstruction increases, the local thickening becomes more pronounced. The radial spreading of the flow is restricted by the obstacle, while discharge remains unchanged. Consequently, flow-velocity vectors become parallel to the break in slope, and deposition is confined to an area adjacent to the break in slope. Because discharge (inflow) persists, the restricted section of the turbidity current increases in depth, and “overtakes” the head. This causes a protrusion in the flow and, consequently, in the deposit, along the break in slope, which increases in intensity as the slope angle increases.

A second validation experiment was performed to assess the capabilities of the model in simulating multiple flows in sequence over an erodible bed. Simulated results were compared to data from an experiment (Violet et al., 2005), in which stratigraphy was created that is meant to be representative of a small subsiding turbidite basin such as is found in e.g. the Gulf of Mexico. The initial topography had the form of a bowl-shaped basin characteristic of salt-withdrawal, and changed in time so as to accentuate the bowl-shape. The discretized grain-size distribution of the sediment contained three

size fractions. The aim of this second validation experiment was to compare the hydrodynamic behaviour of simulated turbidity currents to observations, and to compare the simulated stratigraphy to experimental data, based on geometry (lateral extent, thickness) and mean grain size of individual beds and bed successions.

Based on a comparison of simulated flow behaviour to experimental observations (Violet et al., 2005; Lamb et al., 2004), it seems justified to conclude that the model simulates the flow behaviour with an acceptable degree of accuracy. In all three types of flow events, Violet et al. (2005) observed an upstream migrating bore, the formation of which is attributed to the collision of the turbidity current with the downstream wall of the experimental facility, which contains no moats. In the model, which has open (non-reflective) boundaries, an upstream migrating bore forms as the turbidity current climbs the slope at the downstream end of the basin. The bore, which marks the transition from supercritical to subcritical flow, stabilizes at the upstream end of the basin to form a hydraulic jump in both the simulation and the experiment.

Although the model produces qualitatively realistic stratigraphy, the comparison between experimental and simulated stratigraphy is far from perfect. The sensitivity of model outcome to the drag coefficient c_D has already been illustrated and discussed. In combination with the discretized grain-size distribution, which contains three fractions that range in size from 20 μm to 120 μm , and the somewhat low spatial resolution (grid size of 31x44 cells) used in the simulation, this may result in distinct loci of deposition for the three size fractions, which are not observed in the experiment. The location of these loci of deposition depends partly on the value of c_D . Other differences between the discretized experimental conditions used in the model, and the actual experimental conditions include small differences in initial topography and substrate configuration, and a difference in boundary conditions. Although measures were taken in the experimental set-up to prevent flow reflection at the downstream end of the tank, the turbidity currents can only exit the tank at the downstream end. This may have caused excessive ponding of the turbidity currents to a level where they were completely drowned, as was indeed observed by Violet et al. (2005). In contrast, in the model, open boundaries on all sides allow the turbidity currents to leave the computational domain virtually unobstructed. This difference in boundary conditions is a likely cause for the large discrepancy in the upper half of the stratigraphy which, in the simulation, is almost entirely missing presumably due to the use of open boundaries.

The total run-time of the simulation, i.e., of all 32 flows, is approximately 2.5 hours, which is about 1 hour less than the actual run-time of the 32 experimental flows. However, in the experiment, sediment was allowed to settle for 100 minutes after each flow, which resulted in a total run-time of 56.7 hours. In the model, the simulation of a flow ends when the sediment concentration becomes lower than a user-specified concentration limit (e.g. 0.1% by volume). Typical run-times of single-flow simulations in the first set of validation experiments were in the order of one to two minutes. However, it must be noted that, in both sets of experiments, the spatial resolution was low.

7 SYNTHESIS

7.1 *Conclusions*

The results of the quantitative validation experiments (Chapter 5) show that the simulated hydrodynamic behaviour and geometry of deposits are reasonably similar to experiments. Discrepancies are attributed to limitations of the model in simulating experimental flows, the discretization of initial and boundary conditions, difficulties in matching the high-resolution modelling results to the experimental data, which have a much lower resolution, and processes not explicitly accounted for in the model, such as stratification and the formation of turbulent eddies and instabilities related to the entrainment of water.

The qualitative validation experiments (Chapter 6) have shown that the model reproduces spatial trends in deposit thickness that develop when turbidity currents interact with complex topographic features, such as lateral and transverse flow obstructions, circular obstacles and flow constrictions. An attempt to match simulated results to data from an experiment (Violet et al., 2005), in which stratigraphy was created that is thought to be representative of a subsiding mini-basin turbidite fan system, proved difficult. Although the simulated flow behaviour qualitatively resembles the observed flow behaviour, the match between experimental and simulated stratigraphy was far from perfect. Differences are mainly attributable to the discretization of the initial topography and the grain-size distribution, and to the low spatial resolution in the simulation, which was needed in order to keep the run time within acceptable limits. Furthermore, the difference in outflow boundary conditions between the model and the experiment significantly influences the volume of sediment deposited in the basin. In the experiment, ponding occurs in the basin due to the absence of moats, whereas in the model, open outflow boundaries prevent the occurrence of ponding.

A test of the sensitivity of the model to temporal and spatial resolution (Chapter 5, Paragraph 5.5) showed that the numerical accuracy of the model is more sensitive to differences in spatial resolution than to differences in temporal resolution. Loss of numerical accuracy mainly occurs in areas of discontinuous flow, with the largest differences in position, velocity and density of the flow occurring in areas where the flow spreads perpendicularly to the main flow direction. Volumetric errors, defined as the percentage of the total discharged volume of sediment lost during a simulation, are limited to less than 4% when using the Superbee limiter. Absolute and relative volumetric errors of deposits increase almost linearly with decreasing spatial and temporal resolution. This trend allows an estimation of the absolute and relative errors prior to a simulation, which helps decide upon the temporal and spatial resolution to be used for long-term stratigraphic models involving large numbers of turbidity-current events.

7.2 Suggested improvements

An important assumption in this model is that the shear velocity of the flow is related to the streamwise turbulence-averaged flow velocity by a constant, the drag coefficient (c_D):

$$c_D = \frac{u_*^2}{U^2} \quad (7.1)$$

It parameterizes the drag force exerted by the flow on the bed for a given flow velocity. The drag force can be decomposed into skin friction and form drag. Skin friction is generated by flow-induced viscous stress acting in a direction parallel to the bed. Form drag is generated by flow-induced normal stress acting on the bed, which is mostly due to pressure differences associated with flow separation behind roughness elements such as grains and bedforms (Einstein, 1950, Einstein and Barbarossa, 1952).

Equation 7.1 is essentially a simplification of the law of the wall for turbulent flows, which also relates the shear velocity u_* to the streamwise turbulence-averaged flow velocity U (e.g. Schlichting, 1968)

$$\frac{U}{u_*} \equiv \frac{1}{\sqrt{c_D}} = \underbrace{\frac{1}{\kappa} \ln\left(\frac{z}{k_s}\right)}_{\text{skin friction}} + \underbrace{B\left(f\left(\frac{u_* k_s}{\nu}\right)\right)}_{\text{form drag}} \quad (7.2)$$

where z is a coordinate upward-normal to the bed, k_s is the roughness height and κ represents the Kármán constant ($\kappa \approx 0.4$). The parameter B is a function of the roughness Reynolds number ($u_* k_s / \nu$). Its value depends on the roughness regime, which in turn is determined by the ratio of the height of the roughness elements to the thickness of the viscous part of the boundary layer very close to the bed where turbulence is suppressed. When the roughness height is much larger than the thickness of the viscous part of the boundary layer the flow is in the hydraulically rough regime (Parker, 2004). Keulegan (1938) derived a law-of-the-wall type equation quantifying the drag coefficient in the absence of bedforms:

$$\frac{U}{u_*} = \frac{1}{\sqrt{c_D}} = \frac{1}{\kappa} \ln\left(11 \frac{H}{k_s}\right) \quad (7.3)$$

where H represents flow depth. In this equation, the value of c_D depends on the ratio of flow depth to roughness height. A lower ratio of flow depth to roughness height, which occurs in laboratory experiments, results in higher values of c_D . Since in laboratory experiments the roughness height cannot be down-scaled, the value of c_D depends on the spatial scale of the simulation, with values ranging between 0.002 and 0.06. Higher values of c_D must be imposed for small-scale simulations because of the smaller flow depths involved. In the quantitative validation experiments, c_D has been given a value such that the simulated results match the experimental results. It effectively constitutes a tuning or calibration parameter in the model, which is convenient but not physically rigorous.

A variable c_D , with calculated values based on the level of turbulence and/or boundary-layer parameters, which both vary in space and with time, would improve the model. Parker et al. (1986) proposed to include an equation of balance of turbulent-kinetic energy (TKE), which links the entrainment of sediment from the bed directly to the level of turbulence. In this version of the 1-D model, which consists of the conventional three equations for fluid mass balance, sediment mass balance and fluid momentum plus the equation for balance of TKE, the value of c_D is proportional to the ratio of turbulent-kinetic energy to kinetic energy of the mean flow, but the proportionality parameter is again assumed to be constant for a given flow.

An alternative approach towards a more physical parameterization of the relationship between shear velocity and mean flow velocity is to estimate the bed roughness height, based on diagrams of bedform development at different flow regimes, and for different grain sizes. Having estimated the bed roughness height, a value of c_D can be determined using the relationship between bed roughness and c_D derived by Sloff (1997). When the bed roughness height is known, a value of c_D may be calculated. The value of c_D depends on, amongst others, the height of the velocity maximum which in turn depends on whether the flow is supercritical or subcritical. Sloff (1997) derived velocity profile functions for supercritical and subcritical currents, based on laboratory data from various sources (Chapter 2, Figure 2.10). Depth-integration of these velocity profiles results in expressions that relate the average flow velocity to the shear velocity and the dimensionless bed roughness height for supercritical and subcritical currents. Since the drag coefficient is defined as the ratio of shear velocity to average flow velocity, these expressions may be used to obtain an expression which relates the value of the drag coefficient to the dimensionless bed roughness height, defined as the ratio of bedform height to flow thickness. In this way, the value of c_D in the model can be made to vary in space and time, depending on the roughness height, which itself varies in space and time as a function of flow regime and grain size.

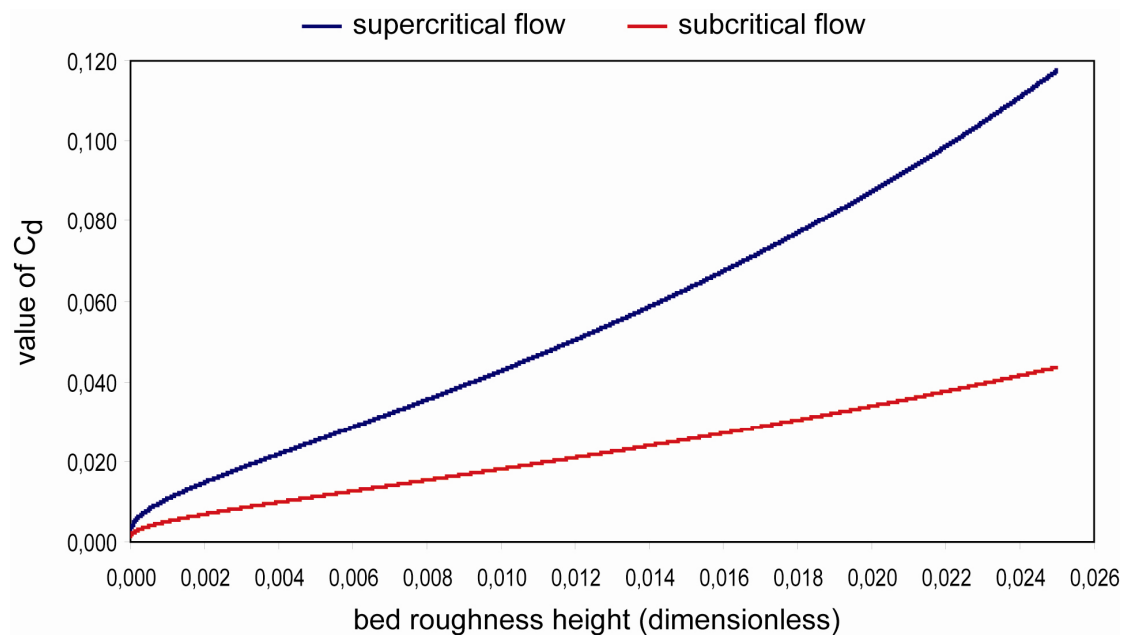


Figure 7.1: Graph of relationships between c_D and bed roughness height for supercritical and subcritical flow, derived by Sloff (1997) based on laboratory data from various sources (see Chapter 2, Figure 2.10 for sources).

Linkage of sediment entrainment to the level of turbulence also provides a constraint on solutions obtained with the model presented and validated in this thesis, specifically in simulations involving sustained, waxing turbidity currents. In such cases, the model allows for strong self-acceleration to a point where the turbulent energy expended in entraining sediment from the bed would exceed the supply of energy to the turbulence. In the absence of a feedback between the level of turbulent-kinetic energy and sediment entrainment in the model, this eventually results in flows that grow to physically unrealistic proportions, with concentrations of suspended sediment far in excess of the capacity of the flow. Conditions favourable to self-acceleration occur on high topographic gradients and in combination with the availability of sediment to be entrained. Such conditions are characteristic of continental slopes and delta fronts. The model presented here is therefore limited to base-of-slope and basin-floor settings, in which the feedback between turbulence and sediment entrainment is assumed to be negligible.

Parameterization of sediment transport and ambient water entrainment in the model is mostly based on empirical relations, the validity of which is usually limited to specific conditions. Furthermore, the assumption of steady-state flow is often assumed in the derivation of empirical relations, whereas, in reality, turbidity currents are highly unsteady. To illustrate the level of empiricism involved in the parameterizations adopted in the model, Figure 7.2 displays a graph of the ambient water entrainment rate versus the Richardson number.

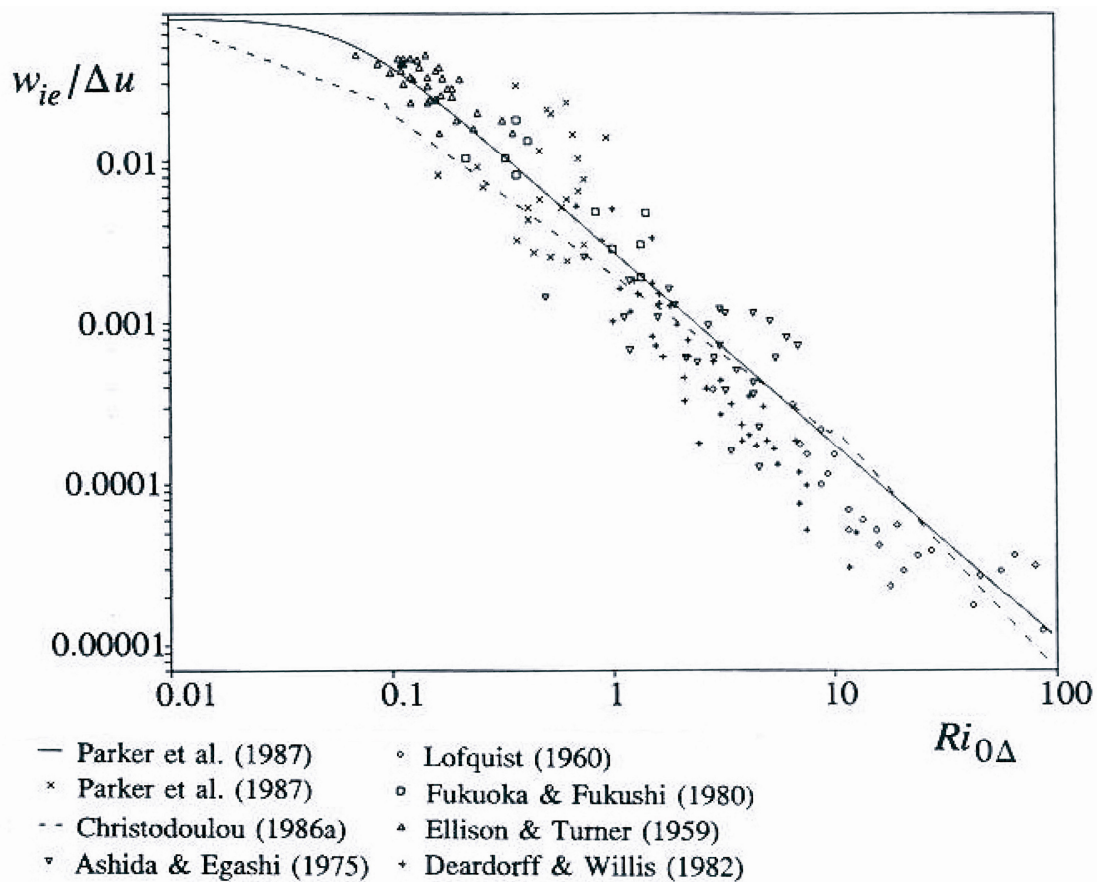


Figure 7.2: Graph of water entrainment rate versus Richardson number (reproduced from Sloff, 1997). Points represent laboratory data from various sources. Lines represent best fit relations by Parker et al. (1987) and Christodoulou (1986a).

The solid line in Figure 7.2 represents the best-fit by Parker et al. (1987), on which the parameterization of water entrainment in our model is based. However, the large scatter in the data points indicates that entrainment rates vary up to one order of magnitude for a given Richardson number. Such differences in the water entrainment rate may drastically alter the behaviour of a modelled turbidity current. If the rate of entrainment is underestimated, slow dilution results in artificially high densities and, consequently, artificially high velocities and rates of erosion. In contrast, if the rate of entrainment is overestimated, the density of the flow decreases rapidly, resulting in flow deceleration, loss of competence and, ultimately, rapid fall-out of sediment from suspension. Run-out length will be limited, and deposition will be localized.

Another possible improvement of the model is related to the absence of cohesive forces between particles in the flow. Recent experimental work by Baas & Best (2002) has shown that, at concentrations of clay above 2% by volume, the turbulence structure and vertical profiles of velocity and concentration are drastically different from their clay-free counterparts on account of the cohesive forces between the clay particles. In order to properly include the effect of cohesion between particles on the flow, the hydrodynamic model would have to be truly three-dimensional and would have to include turbulence to account for vertical variations in velocity and concentration. This requires fundamental changes to the *FanBuilder* model to a point where it would be better to build a new model. Therefore, modelling cohesion effects between particles is not planned in the near-future.

7.3 *Future work*

7.3.1 Field-scale applications

The *FanBuilder* model was developed as a tool to investigate hydrodynamic parameters governing turbidity-current flow, such as bathymetric relief, flow density, and grain-size distribution of the suspended sediment, and their effects on depositional patterns (heterogeneities) observed in turbidite fans. So far, the model has been validated by comparing simulations to experimental data of laboratory-scale flows and deposits. However, in the near future, it will also be used in a study of the conditions of deposition of turbidites in the Tanqua depocentre of the SW Karoo Basin, South Africa. The Tanqua Karoo turbidites provide outstanding three-dimensional exposures, which have enabled researchers (e.g. Hodgson et al., 2006) to collect a high-resolution three-dimensional dataset which is suitable for use in data-constrained stratigraphic modelling.

The turbidites in the Tanqua depocentre comprise four sand-rich basin-floor fans, which were deposited during Permian times, possibly as a result of high-frequency climatically driven glacio-eustatic sea-level cycles. Based on integration of correlated outcrop, core and wireline logs, extensive paleocurrent data and accurately mapped surfaces, a common model of the stratigraphic evolution was developed. Results suggest that subtle seabed topography may have been influential in establishing the position of the boundaries of the fan systems, the internal facies architecture and the paleocurrent directions (Hodgson et al., 2006).

The research to be undertaken aims at estimating the main parameters (density, relief, grain size, volume) of flows responsible for deposition of the basin-floor fans. Of special interest will be the influence of intra-basinal topography on the evolution of observed depositional features, such as e.g. geometry and isopach pattern of the basin floor fans and oblique lateral pinch-outs indicative of flow diversion due to local synsedimentary relief development. Furthermore, and on intra-fan scale, the initiation and development of observed zones of highly amalgamated sheet turbidites, which are thought to be associated with wide zones of low amplitude relief, will be investigated. A high-resolution three-dimensional dataset, which was acquired during the NOMAD project (Hodgson et al., 2006), will be used to constrain the model. It allows for extraction of model input data, such as magnitudes and recurrence intervals of turbidity currents, initial basin-floor topography, geometries of individual turbidite beds, and grain-size distribution of the source sediment. Flow regime may be inferred from sedimentary structures observed in outcrops and cores.

7.3.2 Numerical experiments

An alternative application of the *FanBuilder* model would be to use it to study depositional patterns on a more conceptual level. For example, the driving forces behind the initiation, development, and abandonment of submarine channels are poorly understood. Likewise, and related to this, the development of levees may be linked to the grain-size distribution of the transported sediment. The *FanBuilder* model can be used to explore the conditions favourable to channel-levee initiation, and to assess how the development of channels is governed by e.g. bed slope, sediment composition and variations in magnitude of the turbidity currents. Furthermore, and on a more generic level, it can be used to investigate how the response of turbidity currents to internal and external perturbations affects the resulting deposit. Insight into the depositional process at this level may be helpful in formulating criteria for extrapolation of one-dimensional well data to three-dimensional space.

REFERENCES

- Abbot, M. B. (1979). Computational Hydraulics: Elements of the Theory of Free-surface Flows. London, Pitman. 324 p.
- Akiyama, J. and Stefan, H. G. (1986). "Prediction of turbidity currents in reservoirs and coastal regions." *Proc. Third International Symposium on River Sedimentation*: 1295-1305.
- Alexander, J. and Morris, S. (1994). "Observations on experimental, non-channelized, high-concentration turbidity currents and variations in deposits around obstacles." *Journal of Sedimentary Research* **64**: 899-909.
- Allen, J. R. L. (1971). "Mixing at turbidity-current heads, and its geological implications." *Journal of Sedimentary Petrology* **41**: 97-113.
- Allen, J. R. L. (1985). Principles of Physical Sedimentology. Boston, George Allen and Unwin. 272 p.
- Altinakar, M. S., Graf, W. H. and Hopfinger, E. J. (1990). "Weakly depositing turbidity currents on a small slope." *Journal of Hydraulic Research, IAHR* **28**(1): 55-80.
- Altinakar, M. S., Graf, W. H. and Hopfinger, E. J. (1996). "Flow structure in turbidity currents." *Journal of Hydraulic Research, IAHR* **34**: 713-718.
- Ashida, K. and Egashira, S. (1975). "Basic study on turbidity currents." *Trans. Jpn. Soc. Civ. Engrg, Hydr. Sanit. Engrg Div.* **7**: 83-86.
- Atkins, P. W. (1990). Physical Chemistry. Oxford, Oxford University Press. 995 p.
- Baas, J. H. and Best, J. L. (2002). "Turbulence modulation in clay-rich sediment-laden flows and some implications for sediment deposition." *Journal of Sedimentary Research* **72**(3): 336-340.
- Baas, J. H., van Kesteren, W. and Postma, G. (2004). "Deposits of depletive, quasi-steady high-density turbidity currents: a flume analogue of bed geometry, structure and texture." *Sedimentology* **51**: 1053-1089.
- Bacoccolli, G. and Toffoli, L. C. (1988). "The role of turbidites in brazil's offshore exploration-a review." *Offshore Technology Conference Proceedings* 5559: 379-388.
- Bagnold, R. A. (1954). "Experiments on a gravity-free dispersion of large solid spheres in a Newtonian fluid under shear." *Proceedings of the Royal Society of London* **A225**: 49-63.
- Bagnold, R. A. (1962). "Auto-suspension of transported sediment: turbidity currents." *Proceedings of the Royal Society of London* **A265**: 315-319.

Bagnold, R. A. (1966). "An approach to the sediment transport problem from general physics." *Geological Survey Professional Paper* **422-1**: I1-I37.

Barré de Saint-Venant, A. J. C. (1871). "Théorie du mouvement non permanent des Eaux, avec application aux crues des rivières et à l'introduction des marées dans leur lit (theory of non-permanent movement of waters with application to the floods of rivers and to the introduction of the tides within their bed)." *Comptes Rendus Hebdomadaires des Séances de l'Académie des Sciences, Paris 1871 LXXIII*: 147-154, 237-240

Bates, C. C. (1953). "Rational theory of delta formation." *AAPG Bulletin* **37**(9): 2119-2162.

Bates, P. D., Lane, S. N. and Ferguson, R. I. (2005). Computational Fluid Dynamics: Applications in Environmental Hydraulics. Chichester, Wiley. 531 p.

Bear, J. (1972). Dynamics of Fluids in Porous Media. New York, Elsevier. 784 p.

Benjamin, T. B. (1968). "Gravity currents and related phenomena." *Journal of Fluid Mechanics* **31**(2): 209-248.

Best, J., Kirkbride, A. and Peakall, J. (2001). "Mean flow and turbulence structure of sediment-laden gravity currents: new insights using ultrasonic Doppler velocity profiling." Particulate Gravity Currents: Special Publication of the International Association of Sedimentologists #31. McCaffrey, W. D., Kneller, B. C. and Peakall, J. (Eds.). Oxford, U.K., Blackwell Science Ltd: 159-172.

Bonnecaze, R. T., Hallworth, M. A., Huppert, H. E. and Lister, J. R. (1995). "Axisymmetric particle-driven gravity currents." *Journal of Fluid Mechanics* **294**: 93-121.

Bouma, A. H. (1962). Sedimentology of some flysch deposits: a graphic approach to facies interpretation. Amsterdam, Elsevier. 168 p.

Boussinesq, J. (1877). "Théorie de l'écoulement tourbillant." *Mem. Présentés par Divers Savants Acad. Sci. Inst. Fr.* **23**: 46-50.

Bradford, S. F. and Katapodes, N. D. (1999a). "Hydrodynamics of turbid underflows I: formulation and numerical analysis." *Journal of Hydraulic Engineering, ASCE* **125**(10): 1006-1015.

Bradford, S. F. and Katapodes, N. D. (1999b). "Hydrodynamics of turbid underflows II: aggradation, avulsion, and channelization." *Journal of Hydraulic Engineering, ASCE* **125**(10): 1016-1028.

Bradford, S. F., Katapodes, N. D. and Parker, G. (1997). "Characteristic analysis of turbid underflows." *Journal of Hydraulic Engineering, ASCE* **123**(5): 420-431.

Briggs, L. I. and Pollack, H. N. (1967). "Digital model of evaporite sedimentation." *Science* **155**: 453-456.

- Britter, R. W. and Linden, P. F. (1980). "The motion of the front of a gravity current down an incline." *Journal of Fluid Mechanics* **91**: 531-543.
- Britter, R. W. and Simpson, J. E. (1978). "Experiments on the dynamics of a gravity-current head." *Journal of Fluid Mechanics* **88**: 223-240.
- Brookfield, M. E. (2004). Principles of Stratigraphy. Padstow, Blackwell. 340 p.
- Brørs, B. and Eidsvik, K. J. (1989). "Self-accelerated turbidity-current prediction based upon the dynamic turbulence models." Sediment Transport Modelling. Wang, S. S. (Ed.). Proc. Int. Symp. New Orleans: 190-196.
- Buckee, C., Kneller, B. C. and Peakall, J. (2001). "Turbulence structure in steady, solute-driven gravity currents." Particulate Gravity Currents: Special Publication of the International Association of Sedimentologists #31. McCaffrey, W. D., Kneller, B. C. and Peakall, J. (Eds.), Blackwell Scientific Publishing: 173-188.
- Burgess, P. M. and Hovius, N. (1998). "Rates of delta progradation during highstands: consequences for timing of deposition in deep-marine systems." *Journal of the Geological Society of London* **155**: 217-222.
- Chikita, K. (1989). "A field study on turbidity currents generated from spring run-offs." *Water Resources Research* **25**: 257-271.
- Choi, S.-U. and García, M. H. (2002). "k- ϵ turbulence modelling of density currents developing two-dimensionally on a slope." *Journal of Hydraulic Engineering, ASCE* **128**: 55-62.
- Choi, S. U. and García, M. H. (1995). "Modeling of one-dimensional turbidity currents with a dissipative-galerkin finite-element method." *Journal of Hydraulic Research, IAHR* **33**(5): 1-26.
- Christodoulou, G. C. (1986). "Interfacial mixing in stratified flows." *Journal of Hydraulic Research, IAHR* **23**(2): 77-92.
- Chu, F. H., Pilkey, W. D. and Pilkey, O. H. (1979). "An analytical study of turbidity-current steady flow." *Marine Geology* **33**: 205-220.
- Courant, R. and Hilbert, D. (1962). Methods of Mathematical Physics, Vol. II: Partial Differential Equations. New York, Interscience Publishers. 830 p.
- Crowell, J. C. (1957). "Origin of pebbly mudstones." *Geological Society of America Bulletin* **68**: 993-1009.
- Damuth, J. E., Flood, R. D., Kowsmann, R. O., Gorini, M. A. and Beldersen, R. H. (1988). "Anatomy and growth-pattern of Amazon deep-sea fan revealed by long-range sidescan sonar (GLORIA) and high-resolution seismic studies." *American Association of Petroleum Geologists Bulletin* **72**(885-911).

Davidson, J. F., Harrison, D. and Carvalho, G. D. (1977). "On the liquid-like behaviour of fluidized beds." *Annual Review of Fluid Mechanics* **9**: 55-86.

Deardorf, J. W. and Willis, G. E. (1982). "Investigation of the frozen-turbulence hypothesis for temperature spectra in a convectively-mixed layer." *Physics of Fluids* **25**: 21-28.

Dietrich, E. W. (1982). "Settling velocity of natural particles." *Water Resources Research* **18**(6): 1626–1982.

Doreen Jr, J. M. (1951). "Rubble bedding and graded bedding in Talara Formation of northwestern Peru." *American Association of Petroleum Geologists Bulletin* **47**: 104-128.

Dott Jr, R. H. (1963). "Dynamics of subaqueous gravity depositional processes." *American Association of Petroleum Geologists Bulletin* **47**: 104-128.

Duncan, W. J. (1953). Physical Similarity and Dimensional Analysis. London, Edward Arnold & Co.

Duringer, P., Paicheler, J.-C. and Schneider, J.-L. (1991). "Un courant d'eau peut-il generer des turbidites? Resultats d'experimentations analogiques." *Marine Geology* **99**: 231-246.

Eidsvik, K. J. and Brørs, B. (1989). "Self-accelerated turbidity-current prediction based upon k - ϵ turbulence." *Continental Shelf Research* **9**(7): 617-627.

Einstein, H. A. (1950). "The bed-load function for sediment transportation in open-channel flows." *Technical Bulletin 1026, U.S. Dept. of the Army, Soil Conservation Service*.

Einstein, H. A. and Barbarossa, N. L. (1952). "River channel roughness." *Journal of Hydraulic Engineering, ASCE* **117**: 1085–1103.

Ellison, T. H. and Turner, J. S. (1959). "Turbulent entrainment in stratified flows." *Journal of Fluid Mechanics* **6**: 423-448.

Elverhøi, A., Issler, D., De Blasio, F. V., Iltstad, T., Harbitz, C. B. and Gauer, P. (2005). "Emerging insights into the dynamics of submarine debris flows." *Natural Hazards and Earth System Sciences* **5**: 633-648.

Exner, F. M. (1920). "Zur physik der dünen." *Math. Naturwiss. Klasse, Akad. Wiss. Wien* **129**(2a): 929– 952.

Exner, F. M. (1925). "Über die wechselwirkung zwischen wasser und geschiebe in flüssen." *Math. Naturwiss. Klasse, Akad. Wiss. Wien* **134**(2a): 165– 204.

Fan, J. (1986). "Turbid density currents in reservoirs." *Water International, IWRA* **11**(3): 107-116.

Fan, J. (1991). "Density currents in reservoirs." *Workshop on Management of Reservoir Sedimentation, New Delhi, June 1991*: 3.1.1-3.1.13.

Felix, M. (2001). "A two-dimensional numerical model for a turbidity current." Particulate Gravity Currents, Special Publication of the International Association of Sedimentologists # 31. McCaffrey, W. D., Kneller, B. C. and Peakall, J. (Eds.). Oxford, U.K., Blackwell Science Ltd: 71– 83.

Felix, M. (2002). "Flow structure of turbidity currents." *Sedimentology* **49**: 397–419.

Fildani, A. and Normark, W. R. (2004). "Late quarternary evolution of channel and lobe complexes of Monterey fan." *Marine Geology* **206**(1-4): 199-223.

Fisher, R. V. (1971). "Features of coarse-grained, high-concentration fluids and their deposits." *Journal of Sedimentary Petrology* **41**: 916-927.

Flood, R. D., Manley, P. L., Kowsmann, R. O., Appi, C. A. and Pirmez, C. (1991). "Seismic facies and late quarternary growth of Amazon submarine fan." Seismic Facies and Sedimentary Processes of Modern and Ancient Submarine Fans and Turbidite Systems. Weimer, P. and Link, M. H. (Eds.). New York, Springer-Verlag: 415-433.

French, R. H. (1985). Open-Channel Hydraulics. MacGraw-Hill. 704 p.

Friedman, G. M. and Sanders, J. E. (1997). "Dispelling the myth of seafloor tranquility." *Geotimes* **42**: 24-27.

Fukuoka, S. and Fukushima, Y. (1980). "On the dynamic behaviour of the head of a gravity current in a stratified reservoir." *Proceedings of the Second International Symposium on Stratified Flows*: 164-173.

Fukushima, Y., Parker, G. and Pantin, H. M. (1985). "Prediction of ignitive turbidity currents in Scripps submarine canyon." *Marine Geology* **67**: 55-81.

Galappatti, R. (1983). A depth-integrated model for suspended sediment transport. Communications on Hydraulic and Geotechnical Engineering, 83-7. Delft, The Netherlands, Delft University of Technology: 114.

Galappatti, R. and Vreugdenhil, C. B. (1985). "A depth-integrated model for suspended sediment transport." *Journal of Hydraulic Research, IAHR* **23**(4): 359-377.

García-Navarro, P., Alcrudo, F. and Savorín, J. M. (1992). "1-D Open-channel flow simulation using TVD-MacCormack scheme." *Journal of Hydraulic Engineering, ASCE* **118**(10): 1359-1372.

García, M. H. (1985). Experimental study of turbidity currents. M. Sc. thesis, Dept. of Civil and Mineral Engineering, University of Minnesota, USA: -

García, M. H. (1990). Depositing and eroding sediment-driven flows: turbidity currents. Ph. D. thesis, St. Anthony Falls Hydraulic Laboratory, University of Minnesota, USA: -

García, M. H. (1993). "Hydraulic jumps in sediment-driven bottom currents." *Journal of Hydraulic Engineering, ASCE* **119**(10): 1094-1117.

García, M. H. (1994). "Depositional turbidity currents laden with poorly sorted sediment." *Journal of Hydraulic Engineering, ASCE* **120**(11): 1240-1263.

García, M. H. and Parker, G. (1989). "Experiments on hydraulic jumps in turbidity currents near a canyon-fan transition." *Science* **245**: 393-396.

García, M. H. and Parker, G. (1991). "Entrainment of bed sediment into suspension." *Journal of Hydraulic Engineering, ASCE* **117**(4): 414-435.

García, M. H. and Parker, G. (1993). "Experiments on the entrainment of sediment into suspension by a dense bottom current." *Journal of Geophysical Research* **98**(C3): 4793-4807.

García, M. H. and Parsons, J. D. (1996). "Mixing at the front of gravity currents." *Dynamic Atmosphere and Oceans* **24**: 197-205.

García, M. H., Yu, W. and Parker, G. (1986). "Experimental study of turbidity currents." Advancements in Aerodynamics, Fluid Mechanics and Hydraulics; Proc. Conf. ASCE, Minneapolis, Minnesota. Stefan, H. G., et al. (Ed.). Minnesota: 120-127.

García, R. and Kahawita, R. A. (1986). "Numerical solution of the St. Venant equations with the MacCormack finite-difference scheme." *International Journal for Numerical Methods in Fluids* **6**: 259-274.

Gardner, J. V. and Kidd, R. B. (1983). "Sedimentary processes on the Iberian continental margin viewed by long-range sidescan sonar part I: Gulf of Cadiz." *Oceanol. Acta* **6**: 245-254.

Gardner, M. H. and Borer, J. M. (2000). "Submarine channel architecture along a slope-to-basin profile, permian Brushy Canyon Formation, West Texas (68)." Fine-Grained Turbidite Systems. AAPG Memoir 72 / SEPM Special Publication. Bouma, A. H. and Stone, C. G. (Eds.): 195-215.

Gee, M. J. R., Masson, D. G., Watts, A. B. and Allen, P. A. (1999). "The Saharan debris flow: an insight into the mechanics of long-runout submarine debris flows." *Sedimentology* **46**(317-335).

Griffiths, C. M., Dyt, C., Paraschivoiu, E. and Liu, K. (2001). "SEDSIM in hydrocarbon exploration." Geological Modelling and Simulation: Sedimentary Systems. Merriam, D. F. and Davis, J. C. (Eds.), Kluwer Academic Publishers: 71-98.

- Gustafsson, B. (1975). "The convergence rate of difference approximations for mixed initial boundary value problems." *Mathematics of Computation* **29**: 396-406.
- Hallworth, M. A. and Huppert, H. E. (1998). "Abrupt transitions in high-concentration, particle-driven gravity currents." *Physics of Fluids* **10**: 1083-1087.
- Hampton, M. A. (1972). "The role of subaqueous debris flow in generating turbidity currents." *Journal of Sedimentary Petrology* **45**: 834-844.
- Hampton, M. A. (1975). "Competence of fine-grained debris flows." *Journal of Sedimentary Petrology* **45**: 834-844.
- Harbaugh, J. W. and Bonham-Carter, G. (1970). Computer Simulation in Geology. New York, John Wiley and Sons. 575 p.
- Härtel, C., Meiburg, E. and Necker, F. (2000). "Analysis and direct numerical simulation of the flow at a gravity-current head, part 1: flow topology and front speed for slip and no-slip boundaries." *Journal of Fluid Mechanics* **418**: 189-212.
- Harten, A. (1983). "High-resolution schemes for hyperbolic conservation laws." *Journal of Computational Physics* **49**(3): 357-393.
- Harten, A. and Hyman, J. M. (1983). "Self-adjusting grid method for one-dimensional hyperbolic conservation laws." *Journal of Computational Physics* **50**: 235-269.
- Haughton, P. D. W., Barker, S. P. and McCaffrey, W. D. (2003). "'Linked' debrites in sand-rich turbidite systems - origin and significance." *Sedimentology* **50**: 459-482.
- Heezen, B. C. and Ewing, M. (1952). "Turbidity currents and submarine slumps and the 1929 Grand Banks earthquake." *American Journal of Science* **250**: 849-873.
- Hirsch, C. (1988). Numerical Computation of Internal and External Flows: Volume 1: Fundamentals of Numerical Discretization. J. Wiley & Sons, England. 515 p.
- Hirsch, C. (1990). Numerical Computation of Internal and External Flows: Volume 2: Computational Methods for Inviscid and Viscous Flows. J. Wiley & Sons, England. 691 p.
- Hiscott, R. N. (1994a). "Loss of capacity, not competence, as the fundamental process governing deposition from turbidity currents." *Journal of Sedimentary Research* **A64**: 209-214.
- Hiscott, R. N. (1994b). "Traction-carpet stratification in turbidites - fact or fiction?" *Journal of Sedimentary Research* **A64**: 204-208.
- Hiscott, R. N. (1995). "Traction-carpet stratification in turbidites - fact or fiction? (Reply)." *Journal of Sedimentary Research* **A65**: 704-705.
- Hiscott, R. N. and James, N. P. (1985). "Carbonate debris flows, Cow Head Group, western Newfoundland." *Journal of Sedimentary Petrology* **55**: 735-745.

Hodgson, D. M., Drinkwater, N. J., Flint, S. S., Luthi, S. M., Hodgetts, D., Johannessen, E. J., De Ville Wickens, H., Keogh, K., Kavanagh, J. P. and Howell, J. A. (2006). "Fine-grained submarine fan growth and the distribution of lithofacies and architectural elements: an example from the Skoorsteenberg Formation (Fan 4), Tanqua Depocenter, SW Karoo Basin, South Africa." Atlas of Deepwater Outcrops, AAPG Special Publication (in press). Shew, R., Nilsen, T., Steffans, G. and Studlick, J. (Eds.).

Hoogendoorn, R. M. (2006). The impact of changes in sediment supply and sea-level on fluvio-deltaic stratigraphy. Ph. D. thesis, Department of GeoTechnology, Delft University of Technology, Delft, The Netherlands: 153 p.

Hopfinger, E. J. and Tochon-Danguy, J. C. (1977). "A model study of powder-snow avalanches." *Journal of Glaciology* **19**: 343-356.

Hsu, K. J. (1959). "Flute- and groove-casts in the prealpine flysch, Switzerland." *American Journal of Science* **257**: 529-536.

Hughes-Clarke, J. E., Shor, A. N., Piper, D. J. W. and Mayer, L. A. (1990). "Large-scale current-induced erosion and deposition in the path of the 1929 Grand Banks turbidity current." *Sedimentology* **37**: 613-620.

Huppert, H. E. and Simpson, J. E. (1980). "The slumping of gravity currents." *Journal of Fluid Mechanics* **99**: 785-799.

Hutter, K. (1996). "Avalanche dynamics." Hydrology of Disasters. Singh, V. P. (Ed.), Kluwer Academic Publishers: 317-394.

Ilstad, T., Elverhøi, A., Issler, D. and Marr, J. (2004). "Subaqueous debris-flow behaviour and its dependence on the sand/clay ratio: A laboratory study using particle tracking." *Marine Geology* **213**: 415-438.

Imran, J., Parker, G. and Katapodes, N. (1998). "A numerical model of channel inception on submarine fans." *Journal of Geophysical Research* **103 (C1)**: 1219-1238.

Imran, J. and Syvitski, J. P. M. (2000). "Impact of extreme river events on the coastal ocean." *Oceanography* **13(3)**: pp. 85-92.

Iverson, R. M. (1997). "Physics of debris flows." *Rev. Geophys.* **35**: 245-296.

Johnson, A. M. (1970). Physical Processes in Geology. San Fransisco, Freeman, Cooper and Company. 557 p.

Johnson, A. M. (1984). "Debris flow." Slope Instability. Brunden, D. and Prior, D. B. (Eds.). Toronto, Wiley: 257-362.

Johnson, D. (1938). "The origin of submarine canyons." *Journal of Geomorphology* **1**: 111-340.

- Kelts, K. and Hsu, J. (1980). "Resedimented facies of 1875 Horgen slumps in Lake Zurich and a process model of longitudinal transport of turbidity currents." *Eclogae Geologicae Helveticae* **73**(1): 271-281.
- Keulegan, G. H. (1938). "Laws of turbulent flow in open channels." *National Bureau of Standards Research Paper RP 1151, USA*.
- Keulegan, G. H. (1957). An experimental study of the motion of saline water from locks into fresh-water channels. US. Natl. Bur. Stand., Report 5168.
- Khan, S. M., Imran, J., Bradford, J. S. and Syvitski, J. P. M. (2005). "Numerical modelling of hyperpycnal plume." *Marine Geology* **222-223**: pp.193-211.
- Kirwan Jr., A. D., Doyle, L. J., Bowles, W. D. and Brooks, G. R. (1986). "Time-dependent hydrodynamic models of turbidity currents analysed with data from the Grand Banks and Orleansville events." *Journal of Sedimentary Petrology* **56**(3): 379-386.
- Knapp, R. T. (1938). "Energy balance in streams carrying suspended load." *Trans. Am. Geophys. Union* **1**: 501-505.
- Kneller, B. C. (1995). "Beyond the turbidite paradigm: physical models for deposition of turbidites and their implications for reservoir prediction." Characterization of Deep Marine Clastic Systems. Hartley, A. J. and Prosser, D. J. (Eds.), Geological Society of London Special Publication. **94**: 31-49.
- Kneller, B. C., Bennet, S. J. and McCaffrey, W. D. (1997). "Velocity and turbulence structure of gravity currents and internal solitary waves: potential sediment transport and the formation of wave ripples in deep water." *Sedimentary Geology* **112**: 235-250.
- Kneller, B. C., Bennet, S. J. and McCaffrey, W. D. (1999). "Velocity, turbulence and fluid stresses in experimental gravity currents." *Journal of Geophysical Research, Oceans* **104**: 5281-5291.
- Kneller, B. C. and Branney, M. J. (1995). "Sustained high-density turbidity currents and the deposition of thick massive beds." *Sedimentology* **42**: 607-616.
- Kneller, B. C. and Buckee, C. (2000). "The structure and fluid mechanics of turbidity currents: a review of some recent studies and their geological implications." *Sedimentology* **47**(Suppl. 1): 62-94.
- Kneller, B. C. and McCaffrey, W. D. (1995). "Modelling the effects of salt-induced topography on deposition from turbidity currents." Salt, Sediment and Hydrocarbons; SEPM Gulf Coast Section, Houston. Travis, C. J., Harrison, H., Hudeac, M. R., Vendeville, B. C., Peel, F. J. and Perkins, R. F. (Eds.): 137-145.
- Komar, P. D. (1971). "Hydraulic jumps in turbidity currents." *Geological Society of America Bulletin* **82**: 1477-1481.

- Komar, P. D. (1977). "Computer simulation of turbidity-current flow and the study of deep-sea channels." *The Sea* **6**: 603-621.
- Kostic, S. and Parker, G. (2006). "The response of turbidity currents to a canyon-fan transition: internal hydraulic jumps and depositional signatures." *Journal of Hydraulic Research* **44**(5): 631-654.
- Kubo, Y., Syvitski, J. P. M., Hutton, E. W. H. and Paola, C. (2004). "Experimental and numerical study of topographic effects on deposition from two-dimensional, particle-driven density currents." *Sedimentary Geology* **164**: 311-326.
- Kubo, Y., Syvitski, J. P. M., Hutton, E. W. H. and Paola, C. (2005). "Advance and application of the stratigraphic simulation model 2D-SedFlux: from tank experiment to geological-scale simulation." *Sedimentary Geology* **178**: pp. 187-195.
- Kuenen, P. H. (1937). "Experiments in connection with Daly's hypothesis on the formation of submarine canyons." *Leidse Geol. Meded.* **8**: 327-335.
- Kuenen, P. H. (1950). "Turbidity currents of high density." *Proceedings of the 18th International Geological Congress (1948) Reports pt. 8*: 44-52.
- Kuenen, P. H. (1952). "Estimated size of the Grand Banks turbidity current." *American Journal of Science* **250**: 849-873.
- Kuenen, P. H. (1957). "Sole markings of graded graywacke beds." *Journal of Geology* **65**: 231-258.
- Kuenen, P. H. and Migliorini, C. I. (1950). "Turbidity currents as a cause of graded bedding." *Journal of Geology* **58**: 91-127.
- Lamb, M., Hickson, T., Sheets, B., Marr, J., Paola, C. and Parker, G. (2004). "Surging versus continuous turbidity currents: flow dynamics and deposits in an experimental intraslope minibasin." *Journal of Sedimentary Research* **74**: 148-155.
- Lambert, A. and Giovanoli, F. (1988). "Records of riverborne turbidity currents and indications of slope failures in the Rhone delta of Lake Geneva." *Limnology and Oceanography* **33**(3): 458-468.
- Lambert, A. and Luthi, S. M. (1977). "Lake circulation induced by density currents: an experimental approach." *Sedimentology* **24**: 735-741.
- Lander, J. F. and Lockridge, P. A. (1989). United States tsunamis, U.S. Department of Commerce.
- Larson, R. G. (1999). The Structure and Rheology of Complex Fluids. Oxford, New York, Oxford University Press. 663 p.
- Laval, A., Cremer, M., Beghin, P. and Ravenne, C. (1988). "Density surges: two-dimensional experiments." *Sedimentology* **35**: 73-84.

Lax, P. D. (1957). "Hyperbolic systems of conservation laws II." *Comm. Pure and Applied Mathematics* **10**: 537-566.

Lax, P. D. and Wendroff, B. (1960). "Systems of conservation laws." *Comm. Pure and Applied Mathematics* **13**(2): 217-237.

Lax, P. D. and Wendroff, B. (1964). "Difference schemes for hyperbolic conservation laws with high order of accuracy." *Comm. Pure and Applied Mathematics* **17**(3): 381-398.

Leeder, M. R. (1988). *Sedimentology*. London, Unwin Human Ltd. 344 p.

Leigh, N. S. and Hartley, A. (1992). "Mega debris-flow deposits from the oligo-miocene Pindos foreland basin, western mainland Greece: implications for transport mechanisms in ancient deep-marine basins." *Sedimentology* **39**: 1003-1012.

LeVeque, R. J. (1990). *Numerical methods for conservation laws*. Basel, Birkhäuser-Verlag. 214 p.

Lipman, P. W., Normark, W. R., Moore, J. G., Wilson, J. B. and Gutmacher, C. E. (1988). "The giant submarine Alike debris slide: Mauna Loa, Hawaii." *Journal of Geophysical Research* **93**: 4279-4299.

Lofquist, K. (1960). "Flow and stress near an interface between stratified liquids." *Physics of Fluids* **3**: 158-175.

Lopez, M. (2001). "Architecture and depositional pattern of the quarternary deep-sea fan of the Amazon." *Marine and Petroleum Geology* **18**: 479-486.

Lowe, D. R. (1979). "Sediment-gravity flows: their classification, and some problems of applications to natural flows and deposits." *Geology of Continental Slopes*. Doyle, L. J. and Pilkey, O. H. (Eds.), Society of Economic Paleontologists and Mineralogists Special Publication. **27**: 75-82.

Lowe, D. R. (1982). "Sediment-gravity flows II: depositional models with special reference to the deposits of high-density turbidity currents." *Journal of Sedimentary Petrology* **52**: 279-297.

Lowe, D. R. and Guy, M. (2000). "Slurry-flow deposits in the Britannia Formation (lower cretaceous), North Sea: a new perspective on the turbidity-current and debris-flow problem." *Sedimentology* **47**: 31-70.

Luthi, S. M. (1980a). "Some new aspects of two-dimensional turbidity currents." *Sedimentology* **28**: 97-105.

Luthi, S. M. (1980b). "Die eigenschaften nichtkanalisierte trubestrome: eine experimentelle untersuchung." *Eclogae Geologicae Helveticae* **73**(3): 881-904.

Luthi, S. M. (1981). "Experiments on non-channelized turbidity currents and their deposits." *Marine Geology* **40**: M59-M68.

MacCormack, R. W. (1969). The effect of viscosity in hypervelocity impact cratering. AIAA Paper 69-354, 7th Aerospace Sciences Meeting. Cincinnati, Ohio, USA.

MacCormack, R. W. (1981). A numerical method for solving the equations of compressible viscous flows. AIAA Paper, 81-0110, 19th Aerospace Science Meeting. St. Louis, Missouri, USA.

MacCormack, R. W. and Baldwin, B. S. (1975). A numerical method for solving the Navier-Stokes equations with application to shock - boundary-layer interactions. AIAA Paper 75-1, 13th Aerospace Science Meeting. Pasadena, California, USA.

Marr, J. G., Harff, P. A., Shanmugam, G. and Parker, G. (2001). "Experiments on subaqueous sandy gravity flows: the role of clay and water content in flow dynamics and depositional structures." *Geological Society of America Bulletin* **113**: 1377–1386.

Martinez, P. A. and Harbaugh, J. W. (1993). Simulating Nearshore Environments. Pergamon Press. 265 p.

Mastbergen, D. R. and Van den Berg, D. H. (2003). "Breaching in fine sands and the generation of sustained turbidity currents in submarine canyons." *Sedimentology* **50**: 625-637.

Middleton, G. V. (1966a). "Experiments on density and turbidity currents I: motion of the head." *Canadian Journal of Earth Sciences* **3**: 523-546.

Middleton, G. V. (1966b). "Experiments on density and turbidity currents II: uniform flow of density currents." *Canadian Journal of Earth Sciences* **3**: 627-637.

Middleton, G. V. (1967). "Experiments on density and turbidity currents III: deposition of sediment." *Canadian Journal of Earth Sciences* **4**: 475-505.

Middleton, G. V. (1993). "Sediment deposition from turbidity currents." *Annual Review of Earth and Planetary Sciences* **21**: 89-114.

Middleton, G. V. and Hampton, M. A. (1973). "Sediment-gravity flows: mechanics of flow and deposition." Turbidites and Deep-Water Sedimentation. Middleton, G. V. and Bouma, A. H. (Eds.). Los Angeles, Pacific Section of the Society of Economic Paleontologists and Mineralogists. **Short Course Lecture Notes**: 1-38.

Middleton, G. V. and Southard, J. B. (1984). "Mechanics of sediment movement." *SEPM, Short Course* **3**: 401pp.

Miles, J. (1990). "Richardson's number revisited." Proceedings of the International Symposium on Stratified Flows, ASCE, Pasadena, California, USA. List, E. J. and Jirka, G. H. (Eds.): 1-7.

Milne, J. (1897). "Suboceanic changes." *Geographical Journal* **10**: 129-146, 259-289.

- Mohrig, D., Elverhøi, A. and Parker, G. (1999). "Experiments on the relative mobility of muddy subaqueous and subaerial debris flows and their capacity to remobilize antecedent deposits." *Marine Geology* **154**: 117-129.
- Mohrig, D., Whipple, K. X., Hondzo, M., Ellis, C. and Parker, G. (1998). "Hydroplaning of subaqueous debris flows." *Geological Society of America Bulletin* **110**: 387-394.
- Mulder, T. and Alexander, J. (2001a). "The physical character of subaqueous sedimentary density flows and their deposits." *Sedimentology* **48**: 269-299.
- Mulder, T., Migeon, S., Savoye, B. and Faugeres, J.-C. (2001b). "Inversely-graded turbidite sequences in the deep Mediterranean: a record of deposits from flood-generated turbidity currents?" *Geo Marine Letters* **21**: 86-93.
- Mulder, T., Savoye, B., Syvitski, J. P. M. and Cochonat, P. (1997b). "Origine des courants de turbidité enregistrés à l'embouchure du Var en 1971." *Comptes Rendus de l'Académie de Sciences, Paris, Serie IIA* **322**(4): 301-307.
- Mulder, T., Savoye, B., Syvitski, J. P. M. and Parize, O. (1997a). "Des courants de turbidité hyperpycnaux dans la tête du canyon du Var: données hydrologiques et observations de terrain." *Oceanol. Acta* **20**: 607-626.
- Mulder, T. and Syvitski, J. P. M. (1995). "Turbidity currents generated at river mouths during exceptional discharges to the world oceans." *Journal of Geology* **103**: 285-299.
- Mulder, T., Syvitski, J. P. M., Migeon, S., Faugeres, J.-C. and Savoye, B. (2003). "Marine hyperpycnal flows: initiation, behaviour and related deposits: a review." *Marine and Petroleum Geology* **20**: 861-882.
- Mulder, T., Syvitski, J. P. M. and Skene, K. (1998). "Modelling of erosion and deposition by sediment-gravity flows generated at river mouths." *Journal of Sedimentary Research* **68**(1): 124-137.
- Mulder, Y. and Syvitski, J. P. M. (1996). "Climatic and morphologic relationships of rivers: implications of sea-level fluctuations on river loads." *Journal of Geology* **104**(509-523).
- Munson, B. R., Young, D. F. and Okiishi, T. H. (1998). Fundamentals of Fluid Mechanics. John Wiley and Sons. 877 p.
- Mutti, E. (1985). "Turbidite systems and their relations to depositional sequences." Provenance of Arenites. Zuffa, G. G. (Ed.). Dordrecht, D. Reidel Publishing Company.
- Mutti, E. and Normark, W. R. (1991). "An integrated approach to the study of turbidite systems." Seismic Facies and Sedimentary Processes of Submarine Fans and Turbidite Systems. Weimer, P. and Link, W. H. (Eds.). New York, Springer-Verlag: 75-106.

- Mutti, E. and Ricci Lucchi, F. (1972). "Turbidites of the northern Apennines: introduction to facies analysis." *International Geology Review* **20**: 125-166.
- Mutti, E., Tinterri, R., Benevelli, G., Angella, S. di Biase, D., & Cavanna, G., (2003). "Deltaic, mixed, and turbidite sedimentation of ancient foreland basins." *Marine and Petroleum Geology* **20**: 733-755.
- Nichols, G. (1999). "Processes of transport and sedimentary structure." *Sedimentology and Stratigraphy*. Nichols, G. (Ed.). Oxford, Blackwell Sciences.
- Nissen, S. E., Haskell, N. L., Steiner, C. T. and Coterill, K. L. (1999). "Debris-flow outrunner blocks, glide tracks and pressure ridges identified on the Nigerian continental slope using 3-D seismic coherency." *Leading Edge* **18**: 595-599.
- Normark, W. R. (1970). "Growth patterns of deep-sea fans." *American Association of Petroleum Geologists Bulletin* **54**: 2170-2195.
- Normark, W. R. (1989). "Observed parameters for turbidity-current flow in channels, Reserve fan, Lake Superior." *Journal of Sedimentary Petrology* **59**: 423-431.
- Normark, W. R., Moore, J. G. and Torresan, M. E. (1993). "Giant volcano-related landslides and the development of the Hawaiian Islands." *Submarine landslides: selected studies in the US exclusive economic zone*. Schwab, W. C., Lee, H. J. and Twichel, D. C. (Eds.): 184-196.
- Oreskes, N., Shrader-Frechette, K. and Belitz, K. (1994). "Verification, validation and confirmation of numerical models in the earth sciences." *Science* **263**(4): 641-646.
- Pantin, H. M. (1979). "Interaction between velocity and effective density in turbidity flow: phase-plane analysis, with Criteria for autosuspension." *Marine Geology* **31**: 59-99.
- Paola, C. (2000). "Quantitative models of sedimentary basin filling." *Sedimentology* **47**(suppl 1.): 121-178.
- Parker, G. (1982). "Conditions for the ignition of catastrophically erosive turbidity currents." *Marine Geology* **46**(307-327).
- Parker, G. (2004). "1D sediment transport morphodynamics with application to rivers and turbidity Currents."
from http://cee.uiuc.edu/people/parkerg/morphodynamics_e-book.htm.
- Parker, G., Fukushima, Y. and Pantin, H. M. (1986). "Self-accelerating turbidity currents." *Journal of Fluid Mechanics* **171**: 145-181.
- Parker, G., García, M. H., Fukushima, Y. and Yu, W. (1987). "Experiments on turbidity currents over an erodible bed." *Journal of Hydraulic Research, IAHR* **25**: 123-147.

- Parsons, J. D. (1998). Mixing Mechanisms in Density Intrusions. Ph. D. thesis, University of Illinois, Urbana-Champaign: -
- Parsons, J., Friedrichs, C., Garcia, M. H., Imran, J., Mohrig, D., Parker, G., Pratson, L., Puig, P., Syvitski, J. P. M. and Traykovski, P. (2007). "The mechanics of marine sediment-gravity flows." In: Continental-Margin Sedimentation: From Sediment Transport to Sequence Stratigraphy; IAS Spec. Publ. No. 37: 275-338. Nittrouer, C. A., Austin, J. A., Field, M. E., Kravitz, J. H., Syvitski, J. P. M. and Wiberg, P. L. (Eds.).
- Peakall, J., Ashworth, P. and Best, J. (1996). "Physical modelling in fluvial geomorphology: principles, applications, and unresolved issues." The Scientific Nature of Geomorphology. Rhoads, B. L. and Thorn, C. E. (Eds.). Chichester, John Wiley and Sons: 221-253.
- Peakall, J., McCaffrey, W. D. and Kneller, B.C. (2000). "A process model for the evolution, morphology, and architecture of sinuous submarine channels." *Journal of Sedimentary Research* **70**(3): 434-448.
- Pickering, K. T., Hiscott, R. N. and Hein, F. J. (1989). Deep-marine environments: clastic sedimentation and tectonics. London, Unwin Hyman. 416 p.
- Piper, D. J. W., Cochonat, P. and Morrison, M. (1999). "The sequence of events around the epicentre of the 1929 Grand Banks earthquake: initiation of debris flows and turbidity current inferred from sidescan sonar." *Sedimentology* **46**: 215-234.
- Piper, D. J. W., Shor, A. N. and Hughes Clarke, J. E. (1988). "The 1929 Grand Banks earthquake, slump and turbidity current." Sedimentologic Consequences of Convulsive Geologic Events. Clifton, H. E. (Ed.): 77-92.
- Posamentier, H. W., Erskine, R. and Mitchum Jr, R. (1991). "Models of submarine-fan deposits within a sequence-stratigraphic framework." Seismic Facies and Sedimentary Processes of Submarine Fans and Turbidite Systems. Weimer, P. and Link, W. H. (Eds.). New York, Springer-Verlag: 127-137.
- Postma, G. (1986). "Classification for sediment-gravity-flow deposits based on flow conditions during sedimentation." *Geology* **14**: 291-294.
- Postma, G., Nemec, W. and Kleinspehn, K. L. (1988). "Large floating clasts in turbidites: a mechanism for their emplacement." *Sedimentary Geology* **58**(1): 47-61.
- Prandtl, L. (1952). Essentials of Fluid Dynamics. New York, Hafner Publishing Company
- Pratson, L., Imran, J., Hutton, E., Parker, G. and Syvitski, J. P. M. (2001). "BANG1D: a one-dimensional, Lagrangian model of subaqueous turbid surges." *Computers and Geosciences* **27**(6): 701-716.

- Pratson, L., Imran, J., Parker, G., Syvitski, J. P. M. and Hutton, E. (2000). "Debris flows versus turbidity currents: a modelling comparison of their dynamics and deposits." Fine-Grained Turbidite Systems, AAPG Memoir 72/SEPM Special Publication 68. Bouma, A. H. and Stone, C. G. (Eds.): 57-72.
- Pratson, L. and Ryan, W. B. F. (1994). "Pliocene to recent infilling and subsidence of intraslope basins offshore Louisiana." *American Association of Petroleum Geologists Bulletin* **78**: 1483-1506.
- Prior, D. B. and Coleman, J. M. (1982). "Active slides and flows in underconsolidated marine sediments on the slope of the Mississippi delta." Marine Slides and other Mass Movements. Saxos, S. and Nieuwenhuis, J. K. (Eds.). New York, Plenum Press: 21-49.
- Prior, D. B., Suhayda, J. N., Lu, N.-Z., Bornhold, B. D., Keller, G. H., Wiseman, W. J., Wright, L. D. and Yang, Z.-S. (1989). "Storm-wave reactivation of a submarine landslide." *Nature* **341**: 47-50.
- Prior, D. B., Bornhold, B. D. and Johns, M. W. (1984). "Depositional characteristics of submarine debris flow." *Journal of Geology* **92**: 707-727.
- Rimoldi, B., Alexander, J. and Morris, S. A. (1996). "Experimental density currents entering density-stratified water: analogues for turbidites in Mediterranean hypersaline basins." *Sedimentology* **43**: 527-540.
- Roe, P. L. (1981a). "The use of the Riemann problem in finite-difference schemes." Proceedings of the 7th Conference on Numerical Methods in Fluid Dynamics, 1980. Reynolds, W. C., et al. (Ed.). Berlin, Springer-Verlag. **141**: 354-359.
- Roe, P. L. (1981b). "Approximate Riemann solvers, parameter vectors, and difference schemes." *Journal of Computational Physics* **43**(2): 357-372.
- Rouse, H. (1937). "Modern conceptions of the mechanics of turbulence." *Transcripts of the American Society of Civil Engineers* **102**: 436-505.
- Royhan Gani, M. (2004). "From turbid to lucid: a straightforward approach to sediment-gravity flows and their deposits." *The Sedimentary Record; A Publication of SEPM Society for Sedimentary Geology* **2**(3): 4-8.
- Schlichting, H. (1968). Boundary-Layer Theory. New York, McGraw-Hill. 748 p.
- Schuppers, J. D. (1996). Characterization of deep-marine clastic sediments from foreland basins: outcrop-derived concepts for exploration, production and reservoir modelling. Ph. D. thesis, Department of GeoTechnology, Delft University of Technology, Delft, The Netherlands: 272 p.
- Sengupta, T. K. (2004). Fundamentals of Computational Fluid Dynamics. Hyderabad, University Press. 364 p.

Shanmugam, G. (1996). "High-density turbidity currents: are they sandy debris flows?" *Journal of Sedimentary Research* **66**: 2-10.

Shanmugam, G. (2000). "50 years of the turbidite paradigm (1950s-1990s): deep-water processes and facies models - a critical perspective." *Marine and Petroleum Geology* **17**: 285-342.

Shanmugam, G., Lehtonen, L. R., Straume, T., Syvertsen, S. E., Hodgkinson, R. J. and Skibeli, M. (1994). "Slump and debris-flow dominated upper-slope facies in the cretaceous of the Norwegian North Seas: implications for sand distribution." *American Association of Petroleum Geologists Bulletin* **78**: 910-937.

Shanmugam, G., Moiola, R. J. and Damuth, J. E. (1985). "Eustatic control of submarine fan development." *Submarine Fans and related Turbidite Systems*. Bouma, A. H., Normark, W. R. and Barnes, N. E. (Eds.). New York, Springer-Verlag: 23-28.

Sheldon, P. G. (1928). "Some sedimentation conditions in middle-portage rocks." *American Journal of Science* **15**: 243-252.

Shepard, F. P., Marshall, N. F., McLoughlin, P. A. and Sullivan, G. G. (1979). *Currents in Submarine Canyons and Other Seavalleys*. Ann Arbor, Michigan, USA, The American Association of Petroleum Geologists. 174 p.

Siegenthaler, C. and Buhler, J. (1985). "The kinematics of turbulent suspension currents (turbidity currents) on inclined boundaries." *Marine Geology* **64**: 19-40.

Siegenthaler, C., Fringer, W., Kelts, K. and Wang, S. (1987). "Earthquake and seiche deposits in Lake Lucerne, Switzerland." *Eclogae Geologicae Helvetiae* **80**(1): 241-260.

Signorini, R. (1936). "Determinazione del senso di sedimentazione degli strati nelli formazione arenacea dell' Appennino settentrionale." *Boll. Soc. Geol. Ital.* **55**: 259-267.

Simm, R. W., Weaver, P. P. E., Kidd, R. B. and Jones, E. J. W. (1991). "Late quaternary mass movements on the lower continental rise and abyssal plain off western Sahara." *Sedimentology* **38**: 27-40.

Simpson, J. E. (1997). *Gravity Currents in the Environment and in the Laboratory*. New York, Cambridge University Press

Simpson, J. E. and Britter, R. E. (1979). "The dynamics of the head of a gravity current advancing over a horizontal surface." *Journal of Fluid Mechanics* **94**: 477-495.

Skene, K. I., Mulder, T. and Syvitski, J. P. M. (1997). "INFLO1: A model predicting the behaviour of turbidity currents generated at river mouths." *Computers and Geosciences* **23**(9): 975-991.

Slatt, R. M. (2003). Deepwater turbidite deposits and their economic significance. Exploration and Production: The Oil and Gas Review 2003: 3 p.

Sloff, C. J. (1993a). Analysis of basic equations for sediment-laden flows. Communications on Hydraulic and Geotechnical Engineering, 93-8. Delft, The Netherlands, Delft University of Technology: 54 pages.

Sloff, C. J. (1993b). "Study on modelling the morphology of torrents on volcano slopes." *Journal of Hydraulic Research, IAHR* **31**(3): 333-345.

Sloff, C. J. (1994). Modelling turbidity currents in reservoirs. Communications on Hydraulic and Geotechnical Engineering, 94-5. Delft, The Netherlands, Delft University of Technology: 142 pages.

Sloff, C. J. (1997). Sedimentation in Reservoirs. Ph. D. thesis, Department of Civil Engineering, Delft University of Technology, Delft, The Netherlands: 270 p.

Sohn, T. K. (1995). "Traction-carpet stratification in turbidites - fact or fiction? (Discussion)." *Journal of Sedimentary Research* **A65**: 703-704.

Sohn, T. K. (1997). "On traction-carpet sedimentation." *Journal of Sedimentary Research* **67**: 502-509.

Sohn, T. K. (1999). "Rapid development of gravelly high-density turbidity currents in marine Gilbert-type fan deltas. Lorento Basin, Baja California Sur, Mexico (Discussion)." *Sedimentology* **46**: 757-761.

Southard, J. B. (1971). "Representation of bed configurations in depth-velocity-size diagrams." *Journal of Sedimentary Petrology* **41**(4): 903-915.

Southard, J. B. and Boguchwal, L. A. (1973). "Flume experiments on the transition from ripples to lower flat bed with increasing sand size." *Journal of Sedimentary Petrology* **43**(4): 1114-1121.

Southard, J. B. and Mackintosh, M. E. (1981). "Experimental test of autosuspension." *Earth Surface Processes and Landforms* **6**: 103-111.

Stacey, M. W. and Bowen, A. J. (1988a). "The vertical structure of density and turbidity currents: theory and observations." *Journal of Geophysical Research* **93**: 3528-3542.

Stacey, M. W. and Bowen, A. J. (1988b). "The vertical structure of turbidity currents and a necessary condition for self-maintenance." *Journal of Geophysical Research* **93**: 3543-3553.

Stanley, D. J. (1963). "Vertical petrographic variability in Annot Sandstone turbidites." *Journal of Sedimentary Petrology* **33**: 783-788.

Stoker, J. J. (1957). "Water waves: the mathematical theory with applications." Pure and Applied Mathematics. New York, Interscience publications. **IV**: 567 p.

Stow, D. A. V., Cremer, M., Droz, L., Normark, W. R., O'Connell, S., Pickering, K. T., Stelling, C. E., Meyer-Wright, A. A. and DSDP Leg 96 Shipboard Scientists (1985). "Mississippi fan sedimentary facies, composition and texture." Submarine Fans and Related Turbidite Systems. Bouma, A. H., Normark, W. R. and Barnes, N. E. (Eds.), Springer-Verlag: 259-266.

Stow, D. A. V. and Mayall, M. (2000). "Deep-water sedimentary systems: new models for the 21st century." *Marine and Petroleum Geology* **17**: 125-135.

Stow, D. A. V. and Shanmugam, G. (1980). "Sequence of structures in fine-grained turbidites: comparison of recent deep-sea and ancient flysch sediments." *Sedimentary Geology* **25**: 23-42.

Strang, G. (1968). "On the construction and comparison of difference schemes." *SIAM Journal of Numerical Analysis* **5**: 506-517.

Sullwold Jr, H. H. (1961). "Turbidites in oil exploration." Geometry of Sandstone Bodies. Peterson, J. A. and Osmond, J. C. (Eds.). Tulsa, Oklahoma, American Association of Petroleum Geologists: 63-81.

Sweby, P. K. (1985). "High-resolution TVD schemes using flux limiters." *Lectures in Applied Mathematics* **22**: 289-309.

Syvitski, J. P. M. and Hutton, E. H. (2001). "2D SEDFLUX 1.0C: an advanced process-response numerical model for the fill of marine sedimentary basins." *Computers and Geoscience* **27**(6): 731-754.

Syvitski, J. P. M. and Schafer, C. T. (1996). "Evidence for an earthquake-triggered basin collapse in Saguenay fjord, Canada." *Sedimentary Geology* **104**: 127-153.

Takahashi, T. (2001). "Mechanics and simulation of snow avalanches, pyroclastic flows and debris flows." Particulate Gravity Currents, Special Publication of the International Association of Sedimentologists # 31. McCaffrey, W. D., Kneller, B. C. and Peakall, J. (Eds.). Oxford, Blackwell Science: 11-43.

Taylor, J. C. (1976). "Geological appraisal of the petroleum potential of offshore southern California; the borderland compared to onshore coastal basins." *US Geological Survey Circular 730*: 43.

Tetzlaff, D. M. and Harbaugh, J. W. (1989). Simulating Clastic Sedimentation. New York, Van Nostrand Reinhold. 196 p.

Toro, E. F. (1997). Riemann Solvers and Numerical Methods for Fluid Dynamics. Springer-Verlag. 624 p.

Toro, E. F. (2001). Shock-Capturing Methods for Free-Surface Shallow Flows. London, Wiley and Sons. 326 p.

Turner, J. S. (1973). Buoyancy Effects in Fluids. Cambridge University Press. 367 p.

Van Albada, G. D., Van Leer, B. and Roberts, W. W. (1982). "A comparative study of computational methods in cosmic gas dynamics." *Astron. Astrophysics* **108**: 76.

Van Leer, B. (1974). "Towards the ultimate conservative difference scheme. II: monotonicity and conservation combined in a second-order scheme." *Journal of Computational Physics* **14**: 361–370.

Van Rijn, L. C. (1984). "Sediment transport part II: suspended-load transport." *Journal of Hydraulic Engineering, ASCE* **110**(11): 1613-1641.

Van Rijn, L. C. (1986). "Mathematical models for sediment-concentration profiles in steady flow." Transport of Suspended Solids in Open Channels; Proceedings of Euromech 192. Bechteler, W. (Ed.). Rotterdam, Balkema.

Van Rijn, L. C. (1987). Mathematical modelling of morphological processes in the case of suspended sediment transport. Doctoral Thesis, Civil Engineering, Delft University of Technology, Delft, The Netherlands: 208 p.

Violet, J., Sheets, B., Pratson, L., Paola, C., Beaubouef, R. and Parker, G. (2005). "Experiment on turbidity currents and their deposits in a model 3D subsiding minibasin." *Journal of Sedimentary Research* **75**(5): 820-843.

Visser, C. A. (2005). Thick-bedded deep-marine sandstones in outcrop and subsurface. Ph. D. thesis, Department of GeoTechnology, Delft University of Technology, Delft, The Netherlands: 237 p.

Von Neumann, J. and Richtmeyer, R. D. (1950). "A method for the numerical calculation of hydrodynamic shocks." *Journal of Applied Physics* **21**(3): 232-237.

Walker, R. G. (1978). "Deep-water sandstone facies and ancient submarine fans: models for exploration for stratigraphic traps." *American Association of Petroleum Geologists Bulletin* **62**: 932-966.

Wang, J. S., Ni, H. G. and He, Y. S. (2000a). "Finite-difference TVD scheme for computation of dam-break problems." *Journal of Hydraulic Engineering* **126**(4): 253-262.

Wang, Y., Hutter, K., Gray, J. M. N. T. and Tai, Y. C. (2000b). "Gravity-driven shear flow of a sediment-water mixture: comparison of theory and experiment." Debris-Flow Hazards Mitigation: Mechanics, Prediction, and Assessment. Wieczorek, G. F. and Naeser, N. D. (Eds.), Balkema: 381-386.

Watney, W. L., Rankey, E. C. and Harbaugh, J. W. (1999). "Perspectives on stratigraphic simulation models: current approaches and future opportunities." Numerical Experiments in Stratigraphy: Recent Advances in Stratigraphic and Sedimentologic Computer Simulations. Harbaugh, J. W., Watney, W. L., Rankey, E. C., Slingerland, R., Goldstein, R. H. and Franseen, E. K. (Eds.). Tulsa, SEPM. **62**: 3-21.

Watson, M. P. (1984). "Submarine fans in a developing extensional regime — their significance in the North Sea hydrocarbon province." *AAPG Bulletin* **68**: 538 (abstract).

Weimer, P. and Link, W. H. (1991). "Global occurrences in submarine fan and turbidite systems." Seismic Facies and Sedimentary Processes of Modern and Ancient Submarine Fans and Turbidite Systems. Weimer, P. and Link, W. H. (Eds.). New York, Springer-Verlag: 447 p.

Whelan, M. (1994). "The night the sea smashed Lord's Cove." *Canadian Geographic* **114**(6): 70-73.

Wright, S. and Parker, G. (2004a). "Density stratification effects in sand-bed rivers." *Journal of Hydraulic Engineering, ASCE* **130**(8): 783-795.

Wright, S. and Parker, G. (2004b). "Flow resistance and suspended load in sand-bed rivers: simplified stratification model." *Journal of Hydraulic Engineering, ASCE* **130**(8): 795-805.

Yang, J. Y. and Hsu, C. A. (1993b). "Computations of free-surface flows, part 2: two-dimensional bore diffraction." *Journal of Hydraulic Research, IAHR* **31**(3): 403-413.

Yang, J. Y., Hsu, C. A. and Chang, S. H. (1993a). "Computations of free-surface flows, part 1: one-dimensional dam-break flow." *Journal of Hydraulic Research, IAHR* **31**(1): 19-34.

Zeng, J. and Lowe, D. R. (1997). "Numerical simulations of turbidity-current flow and sedimentation I: theory." *Sedimentology* **44**: 65-104.

Zeng, J., Lowe, D. R., Prior, D. B., Wisenam Jr, W. J. and Bornhold, P. D. (1991). "Flow properties of turbidity currents in Bute inlet, British Columbia." *Sedimentology* **38**: 975-996.

APPENDIX

A.1 List of symbols

α_1	constant used in parameterization of erosion	[-]
α_2	constant used in parameterization of erosion	[-]
α_{EAV}	intensity parameter in empirical artificial viscosity term	[-]
α_{STD}	source term divider	[-]
A	constant ($=1.3 \cdot 10^{-7}$) used in parameterization of erosion	[-]
A	Jacobian matrix associated with flux vector f	
a	internal wave velocity, defined as \sqrt{RCgh}	[m/s]
$b_{(i)}$	fraction of sediment in i^{th} size range present in the bed	[-]
B	constant ($=7.8 \cdot 10^{-7}$) used in parameterization of erosion	[-]
B	Jacobian matrix associated with flux vector g	
c	local suspended sediment concentration	[-]
c_D	coefficient of drag	[-]
C	depth-averaged suspended sediment concentration	[-]
$C_{(i)}$	depth-averaged sediment concentration of i^{th} size fraction	[-]
$C_{b(i)}$	near-bed concentration of sediment in i^{th} size range	[-]
C_e	depth-averaged equilibrium concentration (Galappatti)	[-]
c_{front}	propagation velocity of the front of the flow	[m/s]
δ^v	discrete empirical artificial viscosity term	
$D_{s(i)}$	grain diameter of sediment in i^{th} size range	[m]
D_{s50}	median grain diameter of sediment mixture	[m]
D_{sg}	geometric mean grain diameter of sediment mixture	[m]
D	bulk rate of deposition	[m/s]
D_x	artificial viscosity term x (TVD limited or empirical)	
D_y	artificial viscosity term y (TVD limited or empirical)	
ε_x	sediment mixing coefficient in x-direction (diffusive)	[-]
ε_y	sediment mixing coefficient in y-direction (diffusive)	[-]
ε_z	sediment mixing coefficient in z-direction (diffusive)	[-]
ε_{EAV}	gradient parameter in empirical artificial viscosity term	
e_w	ambient water entrainment coefficient	[-]
$E_{s(i)}$	erosion coefficient for sediment in i^{th} size range	[-]
E	bulk rate of erosion	[m/s]
η	bed elevation	[m]
η_b	bed thickness	[m]
$f_{(i)}$	fraction of sediment in i^{th} size range present in the flow	[-]
Fr	Froude number	[-]
Fr_d	densimetric Froude number	[-]
f	vector of fluxes in x direction	
$\gamma^{(k)}$	entropy-corrected propagation velocity (celerity) of k^{th} wave	[m/s]

g	gravitational acceleration	[m/s ²]
g'	buoyancy-reduced gravitational acceleration	[m/s ²]
$\bar{\mathbf{g}}$	gravitational acceleration vector (g_x, g_y, g_z)	
\mathbf{g}	vector of fluxes in y direction	
h, H	flow depth	[m]
i	grain-size fraction indicator	[-]
k	wave number indicator ($k=1, 2, \dots, m$)	[-]
k_s	roughness height	[m]
κ	Kármán constant ($\kappa \approx 0.4 \pm 0.01$)	[-]
\mathbf{L}_x	left-eigenvector matrix associated to \mathbf{A}, \mathbf{f}	
$\mathbf{l}_{x(k)}$	left-eigenvector associated to k^{th} wave	
\mathbf{L}_y	left-eigenvector matrix associated to \mathbf{B}, \mathbf{g}	
$\mathbf{l}_{y(k)}$	left-eigenvector associated to k^{th} wave	
μ	(dynamic) viscosity	[kg/ms]
m	number of waves (equations) in system ($m=3+n$)	[-]
ν	kinematic viscosity	[m ² /s]
n	number of size fractions in grain-size distribution of sediment	[-]
\mathbf{OP}_x	discretized operator in x-direction	
\mathbf{OP}_y	discretized operator in y-direction	
$\phi_{(k)}$	propagation velocity (celerity, eigenvalue) of k^{th} wave	[m/s]
φ	initial porosity of sediment i.e. at deposition	[-]
ψ	limiter function	
p	local pressure	[Pa]
\bar{p}	local pressure, (Reynolds) average	[Pa]
p'	local pressure, fluctuating part	[Pa]
p_h	local pressure, hydrostatic part	[Pa]
p_d	local pressure, dynamic part	[Pa]
p_{bc}	tuning parameter for bed cohesion	[-]
\mathbf{q}_x	vector of source terms in x-direction	
\mathbf{q}_y	vector of source terms in y-direction	
ρ_s	density of sediment	[kg/m ³]
ρ_w	density of water	[kg/m ³]
ρ_f	density of mixture	[kg/m ³]
$r_{0(i)}$	near-bed concentration ratio for sediment in i^{th} size range	[-]
$R_{p(i)}$	Reynolds particle number	[-]
Ri_b	bulk Richardson number	[-]
Ri_g	gradient Richardson number	[-]
Re	Reynolds number	[-]

R	submerged specific gravity of the sediment	[-]
\mathbf{R}_x	right-eigenvector matrix associated to \mathbf{A} , \mathbf{f}	
$\mathbf{r}_{x(k)}$	right-eigenvector associated to k^{th} wave	
\mathbf{R}_y	right-eigenvector matrix associated to \mathbf{B} , \mathbf{g}	
$\mathbf{r}_{y(k)}$	right-eigenvector associated to k^{th} wave	
σ_ϕ	mean grain diameter of sediment mixture on phi-scale	[ϕ]
S	bed slope	[-]
S_x	bed slope in x-direction	[-]
S_y	bed slope in y-direction	[-]
S_f	friction slope (c_D/Ri_b)	[-]
$\theta_{(k)}$	slope ratio used in formulation of flux limiter	[-]
θ_x	slope angle in transverse flow direction	[-]
θ_y	slope angle in streamwise flow direction	[-]
τ_{xb}	shear stress exerted by the flow on the bed in x-direction	[Pa]
τ_{yb}	shear stress exerted by the flow on the bed in y-direction	[Pa]
τ_{xi}	shear stress exerted by the flow on the water interface in x-dir.	[Pa]
τ_{yi}	shear stress exerted by the flow on the water interface in y-dir.	[Pa]
T	dimensionless adaptation time for re-establishment of equilibrium	[-]
t	time-coordinate	[s]
u_x	local fluid velocity in x-direction	[m/s]
u_y	local fluid velocity in y-direction	[m/s]
u_z	local fluid velocity in z-direction	[m/s]
u^*_x	shear velocity in x-direction	[m/s]
u^*_y	shear velocity in y-direction	[m/s]
u^*	length of shear flow velocity vector, defined as $(u^*_x, u^*_y, 0)$	[m/s]
U_x	depth-averaged velocity of flow in x-direction	[m/s]
U_y	depth-averaged velocity of flow in y-direction	[m/s]
U	length of flow velocity vector, defined as $(U_x, U_y, 0)$	[m/s]
\mathbf{u}	vector of conservative variables	
\mathbf{v}	vector of primitive variables	
$w_{d(i)}$	rate of deposition for sediment in i^{th} size range	[m/s]
$w_{e(i)}$	rate of erosion for sediment in i^{th} size range	[m/s]
w_i	rate of ambient water entrainment at the density interface	[m/s]
$w_{s(i)}$	fall velocity of grains in i^{th} size range	[m/s]
\mathbf{w}	vector of characteristic variables	
$\mathbf{w}(k)$	characteristic variable associated to k^{th} wave	
x	x-coordinate	[m]
y	y-coordinate	[m]
ζ	straining parameter	[-]
z	z-coordinate	[m]
z_b	bed elevation	[m]
$Z_{(i)}$	similarity variable in formulation of erosion rate	[-]

A.2 Operator discretization

In vector form, the operators \mathbf{OP}_x and \mathbf{OP}_y are defined as:

$$\frac{\partial \mathbf{u}}{\partial t} + \frac{\partial \mathbf{f}(\mathbf{u})}{\partial x} = \mathbf{q}_x(\mathbf{u}) \quad \frac{\partial \mathbf{u}}{\partial t} + \frac{\partial \mathbf{g}(\mathbf{u})}{\partial y} = \mathbf{q}_y(\mathbf{u})$$

The vector of dependent variables \mathbf{u} is defined as $\mathbf{u}(h, U_x h, U_y h, C_{(1)} h, \dots, C_{(n)} h)$. However, as already remarked in Paragraph 4.2 (Chapter 4), the non-conservative system of equations performs superior to the conservative system when applied to computations involving discontinuities. The difference is due to the different forms of the momentum equations, which, in non-conservative form, give a much better (sharper) representation of discontinuities. Therefore, in the code of the operators, the mass conservation equations (fluid and suspended sediment) are in conservative form, whereas the momentum conservation equations are in non-conservative form. In the code of the TVD artificial viscosity terms (see next paragraph), all equations are in non-conservative form i.e. with the vector of primitive variables defined as $\mathbf{v}(h, U_x, U_y, C_{(1)}, \dots, C_{(n)})$.

The following sequence of operators advances the computation by $2\Delta t$ (see main text):

$$\mathbf{v}_{(i,j)}^{t+1} = \mathbf{OP}_{y,1} \left(\frac{\Delta t}{2} \right) \mathbf{OP}_{x,1} \left(\frac{\Delta t}{2} \right) \mathbf{v}_{(i,j)}^t$$

$$\mathbf{v}_{(i,j)}^{t+2} = \mathbf{OP}_{x,2} \left(\frac{\Delta t}{2} \right) \mathbf{OP}_{y,2} \left(\frac{\Delta t}{2} \right) \mathbf{v}_{(i,j)}^{t+1}$$

The values of the dependent variables h , U_x , U_y and $C_{(i)} h$ are updated from operator to operator i.e. values from one operator are used in the next operator. The operators in the sequence are defined as follows:

Operator $\mathbf{OP}_{y,1}^P$: predictor step, backward-differenced in y -direction, based on values of primitive variables \mathbf{v} at time t .

$$\begin{pmatrix} h^P \\ U_x^P \\ U_y^P \\ C_{(1)}^P h^P \\ \vdots \\ C_{(n)}^P h^P \end{pmatrix} = \begin{pmatrix} h^t \\ U_x^t \\ U_y^t \\ C_{(1)}^t h^t \\ \vdots \\ C_{(n)}^t h^t \end{pmatrix} - \frac{\Delta t}{\Delta y} \begin{pmatrix} \nabla_y (U_y^t h^t) \\ U_y^t (\nabla_y U_x^t) \\ U_y^t (\nabla_y U_y^t) + \frac{1}{2} Rg C^t [(\nabla_y h^t) + \nabla_y (C^t h^t)] \\ \nabla_y (U_y^t C_{(1)}^t h^t) \\ \vdots \\ \nabla_y (U_y^t C_{(n)}^t h^t) \end{pmatrix} + \Delta t \begin{pmatrix} \alpha_{STD} [e_w^t U^t] \\ 0 \\ -Rg C^t \nabla_y z_b^t - (c_D + e_w^t) \frac{U_y^t U_x^t}{h^t} \\ \alpha_{STD} [w_{s(1)} (b_{(1)}^t e_{s(1)}^t - r_{0(1)}^t C_{(1)}^t)] \\ \vdots \\ \alpha_{STD} [w_{s(n)} (b_{(n)}^t e_{s(n)}^t - r_{0(n)}^t C_{(n)}^t)] \end{pmatrix}$$

Operator $\mathbf{OP}_{y,2}^P$: resembles operator $\mathbf{OP}_{y,1}^C$, but based on values of primitive variables \mathbf{v} at time level corresponding to operator $\mathbf{OP}_{x,2}$ (see sequence of operators above)

Operator $\mathbf{OP}_{y,1}^C$: corrector step, forward-differenced in y-direction, based on predictor values of primitive variables \mathbf{v} from operator $\mathbf{OP}_{y,1}$

$$\begin{pmatrix} h^C \\ U_x^C \\ U_y^C \\ C_{(1)}^C h^C \\ \vdots \\ C_{(n)}^C h^C \end{pmatrix} = \begin{pmatrix} h^t \\ U_x^t \\ U_y^t \\ C_{(1)}^t h^t \\ \vdots \\ C_{(n)}^t h^t \end{pmatrix} - \frac{\Delta t}{\Delta y} \begin{pmatrix} \Delta_y (U_x^P h^P) \\ U_y^P (\Delta_y U_x^P) \\ U_y^P (\Delta_y U_y^P) + \frac{1}{2} RgC^P [(\Delta_y h^P) + \Delta_y (C^P h^P)] \\ \Delta_y (U_y^P C_{(1)}^P h^P) \\ \vdots \\ \Delta_y (U_y^P C_{(n)}^P h^P) \end{pmatrix} + \Delta t \begin{pmatrix} \alpha_{STD} e_w^P U^P \\ 0 \\ -RgC^P \Delta_y z_b^P - (c_D + E_w^t) \frac{U_y^t}{h^t} U_y^P \\ \alpha_{STD} [w_{s(1)} (b_{(1)}^t e_{s(1)}^P - r_{0(1)}^P C_{(1)}^P)] \\ \vdots \\ \alpha_{STD} [w_{s(n)} (b_{(n)}^t e_{s(n)}^P - r_{0(n)}^P C_{(n)}^P)] \end{pmatrix}$$

Operator $\mathbf{OP}_{y,2}^C$: resembles operator $\mathbf{OP}_{y,1}^P$, but values of primitive variables \mathbf{v} based on predictor values from operator $\mathbf{OP}_{y,2}$

Operator $\mathbf{OP}_{x,1}^P$: predictor step, backward-differenced in x-direction, based on values of primitive variables \mathbf{v} from operator $\mathbf{OP}_{y,1}$

$$\begin{pmatrix} h^P \\ U_x^P \\ U_y^P \\ C_{(1)}^P h^P \\ \vdots \\ C_{(n)}^P h^P \end{pmatrix} = \begin{pmatrix} h^t \\ U_x^t \\ U_y^t \\ C_{(1)}^t h^t \\ \vdots \\ C_{(n)}^t h^t \end{pmatrix} - \frac{\Delta t}{\Delta x} \begin{pmatrix} \nabla_x (U_x^t h^t) \\ U_x^t (\nabla_x U_x^t) + \frac{1}{2} RgC^t [(\nabla_x h^t) + \nabla_x (C^t h^t)] \\ U_x^t (\nabla_x U_y^t) \\ \nabla_x (U_x^t C_{(1)}^t h^t) \\ \vdots \\ \nabla_x (U_x^t C_{(n)}^t h^t) \end{pmatrix} + \Delta t \begin{pmatrix} (1 - \alpha_{STD}) [e_w^t U^t] \\ -RgC^t \nabla_x z_b^t - (c_D + e_w^t) \frac{U_x^t}{h^t} U_x^t \\ 0 \\ (1 - \alpha_{STD}) [w_{s(1)} (b_{(1)}^t e_{s(1)}^t - r_{0(1)}^t C_{(1)}^t)] \\ \vdots \\ (1 - \alpha_{STD}) [w_{s(n)} (b_{(n)}^t e_{s(n)}^t - r_{0(n)}^t C_{(n)}^t)] \end{pmatrix}$$

Operator $\mathbf{OP}_{x,2}^P$: resembles operator $\mathbf{OP}_{x,1}^C$, but values of primitive variables \mathbf{v} based on values at time $t + \Delta t$

Operator $\mathbf{OP}_{x,1}^C$: corrector step, forward-differenced in x-direction, based on predictor values of primitive variables \mathbf{v} from operator $\mathbf{OP}_{x,1}$

$$\begin{pmatrix} h^C \\ U_x^C \\ U_y^C \\ C_{(1)}^C h^C \\ \vdots \\ C_{(n)}^C h^C \end{pmatrix} = \begin{pmatrix} h^t \\ U_x^t \\ U_y^t \\ C_{(1)}^t h^t \\ \vdots \\ C_{(n)}^t h^t \end{pmatrix} - \frac{\Delta t}{\Delta x} \begin{pmatrix} \Delta_x (U_x^P h^P) \\ U_x^P (\Delta_x U_x^P) + \frac{1}{2} RgC^P [(\Delta_x h^P) + \Delta_x (C^P h^P)] \\ U_x^P (\Delta_x U_y^P) \\ \Delta_x (U_x^P C_{(1)}^P h^P) \\ \vdots \\ \Delta_x (U_x^P C_{(n)}^P h^P) \end{pmatrix} + \Delta t \begin{pmatrix} (1 - \alpha_{STD}) [e_w^P U^P] \\ -RgC^P \Delta_x z_b^P - (c_D + e_w^t) \frac{U_x^t}{h^t} U_x^P \\ 0 \\ (1 - \alpha_{STD}) [w_{s(1)} (b_{(1)}^t e_{s(1)}^P - r_{0(1)}^P C_{(1)}^P)] \\ \vdots \\ (1 - \alpha_{STD}) [w_{s(n)} (b_{(n)}^t e_{s(n)}^P - r_{0(n)}^P C_{(n)}^P)] \end{pmatrix}$$

Operator $\mathbf{OP}_{x,2}^C$: resembles operator $\mathbf{OP}_{x,1}^P$, but values of primitive variables \mathbf{v} based on predictor values from operator $\mathbf{OP}_{x,2}$

The source terms that parameterize loss of velocity due to bed- and interfacial friction have been linearized to maintain the order and stability of the solution (Sloff, 1997) in the following way:

for predictor steps:

$$x: u_{*x}^2 = (c_D + e_w)U^2 \rightarrow [(c_D + e_w^t)U^t] U_x^t \quad y: u_{*y}^2 = (c_D + e_w)U^2 \rightarrow [(c_D + e_w^t)U^t] U_y^t$$

for corrector steps:

$$x: u_{*x}^2 = (c_D + e_w)U^2 \rightarrow [(c_D + e_w^t)U^t] U_x^P \quad y: u_{*y}^2 = (c_D + e_w)U^2 \rightarrow [(c_D + e_w^t)U^t] U_y^P$$

In the absence of bedload transport, changes in elevation and composition of the bed are completely coupled to the source terms parameterizing exchange of suspended sediment between the turbidity current and the bed. The variable z , which denotes bed elevation, is updated during the predictor and corrector steps of the MacCormack scheme, synchronous with the primary flow variables, to ensure a proper coupling between the flow and the bed. The discretized bed update operators are defined as follows:

$$\text{Operator } \mathbf{OP}_{y,1}: \quad \eta_b^P = \eta_b^t - \frac{\Delta t \alpha_{STD}}{(1-\phi)} \left[\sum_{i=1}^{i=n} w_{s(i)} (r_{0(i)}^t C_{(i)}^t - b_{(i)}^t e_{s(i)}^t) \right]$$

$$\text{Operator } \mathbf{OP}_{y,2}: \quad \eta_b^C = \eta_b^t - \frac{\Delta t \alpha_{STD}}{(1-\phi)} \left[\sum_{i=1}^{i=n} w_{s(i)} (r_{0(i)}^P C_{(i)}^P - b_{(i)}^t e_{s(i)}^P) \right]$$

$$\text{Operator } \mathbf{OP}_{x,1}: \quad \eta_b^P = \eta_b^t - \frac{\Delta t (1 - \alpha_{STD})}{(1-\phi)} \left[\sum_{i=1}^{i=n} w_{s(i)} (r_{0(i)}^t C_{(i)}^t - b_{(i)}^t e_{s(i)}^t) \right]$$

$$\text{Operator } \mathbf{OP}_{x,2}: \quad \eta_b^C = \eta_b^t - \frac{\Delta t (1 - \alpha_{STD})}{(1-\phi)} \left[\sum_{i=1}^{i=n} w_{s(i)} (r_{0(i)}^P C_{(i)}^P - b_{(i)}^t e_{s(i)}^P) \right]$$

The composition of the bed, characterized in terms of fractions of individual grain sizes b_i , is updated only once, at the end of each operator, to ensure that the bed is updated only at the end of a valid computational step, thus preventing unphysical changes to the stratigraphy (e.g. artificial erosion surfaces) caused by the choice of discretization method. The change in the parameter b_i , which denotes the fraction of material in the i^{th} grain size in the bed, is discretized as follows:

$$\begin{pmatrix} b_{(1)}^{t+1} \\ \vdots \\ b_{(n)}^{t+1} \end{pmatrix} = \begin{pmatrix} b_{(1)}^t \\ \vdots \\ b_{(n)}^t \end{pmatrix} + \frac{\Delta t}{(1-\phi)\eta_b^t} \begin{pmatrix} \frac{1}{2} [(D_{(1)}^P + D_{(1)}^C) - (E_{(1)}^P + E_{(1)}^C)] - b_{(1)}^t \Delta_t \eta_b \\ \vdots \\ \frac{1}{2} [(D_{(n)}^P + D_{(n)}^C) - (E_{(n)}^P + E_{(n)}^C)] - b_{(n)}^t \Delta_t \eta_b \end{pmatrix}$$

where $\Delta\eta_b$ is the time derivative of η_b ($\partial\eta_b/\partial t$), quantifying the bulk change in bed thickness. The parameters $D_{(i)}$ and $E_{(i)}$ represent the amount of material of the i^{th} grain size fraction lost by (deposited) and added to (eroded) the turbidity current, defined as:

$$\begin{aligned} D_{(i)}^P &= w_{s(i)} r_{0(i)}^t C_{(i)}^t & D_{(i)}^C &= w_{s(i)} r_{0(i)}^P C_{(i)}^P \\ E_{(i)}^P &= w_{s(i)} b_{(i)}^t e_{s(i)}^t & E_{(i)}^C &= w_{s(i)} b_{(i)}^t e_{s(i)}^P \end{aligned}$$

A.3 TVD artificial viscosity

A.3.1 Roe's linearization technique

The TVD method can be adopted for a non-linear system of equations by using a local linearization technique to decompose the Lax-Wendroff fluxes at the cell interfaces into positive and negative parts. An effective way to achieve this is to use the approximate Riemann solver by Roe (1981a, 1981b), which extends the exact linear solution to the classic Riemann problem to non-linear systems. The classic Riemann problem, often referred to as the “shock tube problem”, finds its origin in gas dynamics, and presents the exact linear solution to the 1-D form of the Euler equations, which constitute the highest level of approximation for non-viscous fluids such as, in this case, a low-density suspension. The Riemann problem can be realized experimentally by the sudden breakdown of a diaphragm in a one-dimensional tube separating two gas states at different pressures and densities (see figure A1.1).

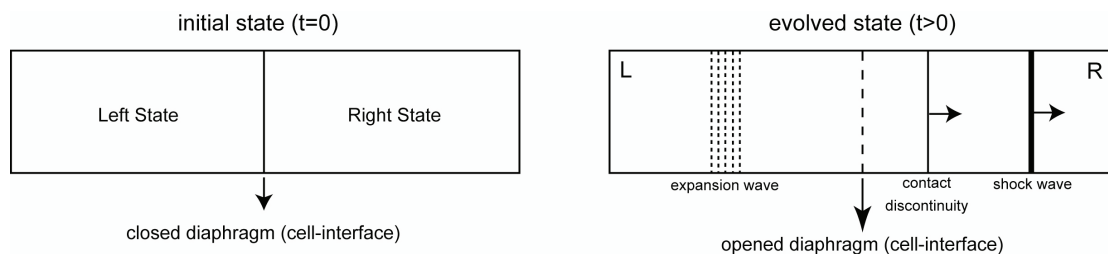


Figure A1.1: Schematic representation of the shock tube problem (after Hirsch, 1990).

At the bursting of the diaphragm, the pressure discontinuity (shock wave) propagates to the right in the low-pressure gas and simultaneously an expansion fan propagates to the left in the high-pressure gas. In addition, the contact discontinuity separating the two gas states, which was originally located at the position of the diaphragm, propagates to the right (Hirsch, 1990).

In numerical form, the cell interfaces can be seen to represent a boundary (the diaphragm) separating (numerical) fluid states in cells left and right of that boundary. However, the presented system of equations is non-linear; hence, the numerical solution is essentially a collection of non-linear Riemann problems, which require a time-consuming iterative solution method (Sloff, 1997). Therefore, Roe proposed a linearization method to extend the exact linear solution to the Riemann problem to non-linear systems. Since the presented two-dimensional system of equations in split form effectively consists of two systems of one-dimensional Euler equations (Chapter 4, Equation 4.10), Roe's approximate Riemann solver can be applied to obtain the linearized numerical fluxes at cell interfaces.

A.3.2 Roe's technique applied to the 1-D systems

Consider the two-dimensional system in split, quasi-linear form:

$$\frac{\partial \mathbf{v}}{\partial t} + \mathbf{A} \frac{\partial \mathbf{v}}{\partial x} = \mathbf{q}_x(\mathbf{v}) \qquad \frac{\partial \mathbf{v}}{\partial t} + \mathbf{B} \frac{\partial \mathbf{v}}{\partial y} = \mathbf{q}_y(\mathbf{v})$$

Here, \mathbf{v} is the vector of primitive variables ($h, U_x, U_y, C_{(1)}, \dots, C_{(n)}$). The vectors $\mathbf{q}_x(\mathbf{v})$, $\mathbf{q}_y(\mathbf{v})$ contain the source terms, some of which are considered to be too small to be of importance to the analysis of the discontinuity (exchange of sediment between the bed and the turbidity current) while others can be linearly averaged over the shock. Hence, in the context of the analysis to follow, they are taken to be zero, which effectively renders the one-dimensional systems homogeneous.

The associated Jacobian matrices \mathbf{A} and \mathbf{B} take the following form:

$$\mathbf{A} = \frac{\partial \mathbf{f}}{\partial \mathbf{v}} = \begin{bmatrix} U_x & h & 0 & 0 & \dots & 0 \\ RgC & U_x & 0 & \frac{1}{2}Rgh & \dots & \frac{1}{2}Rgh \\ 0 & 0 & U_x & 0 & \dots & 0 \\ 0 & 0 & 0 & U_x & \dots & 0 \\ \vdots & \vdots & \vdots & \vdots & \ddots & \vdots \\ 0 & 0 & 0 & 0 & \dots & U_x \end{bmatrix} \qquad \mathbf{B} = \frac{\partial \mathbf{g}}{\partial \mathbf{v}} = \begin{bmatrix} U_y & 0 & h & 0 & \dots & 0 \\ 0 & U_y & 0 & 0 & \dots & 0 \\ RgC & 0 & U_y & \frac{1}{2}Rgh & \dots & \frac{1}{2}Rgh \\ 0 & 0 & 0 & U_y & \dots & 0 \\ \vdots & \vdots & \vdots & \vdots & \ddots & \vdots \\ 0 & 0 & 0 & 0 & \dots & U_y \end{bmatrix}$$

Considering the situation at a cell interface, positioned at ($x = [i+1/2]\Delta x, y = [j]\Delta y$), at time t , the Riemann problem is written as:

$$\frac{\partial \mathbf{v}}{\partial t} + \mathbf{A}(\mathbf{v}_l^t, \mathbf{v}_r^t) \frac{\partial \mathbf{v}}{\partial x} = 0$$

with initial condition:

$$\mathbf{v}_{(x,y)}^t = \begin{cases} \mathbf{v}_l^t & x < [i+1/2]\Delta x \\ \mathbf{v}_r^t & x > [i+1/2]\Delta x \end{cases}$$

The solution to this problem for e.g. time $t+\Delta t$ can be found by means of a characteristic decomposition (e.g. see LeVeque, 1990). Because the system is hyperbolic, the Jacobian \mathbf{A} can be diagonalized by the decomposition:

$$\mathbf{A} = \mathbf{R} \cdot \mathbf{\Lambda} \cdot \mathbf{L}$$

where Λ is the diagonal eigenvalue matrix defined as:

$$\Lambda = \begin{bmatrix} \phi_{(1)} & 0 & 0 & 0 & \dots & 0 \\ 0 & \phi_{(2)} & 0 & 0 & \dots & 0 \\ 0 & 0 & \phi_{(3)} & 0 & \dots & 0 \\ 0 & 0 & 0 & \phi_{(4)} & \dots & 0 \\ \vdots & \vdots & \vdots & \vdots & \ddots & \vdots \\ 0 & 0 & 0 & 0 & \dots & \phi_{(m)} \end{bmatrix}$$

\mathbf{R} is the right-eigenvector matrix, whose columns are formed by the right-eigenvectors $\mathbf{r}_{(k)}$, which are defined as:

$$\mathbf{A} \cdot \mathbf{r}_{(k)} = \phi_{(k)} \mathbf{r}_{(k)}$$

and \mathbf{L} , being the inverse of the matrix \mathbf{R} , is the left-eigenvector matrix, whose columns are formed by the left-eigenvectors $\mathbf{l}_{(k)}$, which can be found through inversion of the matrix \mathbf{R} . Decomposition of the Jacobian \mathbf{A} leads to the following definitions for the matrices \mathbf{R}_x , Λ_x :

$$\mathbf{R}_x = \begin{bmatrix} 1 & 0 & 1 & 1 & \dots & 1 \\ -\frac{a}{h} & 0 & \frac{a}{h} & 0 & \dots & 0 \\ 0 & \frac{1}{h} & 0 & 0 & \dots & 0 \\ 0 & 0 & 0 & -\frac{2C}{h} & \dots & 0 \\ 0 & 0 & 0 & 0 & \ddots & 0 \\ 0 & 0 & 0 & 0 & 0 & -\frac{2C}{h} \end{bmatrix} \quad \Lambda_x = \begin{bmatrix} U_x - a & 0 & 0 & 0 & \dots & 0 \\ 0 & U_x & 0 & 0 & \dots & 0 \\ 0 & 0 & U_x + a & 0 & \dots & 0 \\ 0 & 0 & 0 & U_x & \dots & 0 \\ \vdots & \vdots & \vdots & \vdots & \ddots & \vdots \\ 0 & 0 & 0 & 0 & \dots & U_x \end{bmatrix}$$

where $a = \sqrt{\text{RgCh}}$, which represents the propagation velocity of an internal wave. Decomposition of the Jacobian \mathbf{B} leads to the following definitions for the matrices \mathbf{R}_y and Λ_y :

$$\mathbf{R}_y = \begin{bmatrix} 1 & 0 & 1 & 1 & \dots & 1 \\ 0 & \frac{1}{h} & 0 & 0 & \dots & 0 \\ -\frac{a}{h} & 0 & \frac{a}{h} & 0 & \dots & 0 \\ 0 & 0 & 0 & -\frac{2C}{h} & \dots & 0 \\ \vdots & \vdots & \vdots & \vdots & \ddots & 0 \\ 0 & 0 & 0 & 0 & \dots & -\frac{2C}{h} \end{bmatrix} \quad \Lambda_y = \begin{bmatrix} U_y - a & 0 & 0 & 0 & \dots & 0 \\ 0 & U_y & 0 & 0 & \dots & 0 \\ 0 & 0 & U_y + a & 0 & \dots & 0 \\ 0 & 0 & 0 & U_y & \dots & 0 \\ \vdots & \vdots & \vdots & \vdots & \ddots & \vdots \\ 0 & 0 & 0 & 0 & \dots & U_y \end{bmatrix}$$

Matrices \mathbf{L}_x and \mathbf{L}_y are found through inversion of matrices \mathbf{R}_x and \mathbf{R}_y respectively:

$$\mathbf{L}_x = \begin{bmatrix} \frac{1}{2} & -\frac{h}{2a} & 0 & \frac{h}{4C} & \dots & \frac{h}{4C} \\ 0 & 0 & h & 0 & \dots & 0 \\ \frac{1}{2} & \frac{h}{2a} & 0 & \frac{h}{4C} & \dots & \frac{h}{4C} \\ 0 & 0 & 0 & -\frac{h}{2C} & \dots & 0 \\ \vdots & \vdots & \vdots & \vdots & \ddots & \vdots \\ 0 & 0 & 0 & 0 & \dots & -\frac{h}{2C} \end{bmatrix} \quad \mathbf{L}_y = \begin{bmatrix} \frac{1}{2} & 0 & -\frac{h}{2a} & \frac{h}{4C} & \dots & \frac{h}{4C} \\ 0 & h & 0 & 0 & \dots & 0 \\ \frac{1}{2} & 0 & \frac{h}{2a} & \frac{h}{4C} & \dots & \frac{h}{4C} \\ 0 & 0 & 0 & -\frac{h}{2C} & \dots & 0 \\ \vdots & \vdots & \vdots & \vdots & \ddots & \vdots \\ 0 & 0 & 0 & 0 & \dots & -\frac{h}{2C} \end{bmatrix}$$

The vector of characteristic variables \mathbf{w} (Riemann variables) is coupled to the matrix \mathbf{L} and the vector of primitive variables \mathbf{v} , and can be found through the following transformations:

$$\mathbf{w} = \begin{pmatrix} \mathbf{w}_1 \\ \mathbf{w}_2 \\ \mathbf{w}_3 \\ \mathbf{w}_4 \\ \vdots \\ \mathbf{w}_i \end{pmatrix} = \mathbf{L}\mathbf{v} \quad \mathbf{v}_{(x,y)}^t = \sum_{k=1}^{k=m} \mathbf{w}_{(k)}^t \mathbf{r}_{(k)}^t$$

The latter transformation is an eigenvector expansion of the vector \mathbf{v} , and constitutes the solution of the Riemann problem. With reference to linear wave decomposition, this solution is a superposition of m ($=3+n$) waves, propagating independently and with speed $\phi_{(k)}$ along the characteristics of the system (a curve in the $x-t$ domain in the direction of $\phi_{(k)}$). The wave equations (compatibility equations) have the following form:

$$\frac{\partial \mathbf{w}_{(k)}}{\partial t} + \phi_{(k)} \frac{\partial \mathbf{w}_{(k)}}{\partial x} = 0$$

and can be seen to define a wave with constant shape, advected in time:

$$\mathbf{w}_{(k)(x,y)}^{t+\Delta t} \cdot \mathbf{r}_{(k)(x,y)} = \mathbf{w}_{(k)(x-\phi_{(k)}\Delta t,y)}^t \cdot \mathbf{r}_{(k)(x,y)}$$

The solution to the Riemann problem at a cell interface, positioned at $(x=[i+1/2]\Delta x, y=[j]\Delta y)$, at time t , is to be obtained using primitive variables \mathbf{v} defined at positions left ($[i]\Delta x, [j]\Delta y$) and right ($[i+1]\Delta x, [j]\Delta y$) of the cell interface. Values of \mathbf{v} at the cell interface must be obtained by means of the following linearization, which, in the case of non-conservative dependent variables, is a straightforward arithmetic averaging:

$$\bar{h}_{(i+\frac{1}{2},j)} = \frac{h_{(i+1,j)} + h_{(i,j)}}{2} \quad \sqrt{\text{Rg}\bar{C}_{(i+\frac{1}{2},j)}\bar{h}_{(i+\frac{1}{2},j)}} = \sqrt{\text{Rg}\left(\frac{C_{(i+1,j)}h_{(i+1,j)} + C_{(i,j)}h_{(i,j)}}{2}\right)}$$

$$\bar{U}_{x,(i+\frac{1}{2},j)} = \frac{U_{x,(i+1,j)} + U_{x,(i,j)}}{2} \quad \bar{U}_{y,(i,j+\frac{1}{2})} = \frac{U_{y,(i,j+1)} + U_{y,(i,j)}}{2} \quad \bar{C}_{(i+\frac{1}{2},j)} = \frac{C_{(i+1,j)} + C_{(i,j)}}{2}$$

By replacing the primitive variables \mathbf{v} by their linearized versions, the decomposition of the discontinuity at a cell interface is formulated as:

$$\mathbf{v}_{r,(i+1,j)}^t - \mathbf{v}_{l,(i,j)}^t = \Delta_x \mathbf{v} = \sum_{k=1}^{k=m} (\mathbf{w}_{(k),r(i+1,j)}^t - \mathbf{w}_{(k),l(i,j)}^t) \hat{\mathbf{r}}_{(k)}^t = \sum_{k=1}^{k=m} (\Delta_x \mathbf{w}_{(k)}^t) \hat{\mathbf{r}}_{(k)}^t$$

where $\hat{\mathbf{r}}_{(k)}$ is the right-eigenvector of the Jacobian $\hat{\mathbf{A}}$ associated with eigenvalue $\hat{\phi}_{(k)}$, linearized to approximate values at the cell interface. A similar decomposition can be formulated for the flux differences $\Delta \mathbf{f}$.

The vectors of characteristic variables $\mathbf{w}_x, \mathbf{w}_y$ for the two one-dimensional systems, obtained from the multiplication of matrix \mathbf{L} with vector \mathbf{v} , when differenced over the cell interface, take the following form:

$$(\Delta_x \mathbf{w}_x) = \begin{pmatrix} \frac{1}{2} \left(\Delta_x h - \frac{\bar{h}_x \Delta_x U_x}{d_x} + \frac{\bar{h}_x \Delta_x C}{2\bar{C}_x} \right) \\ \bar{h}_x \Delta_x U_y \\ \frac{1}{2} \left(\Delta_x h + \frac{\bar{h}_x \Delta_x U_x}{d_x} + \frac{\bar{h}_x \Delta_x C}{2\bar{C}_x} \right) \\ - \frac{\bar{h}_x \Delta_x C_1}{2\bar{C}_x} \\ \vdots \\ - \frac{\bar{h}_x \Delta_x C_i}{2\bar{C}_x} \end{pmatrix} \quad (\Delta_y \mathbf{w}_y) = \begin{pmatrix} \frac{1}{2} \left(\Delta_y h - \frac{\bar{h}_y \Delta_y U_y}{d_y} + \frac{\bar{h}_y \Delta_y C}{2\bar{C}_y} \right) \\ \bar{h}_y \Delta_y U_x \\ \frac{1}{2} \left(\Delta_y h + \frac{\bar{h}_y \Delta_y U_y}{d_y} + \frac{\bar{h}_y \Delta_y C}{2\bar{C}_y} \right) \\ - \frac{\bar{h}_y \Delta_y C_1}{2\bar{C}_y} \\ \vdots \\ - \frac{\bar{h}_y \Delta_y C_i}{2\bar{C}_y} \end{pmatrix}$$

where overbars denote arithmetic averages.

The linearized right-eigenvectors $\hat{\mathbf{r}}_{(k)}$ are the columns of the linearized right-eigenvector matrices $\hat{\mathbf{R}}_x$, $\hat{\mathbf{R}}_y$ defined as:

$$\hat{\mathbf{R}}_x = \begin{bmatrix} 1 & 0 & 1 & 1 & \cdots & 1 \\ -\frac{\bar{a}}{h} & 0 & \frac{\bar{a}}{h} & 0 & \cdots & 0 \\ 0 & \frac{1}{h} & 0 & 0 & \cdots & 0 \\ 0 & 0 & 0 & -\frac{2\bar{C}}{h} & \cdots & 0 \\ 0 & 0 & 0 & 0 & \ddots & 0 \\ 0 & 0 & 0 & 0 & 0 & -\frac{2\bar{C}}{h} \end{bmatrix} \quad \hat{\mathbf{R}}_y = \begin{bmatrix} 1 & 0 & 1 & 1 & \cdots & 1 \\ 0 & \frac{1}{h} & 0 & 0 & \cdots & 0 \\ -\frac{\bar{a}}{h} & 0 & \frac{\bar{a}}{h} & 0 & \cdots & 0 \\ 0 & 0 & 0 & -\frac{2\bar{C}}{h} & \cdots & 0 \\ \vdots & \vdots & \vdots & \vdots & \ddots & 0 \\ 0 & 0 & 0 & 0 & \cdots & -\frac{2\bar{C}}{h} \end{bmatrix}$$

and $\bar{a} = \sqrt{RgCh}$.

A.4 Flux limiters

The TVD artificial viscosity term \mathbf{d}_x can be expressed as (Sloff, 1997):

$$\mathbf{d}_{x(i+\frac{1}{2},j)}^t = \frac{1}{2} \sum_{k=1}^{k=m} \left(1 - \Psi_{(k,i+\frac{1}{2},j)}^t\right) \cdot \left| \hat{\phi}_{(k,i+\frac{1}{2},j)}^t \right| \cdot \left(1 - \frac{\Delta t}{\Delta x} \hat{\phi}_{(k,i+\frac{1}{2},j)}^t\right) \cdot \left(\Delta_x \mathbf{w}_{(k,i+\frac{1}{2},j)}^t\right) \cdot \hat{\mathbf{r}}_{(k,i+\frac{1}{2},j)}^t$$

The parameter Ψ is the limiter function, which is applied to each wave that contributes to the total variation in the primitive variables \mathbf{v} across the discontinuity. Since the TVD condition requires that the gradients of the fluxes are to be kept within proper bounds, Ψ itself is defined as a function of ratios θ of consecutive variations of these fluxes (Hirsch, 1990):

$$\Psi_{(k,i+\frac{1}{2},j)}^t = \Psi\left(\theta_{(k,i+\frac{1}{2},j)}^t\right)$$

The definition of the ratio $\theta_{(k)}$ for each wave depends on the direction of propagation of the wave, which, in a one-dimensional system, is defined by the sign of the speed of propagation $\hat{\phi}_{(k)}$. Therefore, $\theta_{(k)}$ is defined such as to ensure that it reflects the ratio of variations in fluxes in upwind direction. For positive propagation speeds, the ratio is defined as (Sloff, 1997):

$$\theta_{(k,i+\frac{1}{2},j)} = \frac{\left[\left| \hat{\phi}_{(k)} \right| \left(1 - \frac{\Delta t}{\Delta x} \left| \hat{\phi}_{(k)} \right| \right) \left(\Delta_x \mathbf{w}_{(k)}\right) \cdot \hat{\mathbf{r}}_{(k)} \right]_{-(i-\frac{1}{2},j)}}{\left[\left| \hat{\phi}_{(k)} \right| \left(1 - \frac{\Delta t}{\Delta x} \left| \hat{\phi}_{(k)} \right| \right) \left(\Delta_x \mathbf{w}_{(k)}\right) \cdot \hat{\mathbf{r}}_{(k)} \right]_{-(i+\frac{1}{2},j)}}$$

For negative propagation speeds, the ratio is defined as (Sloff, 1997):

$$\theta_{(k,i+\frac{1}{2},j)} = \frac{\left[\left| \hat{\phi}_{(k)} \right| \left(1 - \frac{\Delta t}{\Delta x} \left| \hat{\phi}_{(k)} \right| \right) \left(\Delta_x \mathbf{w}_{(k)}\right) \cdot \hat{\mathbf{r}}_{(k)} \right]_{-(i+\frac{3}{2},j)}}{\left[\left| \hat{\phi}_{(k)} \right| \left(1 - \frac{\Delta t}{\Delta x} \left| \hat{\phi}_{(k)} \right| \right) \left(\Delta_x \mathbf{w}_{(k)}\right) \cdot \hat{\mathbf{r}}_{(k)} \right]_{-(i+\frac{1}{2},j)}}$$

To prevent division by zero, it is recommended to add a small number (e.g. $1 \cdot 10^{-8}$) to the denominator.

Various alternatives exist for the definition of the limiter function Ψ , some of which have a smoothing effect on discontinuities whereas others compress them. All limiters are non-linear functions of the above defined ratios, and satisfy the following conditions:

$$0 \leq \frac{\Psi(\theta)}{\theta} \leq 2 \quad \Psi(\theta) \leq 2 \quad \Psi(1)=1$$

Together, these conditions form the second-order TVD region, illustrated in figure A3.4 (shaded region).

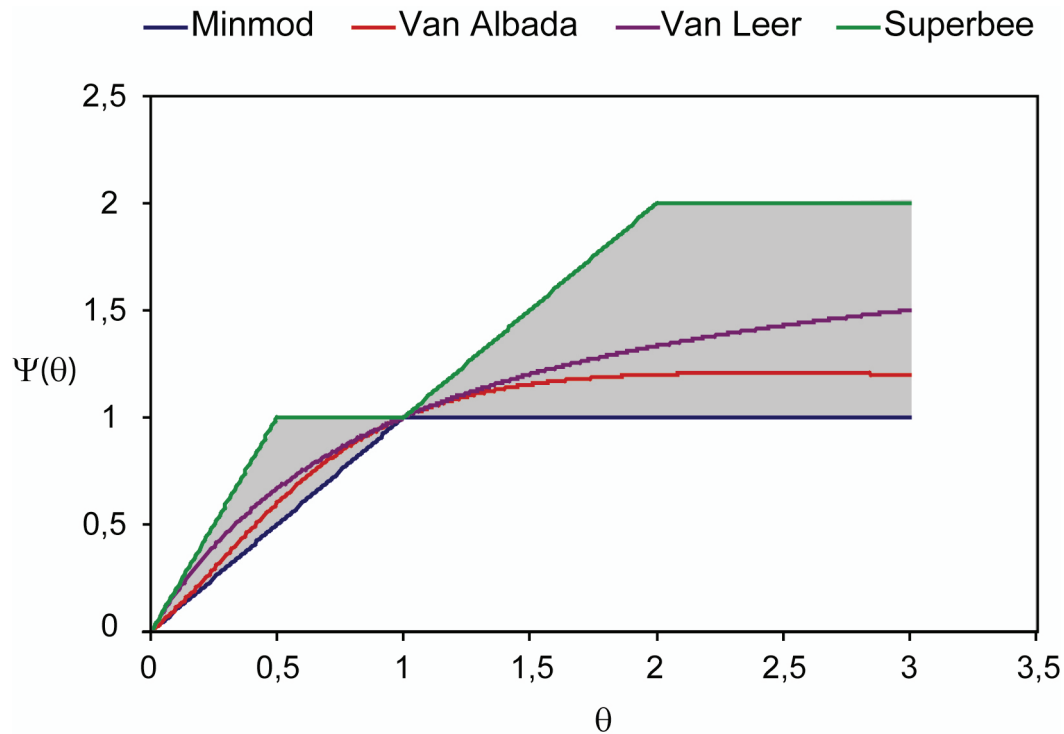


Figure A1.2: Second-order TVD region (shaded) and limiter functions (coloured lines).

For completeness, the limiters that have been used in the context of this model will be shortly reviewed. Details on limiters, part of which has been reproduced here, can be found in e.g. Hirsch (1990).

MinMod limiter: lower limit of the TVD domain, weakest limiter, with highest smoothing behaviour, lowest resolution properties for contact discontinuities

$$\psi(\theta) = \max(0, \min(1, \theta))$$

Van Albada limiter: applied by Van Albada et al. (1982), stronger than *MinMod*, tends to one for large θ

$$\psi(\theta) = \frac{\theta^2 + \theta}{1 + \theta^2}$$

Van Leer limiter: applied by Van Leer (1974), stronger than *Van Albada* limiter, continuous function of θ

$$\psi(\theta) = \frac{\theta + |\theta|}{1 + \theta}$$

Superbee limiter: upper limit of the TVD domain, strongest limiter, with lowest smoothing behaviour, highest resolution properties for contact discontinuities, risk of over-amplification

$$\psi(\theta) = \max(0, \min(2\theta, 1), \min(\theta, 2))$$

A.5 The Entropy Correction

The system of Euler equations admits discontinuous (non-differentiable) solutions, which, from a mathematical point of view, cannot satisfy the differential equations, but are valid solutions of the integral form of the conservation laws. Several forms of discontinuous solutions exist, all of which satisfy the Rankine-Hugeniot jump conditions (Chapter 3, Paragraph 3.2.3). However, not all solutions have a valid physical meaning. The second law of Thermodynamics states that in any physical realizable adiabatic evolution the transformation of a system is accompanied by an increase in entropy. As such, stationary expansion shocks (waves emanating from a stationary discontinuity which doesn't dissipate in time or not at all; Figure A1.3) cannot occur in real flows, because they are characterized by a decrease in entropy (Hirsch, 1990).

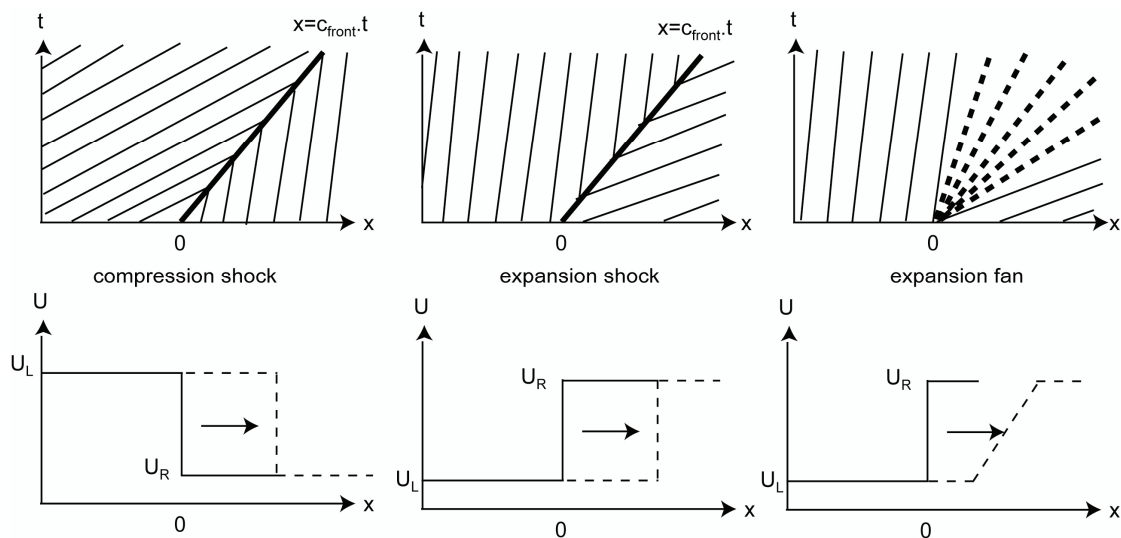


Figure A1.3: Solutions to the Euler equations: a) compression shock, valid solution; b) expansion shock, invalid solution; c) expansion fan, valid solution

However, the system of Euler equations (inviscid flow) does not have a built-in dissipative mechanism (e.g. based on viscosity) to distinguish between the correct physical shocks and the non-physical ones. This mechanism is to be added in the form of the entropy condition. In analogy to the properties of physical compression shocks, the condition to be satisfied by the discontinuous solutions of the hyperbolic conservation laws is that the velocity of propagation ϕ_k (celerity) of waves (having index k) is such that:

$$\phi_{(k),\text{left}} \geq c_{\text{front}} \geq \phi_{(k),\text{right}}$$

This essentially implies that waves to the left (“behind” the front) of the discontinuity overtake the discontinuity, whereas waves to the right (“before” the front) are overtaken by it. Problems occur at points where the flow changes from subcritical to supercritical (a transcritical point) since, in that case, for one of the wave indices k , the waves to the left and right of the discontinuity may diverge, thus carrying information (energy) that originated from the discontinuity away from the discontinuity while the discontinuity itself persists and propagates. This is in violation

with the entropy condition. Following Sloff (1997), the entropy correction by Harten and Hyman (1983) is implemented, which introduces a local expansion fan (Figure A1.3) in the approximate Riemann solution at a transcritical flow point when it is needed, thereby converting the expansion shock into an expansion fan:

$$\left| \hat{\phi}_{(k),(i+\frac{1}{2},j)} \right| = \begin{cases} \left| \hat{\phi}_{(k),(i+\frac{1}{2},j)} \right| & \left| \hat{\phi}_{(k),(i+\frac{1}{2},j)} \right| \geq \gamma_{(k)} \\ \gamma_{(k)} & \left| \hat{\phi}_{(k),(i+\frac{1}{2},j)} \right| < \gamma_{(k)} \end{cases}$$

where

$$\gamma_{(k)} = \max \left[0, \left(\hat{\phi}_{(k),(i+\frac{1}{2},j)} - \phi_{(k),(i,j)} \right), \left(\phi_{(k),(i+1,j)} - \hat{\phi}_{(k),(i+\frac{1}{2},j)} \right) \right]$$

The corrected celerity is to be used in the calculation of the TVD artificial viscosity term and in the calculation of the slope ratio $\theta_{(k)}$.

PROCESS-BASED MODELLING OF TURBIDITY-CURRENT HYDRODYNAMICS AND SEDIMENTATION

REMCO GROENENBERG

SUMMARY

1. INTRODUCTION

Annually an estimated 15 billion tons of sediment (approximately 5.7 billion m^3) is delivered to the continental margins worldwide. The sediment is transported from mountain ranges to the coastline, where rivers debouch into the oceans to form deltas. At and near deltas, long-shore currents, wave action and tides may redistribute and rework the sediment, until it is transported to the deeper oceans by, amongst others, turbidity currents. Turbidity currents are mixtures of sediment and water which flow downslope by virtue of the force of gravity. Gravity acts on the sediment grains in the suspension which, on their way to being deposited, drag the seawater along with them, thereby effectively generating a turbid underflow. Upon reaching lower-slope gradients the gravitational force diminishes and the flow eventually decelerates and spreads. As the flow thus loses its capacity to carry sediment in suspension, grains will start settling out of suspension, first the coarser ones, then successively the finer ones. Individual beds thus deposited are called “turbidites”, and range in thickness from centimetres to meters. Sequential occurrence of turbidity currents over geologic time periods results in turbidite fans with thicknesses of tens to hundreds of meters which are known to contain major petroleum reservoirs throughout the world. Although today only a part of the oil and gas in these petroleum reservoirs is being developed, it is likely that the increase in oil price in recent years will further increase exploration and production efforts in these reservoirs.

In this thesis, the focus is on the flow behaviour of turbidity currents and on how it influences the geometry and internal architecture of turbidite fans. The potential for sedimentary rocks to constitute a good reservoir primarily depends on two properties: porosity and permeability. Porosity is defined as the proportion of space (volume) between the grains available for storage of hydrocarbons. Permeability is a measure of the degree to which the pores are connected with each other, and pertains to the ability of fluids to flow through rock. Porosity and permeability are generally higher in sandstones and lower in siltstones and claystones. Therefore, the distribution of sand, silt and clay in turbidite reservoirs is of primary importance in assessing their production potential. Unfortunately, the typical resolution of the main data used in reservoir characterization is either too low or too localized. Well data have a high resolution, but they cannot be extrapolated far beyond the immediate vicinity of the wellbore without loss of certainty. By contrast, seismic volumes are large. Data cubes may have horizontal dimensions of tens of kilometres and may be up to several kilometres in depth, but the typical vertical resolution is about thirty meters. This means that variations in sand, silt and clay content significantly smaller than ten meters in thickness cannot be resolved. Variations in sand, silt and clay content in turbidite reservoirs typically occur on a

scale of meters to one-hundred meters horizontally and millimetres to meters vertically. Consequently, on the scale of the architectural elements of turbidite reservoirs uncertainty exists on the anatomy and spatial variability of reservoir properties. Quantification of the geometry and distribution of these architectural elements in a reservoir can provide crucial information to assess reservoir volume, connectivity and the distribution of permeability baffles.

In general, two different approaches exist to gaining insight into the distribution of sand, silt and clay in turbidite reservoirs at the interwell scale. The analogue, or 'product-based', approach is to study modern turbidite fans and ancient ones that are now situated in accessible locations above sea level. Alternatively, the 'process-based' approach focuses on the turbidity currents themselves, and investigates how their hydrodynamic evolution influences the distribution of sand, silt and clay in turbidite fans. Because of the hazardous nature of turbidity currents, and their rare occurrence, data on their behaviour under natural conditions are extremely difficult to obtain. Consequently, studies on turbidity-current hydrodynamics and sedimentation rely on scaled-down experimental models and process-based numerical models. Process-based numerical models of turbidity currents improve our understanding by taking into account the interdependence between flow and sedimentation parameters based on elementary physics. In this study, such a process-based numerical model is formulated, analysed, implemented and validated. It will be used at a later stage in field-scale research of hydrodynamic parameters governing turbidity-current flow, such as relief, flow density, and grain-size distribution of the suspended sediment, and their effects on depositional patterns observed in turbidite fans. As such, the work presented here tries to contribute to a better understanding of the geometry and spatial distribution of potential reservoir sands in turbidite fans and thus to help producing reservoirs contained in turbidite fans more efficiently.

3. MATHEMATICAL MODEL

A mathematical model is formulated for turbidity-current flow and sedimentation over arbitrary topography in three dimensions. It employs the layer-averaged equations of balance of fluid mass, sediment mass and momentum in extended form, which describe variations in flow depth, flow velocity and sediment concentration in the streamwise, transverse and upward-normal direction for a turbidity current of low density. A situation is modelled in which a turbidity current flows over a surface representing topography, thereby exchanging sediment with the bed. Concentrations of suspended sediment in the turbidity current are low (< 5% by volume), and hindered settling does not occur. Changes in concentration occur through entrainment of ambient water at the top of the turbidity current, deposition of sediment from the turbidity current and erosion of sediment from the bed by the turbidity current, which is considered fully turbulent ($Re > 3000$). Reynolds stresses and diffusion of sediment, associated to turbulence in horizontal directions, are assumed to be negligible compared to those in vertical directions. Flow depth, flow velocity and sediment concentration are layer-averaged to obtain a single value for each position in space at any given time, under the assumption that vertical profiles of velocity and concentration preserve an approximately similar shape as they change in time or in any of the horizontal directions (no helicoidal flow). Rates of deposition and erosion of sediment are related to the shear velocity, which is parameterized

through a dimensionless drag coefficient. Sediment in suspension and on the bed is assumed to be non-cohesive, and may be composed of one or more grain-size classes. Bed-load transport is not modelled.

4. NUMERICAL IMPLEMENTATION

The mathematical model consists of $3+n$ equations, which together constitute a system of coupled, first-order, quasi-linear and non-homogeneous partial-differential equations (PDE). Here, n represents the number of grain-size fractions in the sediment mixture. The PDEs contain time derivatives representing the change in primary flow variables in time at locations in the flow, space derivatives representing advection of mass (fluid, suspended sediment) and momentum (energy), and source terms representing loss or gain of momentum (gravity, friction), fluid mass (ambient water entrainment) and sediment mass (erosion, deposition). The complexity of the mathematical model requires that a solution is found by means of integration in time and space with an appropriate numerical discretization technique. The finite-difference scheme adopted here is the MacCormack (1969) scheme, a simple and robust explicit scheme of second-order accuracy in time and space. To stretch the computational efficiency of the model, the operator-splitting technique by Strang (1968) is adopted, in which the two-dimensional discretized space operators are split into products of one-dimensional operators that are solved in sequence. By doing this, the stability properties of the scheme are further improved, and the amount of computational work is reduced. Additionally, the implementation of a shock-capturing scheme, which prevents spurious oscillations at the front of the turbidity current and near hydraulic jumps, is facilitated. Shock-capturing is implemented according to the Total Variation Diminishing (TVD) concept, which limits the fluxes between cells such as to ensure that the total variation of the discrete numerical solution (the sum of all the inter-cell fluxes) diminishes in time. To further enhance the numerical representation of the front, the concentration equation is replaced with a simple zero-order extrapolation of the concentration upstream of the front into the front region. The location of the front region is determined by front tracking. At the boundaries of the numerical grid, non-reflective, open in- and outflow boundaries ensure that information can freely enter and exit the computational domain without causing disturbances in the solution.

5. QUANTITATIVE VALIDATION EXPERIMENTS

Results are presented from validation experiments, in which simulated hydrodynamic behaviour (depth, velocity, and density of flows), deposit geometry and spatial distribution of grain sizes are quantitatively compared to data from quasi-steady and waning experimental turbidity currents. The experimental turbidity currents are considered to be representative small-scale analogues for unconfined submarine turbidity currents spreading out onto a semi-horizontal basin floor. Simulated hydrodynamic behaviour and geometry of deposits are very similar to their experimental counterparts. Discrepancies in flow hydrodynamics and deposits are attributed to the upstream part of the experimental basin, which does not comply with the assumption of an infinitely deep basin postulated in the model to adopt the “single-layer” formulation, the discretization of the grain-size distribution of the

sediment, possible irregularities in the experiments such as e.g. small differences in slope, and the influence of processes that are not explicitly taken into account in the model, such as the formation of turbulent eddies and instabilities related to the entrainment of water into the turbidity current. Furthermore, model outcome is shown to be sensitive to the drag coefficient c_D . The drag coefficient parameterizes the drag force exerted by the flow on the bed for a given flow velocity. Its value, which must be estimated from a wide range based on empirical data, has a significant effect on the propagation velocity of the front of the simulated turbidity currents.

The sensitivity of the model to time-step length and grid-cell size is evaluated by comparing the validated modelling results to results of simulations in which a different spatial and temporal resolution is used. Loss of accuracy seems more prominent for differences in spatial resolution than for differences in time resolution, and mainly occurs in areas of discontinuous flow. Absolute and relative errors in deposit thickness increase almost linearly with decrease in temporal and spatial resolution. Recognition of this trend allows an estimation of the absolute and relative errors of a simulation which, in case of stratigraphic models involving multiple turbidity-current events, helps to decide upon the temporal and spatial resolution to be used.

6. QUALITATIVE VALIDATION EXPERIMENTS

Results are presented from two series of validation experiments, in which simulated hydrodynamic (flow depth, velocity, density) and sedimentation (deposit geometry, grain size distribution) values are qualitatively compared to data from small-scale experimental turbidity currents. The first set of validation experiments focuses on hydrodynamics and sedimentation patterns in the presence of complex topographic features commonly encountered in reservoir characterization studies, such as lateral and transversal (basin-bounding) slopes, diapirs and constrictions. A quantitative comparison, which would have been preferred, was impossible due to incompatibilities between the design of the model and the set-up of the experiments. Notwithstanding the differences between the simulated and the experimental flows, the simulated depositional patterns mostly compare well qualitatively with depositional patterns observed in the experiments.

For circular obstacles, and for linear obstacles oriented perpendicular to the streamwise flow direction, the ratio of obstacle height-to-head height determines if and to what extent the turbidity current surmounts the obstacle and deposits sediment downstream of it. For circular obstacles, flow deflection (partial or complete) depends on the height of the obstacle in relation to the height of the head of the turbidity current. The angle of deflection depends on the aspect ratio (width:height) of the circular obstacle. Simulations of turbidity currents encountering circular obstacles with heights well in excess of the height of the head revealed that a ridge of sediment evolves upstream of the obstacle, which extends at an angle of almost 90° to the angle of incidence of the flow. In the case of a turbidity current encountering a constriction, the location of the area of maximum sediment thickness induced by the constriction depends on the drag coefficient c_D . Higher values of c_D result in faster flow deceleration and lower velocities upon reaching the obstacle, and allow grains to be kept in suspension longer after inflow into the model domain. The combined effect

results in the observed upstream shift of maximum deposit thickness. For flows obstructed by linear obstacles oriented parallel to the streamwise flow direction the effect of the flow-restricting parallel obstruction on the deposit is discernible in the form of a local thickening at the break in slope. As the gradient of the lateral obstruction increases, the local thickening becomes more pronounced.

In the second set of validation experiments, simulated results are compared to data from an experiment in which stratigraphy is created that is meant to be representative of a subsiding mini-basin with a turbidite fan system such as found e.g. in the Gulf of Mexico. This experiment, in which the grain-size distribution of the sediment contains three size fractions, may be regarded as the ultimate validation test for the model because it combines a sequence of flows with different initial depths, velocities and densities with complex topography that changes in time. Based on a comparison of simulated flow behaviour to experimental observations, it seems justified to conclude that the model simulates the flow behaviour with an acceptable degree of accuracy. However, although the model produces qualitatively realistic stratigraphy, the comparison between experimental and simulated stratigraphy is far from perfect. Discrepancies are mainly attributed to small differences in initial topography and substrate configuration, differences in boundary conditions between the model and the experimental set-up, and to the sensitivity of model outcome to the drag coefficient c_D . The value of c_D , in combination with the discretized grain-size distribution and the somewhat low spatial resolution used in the simulation, results in distinct loci of deposition for the three size-fractions, which are not observed in the experiment. Furthermore, the difference in outflow boundary conditions between the model and the experiment significantly influences the volume of sediment deposited in the basin. In the experiment, ponding occurs in the basin due to the absence of moats, whereas in the model, open outflow boundaries prevent the occurrence of ponding.

HET PROCES-GEBASEERD MODELLEREN VAN DE HYDRODYNAMICA EN SEDIMENTATIE VAN TROEBELSTROMEN

REMCO GROENENBERG

SAMENVATTING

1. INTRODUCTIE

Rivieren vervoeren wereldwijd jaarlijks 15 miljard ton sediment (ongeveer 5.7 miljard m³) naar de randen van continenten. Het sediment wordt getransporteerd vanuit bergketens naar de kustlijn, waar rivieren uitmonden in zee in de vorm van deltas. In en nabij deltas wordt het sediment geredistribueerd en omgewerkt door kustparallele stromingen en golf- en getijdewerking, totdat het uiteindelijk verder getransporteerd wordt van het continentaal plat naar de diepere delen van de oceanen door, onder andere, troebelstromen. Troebelstromen zijn suspensies van sediment en water die langs continentale hellingen vanaf de randen van het continentaal plat naar beneden stromen onder invloed van de zwaartekracht. De zwaartekracht heeft met name invloed op het sediment in de suspensie, dat op zijn weg naar beneden het water in de directe omgeving meetrekt. Wanneer de troebelstroom de lager gelegen, minder steile delen van de continentale helling bereikt heeft, valt de invloed van de zwaartekracht weg, waardoor de snelheid van de troebelstroom afneemt en de stroom zich min of meer waaivormig uitspreidt over de oceaانبodem. Dientengevolge verliest de troebelstroom haar vermogen om het sediment gesuspendeerd te houden, waardoor het uit de stroom neerdaalt op de oceaانبodem en zo een laag sediment vormt. Een dergelijke laag, waarvan de dikte kan variëren van centimeters tot meters, wordt een “turbidiet” genoemd. Wanneer op geologische tijdschalen wordt gekeken, kunnen gedurende langere perioden troebelstromen geregeld plaatsvinden op ongeveer dezelfde plek, waardoor volumetrisch grote waaivormige sediment lichamen ontstaan met diktes van tientallen tot honderden meters, waarin grote olie- en gasvelden gevonden zijn. Hoewel vandaag de dag uit slechts een deel van deze olie- en gasvelden wordt geproduceerd, is het aannemelijk dat de recente stijging van de olieprijs in de nabije toekomst zal leiden tot een toename van de investeringen in de exploratie en productie van olie- en gasvelden in turbidiet afzettingen.

In dit proefschrift ligt de nadruk op het stromingsgedrag van troebelstromen en op hoe dit de geometrie en interne opbouw van de door hen gevormde sediment lichamen beïnvloedt. De reservoir kwaliteit van het gesteente waaruit dergelijke sediment lichamen bestaan hangt in grote mate af van twee eigenschappen: de porositeit en de permeabiliteit. Porositeit is gedefinieerd als het gedeelte van het totale gesteente volume dat niet gevuld is met zandkorrels. Het is een maat voor de hoeveelheid lege ruimte tussen de zandkorrels (poriën ruimte) die beschikbaar is voor de opslag van olie en gas. De permeabiliteit is een maat voor de verbondenheid van de poriën, en kwantificeert de doorlaatbaarheid van het gesteente met betrekking tot de stroming van olie en gas. Waarden voor porositeit en permeabiliteit zijn over het algemeen hoger in gesteente dat bestaat uit zand, en lager in gesteente dat bestaat uit silt en/of klei. De verdeling van zand, silt en klei in een sediment lichaam is daarom

van groot belang bij het bepalen van de winbaarheid van olie en gas uit dat sediment lichaam. Helaas is de resolutie van de data die gebruikt worden voor de bepaling van de geometrie en de interne opbouw van reservoir gesteente te laag ofwel zijn de data te gelokaliseerd. Data uit putten hebben een hoge resolutie, maar hebben alleen betrekking op gesteente in de directe omgeving van de put. Seismiek daarentegen beslaat over het algemeen een groot gesteente volume, maar heeft een maximale resolutie van ongeveer dertig meter, zodat variaties in zand, silt en klei op kleinere schaal niet kunnen worden waargenomen. De schaal waarop in door troebelstromen gevormde sediment lichamen variaties in zand, silt en klei voorkomen is in de orde van meters tot honderden meters lateraal en millimeters tot meters verticaal. Variaties in korrelgrootte in deze sediment lichamen zijn dus niet goed vast te stellen. Daarom bestaat er over het algemeen grote onzekerheid over de porositeit en permeabiliteit in olie- en gas reservoirs in door troebelstromen afgezet sediment. Onderzoek gericht op het verkrijgen van een beter inzicht in variaties in korrelgrootte in door troebelstromen afgezet sediment kan dus van grote waarde zijn bij de bepaling van de winbaarheid van olie en gas in dergelijke afzettingen.

Er bestaan grofweg twee verschillende benaderingen om inzicht te krijgen in de verdeling van zand, silt en klei in door troebelstromen afgezet sediment. De “produkt-gebaseerde” benadering bestaat uit het bestuderen van in het verleden door troebelstromen afgezet sediment dat nu in de vorm van gesteente boven zeeniveau ligt. De “proces-gebaseerde” benadering legt de nadruk op de troebelstromen zelf, en bestudeert hoe hun stromingsgedrag de verdeling van zand, silt en klei beïnvloedt. Omdat troebelstromen in de natuur over het algemeen catastrofaal van aard zijn, weinig voorkomen en niet van te voren vast te stellen is waar ze precies zullen voorkomen, is het bijzonder lastig om er metingen aan te doen. De proces-gebaseerde benadering is daarom grotendeels afhankelijk van kleinschalige laboratorium experimenten en numerieke modellen. Proces-gebaseerde numerieke modellen vergroten ons inzicht door middel van het bestuderen van de interactie tussen troebelstroming en sediment op basis van elementaire fysica. De formulering, analyse, numerieke implementatie en validatie van zo'n proces-gebaseerd numeriek model wordt in dit proefschrift besproken. Het model zal in een later stadium worden gebruikt voor onderzoek naar de invloed van het stromingsgedrag van troebelstromen op de verdeling van zand, silt en klei in door troebelstromen afgezet sediment op reservoir schaal. Als zodanig poogt het hier gepresenteerde werk bij te dragen tot efficiëntere winning van olie en gas uit troebelstroom afzettingen.

3. WISKUNDIG MODEL

Een wiskundig model is geformuleerd voor het stromingsgedrag van en sedimentatie uit troebelstromen over willekeurige topografie in drie dimensies. Het model is gebaseerd op de dieptegemiddelde balansvergelijkingen voor vloeistof massa, sediment massa en impuls, waarmee variaties in de diepte en snelheid van de troebelstroom en concentratie van gesuspendeerd sediment in willekeurige richting kunnen worden berekend. De gemodelleerde situatie is die waarin een troebelstroom zich uitspreidt over een willekeurig gevormd oppervlak dat de zeebodem voorstelt, waarbij uitwisseling van sediment plaatsvindt tussen de troebelstroom en het oppervlak. De concentratie van gesuspendeerd sediment in de troebelstroom is relatief laag (minder dan vijf procent van het totale volume van de troebelstroom) zodat de

uitval van sediment ongehinderd kan plaatsvinden. Veranderingen in concentratie komen voort uit de insluiting van omgevingswater door de troebelstroom, de uitval van sediment uit de stroom en de opname van op de zeebodem aanwezig sediment door de stroom, die volledig turbulent verondersteld wordt ($Re > 3000$). Reynolds krachten en diffusie van gesuspendeerd sediment als gevolg van turbulentie in horizontale richtingen worden verwaarloosbaar verondersteld in vergelijking tot die in verticale richtingen. De diepte en snelheid van de troebelstroom, en de concentratie van gesuspendeerd sediment worden dieptegemiddeld, zodat op iedere plek in de stroom op ieder willekeurig moment voor deze variabelen slechts één waarde overblijft. Daarbij dient verondersteld te worden dat de profielen van snelheid en concentratie, die de variatie in de waarde van deze variabelen beschrijven in verticale richting, in horizontale richtingen over de gehele troebelstroom dezelfde vorm behouden, ondanks het feit dat de waarden zelf wel van plaats tot plaats en in de tijd kunnen veranderen. Snelheden van afzetting en opname van sediment worden gerelateerd aan de schuifnelheid aan de zeebodem, die geparameteriseerd wordt door middel van een dimensieloze wrijvingscoëfficiënt. Het sediment in suspensie en op de zeebodem wordt verondersteld geen samenbindende eigenschappen te hebben, en kan uit één of meerdere discrete korrelgrootte klassen bestaan. Het transport van sediment op de zeebodem zelf wordt niet expliciet gemodelleerd.

4. NUMERIEKE IMPLEMENTATIE

Het wiskundige model bestaat uit $3+n$ vergelijkingen, die samen een systeem vormen van quasi-lineaire, niet-homogene, partiële differentiaalvergelijkingen van eerste orde. Hierbij neemt de parameter n de waarde aan van het aantal korrelgrootte klassen waaruit het gesuspendeerd sediment bestaat. De vergelijkingen bestaan uit tijdsdifferentialen, die de autogene verandering van stromingsvariabelen in de tijd beschrijven, plaatsdifferentialen, die de autogene verandering van stromingsvariabelen in de ruimte beschrijven, en brontermen, die afname en toename van impuls, vloeistofmassa en sedimentmassa beschrijven als gevolg van respectievelijk wrijving, insluiting van omgevingswater en afzetting en opname van sediment. De complexiteit van het wiskundige model maakt de oplossing ervan op analytische wijze praktisch onmogelijk. Daarom worden de vergelijkingen naar plaats en tijd geïntegreerd en met behulp van een geschikt numeriek schema op discrete punten in een rooster en discrete stappen in de tijd opgelost. Het hiervoor gekozen eindig-verschillen schema van MacCormack (1969) is een simpel en robuust expliciet schema dat tweede-orde nauwkeurig is in plaats en tijd. De efficiëntie van dit schema is verder vergroot door gebruik te maken van de “operator-splitting” techniek van Strang (1969), waarbij de ruimtelijke differentiaaltermen in de van oorsprong tweedimensionale vergelijkingen worden gescheiden in verzamelingen van eendimensionale ruimtelijke differentiaaltermen die steeds na elkaar worden opgelost. Hierdoor worden de stabiliteitsgrenzen van het schema opgerekt, en de hoeveelheid rekenwerk gereduceerd. Een bijkomend voordeel is dat de integratie van een techniek voor de correcte afhandeling van schokken in het schema wordt vergemakkelijkt. Een dergelijk techniek is noodzakelijk omdat daarmee onechte verstoringen in de oplossing worden voorkomen die optreden bij het modelleren van troebelstromen waarin schokken en sprongen voor komen. Die hier gebruikte techniek is gebaseerd op het “Total Variation Diminishing” concept, en limiteert de uitwisseling van massa en impuls tussen cellen zodanig dat de totale variatie in de oplossing, gedefinieerd als

de som van de uitwisselingen tussen alle cellen, in de tijd afneemt, waardoor een stabiele oplossing wordt verkregen. Om de representatie van schok aan de voorkant van de troebelstroom nog verder te verbeteren, wordt de concentratie vergelijking in de cellen die de schok vormen vervangen door een simpele nulde-orde extrapolatie van de concentratie stroomopwaarts van de schok. De bepaling van de hiervoor in aanmerking komende cellen wordt gedaan door middel van een “front-tracking” algoritme dat de locatie van de schok aan de voorkant van de troebelstroom bijhoudt. Op de grenzen van het rooster kan in- en uitstroom vrij plaatsvinden zonder dat reflecties optreden die de oplossing kunnen verstoren.

5. KWANTITATIEVE VALIDATIE EXPERIMENTEN

Resultaten van validatie experimenten worden gepresenteerd, waarin gemodelleerd stromingsgedrag van troebelstromen en de geometrie en korrelgrootte verdeling van de daaruit resulterende afzetting kwantitatief wordt vergeleken met data van kleinschalige troebelstromen opgewekt tijdens laboratorium experimenten. De kleinschalige troebelstromen worden verondersteld representatief te zijn voor grootschalige, in de natuur voorkomende troebelstromen die ongehinderd kunnen uitspreiden over de zeebodem. Het model simuleert het stromingsgedrag van de troebelstromen en de daaruit resulterende afzetting met een zeer acceptabele nauwkeurigheid. Verschillen tussen de door het model geproduceerde uitkomsten en de experimentele werkelijkheid zijn toe te schrijven aan het feit dat in de directe omgeving van de uitstroomopening in het laboratorium experiment de in het model gemaakte aanname van een oneindig diep reservoir niet opgaat, aan de discretizatie van de korrelgrootte verdeling van het sediment, aan mogelijke onregelmatigheden in het laboratorium experiment, zoals kleine verschillen in helling, en aan de invloed van processen in de troebelstromen die niet expliciet in het model zijn opgenomen, zoals de vorming van wervelingen en instabiliteiten die het gevolg zijn van de insluiting van omgevingswater in de troebelstroom. Tevens wordt aangetoond dat de uitkomst van het model afhankelijk is van de waarde van de wrijvingscoëfficiënt c_D , die de schuifspanning kwantificeert die de troebelstroom uitoefent op het sediment op de zeebodem. De waarde van deze wrijvingscoëfficiënt, die dient te worden geschat binnen een op basis van empirische gronden bepaald minimum en maximum, heeft een duidelijk waarneembare invloed op de voortplantingssnelheid van de schok aan de voorkant van de troebelstroom.

De gevoeligheid van het model met betrekking tot de lengte van de tijdstap en afstand tussen punten wordt geëvalueerd door de gevalideerde modelresultaten te vergelijken met resultaten van simulaties waarbij andere resoluties in ruimte en tijd zijn gebruikt. De nauwkeurigheid van het model blijkt gevoeliger voor verschillen in resolutie in de ruimte dan voor verschillen in resolutie in de tijd. Verlies van nauwkeurigheid treedt vooral op plaatsen waar schokken en sprongen voorkomen. Absolute en relatieve fouten in de dikte van de afzettingen nemen lineair toe met een verlaging van de resolutie in zowel ruimte als tijd. Deze vaststelling maakt het in principe mogelijk om voorafgaand aan een modelstudie een schatting te maken van de te verwachten fout in de uitkomst van het model, en helpt zo om de juiste resolutie in ruimte en tijd te kiezen.

6. KWALITATIEVE VALIDATIE EXPERIMENTEN

Resultaten worden gepresenteerd van twee series validatie experimenten, waarin gemodelleerd stromingsgedrag van troebelstromen en de geometrie en korrelgrootte verdeling van de daaruit resulterende afzetting kwalitatief wordt vergeleken met data van kleinschalige troebelstromen opgewekt tijdens laboratorium experimenten. In de eerste set validatie experimenten ligt de nadruk op het stromingsgedrag van en sedimentatie uit troebelstromen die op hun weg complexe topografische obstakels tegenkomen. De vorm en oriëntatie van de obstakels is zo gekozen dat ze representatief zijn voor obstakels die de natuur voorkomen als gevolg van onder andere breukwerking en diapirisme. Een kwantitatieve vergelijking bleek onmogelijk als gevolg van onverenigbare verschillen tussen de opzet van de experimenten en het model. Ondanks de daardoor ontstane verschillen in stromingsgedrag tussen de gemodelleerde en experimentele troebelstromen kan toch geconcludeerd worden dat de gemodelleerde sedimentatie patronen kwalitatief vrij goed overeenkomen met de patronen zoals ze zijn waargenomen in de experimentele afzettingen.

Voor cilindrische obstakels, en voor rechte obstakels met een oriëntatie loodrecht op de hoofdstroomrichting bepaalt de verhouding tussen de hoogte van het obstakel en de hoogte van de voorkant van de troebelstroom of en in welke mate deze over het obstakel heen stroomt en sediment afzet aan de stroomafwaartse kant van het obstakel. Verder kan gezegd worden dat voor cilindrische obstakels, de mate van afbuiging (volledig of gedeeltelijk) van de troebelstroom ook afhangt van de verhouding tussen de hoogte van het obstakel en de hoogte van de voorkant van de troebelstroom. De hoek waaronder de troebelstroom afbuigt hangt af van de verhouding tussen de diameter van het cilindrische obstakel en zijn hoogte. Simulaties met cilindrische obstakels die meer dan 3 keer zo hoog zijn als de hoogte van de voorkant van de troebelstroom tonen aan dat stroomopwaarts van het obstakel een vrij lange en smalle rug van sediment ontstaat met een oriëntatie loodrecht op de hoofdstroomrichting. In simulaties waarin een troebelstroom door een vernauwing stroomt wordt de locatie van het gedeelte van de afzetting met maximale dikte, dat ontstaat als gevolg van de vernauwing, opvallend genoeg bepaald door de waarde van een van de model parameters: de wrijvingscoëfficiënt c_D . Een verklaring hiervoor is dat enerzijds hogere waarden van de wrijvingscoëfficiënt resulteren in een snellere afname van de stroomsnelheid en dus lagere snelheden op de plaats van de vernauwing, waardoor de capaciteit van de troebelstroom om sediment in suspensie te houden geringer is. Anderzijds zorgt een hogere waarde van de wrijvingscoëfficiënt ervoor dat de schuifnelheid aan de bodem hoger is, waardoor de capaciteit van de troebelstroom om sediment in suspensie te houden vergroot wordt. Het gecombineerde effect resulteert in de waargenomen verplaatsingen van de maximale dikte van de afzetting. In simulaties waarin een troebelstroom wordt beperkt door een recht obstakel met een oriëntatie parallel aan de hoofdstroomrichting ontstaat een afzetting met een langgerekte vorm waarvan de maximale dikte bereikt wordt in de directe omgeving van het obstakel. Zowel de lengte als de dikte van het gedeelte van de afzetting waar de dikte maximaal is wordt bepaald door de steilte van het obstakel.

In de tweede serie validatie experimenten worden model resultaten kwalitatief vergeleken met data van een laboratorium experiment waarin stratigrafie is gecreëerd in een situatie die representatief wordt verondersteld voor een zich door zout

diapirisme ontwikkelend minibekken zoals gevonden is in de Golf van Mexico. Het modelleren van dit laboratorium experiment, waarin gebruik wordt gemaakt van sediment met meerdere korrelgrootte klassen, mag gezien worden als de ultieme validatie test voor het model, omdat een 32-tal opeenvolgende troebelstromen wordt opgewekt met verschillende diepten en snelheden, die vervolgens uitstromen over een complexe topografie die tijdens het experiment nog verandert. Een kwalitatieve vergelijking tussen gemodelleerd en geobserveerd stromingsgedrag leert dat het model het stromingsgedrag met een redelijke mate van nauwkeurigheid simuleert. Echter, hoewel het model schijnbaar realistische stratigrafie produceert, is de overeenkomst met de experimentele stratigrafie niet goed. Verschillen worden voornamelijk toegeschreven aan kleine onvolkomenheden in de initiële topografie en het substraat die in het proces van discretizatie van de initiële modelparameters verloren zijn gegaan, aan verschillen tussen het effect van de wanden van de tank in de experimentele opzet en de wijze waarop het effect daarvan wordt afgehandeld in het model, en aan de gevoeligheid van het model met betrekking tot de wrijvingscoëfficiënt c_D . De waarde van de wrijvingscoëfficiënt, in combinatie met de gediscrèteerde korrelgrootte verdeling van het sediment en de vrij lage ruimtelijke resolutie gebruikt in de simulatie, resulteert in duidelijk waarneembare gelokaliseerde sedimentatie van de drie korrelgrootte klassen, die niet wordt waargenomen in het experiment. Tevens bepaalt het verschil tussen het effect van de wanden op de troebelstromen in het experiment, en de afhandeling daarvan in het model in grote mate de hoeveelheid sediment die daadwerkelijk in de het model domein wordt afgezet. In het experiment is de bulk van het door de troebelstromen aangevoerde sediment in de tank afgezet, omdat de troebelstromen niet door en over de wanden van de tank konden stromen, terwijl in het model de wanden van de tank feitelijk niet bestaan zodat ongehinderd uitstroom kan plaatsvinden van nog gesuspendeerd sediment.

CURRICULUM VITAE

Remco Maarten Groenenberg was born in Eindhoven, The Netherlands on March 17, 1972. He graduated from secondary school, Van Maerlant Lyceum in Eindhoven, in 1990. Remco started his academic education in 1990 at Utrecht University, where he studied Geology. He received his MSc degree in 1996 with a major subject in Sedimentology on the response of a sedimentary system to changes in its dynamic equilibrium.

A few months after graduation, he started working in IT for Logica CMG, where he was contracted by Shell Exploration and Production to work on the development of, amongst others, the at that time state-of-the-art *GEOCAP* reservoir modelling suite, and *FastRack* prospect management and risk evaluation software. After three years at Logica CMG, Remco switched to the newly started company JOA Software and Services in 1999. In his two years at JOA, he became project manager for various Shell E&P software development, support and maintenance projects, and worked on *GEOCAP*, well-planner software, and software for three-dimensional visualization of the behaviour of a rotating drill string.

In 2001, after five years in IT, Remco decided to make a career change and started his Ph. D. research on numerical modelling of turbidity-current hydrodynamics and sedimentation at the department of Geotechnology, Delft University of Technology. It resulted in this dissertation.

Remco is still working at the department of Geotechnology, now as a post-doctorate associate, where he continues to work on numerical modelling of turbidity-current hydrodynamics and sedimentation, but now with focus on model validation and application at the field-scale.



LIST OF PUBLICATIONS

Groenenberg, R. M., Athmer, W., Donselaar, M. E., Sokoutis, D. and Willingshofer, E. (2007a). "Numerical modelling of turbidity-current hydrodynamics and sedimentation in a faulted-margin setting." *Abstract ID# 109739, Theme I Deep Water Reservoirs, AAPG Annual Convention and Exhibition, April 1-4, 2007, Long Beach, California, USA.*

Groenenberg, R. M., Hodgson, D. M. and Luthi, S. M. (2007b). "Controls on the geometry and internal architecture of submarine fan elements, Tanqua Depocentre, Karoo Basin, South Africa: Insights from process-based modelling." *Abstract ID# 110817, Theme I Deep Water Reservoirs, AAPG Annual Convention and Exhibition, April 1-4, 2007, Long Beach, California, USA.*

Groenenberg, R. M. (2006). "3-D Modelling of turbidite fan stratigraphy." *In: Programme and Abstracts 8th Dutch Earth-Scientific Conference (NAC8), Veldhoven, The Netherlands, April 2006: pp. 87.*

Groenenberg, R. M. and Hodgson, D. M. (2005). "3-D Modelling of turbidite fan stratigraphy." *In: Abstracts Workshop on modelling Turbidity Currents and related Gravity Currents, March 13-15, 2005, Santa Barbara (CAL), USA: 1 p.*

Groenenberg, R. M., Dijk, M. van, Weltje, G. J. and Postma, G. (2004). "Physical and numerical modelling related to prodelta environments; a review and assessment of existing models and experimental data described in the literature." *1st year contribution to EURODELTA Work Package 9, International EuroDelta Project, Jan. 2004: 86 p.*

Groenenberg, R. M. (2004). "Process-response modelling of turbidite fan stratigraphy: controls on variations in depositional architecture." *In: Programme and Abstracts 7th Dutch Earth-scientific Conference (NAC7), Veldhoven, The Netherlands, April 2004: pp. 4.3.*

Groenenberg, R. M., Weltje, G. J. and Storms, J. E. A. (2003). "Changes in delta morphology during sea level cycles: a quantitative approach." *In: Abstract Book COMDELTA, open conference on comparing Mediterranean and Black Sea Prodeltas, 26-28 October 2003, Aix-en-Provence, France: pp. 40-41.*

Storms, J. E. A., Weltje, G. J., Cattaneo, A. and Groenenberg, R. M. (2003). "Simulation of late-quaternary evolution of the northern Adriatic Sea." *In: Abstract Book COMDELTA, open conference on comparing Mediterranean and Black Sea Prodeltas, 26-28 October 2003, Aix-en-Provence, France: pp. 128-129.*

Weltje, G. J., Storms, J. E. A., Groenenberg, R. M. and Geel, C. R. (2003). "Process-response modelling of ocean-margin stratigraphy: constraints from the geological record." *In: Proc. Ocean Margin Research Conference (OMARC), Paris, France: pp. 162.*

Groenenberg, R. M. and Weltje, G. J. (1996). "Calculation of residual sediment-transport patterns on the basis of spatial trends in grain-size distributions: a test of the McLaren method." *Report (Confidential) on research by order of the Dutch Directorate for Public Works and Watermanagement, Sedimentology section, Faculty of Earth Sciences, University of Utrecht*: 58 p.